Theses and Dissertations

December 2013

Beyond the Standard Model: LHC Phenomenology, Cosmology from Post-inflationary Sources, and Dark Matter Physics

Brian J. Vlcek
University of Wisconsin-Milwaukee

BEYOND THE STANDARD MODEL:

LHC PHENOMENOLOGY,

COSMOLOGY FROM POST-INFLATIONARY SOURCES,

AND DARK MATTER PHYSICS

by

Brian J. Vlcek

A Dissertation Submitted in

Partial Fulfillment of the

Requirements for the degree of

Doctor of Philosophy

in Physics

at

The University of Wisconsin–Milwaukee

December 2013

ABSTRACT

BEYOND THE STANDARD MODEL:
LHC PHENOMENOLOGY,
COSMOLOGY FROM POST-INFLATIONARY SOURCES,
AND DARK MATTER PHYSICS

by

Brian J. Vlcek

The University of Wisconsin–Milwaukee, August 2013
Under the Supervision of Professors Xavier Siemens and Luis Anchordoqui

It is the goal of this dissertation to demonstrate that beyond the standard model, certain theories exist which solve conflicts between observation and theory – conflicts such as massive neutrinos, dark matter, unstable Higgs vacuum, and recent Planck observations of excess relativistic degrees of freedom in the early universe. Theories explored include a D-brane inspired construct of $U(3) \times Sp(1) \times U(1) \times U(1)$ extension of the standard model, in which we demonstrate several possible observables that may be detected at the LHC, and an ability to stabilize the Higgs mechanism. The extended model can also explain recent Planck data which, when added to HST data gives an excess of relativistic degrees of freedom of $\Delta N = 0.574 \pm 0.25$ above the standard result. Also explored is a possible non-thermal dark matter model for explanation of this result. Recent observations of *Fermi* bubble results indicate a signal of a 50 GeV dark matter particle annihilating into $b\bar{b}$, with a thermally averaged annihilation cross section corresponding to $\langle \sigma_b v \rangle \sim 8 \times 10^{-27} \text{ cm}^3/\text{s}$, spurs interest in a Higgs portal model suggested by Steven Weinberg. Other implications of this model are also explored such as its ability to explain dark matter direct detection results along with LHC Higgs data, and Planck data. Particle physics is complimented by possible stochastic gravitational wave searches for which a model of second order global phase transitions is explored. These transitions generate gravitational wave spectra with amplitudes of order $\Omega_{gw}h^2 \sim 10^{-24} - 10^{-15}$. Furthermore, techniques into such calculations are investigated in hopes to improve the stability required in such lattice simulations.

TABLE OF CONTENTS

LIST OF FIGURES

LIST OF TABLES

ACKNOWLEDGMENTS

Units and Conventions

- This dissertation makes use of the Einstein summing convention, where repeated indices are summed, *e.g.* $A_\mu A^\mu = A_0 A^0 + A_1 A^1 + \cdots + A_n A^n$.

- Unless otherwise specified, the Minkowski metric is given in the mostly minus form of $g_{\mu\nu} = \text{diag}[1, -1, -1, \ldots, -1]$ where there is d entries of -1 along the diagonal for $d+1$ space-time dimensions.

- This dissertation also uses natural units where $c = 1\ l_n t_n^{-1}$, $\hbar = 1\ m_n l_n^2 t_n^{-1}$, and $k_b = 1\ m_n l_n^2 t_n^{-2} T_n^{-1}$ where m_n, l_n, t_n, T_n are the units of natural mass, length, time, and temperature respectively. When using natural units, it is common practice to omit the natural unit symbols (m_n, l_n, t_n, T_n) and solely represent units in terms of energy for which several common units may be represented by [1]

$$
\begin{aligned}
\hbar c &= m_n l_n^3 t_n^{-2} \approx 197 \text{ MeV fm} \rightarrow 1 \text{ fm} = 5.08 \times 10^{-3} \text{ MeV}^{-1}, \\
c &= l_n t_n^{-1} \approx 3 \times 10^{11} \text{ fm ps}^{-1} \rightarrow 1 \text{ ps} = 1.52 \times 10^9 \text{ MeV}^{-1}, \\
k_b &= m_n l_n^2 t_n^{-2} T_n^{-1} \approx 8.62 \times 10^{-11} \text{ MeV K}^{-1} \rightarrow 1\text{K} = 8.62 \times 10^{-11} \text{ MeV}, \\
M_{pl} &= \sqrt{\hbar c / G} \approx 1.22 \times 10^{19} \text{ GeV c}^{-2} \rightarrow G^{-1/2} = M_{pl} = 1.22 \times 10^{19} \text{ GeV},
\end{aligned}
$$

where the arrows show the omission of natural units, G is Newton's gravitational constant, and M_{pl} the Planck mass. Natural units allow representation of units in terms of energy.

PREFACE

Part I on BSM particle physics phenomenology is based on material from:

- Luis A. Anchordoqui, Ignatios Antoniadis, Haim Goldberg, Xing Huang, Dieter Lüst, Tomasz R. Taylor, and **Brian Vlcek**
  LHC Phenomenology and Cosmology of String-Inspired Intersecting D-Brane Models,
  Phys. Rev. D **86**, 066004 (2012) [arXiv:1206.2537 [hep-ph]].

- Luis A. Anchordoqui, Ignatios Antoniadis, Haim Goldberg, Xing Huang, Dieter Lüst, Tomasz R. Taylor, and **Brian Vlcek**
  Vacuum Stability of Standard Model^{++},
  JHEP **1302**, 074 (2013) [arXiv:1208.2821 [hep-ph]].

Part II on gravitational waves is based on the following paper:

- John T. Giblin, Jr., Larry R. Price, Xavier Siemens, and **Brian Vlcek**
  Gravitational Waves from Global Second Order Phase Transitions,
  JCAP **1211**, 006 (2012) [arXiv:1111.4014 [astro-ph.CO]].

Part III on dark radiation and dark matter is based on material from:

- Luis A. Anchordoqui, Haim Goldberg, and **Brian Vlcek**
  Tracing the Interplay between Non-Thermal Dark Matter and Right-Handed Dirac Neutrinos with LHC Data, in Proceedings of the 33rd International Cosmic Ray Conference (ICRC 2013), Rio de Janeiro, Brazil, 2 - 9 July;
  [arXiv:1305.0146 [astro-ph.CO.]].

- Luis A. Anchordoqui and **Brian J. Vlcek**
  W-WIMP Annihilation as a Source of the Fermi Bubbles,
  Phys. Rev. D **88**, 043513 (2013) [arXiv:1305.4625 [hep-ph]].

Chapter 1

Introduction

Modern physics is built on two outstanding theories, the standard model (SM) of particle physics and the concordance model of cosmology (ΛCDM cosmology) [1]. The SM [2] is built on a mathematical footing known as quantum field theory (QFT) to describe the notions of quantum uncertainty to fields rather than point like particles. This, along with principles of symmetry, allows physicists to accurately predict the outcomes of experiments of elementary particles down near the range of approximately 2.5×10^{-20} m. To give some perspective of that scale, the radius of a hydrogen atom is about 0.5×10^{-10} m (the Bohr radius). If this scale is magnified to the size of a major city (taken to be 20 km), we would have knowledge of what's going on at the atomic level (10^{-10} m) of the city model! On the other end of the length spectrum, we have the ΛCDM model of cosmology, built upon Einstein's theory of general relativity (GR) [3]. The ΛCDM model predicts the large scale behavior of the cosmos out to 13.7×10^{9} lyr $= 1.3 \times 10^{26}$ m [4]. Both theories are considered standard for physicists, however they cannot be final theories of their respective subjects. They are effective theories, in the same sense that Newton's laws effectively describe projectiles and many other things at the macroscopic-scale, but it would be incorrect to use it to predict motions of electrons, nor the motions of highly relativistic objects [5], there is a scale at which you use the laws of quantum physics, or general relativity.

The SM and the ΛCDM model must somehow agree in their respective predictions to give a consistent theory of our observable universe. One would expect that the SM is somehow more elementary as the physics of the very small should be able to describe the physics of the very large if taken to the effective limit. The very name ΛCDM tells of our ignorance; "Λ" is the

canonical symbol for the unknown term in the Einstein field equations of GR that creates a repulsive like effect of gravity [6]. Currently this energy is associated with the non-zero energy of free space and is known as dark energy and accounts for 68.6% of the energy density of the universe. The CDM is cold dark matter, which accounts for 26.5% of the matter content of the universe [7]. The rest of the universe is ordinary matter, for which the SM seems to correctly describe. Where is the dark matter and dark energy in our current understanding of particle physics? One glaring problem of our model of cosmology is that it is a classical theory and thus cannot correctly describe the state of the universe at the time of the big bang.

As it stands today, the SM is incomplete. One of the main reasons is that it does not include gravity as one of the interactions. As well, after the recent (at the time of writing this) Higgs like particle discovery [8, 9], with an apparent mass of $m_H = 125$ GeV, the SM seems to have an unstable vacuum. This means that the current formulation of the SM cannot be correct. There are many other reasons to suspect the SM is an effective theory. These issues motivate the subject known as beyond the SM physics (BSM), where one attempts, through demanding new symmetries of the Lagrangian of the SM, to predict new particles or interactions. Of the proposed theories, two are by far the most popular, supersymmetry (SUSY) and string theory, though they are related. In Part I of this dissertation, we look at a possible extension of the SM through a string theoretical basis which imposes additional $U(N)$ symmetries on the Lagrangian of particle physics, rather than $SU(N)$ which is what the SM uses in its current formulation. We will explore the phenomenology of this new model, including LHC signals, and cosmological observables.

One key concept of the ΛCDM model is the concept of inflation put forward by Guth in 1981 [10]. It is widely accepted as the correct mechanism of flattening the universe (this will be expounded upon in Sec. 1.2.4). One exciting feature of inflation is that it takes whatever physics is occurring at the quantum level before the universe undergoes rapid expansion and magnifies it to the cosmic level! This is considered as one of the main reasons for large scale anisotropies in the cosmic microwave background (CMB) as seen in Fig. 1. We might be able to exploit this magnification and search for physics that goes beyond what the standard model offers by observing effects in CMB anisotropies and theoretically a CMB-like background of gravitons. We would expect to observe these gravitons in future interferometric gravitational
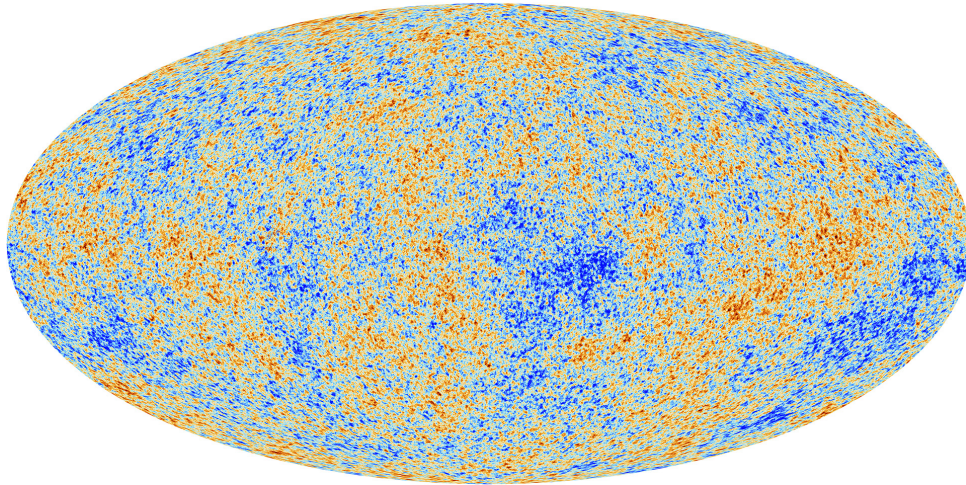
Figure 1 : The highest resolution full sky anisotropy map from generated from the Planck 2013 results [11].

wave observatories such as the laser interferometer gravitational wave observatory (LIGO) (admittedly a much more advanced detector would be needed but the concept is the same). My work in Sec. 3.1 explains the methods used to calculate what the observed background would be, given a model for the relevant fields at the time immediately after inflation.

It is also interesting to look at CMB anisotropies as probes of BSM physics, specifically in the form of dark radiation. Dark radiation is the term used to describe the excess relativistic degrees of freedom (r.d.o.f.) recently reported by the Planck Collaboration [7]. This excess results from combing data from the Planck, and the Hubble Space Telescope result of $h = 0.738 \pm 0.024$ [12], yielding $\Delta N = 0.574 \pm 0.25$. Planck data suggests the excess is statistically significant, but is as of yet unexplained by SM physics, this along with other observations will be reviewed in Sec. 4.1 of this dissertation. One possible solution to this problem is the inclusion of right chiral counterparts of the SM neutrinos which solves both neutrino masses(to be examined in the next section) and the possible r.d.o.f. excess. In Sec. 4.1 we will explore how adding right chiral neutrinos, as well as relativistic dark matter into the ΛCDM model, may explain an excess in r.d.o.f., as well as setting limits on possible observables of an additional gauge boson at the LHC.

CMB anisotropies observations are also complimented by observations of merging galaxy clusters [13] and rotation curves [14] in suggesting dark matter. The current theories suggest

weakly interacting massive particles (WIMPs) are fermionic fields that explain all the observations associated with dark matter. In the last section we will discuss a Higgs portal mechanism into exploring interactions of WIMPs with visible matter, specifically by exploring the implications of a Higgs portal model suggested by Weinberg [15], and possible detections in LHC data.

1.1 Review of the SM of Particle Physics

1.1.1 States of Definite Chirality and Spinors

Before we try to expand on the SM, we review how it is currently formulated, while exposing its weakness along the way. We start with the assumption that the reader has some knowledge of the mathematics of quantum field theory so that we may focus on the Lagrangian formulation of the SM, as well as knowledge with the workings of relativistic quantum mechanics. When we construct theories, we start with a symmetry we think nature has and see what that forces the Lagrangian to look like. One symmetry group that any theory must posses is invariance of operators of the Poincaré group, which consists of translations, Lorentz boosts of special relativity and rotations in space. All of which seem to be symmetries of all the known laws of physics. Another experimental fact we must consider is that there are two different types of elementary particles, bosons having integer spin, and fermions having half-integer spins. When constructing representations of the Lorentz group it turns out that you essentially can have two different spin $1/2$ particles that furnish the representation, which are called chiral states. If the particles have no mass then their helicities (spin handedness along their directions of motion) are the same as their chirality. The two chiral states are the left handed spin $1/2$ fermions f_L and the right handed spin $1/2$ fermions f_R. However we do not observe massless fermions in the universe, so how do we justify Lorentz invariance, spin $1/2$ particles, and massive states? The currently accepted answer is that if a fermion has mass then it is viewed as changing from one chiral state to the other by interacting with the vacuum of QFT as depicted in Fig. 2. With the two different states we write a Lorentz invariant Lagrangian for "free" fermions (free in the sense that we observe fermions in massive states and consider them free though the Lagrangian
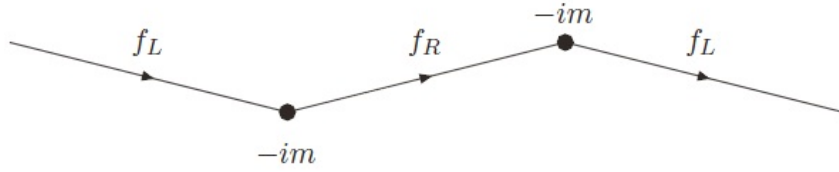
Figure 2 : A fermion is viewed as a chiral states exchanging helicities by interactions with the vacuum as indicated by the dark points in the figure above.

below is not technically free)

$$\mathcal{L}_f = i f_L^\dagger \bar{\sigma}^\mu \partial_\mu f_L + i f_R^\dagger \sigma^\mu \partial_\mu f_R - m(f_R^\dagger f_L + f_L^\dagger f_R), \tag{1.1.1}$$

where $\sigma^\mu = (1, \vec{\sigma})$ and $\bar{\sigma}^\mu = (1, -\vec{\sigma})$ with $\vec{\sigma}$ the Pauli matrices that may be familiar from ordinary quantum mechanics. We have also used the Einstein summation procedure for repeated indices.

We compact this notation from 2-component spinors f_L, f_R to a 4-component Dirac spinor,

$$f = \begin{pmatrix} f_R \\ f_L \end{pmatrix}. \tag{1.1.2}$$

This allows us to write the Dirac Lagrangian for free massive fermions

$$\mathcal{L}_f = \bar{f}(i\gamma^\mu \partial_\mu - m)f, \text{ where } \gamma^\mu = \begin{pmatrix} 0 & \bar{\sigma}^\mu \\ \sigma^\mu & 0 \end{pmatrix}, \tag{1.1.3}$$

and with $\bar{f} = f^\dagger \gamma^0$. The important property of the gamma matrices $\{\gamma^\mu, \gamma^\nu\} = 2g^{\mu\nu} I_{4\times4}$, where $g^{\mu\nu}$ is the Minkowski flat metric and $I_{4\times4}$ a four dimensional identity matrix should be noted. To demonstrate this does in fact describe relativistic fermions we do a quick calculation using the principle of least action which gives

$$\partial_\mu \left(\frac{\partial \mathcal{L}_f}{\partial \bar{f},_\mu} \right) - \frac{\partial \mathcal{L}_f}{\partial \bar{f}} = 0,$$
$$(i\gamma^\mu \partial_\mu - m) f = 0,$$
$$(-i\gamma^\nu \partial_\nu - m)(i\gamma^\mu \partial_\mu - m) f = 0,$$
$$(\partial^\mu \partial_\mu + m^2) f = 0. \tag{1.1.4}$$

The last equation is the Klein-Gordon equation or the quantum version of the special relativistic energy relation $p_\mu p^\mu = p^2 = m^2$. From this point forward we will use the notation $p_\mu p^\mu = p^2$, it should be apparent when contraction of indices is used versus the squaring of a c-number.

1.1.2 Gauge Theories

Guided by Lorentz invariance and observation of the spin $1/2$ nature of fermions, we were able to construct a relativistic Lagrangian, which has a symmetry we did not intend to supply to it. Spinors undergoing the transformation

$$f \to e^{-i\theta} f, \tag{1.1.5}$$

where θ is some real number, leave the Dirac Lagrangian invariant. In fact if we have multiple species of fermions f_i we can repeat the same Dirac Lagrangian for each species which will have a more complex but similar symmetry

$$\mathcal{L}_{\text{fermion}} = \bar{f}_i \left(i\delta_{ij}\gamma^\mu\partial_\mu - m_{ij} \right) f_j, \tag{1.1.6}$$

where m_{ij} is a diagonal mass matrix and we sum over i, j with a Euclidean metric. We perform a transformation on the collection of spinor species given by

$$f_i \to e^{-i\theta^a (T^a)_{ij}} f_j = \left(e^{-i\Theta} f \right)_i, \tag{1.1.7}$$

with T^a, a collection of matrices, and θ^a a collection of real numbers. In the second equality, I compacted the notation with $\Theta = \theta^a T^a$ (summing over internal group indices with a Euclidean metric) and

$$f = \begin{pmatrix} f_1 \\ f_2 \\ \vdots \end{pmatrix}. \tag{1.1.8}$$

The fermion Lagrangian will remain invariant under this transformation[1] if $(T^a)^\dagger = T^a$. Operators constructed with this requirement such as $U = e^{i\Theta}$ will necessarily be unitary $U^\dagger U = 1$. It is then said that the collection of N relativistic massive fermions will be invariant under operation of the global symmetry of the $U(N)$ group (why it is called global will become apparent below).

Now we change from θ^a being real numbers to $\theta^a(x)$ now being real functions of space-time. The transformation $U(x)$ now depends on one's position in space-time; which are termed local $U(N)$ gauge transformations. The Lagrangian is no longer invariant under local $U(N)$

---

[1]Note that T^a and γ^μ commute as one operates on the spinors, and one mixes the spinor species.

transformations, and the action of the gauge group operator leaves us with

$$\mathcal{L}_f \rightarrow \mathcal{L}_f + \bar{f}\left(\gamma^\mu \partial_\mu \Theta\right) f. \tag{1.1.9}$$

The problem is the derivative in the original Lagrangian. If we construct a derivative operator D_μ that transforms like $D_\mu \rightarrow U D_\mu U^\dagger$ then we will be able to construct a Lagrangian that is invariant to local $U(N)$ transformations. We accomplish this by introducing gauge fields so the derivative term becomes

$$D_\mu = \partial_\mu - ig T^a W_\mu^a(x) = \partial_\mu - ig W_\mu, \tag{1.1.10}$$

where under gauge transformations $W_\mu \rightarrow e^{i\Theta} W_\mu e^{-i\Theta} - \frac{1}{g} \partial_\mu \Theta$. Note that I have introduced a compact notation $W_\mu = T^a W_\mu^a$. Interestingly, if the gauge group is $U(1)$, then the gauge transformation rule is that of electrodynamics. Requiring invariance of the Lagrangian to operators of $U(N)$ we are able to write our new Lagrangian as

$$\mathcal{L}_f = \bar{f}\left(i\gamma^\mu D_\mu - m\right) f. \tag{1.1.11}$$

However we did not write the most general local gauge invariant terms. We left out a gauge field kinetic. We define the gauge field strength by

$$F_{\mu\nu} = \partial_\mu W_\nu - \partial_\nu W_\mu + [W_\mu, W_\nu]. \tag{1.1.12}$$

This transforms under local gauge transformations like $F_{\mu\nu} \rightarrow U F_{\mu\nu} U^\dagger$ so we may make a gauge invariant kinetic term from this by use of the permutative property of the trace operation

$$\frac{1}{2}\text{Tr}\left(F^2\right) \rightarrow \frac{1}{2}\text{Tr}\left(UFU^\dagger UFU^\dagger\right) = \frac{1}{2}\text{Tr}\left(U^\dagger U F^2\right) = \frac{1}{2}\text{Tr}\left(F^2\right). \tag{1.1.13}$$

If we restrict ourselves to using the sub group of $U(N)$ to that of $SU(N)$ then we have $\text{Tr}\left(T^a T^b\right) = \frac{1}{2}\delta^{ab}$ which allows us to explicitly write the kinetic term for the gauge fields

$$\frac{1}{2}\text{Tr}\left(F^2\right) = \frac{1}{2}\text{Tr}\left(F_{\mu\nu}^a F_b^{\mu\nu} T^a T^b\right) = \frac{1}{4}F_{\mu\nu}^a F_a^{\mu\nu}. \tag{1.1.14}$$

All together we write out the local $SU(N)$ gauge invariant Lagrangian of N types of relativistic fermions as

$$\begin{aligned}
\mathcal{L} &= \bar{f}\left(i\gamma^\mu D_\mu - m\right) f - \frac{1}{2}\text{Tr}\left(F^2\right), \tag{1.1.15} \\
&= \bar{f}_i\left(i\delta_{ij}\gamma^\mu \partial_\mu - m_{ij}\right) f_j + g\left(\bar{f}_i \gamma^\mu \left(T^a\right)_{ij} f_j\right) W_\mu^a - \frac{1}{4}F_{\mu\nu}^a F_a^{\mu\nu}. \tag{1.1.16}
\end{aligned}$$

$$\tag{1.1.17}$$

It is important to notice that the Lagrangian cannot have a mass term $m_a^2 W_a^\mu W_\mu^a$ as it will break the local $SU(N)$ gauge invariance.

1.1.3 Electroweak Model

The final formulation of the SM didn't occur until 1967 when three seminal papers [16, 17, 18] formed the Glashow-Weinberg-Salam (GWS) electroweak model of interactions. This, combined with Higgs paper [19] on symmetry breaking with a non-zero vacuum expectation value of a scalar field, allowed one to reconcile data with theory. As well the work of Feynman, Bjorken, t'Hooft, among others culminated in adding in QCD to the SM for which the Nobel Prize of 2004 was awarded to Gross, Politzer and Wilczek for there asymptotic freedom work allowing perturbative calculations to pave the way for QCD analysis in particle collider experiments [20, 21, 22, 23] . The GWS model is built by imposing a $SU_L(2) \times U_Y(1)$ symmetry. The subscript L on $SU(2)$ indicates that left handed chiral states participate differently in the gauge group operations, than the right handed chiral states. The right handed chiral states are said to be singlets of the $SU_L(2)$ symmetry; which means they transform under the symmetry operation as a scalar (no transformation) and effectively do not couple to the gauge bosons associated with that symmetry. The Y for $U(1)$ is deemed hypercharge and is similar to the charge in electromagnetism, however as we will see via the Weinberg mixing of $SU_L(2)$ and $U_Y(1)$ gauge bosons, we will form the electromagnetic gauge field we are familiar with.

Starting with the covariant derivative (D_μ operator), we have 4 gauge bosons associated with the symmetry group

$$D_\mu = \partial_\mu - ig_2 \tau^a W_\mu^a - igY B_\mu. \tag{1.1.18}$$

The operator Y acting on multiplets has eigenvalues that are the hypercharge of that multiplet. This does not affect the gauge invariance so it is allowed in our formulation. Further, we have $\tau^a = \sigma^a/2$ where σ^a are the Pauli matrices. This allows τ^a to form the generators of $SU(2)$ in the fundamental representation.

In the SM the left chiral the lepton sector doublet for one generation is,

$$E_L = \begin{pmatrix} \nu_L \\ e_L \end{pmatrix}, \tag{1.1.19}$$

the subscript L on the Dirac spinors composing the doublet are to inform you that this spinor only contains left handed chiral components. Typically this doublet is obtained by projecting out the right chiral state from the Dirac spinor used in quantum electrodynamics (QED) via the relation

$$e_L = P_L e = \frac{1}{2} \left(1 - \gamma^5 \right) e. \tag{1.1.20}$$

Along with the left chiral doublet we have a $SU_L(2)$ singlet (which is the right chiral state e_R), using the doublet and the singlet, we complete our leptonic sector for the SM for one generation, which results in

$$\mathcal{L}_{\text{Lepton}} = \bar{E}_L i\gamma^\mu D_\mu E_L + \bar{e}_R i\gamma^\mu D_\mu e_R - \frac{1}{4} W^a_{\mu\nu} W^{\mu\nu}_a - \frac{1}{4} B^{\mu\nu} B_{\mu\nu}, \tag{1.1.21}$$

where $W^a_{\mu\nu}$, $B_{\mu\nu}$ are the field strengths for $SU_L(2)$, $U_Y(1)$ gauge bosons respectively.

Notice we do not have masses for any of the leptons involved; the SM in this form cannot be recognized as physically relevant. To put it in a form that is physically meaningful, we make a change of basis for the gauge fields,

$$\begin{pmatrix} W^+_\mu \\ W^-_\mu \\ Z^0_\mu \\ A_\mu \end{pmatrix} = \begin{pmatrix} \frac{1}{\sqrt{2}} & -\frac{i}{\sqrt{2}} & 0 & 0 \\ \frac{1}{\sqrt{2}} & \frac{i}{\sqrt{2}} & 0 & 0 \\ 0 & 0 & \cos(\theta_w) & -\sin(\theta_w) \\ 0 & 0 & \sin(\theta_w) & \cos(\theta_w) \end{pmatrix} \begin{pmatrix} W^1_\mu \\ W^2_\mu \\ W^3_\mu \\ B_\mu \end{pmatrix}. \tag{1.1.22}$$

We also define a new operator $Q = \tau^3 + Y$ which we identify as electrical charge we are familiar with; as well we define $\tau^\pm = \tau^1 \mp i\tau^2$. In this new basis the covariant derivative takes the form

$$D_\mu = \partial_\mu - i\frac{g_2}{\sqrt{2}}\tau^- W^+_\mu - i\frac{g_2}{\sqrt{2}}\tau^+ W^-_\mu - i\frac{g_2}{\cos(\theta_w)} \left(\tau^3 - \sin^2(\theta_w)Q \right) Z^0_\mu - ieQA_\mu, \tag{1.1.23}$$

where $\tan(\theta_w) = g/g_2$ and $e = g_2 \sin(\theta_w)$, the elementary charge of an electron. Additionally we choose $Y E_L = -\frac{1}{2}E_L$ and $Y e_R = -e_R$, which allows us to expand the Lagrangian (with the gauge field kinetic terms not shown) as

$$\begin{aligned} \mathcal{L}_{\text{Lepton}} &= \bar{\nu}_L i\gamma^\mu \partial_\mu \nu_L + \bar{e}_L i\gamma^\mu \partial_\mu e_L + \bar{e}_R i\gamma^\mu \partial_\mu e_R + \frac{g_2}{\sqrt{2}} \left(\bar{\nu}_L \gamma^\mu e_L \right) W^+_\mu \\ &+ \frac{g_2}{\sqrt{2}} \left(\bar{e}_L \gamma^\mu \nu_L \right) W^-_\mu + \frac{g_2}{\cos(\theta_w)} \left(\frac{1}{2} + \sin^2(\theta_w) \right) \left(\bar{\nu}_L \gamma^\mu \nu_L \right) Z^0_\mu \\ &- \frac{g_2}{\cos(\theta_w)} \left(\frac{1}{2} - \sin^2(\theta_w) \right) \left(\bar{e}_L \gamma^\mu e_L \right) Z^0_\mu \\ &- e \left(\bar{e}_L \gamma^\mu e_L \right) A_\mu - e \left(\bar{e}_R \gamma^\mu e_R \right) A_\mu + \dots \end{aligned} \tag{1.1.24}$$

If we put this in terms of Dirac spinors of QED, we have

$$
\begin{aligned}
\mathcal{L}_{\text{Lepton}} &= \bar{\nu}\, i\gamma^\mu \partial_\mu P_L \nu + \bar{e}\, i\gamma^\mu \partial_\mu e \\
&+ \frac{g_2}{\sqrt{2}} \left(\bar{\nu}\gamma^\mu P_L e\right) W_\mu^+ + \frac{g_2}{\sqrt{2}} \left(\bar{e}\gamma^\mu P_L \nu\right) W_\mu^- \\
&+ \frac{g_2}{\cos(\theta_w)} \left(\frac{1}{2} + \sin^2(\theta_w)\right) \left(\bar{\nu}\gamma^\mu P_L \nu\right) Z_\mu^0 \\
&- \frac{g_2}{\cos(\theta_w)} \left(\frac{1}{2} - \sin^2(\theta_w)\right) \left(\bar{e}\gamma^\mu P_L e\right) Z_\mu^0 \\
&- e \left(\bar{e}\gamma^\mu e\right) A_\mu + \ldots
\end{aligned}
\tag{1.1.25}
$$

In this form we see we have charged vector-axial currents mediated by $W_\mu^\pm$ bosons. As well we have the typical vector current of quantum electrodynamics $\bar{e}\gamma^\mu e$ mediated by the neutral photon A_μ boson. There is also a third vector-axial current that also has neutral currents and a neutral mediator (the Z_μ^0 boson). It is important to note that we have not included a right chiral state for the neutrino as it is consistently experimentally found in a left handed chiral state.

We are able to include quarks and finish the SM gauge theory by repeating the process with the multiplets for the first generation of quarks

$$
Q_L = \begin{pmatrix} u_L \\ d'_L \end{pmatrix}, \ u_R, \ d'_R.
\tag{1.1.26}
$$

We use the symbol d'_L and not d_L because mass eigenstates of the quarks are not the same as the flavor eigenstates with the weak force interacts with. The Cabibbo-Kobayashi-Maskawa (CKM) matrix relates the mass eigenstates to the flavor eigenstates by a mixing matrix

$$
(d'_L)^i = V^{ij}(d_L)^j,
\tag{1.1.27}
$$

where $(d_L)^j$ generically denotes (d_L, s_L, b_L) for the down, strange, and bottom quarks of definite flavor and left handed chirality. To complete the SM we also include the strong interaction by adding in an $SU_c(3)$ gauge coupling, whose gauge fields comprise 8 gluons, g_μ^a. The covariant derivative now takes the form

$$
D_\mu = \partial_\mu - igY B_\mu - ig_2 \tau^a W_\mu^a - ig_3 \frac{\lambda^a}{2} g_\mu^a,
\tag{1.1.28}
$$

where λ^a are the Gell-Mann matrices of the fundamental representation of $SU(3)$. It should be

understood that $u_{L,R},\ d_{L,R}$ are $SU_c(3)$ color triplets of the form

$$u_L = \begin{pmatrix} u_L^r \\ u_L^b \\ u_L^g \end{pmatrix}, \tag{1.1.29}$$

with the (r, b, g) indicating the color charge of the particle. Even after adding in quarks and the strong interaction to the model, this cannot be the final picture, as we are left with massless, gauge bosons of $SU_L(2) \times U_Y(1)$ which experimentally is not correct. The standard solution to this problem is use of the Higgs mechanism.

1.1.4   The Higgs Mechanism

The Higgs mechanism allows us to generate masses for particles in the GWS model by adding a scalar field, the so called Higgs field. The simplest model is generated by specifying the Higgs field as a complex $SU_L(2)$ doublet

$$H = \begin{pmatrix} \phi^+ \\ \phi^0 \end{pmatrix}. \tag{1.1.30}$$

Using the $SU_L(2) \times U_Y(1)$ gauge invariance, we can choose a gauge where the Higgs field takes the convenient form

$$H \rightarrow e^{i\alpha} e^{i\theta^a \tau^a} H = \begin{pmatrix} 0 \\ \phi \end{pmatrix}, \tag{1.1.31}$$

where ϕ is a real scalar function. The Higgs mechanism requires that we choose some potential for the Higgs field $V(\phi)$ such that its minimum value is non-zero. The SM employs the "Mexican hat" potential; which along with the kinetic gauge invariant terms, the scalar part of the SM Lagrangian takes the form

$$\mathcal{L}_{\text{scalar}} = (D_\mu H)^\dagger (D^\mu H) - \mu^2 |H|^2 - \lambda |H|^4. \tag{1.1.32}$$

If we were to proceed from this without further revision we would have difficulty doing any calculations as QFT calculations make wide use of the LSZ formula (for a review of the LSZ formula see [24]) for calculating cross sections and decay rates. The LSZ formula requires that the fields involved in the calculation have a zero vacuum expectation value (vev), that is we need

$\langle 0|\phi|0\rangle = 0$. It is possible to show through calculating the quantum action [25] for scalar fields that $\langle 0|\phi|0\rangle = \phi_c$ where $\frac{\partial V(\phi)}{\partial \phi}|_{\phi_c} = 0$, that is ϕ_c is at the minimum of the effective potential which at leading order is the classical potential. By calculating the Higgs field minimum below

$$\frac{\partial V}{\partial H^\dagger} = \left(\mu^2 + 2\lambda|H|\right) H = 0$$
$$\phi_c = 0, \ \pm\sqrt{\frac{-\mu^2}{2\lambda}}, \tag{1.1.33}$$

we deduce the vev of the scalar field. However, we must not choose $\phi_c = 0$ as the vev as this corresponds to a false vacuum as it is an unstable point of the potential. Instead, we purpose that $-\mu^2 > 0$ and $\lambda > 0$, giving us a real minimum. This allows us to expand the Higgs field around the vacuum expectation value $\langle 0|\phi|0\rangle = \frac{v}{\sqrt{2}} = \sqrt{\frac{-\mu^2}{2\lambda}}$, thereby putting the Higgs field in the form

$$H = \begin{pmatrix} 0 \\ \frac{1}{\sqrt{2}}\left(v + h\right) \end{pmatrix}, \tag{1.1.34}$$

where h is a real scalar field that satisfies $\langle 0|h|0\rangle = 0$ and thus is appropriate for use in the LSZ formula. This expansion around the vev will give us mass terms in our Lagrangian, where we also assume that the Higgs field is electrically neutral, $QH = 0$

$$\begin{aligned}
\mathcal{L}_{\text{scalar}} &= \tfrac{1}{2}\partial_\mu h \partial^\mu h + \tfrac{g_2^2 v^2}{4} W_\mu^- W_+^\mu + \tfrac{g_2^2 v^2}{8\cos^2(\theta_w)} Z_\mu^0 Z_0^\mu \\
&\quad + \tfrac{g_2^2 v}{2} h W_\mu^- W_+^\mu + \tfrac{g_2^2 v}{4} h Z_\mu^0 Z_0^\mu \\
&\quad + \tfrac{g_2^2}{4} h^2 W_\mu^- W_+^\mu + \tfrac{g_2^2}{8\cos^2(\theta_w)} h^2 Z_\mu^0 Z_0^\mu \\
&\quad - (-\mu^2) h^2 - \sqrt{-\mu^2\lambda}\, h^3 - \tfrac{\lambda}{4} h^4.
\end{aligned} \tag{1.1.35}$$

This allows us to identify the masses of the particles in the theory as well as relations between them

$$M_W = \frac{g_2 v}{2},$$
$$M_Z = \frac{g_2 v}{2\cos(\theta_w)} \to M_W = M_Z \cos(\theta_w), \tag{1.1.36}$$
$$m_H^2 = -2\mu^2.$$

The Higgs mechanism can also be used to give masses to the leptons by including Yukawa interactions of the form

$$\begin{aligned}
Y_e \left(\bar{E}_L H\right) e_R + h.c. &= \tfrac{Y_e v}{\sqrt{2}} \bar{e}_L e_R + \tfrac{Y_e}{\sqrt{2}} h \bar{e}_L e_R + h.c. \\
&= m_e \bar{e}e + \tfrac{m_e}{v} h \bar{e}e,
\end{aligned} \tag{1.1.37}$$

where $h.c.$ stands for the hermitian conjugate of the entirety of the preceding equation. However this only generates a mass term for the lower spinor of the $SU_L(2)$ doublet. It is easy to add a

gauge invariant term that will generate a mass for the upper spinor of the $SU_L(2)$ doublet by adding a term like

$$Y \left(\bar{E}_L i\sigma^2 H \right) \nu_R + h.c. \ . \tag{1.1.38}$$

This term is absent in the SM for leptons, and therefore leaves neutrinos massless.

This is where we encounter our first error in the SM. From 1968 the Homestake experiment performed by Davis, Jr. and collaborators [26] suggested that the flux of solar neutrinos was not what the SM would predict when coupled to the standard solar model of the time. The generally accepted explanation for this is called neutrino oscillations. It takes the idea that the neutrino flavor states $(\nu_e, \nu_\mu, \nu_\tau)$ are not the same as the mass eigenstates, and can be expressed as the linear combination of the mass eigenstates

$$|\nu_f\rangle = \sum_m U_{fm}|\nu_m\rangle, \tag{1.1.39}$$

where ν_f are neutrino states of definite flavor and ν_m are neutrino states of definite mass. If we appeal to quantum mechanics we can calculate the probability that a neutrino of a definite flavor changes into a different flavor state. States of definite mass have a wave function of the form

$$|\nu_m(t)\rangle = e^{-i(Et-pz)}|\nu_m\rangle \approx e^{-i\left(\frac{m^2}{2E}z\right)}|\nu_m\rangle. \tag{1.1.40}$$

Which follows from the approximation that the neutrino is highly relativistic. This allows us to calculate the transition probability

$$
\begin{aligned}
P(f_2 \to f_1) &= |\langle \nu_{f_1} \mid \nu_{f_2}(t)\rangle|^2 = |\sum_{a,b} U^\dagger_{af_1} U_{f_2 b} e^{-i\frac{m_b^2}{2E}z}\langle \nu_a \mid \nu_b\rangle|^2, \\
&= |\sum_b U^\dagger_{bf_1} U_{f_2 b} e^{-i\frac{m_b^2}{2E}z}|^2, \\
&= \delta_{f_1 f_2} - 4\sum_{a>b} \text{Re}\left(U^\dagger_{af_1} U_{f_2 a} U_{f_1 b} U^\dagger_{bf_2} \right) \sin^2\left(\frac{\Delta m_{ab}^2 z}{4E}\right) \\
&\quad + 2\sum_{a>b} \text{Im}\left(U^\dagger_{af_1} U_{f_2 a} U_{f_1 b} U^\dagger_{bf_2} \right) \sin^2\left(\frac{\Delta m_{ab}^2 z}{2E}\right), \\
\Delta m_{ab}^2 &= m_a^2 - m_b^2.
\end{aligned}
\tag{1.1.41}
$$

Based on the above, we see that if there are neutrinos with different but very small masses compared to their energies, then the flavor states oscillate between each other as they propagate through space. Thus, it is possible that the deficit measurement of ν_e from solar neutrinos are

from fluctuations into ν_μ, and ν_τ. Testing this idea with reactors and accelerator beams is still on going but has been confirmed multiple times such as in Kamiokande and Super-Kamiokande Cherenkov detectors, MiniBooNE and MINOS at Fermilab and the Soudan Mine, as well as others.

Adding the Yukawa interaction term with right chiral neutrinos requires an extra level of fine tuning to the SM formulation. Fine tuning is considered theoretically un-natural,*i.e.*, to have various Yukawa couplings of strength $< \mathcal{O}(10^{-11})$ so that the neutrino masses come out to be < 2 eV [1], while the electron has a coupling of order $\mathcal{O}(10^{-6})$. The SM is not without its own fine tuning as the top coupling is of order $\mathcal{O}(0.1)$, however it would only serve to increase the level of fine tuning by introducing right chiral neutrinos. One mechanism to solve this naturalness problem is to introduce massive Majorana neutrinos as well and evoke the see-saw mechanism, which will allow for very light neutrinos and very massive additional neutrinos. For a review of the see-saw mechanism, see [27].

1.1.5   Problems with the Higgs: Naturalness

Since the SM inception, it has been experimentally verified time and time again. Shown in Fig. 3 is a comparison of measured values versus their SM predicted values [28]. The pull on the figure is an indication of how many standard deviations the observed value and the predicted value are separated by, (Pull) $\sigma_{\mathrm{measured}} = M - P$ where M is the measured observable and P the predicted value. The average of the pulls gives $\langle \mathrm{Pull} \rangle = -0.12$ showing how good of a theory the SM is. Of course we know the SM cannot be the final theory. Many of the problems associated with the SM arise because of our use of the Higgs field. To highlight this issue, we look at 1-loop corrections to the mass of the particles.

The topic of renormalization is a complicated subject; however, it comes down to one issue: we do not know the relevant physics at high energies, and in loop calculations physics at all scales appear. It is known that if one could calculate all the observables in a theory via the bare parameter values then you would not have an issue with renormalization. However, since we cannot turn off and on interactions, we cannot measure the values of the bare parameters, even with this constraint, bare values makes a great conceptual tool. The physical parameters measured will be related to their bare values through relations that can be calculated via Feynman

	Measurement	Pull	Pull -3 -2 -1 0 1 2 3
m_Z [GeV]	91.1871 ± 0.0021	.08	
Γ_Z [GeV]	2.4944 ± 0.0024	-.56	
σ^0_{hadr} [nb]	41.544 ± 0.037	1.75	
R_e	20.768 ± 0.024	1.16	
$A^{0,e}_{fb}$	0.01701 ± 0.00095	.80	
A_e	0.1483 ± 0.0051	.21	
A_τ	0.1425 ± 0.0044	-1.07	
$\sin^2\theta^{lept}_{eff}$	0.2321 ± 0.0010	.60	
m_W [GeV]	80.350 ± 0.056	-.62	
R_b	0.21642 ± 0.00073	.81	
R_c	0.1674 ± 0.0038	-1.27	
$A^{0,b}_{fb}$	0.0988 ± 0.0020	-2.20	
$A^{0,c}_{fb}$	0.0692 ± 0.0037	-1.23	
A_b	0.911 ± 0.025	-.95	
A_c	0.630 ± 0.026	-1.46	
$\sin^2\theta^{lept}_{eff}$	0.23099 ± 0.00026	-1.95	
$\sin^2\theta_W$	0.2255 ± 0.0021	1.13	
m_W [GeV]	80.448 ± 0.062	1.02	
m_t [GeV]	174.3 ± 5.1	.22	
$\Delta\alpha^{(5)}_{had}(m_Z)$	0.02804 ± 0.00065	-.05	

-3 -2 -1 0 1 2 3

Figure 3 : SM predictions versus experimental observation, where (Pull) $\sigma_{\mathrm{measured}} = M - P$ where M is the measured observable and P the predicted value From Ref. [28].

diagrams. For example, the lowest order corrections to QED fermion bare masses (m_0) is given by the diagram in Fig. 4. These diagrams result in the expression for the two point Green's

Figure 4 : The fermion experiences self interactions with the photon of QED, this leads to a correction of the bare mass parameter of the Lagrangian for QED.

function, in momentum space

$$\langle 0|T\{\bar{\psi}(p)\psi(0)\}|0\rangle = \frac{i(p\cdot\gamma + m_0)}{p^2 - m_0^2} + \frac{i(p\cdot\gamma + m_0)}{p^2 - m_0^2} iA \frac{i(p\cdot\gamma + m_0)}{p^2 - m_0^2} . \tag{1.1.42}$$

This is understood as a modification of the m_0 parameter to the particle's physical mass (m_p)

given by

$$
\begin{aligned}
m_p &= m_0 + iA, \\
A &= -e_0^2 \int \frac{d^4 k}{(2\pi)^4} \frac{\gamma^\mu \left(\gamma^\nu k_\nu + m_0\right) \gamma_\mu}{\left(k^2 - m_0^2\right) k^2}, \\
&= -i m_0 \frac{e_0^2}{2\pi^2} \int_0^\Lambda dk_E \frac{k_E}{\left(k_E^2 + m_0^2\right)}, \\
&\approx -i m_0 \frac{2\alpha_0}{\pi} \log\left(\frac{\Lambda}{m_0}\right) + \mathcal{O}\left(\alpha_0^2\right).
\end{aligned}
\tag{1.1.43}
$$

Since quantum physics allows the particles in a loop to have any energy/momentum, then as we go up in energy scale through the integration, we should expect the relevant physics to change, so much so that we don't know if the current theory is correct through out the integration region. To quantify this, we impose a cut-off of the momentum integral at Λ in calculating the loop value, representing our confidence in the theory at scales below Λ. The physically observed mass of the particle is m_p and we can relate the physical mass to the bare mass m_0 via

$$
m_0 = m_p \left(1 - \frac{2\alpha}{\pi} \log\left(\frac{\Lambda}{m_p}\right) + \mathcal{O}\left(\alpha^2\right)\right).
\tag{1.1.44}
$$

We have replaced α_0 by α because corrections to α_0 are $\mathcal{O}\left(\alpha_0^2\right)$ and thus do not appear at the α order. From this we can deduce that even if $\Lambda = 10^{16}$ GeV then $m_0 - m_p = -0.10$ amazingly even if we use the physical mass m_p in our calculations when we should have been using the bare mass m_0, we are only making an error of 10%. It is said to be natural in QED for fermions to have a low mass, as contributions from very high energies do not significantly change the bare mass of the particle.

If we repeat this calculation for a scalar field we get a much different result. Corrections of a ϕ^4 scalar field to the mass of the particle are given by the diagram in Fig. 5 This diagram

Figure 5 : The scalar field experiences self interactions, which leads to a correction of the bare mass parameter of the Lagrangian for scalar fields that is much different than that of QED.

results in the modification of the bare mass of the scalar field particle given as

$$
\begin{aligned}
m_p^2 &= m_0^2 - iA \,, \\
A &= \frac{\lambda_0}{2} \int \frac{d^4 k}{(2\pi)^4} \frac{1}{k^2 - m_0^2} \approx -i\frac{\lambda_0}{32\pi^2} \left(\Lambda^2 - 2m_0^2 \log \left[\frac{\Lambda}{m_0} \right] \right) .
\end{aligned}
\tag{1.1.45}
$$

From this we see that $m_p^2 - m_0^2 \approx -\frac{\lambda_0}{32\pi^2}\Lambda^2$. Given the recent discovery of a Higgs-like particle with a mass of $m_H = 125$ GeV, it seems that if $\Lambda = 10^{16}$ GeV we are making a very large mistake using the tree level mass m_p when we should be using the bare mass of the scalar field m_0, as it is natural for the bare mass to be very large. This is odd as perturbation theory requires λ_0 to be small but it would seem to agree with experiment that λ_0 must be very, very small on the order of 10^{-32}! While the bare mass term would be on order of 10^2 it would be very odd (un-natural) to have a theory where the parameters vary in strength so wildly! This is also known as a fine-tuning problem, and is a main motivator for beyond the standard model physics, especially supersymmetry which solves this issue by removing exclusively scalar field quantum corrections.

1.1.6 Problems with the Higgs: Stability

The Higgs mechanism depends on a non-zero, real vacuum expectation value. It must be that the observed non-zero vacuum expectation value measured at all energy interactions is non-zero and real. So it must be that the physical couplings $\lambda(Q), \mu^2(Q)$ at the scale Q, must have $-\mu^2(Q) > 0 \to m_H^2(Q) > 0$, and $\lambda(Q) > 0$. If we consider the self coupling the dominate term in the Higgs interactions, then the renormalization for $\lambda(Q)$ at first order gives

$$
\lambda(Q) = \frac{\lambda(q)}{1 - \lambda(q)\frac{3}{4\pi^2} \log\left(\frac{Q^2}{q^2}\right)},
\tag{1.1.46}
$$

while $-\mu(Q)^2$ stays essentially fixed over a large range of Q. If we rewrite the renormalization equation in terms of the Higgs mass we get a lower bound on what the Higgs mass can be,

$$
Q < m_H \exp\left(\frac{4\pi^2 v^2}{3 m_H^2} \right),
\tag{1.1.47}
$$

where Q is the scale of new physics. There is also another limit in which this calculation will no longer be correct, if $\lambda(Q) > 1$. The calculation is based on perturbation theory so it should be that $\lambda(Q) \ll 1$, and using this as a bound gives

$$
Q < M_H \exp\left(\frac{4\pi^2}{3} \frac{v^2}{m_H^2} \left(1 - \frac{m_H^2}{2v^2} \right) \right).
\tag{1.1.48}
$$

If we include all of the couplings of the SM we get a bound on the Higgs mass and Λ shown in Fig. 6. For a Higgs mass $m_H = 125$ GeV, this indicates to us the SM vacuum is no longer
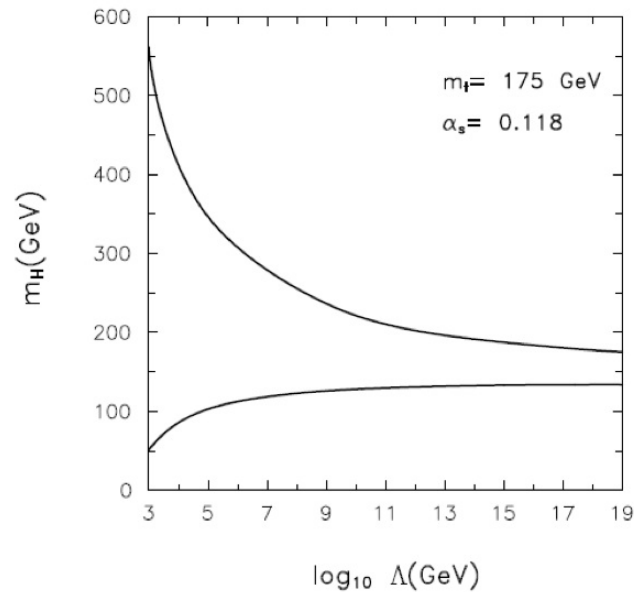
Figure 6 : Stability of the Higgs vacuum under the SM requires the mass of the Higgs to fall with the curves at the given energy scale Λ which you expect the SM to still be correct . Taken from Ref. [28].

stable at around $Q = 10^9 - 10^{10}$ GeV, and should be taken as an indication of some new physics around this scale.

1.1.7 Accidental Symmetries of the SM

Besides the gauge symmetries and space-time symmetries of the SM we also have accidental symmetries that occur. Noether's theorem states that any symmetries of the action correspond to conserved currents. These accidental symmetries are global $U(1)$ symmetries that are associated with Baryon number B and Lepton number L conservation, and are enacted by the transformations of the form

$$E_L \rightarrow e^{i\beta} E_L, \; e_R \rightarrow e^{i\beta} e_R; \tag{1.1.49}$$

with a similar $U(1)$ transformation for quarks that corresponds to Baryon number conservation. In some grand unified theories (GUT) the decay of a proton is possible, though experiment suggests that the half life of the proton is at least 10^{33} years [29]. If proton decay is possible then the Baryon and Lepton number will be violated, however $B - L$ will not be.

1.1.8 Anomalies

Chiral theories coupled with gauge theories typically are not consistent. The SM has interaction currents that have an axial term of the form

$$J_A^\mu = \bar{\nu}\gamma^\nu\gamma^5 e. \tag{1.1.50}$$

This is a problem for QFT because renormalization of divergent gauge field theories such as the SM depend on interaction currents to respect their current conservation equations [30]. However, axial currents do not remain conserved at the quantum level. Triangle diagrams of the type depicted in Fig. 7 have the potential to break the conservation of currents. In the SM
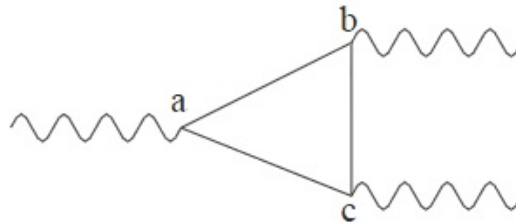
Figure 7 : Triangle diagrams like this one can show the delicate balance required on gauge theories with chiral matter fields to remain renormalizable.

we have both axial and vector currents and this problem persists. The anomalies must cancel if the SM is to remain renormalizable, which is only possible by modifying the particle spectrum of the theory.

The anomaly will no longer be present if $\text{Tr}[T^a\{T^b, T^c\}] = 0$ where T^a, T^b, T^c are the generators of the gauge transformations of the SM at the interaction vertices of the triangle diagram. If we consider a triangle diagram containing only $SU_L(2)$ gauge bosons then

$$\text{Tr}[\sigma^a\{\sigma^b, \sigma^c\}] = 2\delta^{bc}\,\text{Tr}[\sigma^a] = 0. \tag{1.1.51}$$

We have no inherent anomalies with $SU_L(2)$, so there is no need to modify the particle spectrum. However, considering two vertices having $SU_L(2)$ gauge bosons W_μ^3 and one vertex with a $U_Y(1)$ boson (the generator of the $U_Y(1)$ gauge symmetry is the hypercharge Y), the trace

then evaluates to

$$\text{Tr}[Y(\tau^3)^2] = \sum_L Y_i(\tau_i^3)^2 + \sum_R Y_i(\tau_i^3)$$
$$= 2(-1) + 3 \cdot 2 \cdot \tfrac{1}{3}. \tag{1.1.52}$$

The use of the trace here is generalized to include a sum over all possible particles circulating in the loop of the triangle. Let us examine this result, $2(-1)$ comes from the 2 left chiral parts of E_L while $3 \cdot 2 \cdot \frac{1}{3}$ comes from the left chiral part of the quark content Q_L (the 3 because of the 3 different colors the quark can posses). If you repeat the process you are lead to the conclusion that anomalies can only cancel if the SM has complete $(e_R, E_L, Q_L, u_R, d_R)$ particle spectrums for each generation. In fact this result was used to predict the top quark's existence [31] in 1973 by Maskawa, and Kobayashi.

1.1.9 Beyond the SM

The symmetries allowed in the SM make up a great deal of how it works, but massive neutrinos and accidental symmetries have yet to be explained. There are other problems plaguing the SM the most obvious of which is its absence of gravity. Gravity presents a problem for the SM, as it is very very weak compared to the rest of the gauge couplings. Consider that that electroweak interactions occur at the scale of $M_Z = 91$ GeV while the relevant scale of gravitational interaction is $M_{pl} \approx 10^{19}$ GeV. How can any unified theory overcome this enormous scale difference? One popular theory that can solve such a problem is the inclusion of extra dimensions. If you consider Guass's equation to be fundamental[2] for any number of dimensions D with $M_{pl}^{(D)}$ the fundamental gravitational scale for D dimensions, then Guass's law is

$$\nabla \cdot \mathbf{G}^{(D)} = \frac{4\pi}{\left(M_{pl}^{(D)}\right)^2} \rho^{(D)}. \tag{1.1.53}$$

If we then consider a ring of mass distributed around a compactified dimension that takes the shape of a cylinder of radius R then we can then write $\rho^{(5)} = m\, \delta^{(3)}(\mathbf{x})$ (the 5 indicates the one extra spatial direction added from the usual $3+1$ dimensions we are used to). If we integrate out the compactified dimension we would find a point mass in 3 spatial dimensions with a mass density of the form $\rho^{(4)} = M\delta^{(3)}(\mathbf{x})$ the question is what is the relation between the two mass

---

[2]This derivation follows that of [32].

densities? Upon integration we can find the result:

$$M = \int_{-\infty}^{\infty} dx_1 dx_2 dx_3 \int_0^{2\pi R} dx_4 m \, \delta^{(3)}(\mathbf{x}),$$

$$M = m \, 2\pi R \rightarrow \rho^{(5)} = \frac{1}{2\pi R}\rho^{(4)}. \tag{1.1.54}$$

Adding this to our Guass's equation gives

$$\nabla \cdot \mathbf{G}^{(4)} = \frac{4\pi}{(2\pi R)\left(M_{pl}^{(5)}\right)^2}\rho^{(4)} = \frac{4\pi}{\left(M_{pl}^{(4)}\right)^2}\rho^{(4)}. \tag{1.1.55}$$

This tells us the fundamental scale of gravity $M_{pl}^{(4)} = \sqrt{2\pi R}M_{pl}^{(5)}$, if $2\pi R > 1$ then $M_{pl}^{(4)}$ becomes larger than the fundamental scale of gravitational physics. This procedure generalizes to many compactified dimensions so that the final form is

$$M_{pl}^{(4)} = \sqrt{V_c}M_{pl}^{(4+d)}, \tag{1.1.56}$$

where V_c is the volume of the d additional compactified dimensions. With extra dimensions it becomes easier to unify gravity with the other three known forces and extra dimensions are a general attribute of string theory, though these extra spatial dimensions have yet to have been detected [33, 34, 35, 36, 37, 38, 39, 40, 41, 42].

Along with the absence of gravity in the SM, we must also ask why does the SM repeat the same rules for 3 generations. This should be looked upon like a periodic table, the same behavior of certain elements in chemical reactions ends up being explained by a simpler unifying model of electrons and atomic shells. We should take the 3 generations repeating in higher masses but same interactions as a hint of a substructure to the SM. The SM is viewed as an effective field theory at the present moment and experiments conducted at the Large Hadron Collider (LHC) at CERN may offer hints at what is beyond the SM. Many theories are currently exploring possible extensions, one of which will be discussed in part I of this dissertation.

1.2 Review of ΛCDM Cosmology

Cosmology also can provide us with a window into BSM physics. Using cosmology to explore new physics requires knowledge of the current standard model of cosmology known as the ΛCDM model. We will review some of the main results of ΛCDM as it will be used for calculations of gravitational wave stochastic background which will be explored in Part II of this

dissertation. As well, ΛCDM is used for searches for extra relativistic degrees of freedom during the early universe that the SM does not account for. As this is not a comprehensive review, it is assumed the reader has knowledge of the theory of general relativity and has experience with these results.

1.2.1 FRW metric

The universe on the large scale (larger than 10^2 Mpc) seems to be isotropic and homogenous. If one asks what is the most generally isotropic and homogenous metric one can formulate, we are lead to the Friedmann-Robertson-Walker (FRW) metric [43, 44, 45, 46, 47]

$$ds^2 = dt^2 - a(t)^2 \left(\frac{dr^2}{1 - kr^2} + r^2 d\Omega^2 \right), \tag{1.2.1}$$

where $a(t)$ is known as the scale factor, and k indicates the curvature of the universe, with $k = 1$ corresponding to closed, $k = 0$ to flat, and $k = -1$ to open. In equation (1.2.1) the Ω is the solid angle familiar to spherical coordinates. The use of this metric alone allows us to make an interesting observation, that the all objects a proper distance d_p away (and considered at coordinate distance R away from the origin) are moving with a velocity proportional to their proper distance as can be seen below,

$$d_p = a(t) \int_0^R \frac{dr}{\sqrt{1 - kr^2}} \rightarrow v_p = \dot{a}(t) \int_0^R \frac{dr}{\sqrt{1 - kr^2}} = \frac{\dot{a}(t)}{a(t)} d_p = H(t) d_p. \tag{1.2.2}$$

In (1.2.2) the value $H(t)$ is the well known Hubble's constant [48]. Strictly, $H(t)$ actually isn't a constant in this equation, however if it varies slowly compared to observation time then it can be approximated to be constant. This embodies the concept of the expanding universe, with everything at a radial distance d_p moving away with the same velocity. This immediately leads to the idea of the Big Bang, as all the objects move closer together as you reverse time. Solving for the age of the universe requires you to know the form of the scale factor $a(t)$. You can solve for t in terms of H_0, the Hubble constant measured today, thus calculating the age of the universe. Even from this concept of a finite age of the universe many things can be deduced about what we should observe today, most importantly the CMB which we shall touch on in the next section.

If we apply the FRW metric to the Einstein field equations with the modification of a cosmological constant Λ, which does not break the general coordinate symmetry of GR, we arrive

at the Friedmann equations

$$\left(\frac{\dot{a}}{a}\right)^2 + \frac{k}{a^2} = \frac{8\pi}{3}\frac{1}{M_{pl}^2}\rho + \frac{\Lambda}{3},$$

$$\frac{\ddot{a}}{a} = -\frac{4\pi}{3}\frac{1}{M_{pl}^2}\left(\rho + 3P\right) + \frac{\Lambda}{3}. \qquad (1.2.3)$$

We have assumed the matter content is a homogenous perfect fluid with mass-energy density ρ and pressure P. If we re-express this equation in terms of the Hubble constant, we get

$$1 + \frac{k}{a^2 H^2} = \frac{8\pi}{3}\frac{1}{M_{pl}^2 H^2}\left(\rho + \frac{\Lambda M_{pl}^2}{8\pi}\right) \rightarrow \frac{k}{a^2 H^2} = 1 - \Omega,$$

$$\Omega = \frac{8\pi}{3}\frac{1}{M_{pl}^2 H^2}\left(\rho + \frac{\Lambda M_{pl}^2}{8\pi}\right) = \frac{\sum_i \rho_i}{\rho_c}, \qquad (1.2.4)$$

where ρ_i is the energy density content for different types of matter, *e.g.* baryonic matter, radiation, dark energy, *etc*. We can see if $\Omega = 1$ then the universe is flat, $k = 0$. This only occurs if the universe has an energy density equal to the critical density $\rho_c = 3M_{pl}^2 H^2/8\pi$. Given that the universe is free to have any content, there are infinitely many more configurations of the universe not having this exact critical density, so it would be a surprise to find that the matter content is such that $\Omega = 1$. Combining the two Friedmann equations gives

$$\dot{\rho} + 3\frac{\dot{a}}{a}\left(\rho + P\right) = 0, \qquad (1.2.5)$$

which is a different statement of the 1st law of thermodynamics for a universe with 3 spatial dimensions. To demonstrate equation (1.2.5) is the 1st law of thermodynamics, consider a sphere of proper volume $V(t) = \frac{4\pi}{3}a(t)^3 r_0^3$, then $dQ = dU + PdV$ gives

$$\begin{aligned} dQ &= d(\rho V) + PdV, \\ dQ &= (d\rho)V + (\rho + P)\,dV, \\ dQ &= \dot{\rho} + \frac{\dot{V}}{V}\left(\rho + P\right), \\ dQ &= \dot{\rho} + 3\frac{\dot{a}}{a}\left(\rho + P\right) = 0. \end{aligned} \qquad (1.2.6)$$

As a consequence of a homogenous universe, there can be no heat flow $dQ = 0$. This forces the entropy to be constant, $dS = dQ/T = 0$. The conservation of entropy allows us to derive a

useful result[3]

$$
\begin{aligned}
0 &= dQ = TdS = d(\rho V) + PdV = Vd\rho + (\rho + P)dV, \\
TdS &= T\left(\left(\frac{\partial S}{\partial T}\right)dT + \left(\frac{\partial S}{\partial V}\right)dV\right) \to T\left(\frac{\partial S}{\partial T}\right) = V\frac{\partial \rho}{\partial T}, \quad \left(\frac{\partial S}{\partial V}\right) = \frac{\rho + P}{T}, \\
\frac{\partial^2 S}{\partial V \partial T} &= \frac{\partial^2 S}{\partial T \partial V} \to \frac{\partial^2 S}{\partial T \partial V} = \frac{1}{T}\rho' = -\frac{\rho + P}{T^2} + \frac{\rho' + P'}{T}, \\
dP &= \frac{\rho + P}{T}dT,
\end{aligned}
$$
(1.2.7)

where $\rho' = d\rho/dT$, and $P' = dP/dT$. This allows an expression for the entropy per unit volume

$$
\begin{aligned}
dS &= \frac{1}{T}d((\rho + P)V) - \frac{V}{T}dP = \frac{1}{T}d((\rho + P)V) - \frac{V}{T^2}(\rho + P) = d\left(\frac{(\rho + P)V}{T}\right), \\
s &= \frac{S}{V} = \frac{\rho + P}{T} + \text{const.}
\end{aligned}
$$
(1.2.8)

We take as the definition of s to be the case where const $= 0$. For calculations we typically only count relativistic species as contributing towards the entropy per unit volume. Why is this? We can make use of statistical mechanics to derive the pressure and energy density for fermions and bosons,

$$
\rho = \int \frac{d^3p}{(2\pi)^3}\frac{g\,E}{e^{\beta E} \pm 1}, \quad P = \int \frac{d^3p}{(2\pi)^3}\frac{p}{3E}\frac{g}{e^{\beta E} \pm 1},
$$
(1.2.9)

where $E = \sqrt{p^2 + m^2}$, $\beta = 1/T$, and g is the degeneracy for the respective particle for the energy level E. With $e^{\beta E} \pm 1$ we use the $+$ for fermions and $-$ for bosons. In the highly relativistic limit ($m\beta \ll 1$) the particles behave as massless, and the results of equation (1.2.9) give for bosons and fermions respectively,

$$
P = \frac{1}{3}\rho = \left(1, \frac{7}{8}\right)g\frac{\pi^2}{30}T^4 \to s = \left(1, \frac{7}{8}\right)g\frac{2\pi^2}{45}T^3.
$$
(1.2.10)

While in the non-relativistic limit ($m\beta \gg 1$) the pressure and energy density are the same for bosons and fermions

$$
\rho = g\,m\left(\frac{mT}{2\pi}\right)^{3/2}e^{-\beta m}, \quad P = \frac{\rho}{m}T \to s = \frac{g}{T}\left(\frac{mT}{2\pi}\right)^{3/2}(1 + T/m)e^{-\beta m}.
$$
(1.2.11)

The suppressive nature of the $\exp(-\beta m)$ makes the non-relativistic particles contribute significantly less to the pressure, energy density, and entropy of the universe compared to the

---

[3]derivation follows that of [49].

relativistic particles. In most cases it will be appropriate to ignore the contributions from non-relativistic species when considering the thermodynamics of the universe.

After our discussion of thermodynamics, we now can determine for the simplest cases, the equation of state of the perfect fluids dominating the stress energy tensor for the universe. With this information we can determine the effect on the scale factor. In general the equation of state can typically be related to the energy density ρ through a temperature dependent constant $P = w\rho$. For example, if we consider radiation (highly relativistic particles), we see in equation (1.2.10) that $P = \rho/3$. While dust (non-relativistic matter) would essentially have no internal kinetic energy ($T/m \approx 0$), we may then fix the pressure for dust as $P = 0$. For these two cases the scale factor evolves like

$$\dot{\rho} + 3\frac{\dot{a}}{a}\left(1 + w\right)\rho = 0,$$
$$\frac{d\rho}{\rho} = -3\left(1 + w\right)\frac{da}{a},$$
$$\rho(a)a^{3(1+w)} = \rho_0 a_0^{3(1+w)}, \tag{1.2.12}$$

which tells us that for matter dominated universes, we have $\rho_m \propto a(t)^{-3}$, and for radiation dominated, $\rho_r \propto a(t)^{-4}$. The first Friedmann equation (1.2.4) with $k = 0$ (the $k = 0$ result will be used later on) can give us more detail of the scale factor by inclusion of equation (1.2.12) we have

$$\frac{\dot{a}}{a} = \sqrt{\frac{8\pi}{3}\frac{\rho_0}{M_{pl}^2}}a^{-\frac{3(1+w)}{2}} \rightarrow a^{\frac{3(1+w)}{2}-1}da = \sqrt{\frac{8\pi}{3}\frac{\rho_0}{M_{pl}^2}}dt,$$
$$a(t) \propto t^{\frac{2}{3(1+w)}}. \tag{1.2.13}$$

We have assumed the condition $a(t_0 = 0) = 0$ in the result. With Eq. (1.2.13) the solutions for matter dominated universes is $a(t) \propto t^{\frac{2}{3}}$ and radiation dominated universes is $a(t) \propto t^{\frac{1}{2}}$.

1.2.2 Cosmic Microwave Background

If we look at the thermal history of the universe by rewinding time, we are also bringing all the the matter in the universe into a smaller volume, thus increasing the density. When rewinding time the cosmic redshift of photons will reach a point at which all photons will have energies above $Q = 13.6$ eV, the binding energy of hydrogen. At this point the hydrogen disassociates into free protons and electrons. This matter will then be in a Baryon photon plasma state. When the universe expands, there is a point where the photons ionizing the hydrogen will no longer be within the mean free path for ionization, so the photons start to freely stream in the universe. Since the universe is assumed to be homogenous then we should expect this to occur

everywhere in the universe. We would expect to be able to observe these free streaming photons today redshifted to a longer wavelength. We also expect that the spectrum of photons is that of a blackbody as they originate from thermal equilibrium of free protons and electrons.

To calculate the temperature at the time of recombination (the point at which stable hydrogen forms) we examine the process that produces thermal equilibrium in this era, namely the photo dissociation and recombination $H + \gamma \leftrightarrow p^+ + e^-$. It is useful to define $X = n_p/(n_p + n_H)$, where X is the fraction of ionized matter. We should expect that the hydrogen (and other elements that are being produced) are non-relativistic and have a Boltzmann-like thermal distribution so that the number density for a type of particle x with degeneracy g_x is

$$n_x = g_x \left(\frac{m_x}{2\pi\beta} \right)^{3/2} e^{-\beta m_x}. \tag{1.2.14}$$

We also assume that the universe as a whole is electrically neutral which then requires $n_p = n_e$ (all electrically charged particles are in their most stable state). This allows us to express the ratio of the number densities of hydrogen, protons, and electrons as,

$$\frac{n_H}{n_p n_e} = \frac{g_H}{g_e g_p} \left(\frac{m_H}{m_e m_p} \right)^{3/2} (2\pi\beta)^{3/2} e^{\beta(m_e + m_p - m_H)}, \tag{1.2.15}$$

$$\approx \left(\frac{m_e}{2\pi\beta} \right)^{-3/2} e^{\beta Q}. \tag{1.2.16}$$

This is known as the Saha equation [4]. In this expression $g_H = 4$, $g_p = 2$, $g_e = 2$ and to a good approximation $m_H = m_p$. In Eq. (1.2.16), $Q = 13.6$ eV, the binding energy of the first orbital of the hydrogen atom. Re-arranging our fractional ionization expression gives

$$n_H = \frac{1 - X}{X} n_p, \tag{1.2.17}$$

which can be related to the number density of photons n_γ via an additional relation of $\eta = (n_p + n_H)/n_\gamma = n_p/(X n_\gamma)$ where $n_\gamma = (2\zeta(3)/\pi^2)T^3$. This results in

$$n_p = \eta X n_\gamma = \eta X \frac{2\zeta(3)}{\pi^2} \frac{1}{\beta^3},$$

$$\frac{1-X}{X^2} = \eta \frac{2\zeta(3)}{\pi^2} T^3 \left(\frac{m_e T}{2\pi} \right)^{-3/2} \exp[\beta(13.6 \text{ eV})], \tag{1.2.18}$$

$$\frac{1-X}{X^2} = 3.84 \, \eta (m_e \beta)^{-3/2} e^{\beta Q}.$$

The time of recombination is defined as the time when $X = 1/2$ and we can find η at the time of recombination by measuring $n_p + n_H$ and n_γ today and taking into account that number

densities scale like $a(t)^{-3}$ and thus η remains fixed for all time. Measurements of baryonic matter today show $\Omega_{b,0} \approx 0.05$, which is accomplished by measuring abundance of light elements in galaxies. This allows us to find the number density of baryonic matter today. We can assume that the baryonic matter is non-relativistic so its energy is dominated by mass energy, which is mostly in the form of hydrogen or free protons which both have a mass of nearly $m_p = 938 \text{ MeV}/c^2$. We find

$$n_{b,0} = \frac{\rho_c \Omega_{b,0}}{m_p c^2} \approx 0.5 \, h^2 \, \text{m}^{-3}, \tag{1.2.19}$$

where $H = 100h$ km/s/Mpc. To make our calculation more precise we can use the measured CMB temperature of $T = 2.7$ K. An interesting note is without measuring a photon background you could use the fact that we cannot see a uniform background at night so it must be that $T_{\gamma,0} < 6 \, K$ so that the peak of the blackbody radiation today lies, at most, in the infrared, but the rest of this section takes the value of $T = 2.7$ K. This gives $n_{\gamma,0} \approx 3.81 \times 10^8 \, \text{m}^{-3}$. Using $h = 0.7$, $\eta \approx 6.43 \times 10^{-10}$; this allows us to find the temperature at which recombination is half way complete to be approximately $T \approx 3,773 \, K$.

We can also find the temperature at which the photon background decouples from interactions with electrons. We can approximate the conditions for decoupling by using the equation for mean free path distance, is $d = 1/(n\sigma)$, where σ is the interaction cross section and n the number density of interaction points. In an expanding universe a particle cannot exceed the particle horizon distance d_p, the furthest distance a particle moving at the speed of light can travel since the big bang. During the time of radiation dominance the horizon distance is $d_p = 1/H$ and in the time of matter dominance is $d_p = 2/H$; in both cases the length scale is set by $1/H$ the Hubble horizon distance. If the mean free path becomes larger than the particle horizon, then the particles can no longer interact and become free streaming. This gives the relation, $d \geq d_p \to \Gamma = n\sigma \leq H$. For photons scattering off bound electrons and non-relativistic free electrons, we approximate the interaction cross section by the dominant Thomson cross section $\sigma_e \approx 8\pi\alpha^2/(3m_e^2)$. This allows us to calculate the approximate temperature of the photons when they began free streaming by first calculating the interaction rate,

$$\Gamma(T) = n_e(T)\sigma_e = \frac{X(T)n_{b,0}}{a(T)^3}\sigma_e. \tag{1.2.20}$$

The Friedmann equations allow us to replace the scale factor with a relation to the dominant

matter term during decoupling (the universe is a matter dominated phase at this time)

$$H = \frac{H_0}{a^{3/2}} \Omega_{m,0}^{1/2}. \tag{1.2.21}$$

We use $\Omega_{m,0} \approx 0.3$, (a result determined by analysis of CMB anisotropies and the discrepancy between $\Omega_{m,0} > \Omega_{b,0}$ leading to more evidence of dark matter). With the decoupling condition $\Gamma(T) = H(T)$ we can determine when the photons decouple:

$$\begin{aligned}
\frac{X(T)}{a(T)^{3/2}} &= \left(\frac{H_0 \Omega_{m,0}^{1/2}}{n_{b,0} \sigma_e} \right), \\
X(T)T^{3/2} &= T_0^{3/2} \left(\frac{H_0 \Omega_{m,0}^{1/2}}{n_{b,0} \sigma_e} \right), \\
T_\gamma^{\text{dec}} &\approx 2945 \ K.
\end{aligned} \tag{1.2.22}$$

In the second line we used the fact that as the photons red-shift the spectrum retains its shape but moves to lower energies. This allows us to relate the temperature of the photons with the scale factor as $T(t) = T_0/a(t)$, where T_0 is the temperature of the photons measured today and the convention $a(\text{today}) = 1$ is used. With a matter dominated universe from the point of free streaming to today, this corresponds to a time of $t \approx 539,066$ years after the big bang.

Presumably there should also be stochastic backgrounds from all particle types that decouple from interactions at certain temperatures. Consider a neutrino background which we can estimate would become free streaming at $\Gamma = n_e \langle \sigma \rangle \propto G_F^2 T^5$.[4] With $H \propto T^2/M_{pl}$, which gives us an order of magnitude estimate of (a similar argument is presented in [49] p. 74)

$$\frac{G_F^2 T^5}{T^2/M_{pl}} \approx \left(\frac{T}{1 \text{ MeV}} \right)^3. \tag{1.2.23}$$

For temperatures around $T_\nu = 10^{10} \ K$, well before the photons decouple, the neutrinos decouple from the plasma and become free streaming. The effect of theses additional relativistic particles will be seen when we examine CMB anisotropies, and will play a crucial role in searching for BSM, discussed in Sec. 4.1. Furthermore, we expect a gravitational wave background at an even earlier time! However this background will be overpowered by any other sources of stochastic gravitational waves produced at later times. We will investigate such a process in Part II of this dissertation.

---

[4]Valid when the reactions $e + \nu_e \leftrightarrow e + \nu_e$ and $e^+ + e^- \leftrightarrow \nu_e + \bar{\nu}_e$ falls out of equilibrium, which occurs when the electrons are still relativistic but have center of mass energies far from the $W^\pm$ resonance so Fermi's constant G_F is appropriate to use.

1.2.3   Cosmic Parameter Measurement

In 1965 Penzias and Wilson of Bell Labs detected a cosmic background of 3.5 K. However it was Dickem, Peebles and Wilkinson who would interpret the excess power at 3.5 K as the cosmic photon background [50]. Penzias and Wilson would go on to receive the Nobel prize in physics in 1978 for this discovery. The Cosmic Background Explorer (COBE) satellite would show that the sky is filled with a black-body radiation at a temperature of 2.7 K [51] as depicted in Fig. 8.
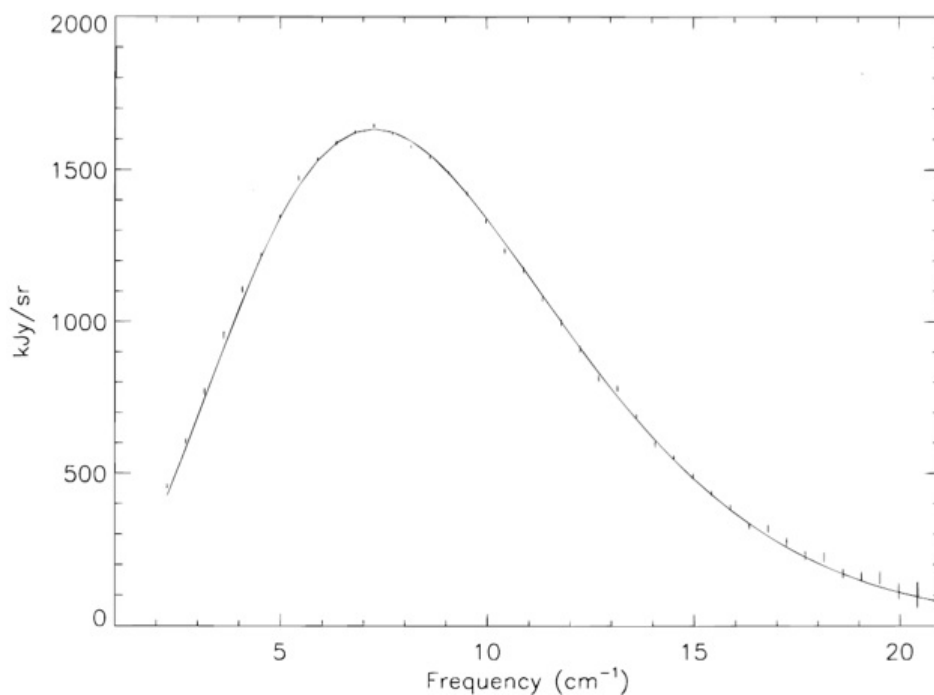
Figure 8 : Black-body curve corresponding to $T = 2.7$ K from the COBE, FIRAS detector [51].

We expect to find that since the universe is homogenous on large scales today, it has always been homogenous, even during the period of photon decoupling. It should not be surprising that each causal patch of the sky has a black-body spectrum with a temperature near 2.7 K because of this homogeneity. Some differences from patch to patch are to be expected as the universe cannot be perfectly homogenous or else it is unclear how galaxies could form. These small differences in temperatures in the CMB are called CMB anisotropies. The CMB anisotropies were measured with a resolution of 10 arc-minutes by the Planck ESA-NASA satellite and whose results were released 20 March 2013 [7]. Previously, the Wilkinson Microwave Anisotropy

Probe (WMAP) had measured the CMB anisotropies with the highest resolution and released its 9-year data in December 2012. Surprisingly the differences in temperature from causal patch to causal patch are on the order of 10^{-5}. How can it be that the early universe is so homogenous even for places out of causal contact? This is known as the horizon problem and will be addressed in the next section.

Measurement of the anisotropies provides a method of measuring several cosmological parameters, such as the curvature, total matter content, and baryonic content, among other things. A review of the analysis and interpretation of the CMB anisotropies can be found in reference [52]. The results of the measurement of the anisotropies forms the ΛCDM model of cosmology. The main results of which are listed in Fig. 9. Measurements of these parameters suggests that
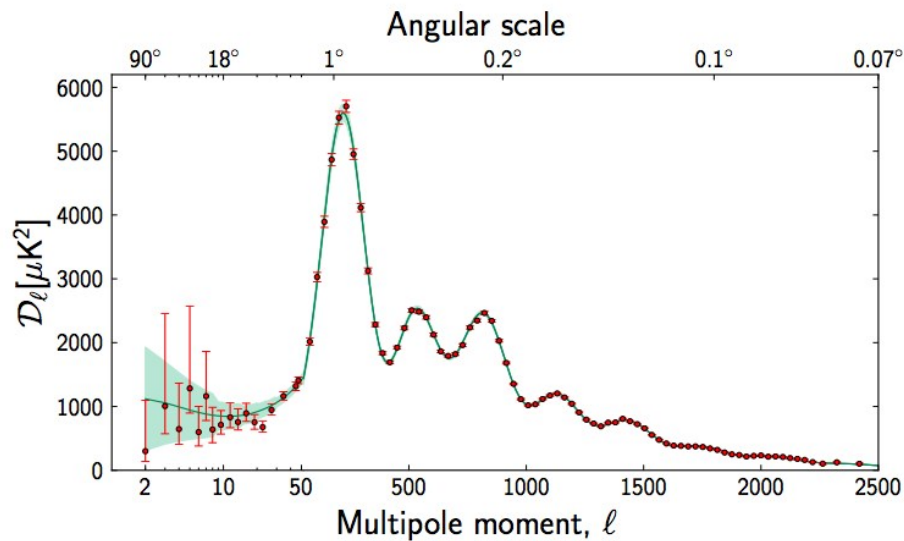
WMAP 9 Year and Planck Cosmological Parameters Best Fit with 1σ Variance.

Parameter	WMAP 9 yr	Planck 2013
Age of the Universe	$13.74 \pm 0.11 \times 10^9$ yrs	$13.813 \pm 0.058 \times 10^9$ yrs
Hubble Constant H_0	70.0 ± 2.2 (km/s)/Mpc	67.3 ± 1.2 (km/s)/Mpc
Ω_b	0.0463 ± 0.0024	0.0487 ± 0.0023
Ω_{CDM}	0.233 ± 0.023	0.265 ± 0.015
Ω_Λ	0.721 ± 0.025	0.686 ± 0.020
$1 - \Omega$	$-0.037^{+0.044}_{-0.042}$	0.000300 ± 0.025

Figure 9 : ESA-NASA Planck mission anisotropy multipole data, with ΛCDM best fit curve that determines cosmological parameters. The anisotropy multipole map is decomposed into Legendre polynomials $\langle \frac{\delta T}{T}(\hat{n}) \frac{\delta T}{T}(\hat{n}') \rangle_{\hat{n} \cdot \hat{n}' = \cos(\theta)} = \frac{1}{4\pi} \sum_{l=0}^{\infty} (2l+1) C_l P_l(\cos(\theta))$, where $\mathcal{D}_l = l(l+1)C_l/2\pi$, figure from Planck results [53] and data for WMAP taken from reference [54].

we are living in a flat universe $(k = 0)$ in the FRW metric, which we saw can be accomplished if the energy content of the universe is exactly equal to the critical energy density. However, we see that the baryonic matter can only account for 5% while the rest of the gravitationally interacting matter must be some other type of matter refereed to as dark matter, which accounts for 25% of the energy content of the universe. The remainder of energy we assume is in some form of energy associated with free space known as dark energy which accounts for the remaining 70%. Observations also suggest that we are now in an era of accelerating expansion, as discovered by Perlmutter, Schmidt, and Riess, who observed distant supernovae and from this deduced that the universe is currently transitioning from a matter dominated phase to a dark energy dominated phase [55, 56, 57]. They received the 2011 Nobel prize in physics for this result.

It seems interesting that after 13.7 billion years of evolution that the energy content of the universe is still such that it suggests $k = 0$. This is known as the flatness problem, as it seems odd that given all values possible for Ω it should be 1. Furthering the mystery of this result, many theories that go beyond the standard model of particle physics predict magnetic monopoles which have never been discovered, so if these magnetic monopoles are created at very high energies where GUTs may be the correct physics, typically in the range of $E \approx 10^{16}$ GeV, then where are these magnetic monopoles today? It would be in 1980 when Guth suggested a mechanism, known as inflation [10], that would solve all problems associated with the CMB at once.

1.2.4 Inflation

The scale factor can also have an exponential solution if we consider the cosmological constant Λ to be the dominate form of matter in the universe. If we look at the Einstein field equations with the cosmological term being the dominate term, we have

$$R_{\mu\nu} - \frac{1}{2}g_{\mu\nu}R \approx g_{\mu\nu}\Lambda, \tag{1.2.24}$$

Which allows us to associate the matter as a perfect fluid with $\rho = \Lambda$ and $P = -\rho$, so that the equation of state has $w = -1$. The Friedmann equations then gives

$$\frac{\ddot{a}}{a} = \frac{8\pi}{3M_{pl}^2}\Lambda > 0 \rightarrow a(t) \propto e^{Ht} \text{ with } H = \sqrt{\frac{8\pi}{3M_{pl}^2}\Lambda}\,. \tag{1.2.25}$$

The result is an era of exponential expansion, known as inflation. An era of exponential expansion solves the flatness, horizon, and monopole problem all at once. The Friedmann equation during this inflationary period is

$$1 - \Omega = \frac{k}{H^2 a(t)^2} \rightarrow 1 - \Omega = \frac{k}{H^2} e^{-2Ht}. \tag{1.2.26}$$

As a consequence of inflation we can see that $\Omega \rightarrow 1$ as time gets larger. With inflation, regardless of the initial value of k, the universe expands rapidly and forces $1 - \Omega \rightarrow 0$. The monopole problem can be solved by assuming that inflation takes place right around the time that GUTs are valid or when $k_B T \approx 10^{16}$ GeV which corresponds to a time $t \approx 10^{-36}$ s. If any monopoles exist at the time of inflation they will be exponentially diluted as number density goes like $a(t)^{-3} \rightarrow e^{-3Ht}$. The horizon problem can also be solved by inflation. Before the inflation of the universe we assume the universe is in a radiation dominated era. In this case the particle horizon is given by

$$d_p(t_b) = a(t_b) \int_0^{t_b} \frac{dt'}{a(t')} = t_b^{1/2} \int_0^{t_b} \frac{dt'}{t'^{1/2}} = 2t_b \approx 6 \times 10^{-28} \text{ m}, \tag{1.2.27}$$

where the time before inflation is given as $t_b \approx 10^{-36}$ s. Given that this is a very small distance, all of the universe should be in thermal equilibrium at this time. At this point in the history of the universe inflation begins and ends at a time t_e. We should also note that at the time of inflation the Hubble parameter is $H(t_b) = 5 \times 10^{35}$ Hz, which remains constant during inflation; the particle horizon then becomes

$$d_p(t_e) = 2t_b e^N - \frac{1}{H} + \frac{e^N}{H}, \tag{1.2.28}$$

where $N = H(t_e - t_b)$. If $N = 100$ (which corresponds to $t_e = 2 \times 10^{-34}$ s) then $d_p(t_e) \approx 3.2 \times 10^{16}$ m. The universe then proceeds along the standard thermal history where the large scale homogeneity is frozen in by the inflation. This allows the whole visible universe to be in causal contact at the time of recombination thus it is not surprising that the temperature variation of the CMB is so small.

The dynamics of inflation is typically described by a quasi-classical field called the inflaton. Obviously during such small time scales before inflation, we should be using quantum field theory, but a classical field will capture the essence of inflation. If we consider a scalar field with a generalized potential $V(\phi)$ with minimal coupling to the gravitational field, we can

calculate the associated energy density and pressure that is coupled to gravity , with the the result

$$S \;=\; \int d^4x \sqrt{-g}\left(\frac{1}{2}\partial\phi^2 - V(\phi)\right) \to T_{\mu\nu} = -\frac{2}{\sqrt{-g}}\frac{\delta(\sqrt{-g}\mathcal{L})}{\delta g^{\mu\nu}},$$

Ignoring the spatial variations of the inflaton as we assume high levels of homogeneity, we have the terms of a perfect fluid

$$\begin{aligned}
\rho &= \frac{1}{2}\dot{\phi}^2 + V(\phi), \\
P &= \frac{1}{2}\dot{\phi}^2 - V(\phi).
\end{aligned}$$
(1.2.29)

If the potential initially is in a state of $\dot{\phi} \ll V$ then we have the conditions for inflation which are $\rho \approx V(\phi)$ and $P \approx -V(\phi)$, which as we saw gives exponential expansion when these conditions are met. This initial state of the inflaton is the concept of slow roll inflation. The least action principle for the inflaton gives

$$\ddot{\phi} + 3\frac{\dot{a}}{a}\dot{\phi} = -\frac{dV}{d\phi}.$$
(1.2.30)

Equation (1.2.30) describes approximately the motion of an oscillator with a dampening term proportional to H. If the inflaton starts in a false vacuum then it slowly rolls towards the minimum of V where $dV/d\phi = 0$, then during this transition time we will have an inflationary era of the universe. The inflaton is then dampened as it oscillates about the true vacuum and eventually will decay to the true vacuum value. We will explore what this implies for gravitational wave observations in Part II.

1.2.5   Reheating

The inflationary scenario introduces a rapid expansion of space, and as a consequence the universe would be cold and have a low density. This presents a problem for standard big bang cosmology where we need some sort of way to return to a state of high density and high temperature so that a radiation dominated phase occurs after inflation. Work in the early 80's to the 90's (by Linde, Kofman, Starobinsky among others [58]), found a method of decaying inflaton field particles into standard model particles which would then interact and thus thermalize reheating the universe. This thermalized state would be proceeded by a state of non-thermal

equilibrium when the particles first come into existence, a pre-heating state. During this state there can be large inhomogeneities in the universe before thermalization smooths the inhomogeneities and thus this can lead to a stochastic gravitational wave background, similar to the CMB.

In the pre-heating phase the inflaton is oscillating about the minimum of its potential $V(\phi)$ after inflation has already occurred. If another scalar field χ is coupled to the inflaton, then the equations of motion are

$$
\begin{aligned}
\mathcal{L} &= \sqrt{-g}\left(\frac{1}{2}\partial\phi^2 + \frac{1}{2}\partial\chi^2 - \frac{1}{2}g^2\chi^2\phi^2 - V(\phi)\right), \\
&\downarrow \\
\ddot{\phi} &- \frac{1}{a^2}\nabla^2\phi + 3\frac{\dot{a}}{a}\dot{\phi} + g^2\chi^2\phi = -\frac{\partial V}{\partial\phi}, \\
\ddot{\chi} &- \frac{1}{a^2}\nabla^2\chi + 3\frac{\dot{a}}{a}\dot{\chi} + g^2\phi^2\chi = 0.
\end{aligned}
\tag{1.2.31}
$$

If the amplitude of $\phi \gg \chi$ then we can approximately ignore the term $g^2\chi^2\phi$ which implies the inflaton decays via the dampening term $3\dot{a}/a$. However for χ we can see its equation of motion resembles that of an oscillator with drag and a time dependent frequency term. It is useful at this point to decompose χ into spatial Fourier modes which gives

$$
\ddot{\chi}_k + 3\frac{\dot{a}}{a}\dot{\chi}_k + \left(\frac{k^2}{a(t)^2} + g^2\phi(t)^2\right)\chi_k = 0.
\tag{1.2.32}
$$

This describes a field that has similar properties of a person on a swing. Consider a person on a swing pumping their legs. What they are doing is changing the length of the pendulum they are attached to by extending and retracting their legs. Done with the right frequency, they can increase their amplitude of the swing/pendulum [59], a condition is known as parametric resonance. Equation (1.2.32) has a time dependent frequency, so we expect for some modes, the inflaton oscillating about its minimum will increase the amplitude of χ_k for particular modes k.

If we recall in flat space-time QFT, we can create a number operator for mode k, via the expansion of a scalar field as is done below,

$$
\begin{aligned}
\phi(x) &= \int \frac{d^3k}{(2\pi)^3}\phi_k(t)e^{i\vec{k}\cdot\vec{x}} = \int \frac{d^3k}{(2\pi)^3}\left(a_k(t) + a_k^\dagger(t)\right)e^{i\vec{k}\cdot\vec{x}}, \\
\pi(x) &= \partial_0\phi(x) = \int \frac{d^3k}{(2\pi)^3}\left(\dot{a}_k(t) + \dot{a}_k^\dagger(t)\right)e^{i\vec{k}\cdot\vec{x}},
\end{aligned}
\tag{1.2.33}
$$

where $a_k(t)$ are the solutions to spatially Fourier decomposed equations of motion. For example, in Minkowski space, we could have for a scalar field with potential $V = \frac{1}{2}m^2\phi^2$, the

equations of motion give

$$\ddot{\phi} - \nabla^2\phi + m^2\phi = 0 \rightarrow \ddot{\phi}_k + \left(k^2 + m^2\right)\phi_k = 0, \tag{1.2.34}$$

which has solutions of the form $a_k(t) \propto e^{\pm i\sqrt{k^2+m^2}t}$. We can construct a generalized number operator so long as $-2i[a_k^\dagger(t = 0), \dot{a}_{k'}(t = 0)] = (2\pi)^3\delta^{(3)}(k - k')$ (this is simply $[\phi(x), \pi(x')] = i\delta^{(3)}(x - x')$ in terms of mode expansion operators) is satisfied. The number operator for mode k can then be expressed as

$$N_k(t) = a_k^\dagger(t)a_k(t). \tag{1.2.35}$$

We can re-express this is in terms of the Fourier modes of the fields. In our flat space example solution, this is

$$N_k(t) = \frac{\omega_k}{2}\left(\phi_k^2 + \left(\frac{\dot{\phi}_k}{\omega_k}\right)^2\right). \tag{1.2.36}$$

When a mode of χ_k increases, the generalization of this procedure can be interpreted at a quasi-classical level as the act of particle creation. Thus, via parametric resonance with the inflaton, field particles can be generated, at which point standard interactions occur and thermalize the system. The full description of this system is non-linear and numerical integration methods must be employed for detailed study. In part II we will examine how we can calculate the effect of this particle creation on a stochastic background of gravitational waves, and how to do so in new inventive ways.

1.3 The Dark Sector

The ΛCDM model of cosmology predicts that we know almost nothing about approximately 94% of the content of the universe, where 68% is in the form of dark energy and 26% is in the form of dark matter [7]. To explain these dark properties, it is proposed that one needs to modify general relativity, possibly by modifying the Einstein field equation, adding some higher order curvature terms of the form

$$G_{\mu\nu} = R_{\mu\nu} - \frac{1}{2}g_{\mu\nu}R + \mathcal{O}(R^2) = \frac{8\pi}{3M_{pl}^2}T_{\mu\nu}, \tag{1.3.1}$$

or one can use models such as in modified newtonian dynamics theories (MoND) [60]. Not modifying the Einstein field $G_{\mu\nu}$, one can explain dark properties by adding in new particles, so called dark matter.

1.3.1 Dark Matter Particles

The theory of dark matter has gained evidence for existence through observations of galactic rotation curves, showing that objects far from the galactic core exhibit a higher velocity than that expected from Newtonian gravity, most famously demonstrated in [14] and can be seen in Fig. 10. Gravitational lensing observations lend credence to the dark matter coming from massive particles, techniques of which are reviewed in [61]. One such dramatic example is that of the bullet cluster collision that demonstrates through lensing effects that dark matter interacts with visible matter weakly [13] as seen in Fig. 11. It is popularly theorized that the explanation for
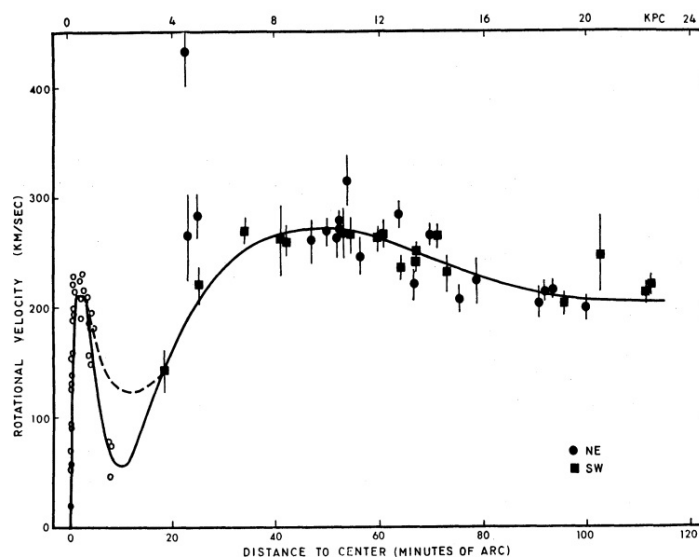
Figure 10 : The rotation curve for the Andromeda galaxy M31, as observed in [14] demonstrates that rather than the expected $v_r \propto r^{-1/2}$ fall off from Newtonian gravity, the rotational velocity of objects in M31 exhibit flattening suggesting additional non-electromagnetically interacting mass to keep the visible matter bound to the galaxy.

dark matter comes in the form of weakly interacting massive particles (WIMPs) [62]. Weakly interacting in that they must not interact with ordinary matter very strongly or else we would have detected such matter. The SM does not predict any weakly interacting matter other than neutrinos, however, neutrinos in the SM are massless and thus move at the speed of light and cannot form the cold dark matter needed to explain the evolution of the universe. Models that extend the symmetry of the SM such as SUSY are popular theories for WIMPs because they predict as yet unseen particles that may explain the dark matter [63]. It is then generally theorized that the full particle theory being incomplete consists of the visible sector, that which
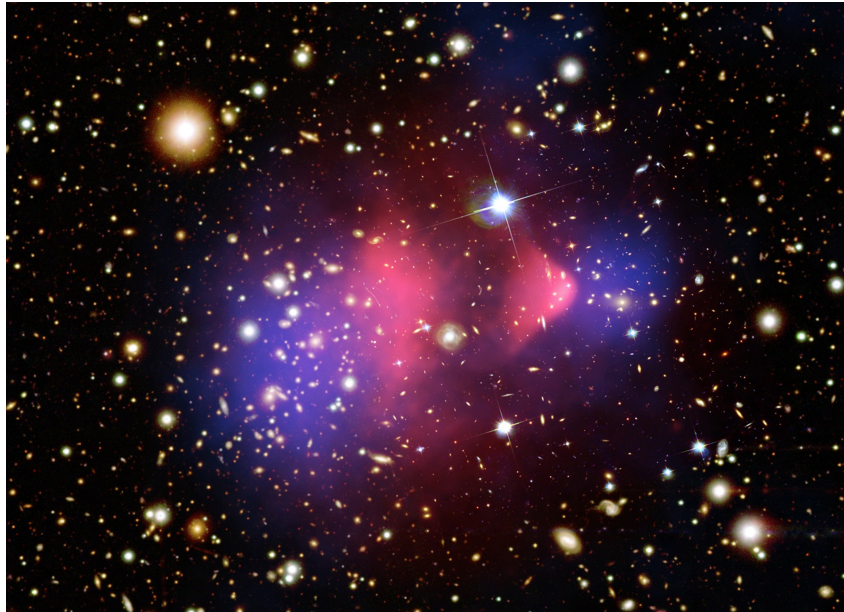
Figure 11 : Pictured is the the merging of the galaxy cluster in 1E0657-56. The intracluster medium contains the majority of baryonic mass contained in galaxy clusters. This hot baryonic mass emits photons in the X-ray range, depicted in pink and imaged from NASA's Chandra space telescope. The shock wave on the right of the image indicates that the two clusters have passed through each other due to gravitational attraction. However gravitational lensing maps the majority of the mass not with the X-ray emitting centers, but beyond this matter, mapped in blue/purple. This indicates a form of matter has passed through the baryonic matter, under the influence of gravity and potentially a weakly interacting force. This image provides further evidence for dark matter particles as WIMPs [65].

forms ordinary matter and is described by the SM, and that of the dark sector (DS), which forms the matter content of dark matter

$$\mathcal{L} = \mathcal{L}_{SM} + \mathcal{L}_{DS} \ . \tag{1.3.2}$$

To have any hope of detecting such a sector there must be some connection between the dark sector and the visible. One of the simplest models of connecting the dark sector to the visible is through the least well probed particle of the SM[5], the Higgs boson. Such models are deemed Higgs portal models [64], the structure of these models can be seen in Fig. 12. In Sec. 4.1 we shall explore a Higgs portal model put forth by Weinberg [15] and its validity to explain observed phenomena. One key observational requirement of any dark matter theory is its requirement to reproduce the correct thermal relic density of cold dark matter as observed today $\Omega_{\text{CDM}} = 0.265 \pm 0.015$ [7]. The connection to the relic density and the underlying particle physics model as formulated in [66], which applies the Boltzmann equation in an expanding

---

[5]Least well probed at the time of this writing.
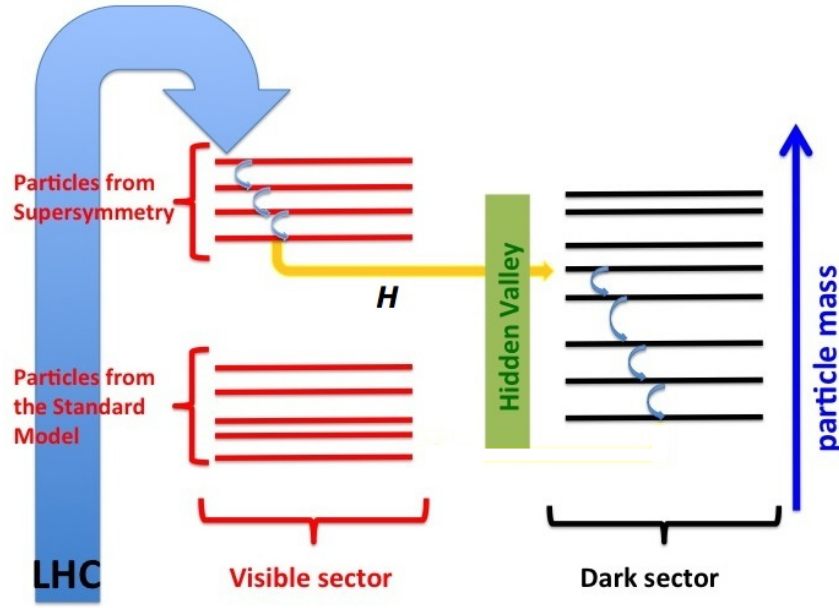
Figure 12 : The SM is being probed by the LHC and may reveal SUSY particles which may make up some of the dark sector, while the Higgs particle (indicated by the H) may be the only mediator with the dark sector having its on dynamical theory of light particles, the lightest stable particle (LSP) making up the majority of the cold dark matter today. Image modified from [67]

universe, connects the annihilation cross section of dark matter particles calculated from a particle theory to that of the relic density. The Boltzmann equation in an expanding universe is given as[6]

$$\dot{n}_w + 3Hn_w = -\langle \sigma v \rangle (n_w^2 - n_{\text{EQ}}^2) \,, \tag{1.3.3}$$

where n_w is the number density of WIMPS in a comoving frame, $\langle \sigma v \rangle$ the total thermally averaged annihilation cross section, Möller velocity product, and n_{EQ} is the number density when the WIMPs are in thermal equilibrium. The number density in equilibrium is expressed by, for example taking the WIMPS to be fermions, as

$$n_{\text{EQ}} = \int \frac{d^3k}{(2\pi)^3} \frac{g_{\text{f}}}{e^{E/T} + 1} \,, \tag{1.3.4}$$

where g_{f} is the degeneracies of the energy state E; typically the number of spin states the particle possesses and we will assume as such. In the non-relativistic approximation $m_w \gg T$ (m_w the mass of the WIMP) equation (1.3.4) takes the form of equation (1.2.14) repeated here for connivence

$$n_{\text{EQ}} = g_{\text{f}} \left(\frac{m_w T}{2\pi} \right)^{3/2} e^{-m_w/T}. \tag{1.3.5}$$

---

[6]The following derivation follows closely that of [49]

Equation (1.3.4) also makes use of the total annihilation cross section for the WIMP with the Möller velocity a detailed calculation of which is model dependent. By a change of variable $x = m_w/T$, $Y = n_w/s$, equation (1.3.4) takes a much simpler form by virtue of the conservation of entropy $sa^3 = \text{const}$,

$$\frac{dY}{dx} = -\frac{x\langle\sigma v\rangle s}{H(m)}\left(\frac{k}{1/2}\right)\left(Y^2 - Y_{\text{EQ}}^2\right) \ , \ Y_{\text{EQ}} = \sqrt{\frac{45}{32\pi^7}}\frac{g_{\text{f}}}{g_S(x)}x^{3/2}e^{-x} \ , \qquad (1.3.6)$$

where

$$s = g_S(x)\frac{2\pi^2}{45}m_w^3 x^{-3} \ , \ H = H(m)x^{-2} = m_w^2\frac{\sqrt{g_\rho(x)}}{M_{pl}}\sqrt{\frac{8\pi^3}{30}}\ x^{-2} \ , \ a(t) \propto t^k \ , \qquad (1.3.7)$$

which results in

$$-\frac{x\langle\sigma v\rangle s}{H(m)} = -\sqrt{\frac{\pi}{45}}m_w M_{pl}\frac{g_S(x)}{\sqrt{g_\rho(x)}}x^{-2}\langle\sigma v(x)\rangle \ . \qquad (1.3.8)$$

The solutions of (1.3.6) formally must be found by numerical methods, however approximate methods can be employed to give useful results. To find approximate solutions we express (1.3.6) in terms of $Y = Y_{\text{EQ}} + \Delta$, where Δ expresses the deviation from equilibrium (we proceed with $k = 1/2$ for decoupling in the radiation dominated era)

$$\frac{d\Delta}{dx} = -\frac{dY_{\text{EQ}}}{dx} - \sqrt{\frac{\pi}{45}}m_w M_{pl}\frac{g_S(x)}{\sqrt{g_\rho(x)}}x^{-2}\langle\sigma v(x)\rangle\ \Delta(\Delta + 2Y_{\text{EQ}}) \ . \qquad (1.3.9)$$

The thermal history of particle density can be understood by (1.3.3); if the averaged annihilation cross section term $\langle\sigma v\rangle$ is dominating the Hubble dampening term $3Hn_w$, then the particle distribution remains close to that of the equilibrium distribution any small deviation from equilibrium is resorted to the equilibrium distribution as can be seen in expanding (1.3.3) in first order deviations from n_{EQ} through $n_w = n_{\text{EQ}} + \Delta_n$. Under the assumption of good thermal contact Eq. (1.3.9) becomes,

$$\frac{d\Delta_n}{dt} + 2\Gamma\Delta_n \approx 0 \ , \Gamma = \langle\sigma v\rangle n_{\text{EQ}} \ , \qquad (1.3.10)$$

which gives solutions $\Delta \propto \exp(-2\Gamma t)$, killing any deviations on the scale $1/\Gamma$. At some point the Hubble dispensation term starts to dominate and the Boltzmann equation admits solutions where the number density simply scales as a^{-3},

$$\dot{n}_w \approx -3Hn_w \to n_w = n_w(\tau)\left(\frac{a(\tau)}{a(t)}\right)^3 \ . \qquad (1.3.11)$$

At some cross over time when approximately $\Gamma \approx H$ the number density n_w is frozen in and then scales as a^{-3}. We can exploit this fact to make approximate solutions to (1.3.9). Near the freeze out temperature, expressed as x_f, the deviation from equilibrium should be small and thus $\dot{\Delta} \approx 0$ and we consider only first order Δ deviations. Under this restriction Eq. (1.3.9) takes the form

$$\frac{1}{Y_{\text{EQ}}} \frac{dY_{\text{EQ}}}{dx} \approx -2\sqrt{\frac{\pi}{45}} m_w M_{pl} \frac{g_S(x)}{\sqrt{g_\rho(x)}} x^{-2} \langle \sigma v(x) \rangle \, \Delta \, . \tag{1.3.12}$$

The left hand side can be simplified under the assumption that the freeze out temperature occurs at a non-relativistic temperature, typically given by the condition $x_f \gg 3$. So long as the freeze out occurs at a temperature where $g_S'(x)/g_S(x) \approx 0$ then equation (1.3.12) admits solutions of the form

$$\Delta \approx \sqrt{\frac{45}{\pi} \frac{g_\rho(x_f)}{g_S^2(x_f)}} \frac{x_f^2}{m_w M_{pl} \langle \sigma v(x_f) \rangle} \, . \tag{1.3.13}$$

The convention is to consider a particle decoupled when $\Delta = c Y_{\text{EQ}}$ with c some number of order 1, solving for this condition leads to

$$\sqrt{\frac{45}{8\pi^6}} c \frac{g_{\text{f}}}{\sqrt{g_\rho(x_f)}} m_w M_{pl} x_f^{-1/2} \langle \sigma v(x_f) \rangle \approx e^{x_f} \, , \tag{1.3.14}$$

which admits approximate solutions from self substitution of the form

$$
\begin{aligned}
x_f &= \ln\left[\sqrt{\frac{45}{8\pi^6}} c \frac{g_{\text{f}}}{\sqrt{g_\rho(x_f)}} m_w M_{pl} x_f^{-1/2} \langle \sigma v(x_f) \rangle \right] - \frac{1}{2} \ln\left[x_f \right] \, , \\
x_f &\approx \ln\left[\sqrt{\frac{45}{8\pi^6}} c \frac{g_{\text{f}}}{\sqrt{g_\rho(x_f)}} m_w M_{pl} x_f^{-1/2} \langle \sigma v(x_f) \rangle \right] \\
&\quad - \frac{1}{2} \ln\left[\ln\left[\sqrt{\frac{45}{8\pi^6}} c \frac{g_{\text{f}}}{\sqrt{g_\rho(x_f)}} m_w M_{pl} x_f^{-1/2} \langle \sigma v(x_f) \rangle \right] \right] + \ldots
\end{aligned}
$$
$$\tag{1.3.15}$$

After the freeze out occurs we know the distribution should only be slightly effected by the residual annihilations such that after freeze out $Y \gg Y_{\text{EQ}}$ since Y_{EQ} has exponential decay, after freeze out $\Delta \approx Y$. From equation (1.3.9) we can find the value of $Y(x_0)$, where x_0 is the value taken today as

$$\frac{1}{Y(x_0)} \approx \frac{1}{Y_{\text{EQ}}(x_f)} + \sqrt{\frac{\pi}{45}} m_w M_{pl} \int_{x_f}^{x_0} \frac{g_S(x)}{\sqrt{g_\rho(x)}} x^{-2} \langle \sigma v(x) \rangle \, . \tag{1.3.16}$$

A key observation is that so long as $x^{-2} \langle \sigma v(x) \rangle$ dies off quickly as a function of x then the term containing $\langle \sigma v \rangle$ contributes very little and $Y(x_0) \approx Y_{\text{EQ}}(x_f)$, this will come back in Sec. 4.2.8

as we consider a case where $\langle \sigma v \rangle$ grows for $x \to \infty$. We will continue with the assumption that the term $\langle \sigma v \rangle$ doesn't contribute to the the yield Y today.

We may now compute the thermal relic density by

$$\Omega_{\text{CDM}} = \frac{\rho_w(\text{today})}{\rho_c} = \frac{8\pi \, m_w s_0 Y(x_0)}{3 H_0^2 M_{pl}^2} \, , \qquad (1.3.17)$$

If we take $c = 1$ in equation (1.3.14) and $T_0 = 2.7$ K the result is

$$\Omega_{\text{CDM}} h^2 \approx 4 \times 10^{-11} \frac{x_f^{3/2}}{\sqrt{g_\rho(x_f)} \langle \sigma v(x_f) \rangle} \text{ GeV}^{-2} \, . \qquad (1.3.18)$$

The Eq. (1.3.18) gives for $\Omega_{\text{CDM}} h^2 = 0.112$ (computed with $h \approx 0.67$ from [7]) and an example $x_f = 20$, $g_\rho(x_f) \approx 100 \to m_w = 200$ GeV gives the requirement

$$\langle \sigma v(x_f = 20) \rangle = 3.9 \times 10^{-26} \text{cm}^3 \text{s}^{-1} \, . \qquad (1.3.19)$$

though the flatness of g_ρ in certain regions makes the result insensitive to the particle mass.

Besides a dark sector theory giving the correct relic density, dark matter also allows an explanation to recent observations of excess relativistic degrees of freedom from that of the SM in CMB analyses, the details of which are left to Sec. 4.1.

1.3.2 Dark Matter Direct Detection

On a more microscopic scale, if dark matter has interactions with the visible sector, then there should be some measurable effect of the particle's interactions. Currently, direct detection measurements are being performed by several collaborations, which include DAMA/LIBRA [68], CoGeNT [69, 70], CRESST [71], and CDMS [72]. The essential principle of direct detection searches is to measure the recoil and subsequent phonons (mK temperature changes) in various materials resulting from interactions of dark matter with stable nuclei. In this experimental setup, one might assume that as the Earth moves through the Galactic halo of dark matter particles as represented in Fig. 13; with this model, at various times of the year, one expects to observe different behavior in your measurements as the relative flux of dark matter particles changes as the Earth moves with and against the WIMP wind. As of 2010 the DAMA/LIBRA [68] Collaboration's observations suggest such an annual modulation of dark matter interaction signals, in accordance to the Earth's relative motion to the galactic halo, the
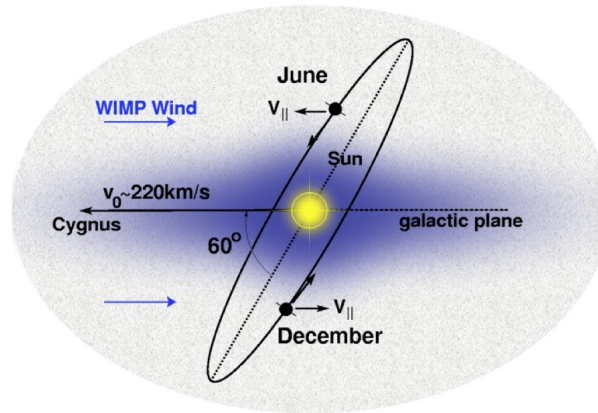
Figure 13 : As the Earth orbits the sun, the relative velocity of the Earth with the dark matter halo of the milky way has a period of 1 year. This should have an effect on the number of incident collisions for dark matter direct detection searches (image taken from [67]).
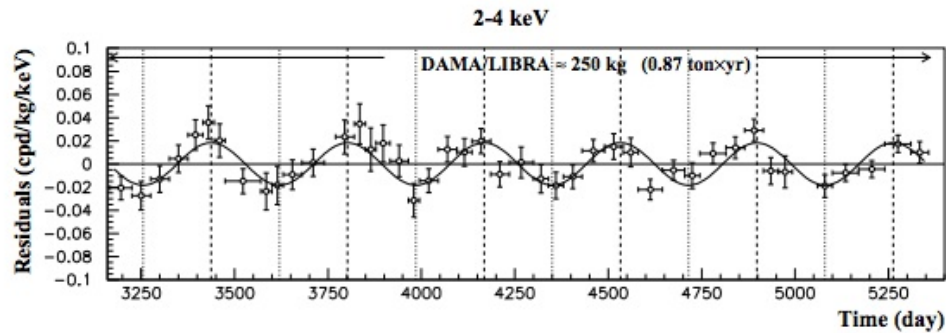
Figure 14 : Annual modulation data in dark matter direct detection searches observed from the DAMA/LIBRA Collaboration for a little over 5 years of data [68].

results are shown in Fig. 14. These direct detection searches also help to place upper limit constraints on dark sector physics. Interaction cross-sections limits can be seen in Fig. 15 from [73]. Interestingly, several collaborations, as of June 2013, have hinted at a possible signal in the $m_w \approx 10$ GeV range [74] 16. In Sec. 4.2 we will explore what the Higgs portal models can tell us in light of these new developments.
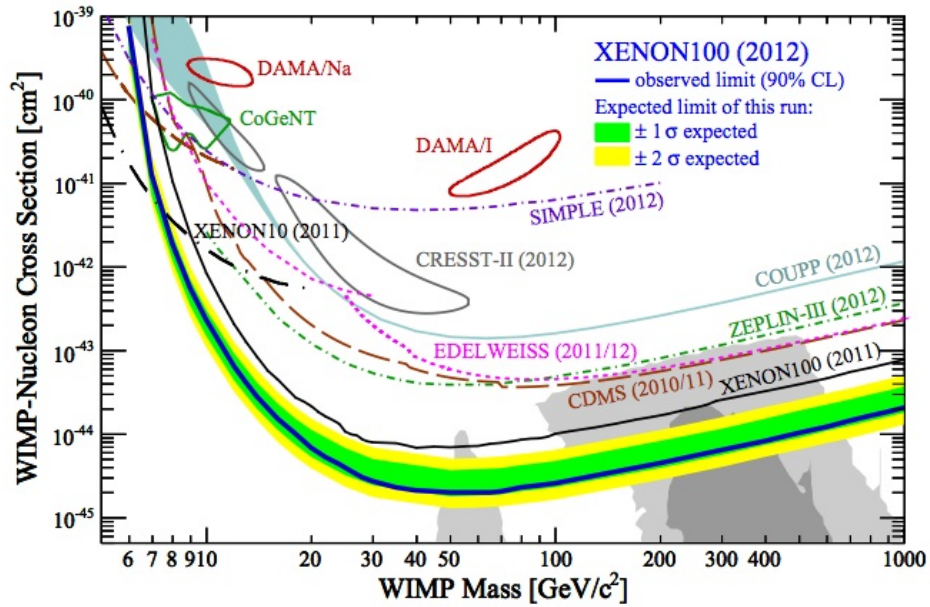
Figure 15 : Limits on Nucleon WIMP cross sections by various collaborations. Cross sections are of the order $\mathcal{O}(10^{-39} - 10^{-45})$ cm^2. Image adopted from [73]
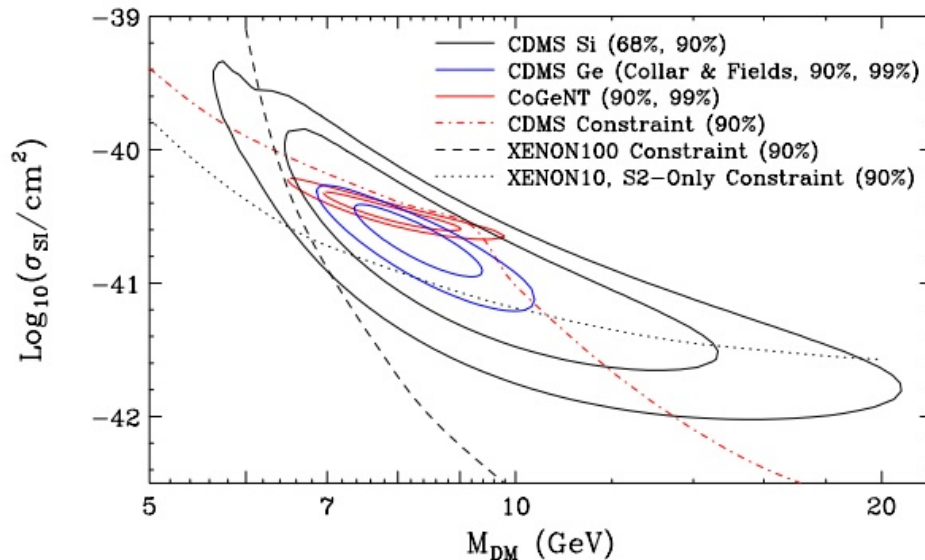
Figure 16 : Several collaborations have started to converge on a direct detection limit that suggest a dark matter particle with mass around 10 GeV [74] though issues with the Xenon100 data exsist [73].

Part I:

$$U_B(3) \times SU_L(2) \times U_L(1) \times U_{I_R}(1) \to \text{SM}^{++}$$

Chapter 2

Extending the Standard Model

2.1 Strings, D-branes, and the SM

Exploring beyond the SM requires us to find new concepts that allow us to make modifications to the SM Lagrangian; one of the most highly regarded BSM theories is string theory. The central idea of string theory is that all fundamental particles (leptons, quarks, and gauge bosons) are not point particles but rather one dimensional objects, strings. The use of strings as the fundamental objects of a QFT leads to a consistent quantum theory of gravity in its spectrum. String theory unites gravity and the other known forces into a consistent framework. The use of quantum theory to the concepts of strings requires the theory to have more than the 3+1 dimensions of space-time, 26 in the bosonic string case and 10 in superstring theory. We do not observe a space-time dimension higher than 4 in current experiments, and do not find a departure from the inverse square law of gravity for distances greater than 56 μm, which sets a limit of one extra compact spatial dimension of $R \leq 44\ \mu$m [75]. To keep string theory as a viable theory, the idea of D-branes was introduced to connect string theory to experiment [76, 77].

Dp-branes are p dimensional objects to which string end points can be attached to, (strings having Dirichlet boundary conditions, or considered fixed at their end points). By attaching strings to D-branes, extra spatial dimensions are still a possibility as the particles of the SM can be forced to be bound to D-branes in the form of open strings, while the mediators of gravity (gravitions), closed strings, are free to move into the extra-dimensional space. As was shown

earlier, the inclusion of extra spatial dimensions solves the hierarchy problem of the SM. Within the spectrum of particles (string states) are vector gauge bosons, as well as the SM fermionic content [32]; with all the content of the SM + gravity it is natural to try to construct something similar to the SM. Multiple D-branes provide a possible solution to construction of string-like SM. By having multiple D-branes, strings can attach one endpoint on one brane and its other endpoint on an entirely separate brane. By attaching strings to multiple branes and having the branes at the same location (without the branes at the same location the gauge bosons may acquire mass, which we do not want) a $U(N)$ gauge symmetry is realized on the brane.

Stacking multiple branes together allows us to form something very close to the SM; a brane world consisting of a 3-stack of branes, intersecting a 2-stack of branes and finally a single brane contains the SM [78]. These 3 stacks of branes will contain the gauge group $U_B(3) \times U_L(2) \times U_Y(1)$, which contains the SM gauge group as a subgroup. To make the multiple brane approach to the SM applicable to experiment such as the LHC, the required string scale must be set at the TeV scale and thus requires extra dimensions of the length 1 millimeter to a Fermi (10^{-15} m) [79]. Regge recurrences (string excitations) most distinctly manifest in the $\gamma+$ jet [80, 81] and dijet [82, 83, 84] spectra resulting from their decay. The recent search for such narrow resonances in data collected during the LHC7 run now excludes a string scale below 4 TeV [85, 86, 87]. Alternatively it is still possible that the string scale is actually closer to the Planck scale, $l_p \approx 1.6 \times 10^{-35}$ m and still get signals at the LHC as we will show below.

To increase the scale of string theory more towards the Planck scale, we include an extra 1-stack D-brane to the 3 stacks of D-branes that can represent the SM. This additional 1-stack D-brane will supply us with an additional $U(1)$ gauge symmetry to that of the gauge group $U_B(3) \times U_L(2) \times U_Y(1) \rightarrow U_B(3) \times U_L(2) \times U_L(1) \times U_{I_R}(1)$, where we have chosen to gauge lepton number via $U_L(1)$, this then naturally explains the accidental symmetry included with the SM of conservation of lepton number; we also include an additional charge I_R. we have a special case for the $U_L(2)$ brane, since even powers of the $U(2N)$ group can be reduced to members of the symplectic group $Sp(N)$. With this in mind, we have $U_L(2) \rightarrow Sp_L(1) \cong SU_L(2)$, which alleviates the need for an extra, as yet unobserved gauge boson associated with $U_L(2)$, as depicted in Fig. 17 for the 3 intersecting d-brane stacks, and Fig. 18 for the 4
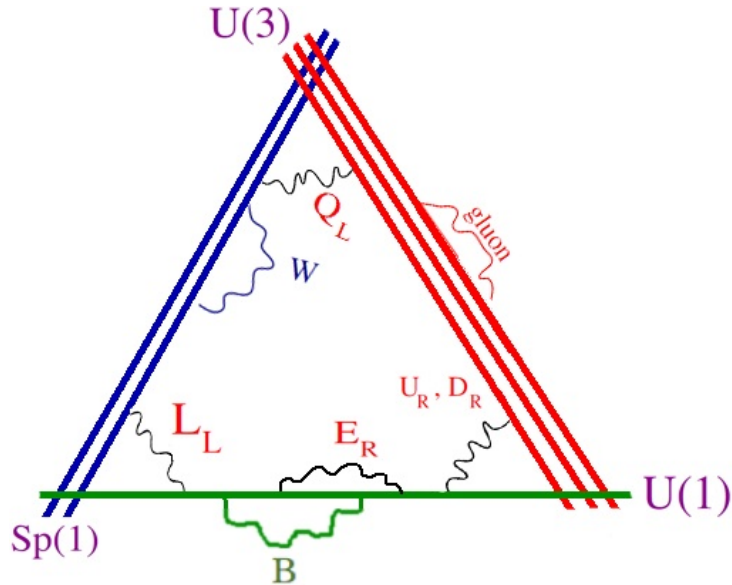
Figure 17 : The use of 3 brane stacks can be used to find the minimal representation of the SM within string theory, while still keeping the possibility of large extra spatial dimensions as a possibility.

intersecting d-brane stacks.

To understand the new consequences of this model, it helps to identify the SM from its construction. This can be done by recognizing that any unitary group $U(N)$ can be decomposed to

$$U(N) \to U(1) \times SU(N). \tag{2.1.1}$$

By performing the decomposition to $U(1)$ and $SU(N)$ we must consider the coupling strengths of the decomposed $U(1)$ part and $SU(N)$. It should be that at the string scale the underlying symmetry of $U(N)$ is restored, while at scales less than the string scale a symmetry breaking can make them appear to have different coupling strengths. We ensure the $U(N)$ symmetry is released at the string scale by requiring that the gauge transformations have a common normalization. We write our $U(N)$ gauge transformation as a multiplication of a $U(1)$ transformation expressed as $\exp(iX)$ with X proportional to a $N \times N$ identity matrix, and a $SU(N)$ transformation written as $\exp(iT^a\theta^a)$, where the T^a are generators of the $SU(N)$ symmetry. We can use the trace operator normalization of the $SU(N)$ group as a guide to the proper normalization
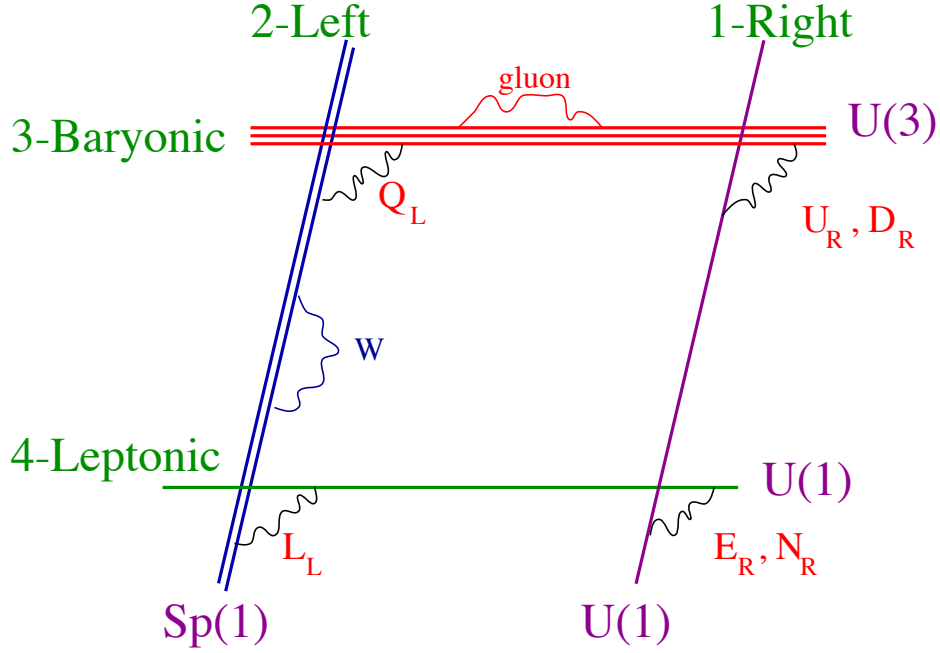
Figure 18 : The addition of the $U_{I_R}(1)$ brane can alleviate the issues of a 1 TeV string scale of the 3 brane construction. Above the gauge group of the 4 brane construction is $U(3)_B \times Sp(1)_L \times U(1)_L \times U(1)_{I_R}$.

of the X operator via [88]

$$
\begin{aligned}
\text{Tr}\left(T^a T^b\right) &= \frac{1}{2}\delta^{ab} \rightarrow \text{Tr}\left(X^2\right) = \frac{1}{2}, \\
\text{Tr}\left(X^2\right) &= \text{Tr}\left(c^2 I\right) = c^2 N \rightarrow c = \frac{1}{\sqrt{2N}}.
\end{aligned}
\tag{2.1.2}
$$

We can then identify X as the identity as long as we transfer the $1/\sqrt{2N}$ to the coupling associated with X; this ensures that we will recover the $U(N)$ symmetry at the string scale. With the decomposition of $U_B(3)$, the gauge group of the 4 brane model becomes $U_B(1) \times SU_c(3) \times SU_L(2) \times U_L(1) \times U_{I_R}(1)$, where now we have gauge field associated with baryon number via $U_B(1)$. Again one of the accidental symmetries of the SM naturally becomes gauged in this model; this then can be used to ensure proton stability. With this gauge group as the underlying symmetry, a covariant derivative can be constructed as

$$
D_\mu = \partial_\mu - ig_3 T^a G_\mu^a - ig_3' Q_B C_\mu - ig_2 \tau^a W_\mu^a - ig_1' Q_{I_R} B_\mu - ig_4' Q_L X_\mu,
\tag{2.1.3}
$$

where it must be enforced at the string scale that $g_3'(M_s) = g_3(M_s)/\sqrt{3 \cdot 2}$ and we identify C_μ as the the $U(1)$ gauge boson associated with conservation of baryon number.

Table 1 : Chiral fermion spectrum of the $U(3)_B \times Sp(1)_L \times U(1)_L \times U(1)_{I_R}$ D-brane model with charges Q_B Baryon number, Q_L Lepton number, Q_{I_R} additional U(1) charge, Q_Y hypercharge of the SM. The label for the field will be used to compactify expression in other sections. The fields are labeled such that $\mathcal{F}_i$ is field i , for example $\mathcal{F}_1 = u_R$, $\mathcal{F}_2 = d_R, \ldots$

Label	Fields	Representation	Q_B	Q_L	Q_{I_R}	Q_Y
1	u_R	$(3,1)$	1	0	1	$\frac{2}{3}$
2	d_R	$(3,1)$	1	0	-1	$-\frac{1}{3}$
3	E_L	$(1,2)$	0	1	0	$-\frac{1}{2}$
4	e_R	$(1,1)$	0	1	-1	-1
5	Q_L	$(3,2)$	1	0	0	$\frac{1}{6}$
6	n_R	$(1,1)$	0	1	1	0
7	H	$(1,2)$	0	0	1	$\frac{1}{2}$
8	H''	$(1,1)$	0	-1	-1	0

In addition to extra gauge bosons, we also include in the model right chiral neutrino fields n_R, so that we can agree with the observation of neutrino oscillations. As long as the right chiral neutrino fields remain neutral with respect to hypercharge, it will not break the SM. The matter content of the 4 brane model is summarized in Table 1. The SM makes use of a Higgs doublet field to give mass to three gauge bosons. Allowing a Higgs doublet field and a single scalar field to the 4 brane model, we can give masses to 3 gauge bosons using the Higgs doublet and give mass to 1 of the additional gauge bosons. This leaves 8 massless fields, which we will take to be the gluons of the SM; 1 massless gauge boson we can eventually associate to the photon field. This still leaves an additional $U(1)$ gauge boson massless. We will give a mass to this additional $U(1)$ via a Stückelberg mechanism. More will be said on the Stückelberg mechanism in the following sections.

2.1.1 The Effective Lagrangian

The particle content in the theory has been specified, and at this point we construct an effective Lagrangian within which we can identify the SM. We identify $SU_B(3)$ with $SU_c(3)$, the color gauge group from the SM which is represented by 8 gluons with field strength

$$G^a_{\mu\nu} = \left(\partial_\mu G^a_\nu - G\partial_\nu G^a_\mu + g_3 f^{abc} G^b_\mu G^c_\nu\right), \; i f^{abc} T^a = [T^b, T^a], \; T^a \in SU(3). \qquad (2.1.4)$$

Associated with the $U_B(1), U_L(1)$, and $U_{I_R}(1)$ we have the gauge fields C_μ, X_μ, and B_μ, respectively. The field strengths are given by the expressions

$$
\begin{aligned}
F^{(1)}_{\mu\nu} &= \partial_\mu B_\nu - \partial_\nu B_\mu, \\
F^{(3)}_{\mu\nu} &= \partial_\mu C_\nu - \partial_\nu C_\mu, \\
F^{(4)}_{\mu\nu} &= \partial_\mu X_\nu - \partial_\nu X_\mu.
\end{aligned}
\qquad (2.1.5)
$$

We can construct the field strength for the $SU_L(2)$ gauge field as

$$W^a_{\mu\nu} = \left(\partial_\mu W^a_\nu - \partial_\nu W^a_\mu + g_2 \epsilon^{abc} W^b_\mu W^c_\nu\right), \; i\epsilon^{abc}\tau^a = [\tau^b, \tau^a], \; \tau^a \in SU(2). \qquad (2.1.6)$$

The kinetic expression for the gauge fields, also known as the Yang-Mills part of the Lagrangian, is the gauge invariant expression

$$\mathcal{L}_{YM} = -\frac{1}{4}\left(G^a_{\mu\nu}G^{\mu\nu}_a + W^a_{\mu\nu}W^{\mu\nu}_a + F^{(1)}_{\mu\nu}F^{\mu\nu}_{(1)} + F^{(3)}_{\mu\nu}F^{\mu\nu}_{(3)} + F^{(4)}_{\mu\nu}F^{\mu\nu}_{(4)}\right). \qquad (2.1.7)$$

We include the fermion fields via our standard gauge invariant expression as

$$
\begin{aligned}
\mathcal{L}_{\text{fermion}} &= i\bar{Q}_L\gamma_\mu D^\mu Q_L + i\bar{u}_R\gamma_\mu D^\mu u_R + i\bar{d}_R\gamma_\mu D^\mu d_R + i\bar{E}_L\gamma_\mu D^\mu E_L \\
&\quad + i\bar{e}_R\gamma_\mu D^\mu e_R + i\bar{n}_R\gamma_\mu D^\mu n_R,
\end{aligned}
\qquad (2.1.8)
$$

where it is understood that we repeat these interactions for each generation of particles. To give the particles mass, we include the Yukawa interactions as they were in the SM, however we include a Yukawa term for the right chiral neutrino field

$$\mathcal{L}_Y = -Y_d\left(\bar{Q}_L H\right)d_R - Y_u\left(\bar{Q}_L i\sigma^2 H^*\right)u_R - Y_e\left(\bar{E}_L H\right)e_R - Y_N\left(\bar{E}_L i\sigma^2 H^*\right)n_R + h.c.\,,$$
$$(2.1.9)$$

where the Yukawa couplings Y_i are matrices in flavor space (*i.e.* the CKM matrix is absorbed into the definitions of Y_i).

Since this is an effective Lagrangian of the underlying string theory, it is possible to have terms that have mass dimension greater than 4, which would be considered non-renormalizable and thus non-fundamental, but knowing that this is an effective theory, terms with mass dimension greater than 4 are considered acceptable. However, we avoid this complication in the Lagrangian by setting the string scale well outside the scope of LHC physics, where our phenomenological analysis takes place in the following sections. By choosing the string scale $M_s \geq 10^{14}$ GeV, we ensure that operators with mass dimension greater than 4 in the Lagrangian are suppressed in our phenomenological analysis. We must also state that there cannot be any terms involving H'' and have mass dimension 4 ensuring conservation of lepton number.

To include the Higgs fields, we form the scalar sector of the effective Lagrangian as

$$\mathcal{L}_{\text{scalar}} = (D^\mu H)^\dagger D_\mu H + (D^\mu H'')^\dagger D_\mu H'' - V(H, H''), \tag{2.1.10}$$

with the potential given as

$$V(H, H'') = \mu_1^2 |H|^2 + \mu_2^2 |H''|^2 + \lambda_1 |H|^4 + \lambda_2 |H''|^4 + \lambda_3 |H|^2 |H''|^2. \tag{2.1.11}$$

Minimization of the potential results in two separate vevs for each Higgs field; those vevs are represented as

$$\langle H \rangle = \frac{1}{\sqrt{2}} \begin{pmatrix} 0 \\ v \end{pmatrix} \quad \text{and} \quad \langle H'' \rangle = \frac{1}{\sqrt{2}} v''. \tag{2.1.12}$$

The doublet vev denoted v is taken to be that of the SM while the singlet vev denoted v'' will be used to give mass to one of the gauge bosons not part of the SM.

The effective theory in this form makes it difficult to identify the SM. We require a change of basis of the 3 additional $U(1)$ gauge bosons, such that a linear combination of C_μ, B_μ, X_μ form the hypercharge gauge boson of the SM Y_μ, along with two other $U(1)$ gauge bosons, Y'_μ, and Y''_μ. We accomplish this via an $SO(3)$ matrix, or a rotation, parameterized by three Euler angles as is shown below (θ, ψ, ϕ) [89]

$$\mathbb{R} = \begin{pmatrix} C_\theta C_\psi & -C_\phi S_\psi + S_\phi S_\theta C_\psi & S_\phi S_\psi + C_\phi S_\theta C_\psi \\ C_\theta S_\psi & C_\phi C_\psi + S_\phi S_\theta S_\psi & -S_\phi C_\psi + C_\phi S_\theta S_\psi \\ -S_\theta & S_\phi C_\theta & C_\phi C_\theta \end{pmatrix}, \tag{2.1.13}$$

where we have $C_\theta = \cos(\theta)$ and $S_\psi = \sin(\psi)$ and similar notation for the other angles. After performing this rotation on the $U(1)$ gauge bosons with the relation

$$\begin{pmatrix} C_\mu \\ X_\mu \\ B_\mu \end{pmatrix} = \mathbb{R} \begin{pmatrix} Y_\mu \\ Y'_\mu \\ Y''_\mu \end{pmatrix}, \tag{2.1.14}$$

our covariant derivative is brought into the form

$$\begin{aligned} D_\mu &= \partial_\mu - iY_\mu \left(-S_\theta g'_1 Q_{I_R} + C_\theta S_\psi g'_4 Q_L + C_\theta C_\psi g'_3 Q_B\right) \\ &- iY'_\mu \left[C_\theta S_\phi g'_1 Q_{I_R} + (C_\phi C_\psi + S_\theta S_\phi S_\psi)\, g'_4 Q_L + (C_\psi S_\theta S_\phi - C_\phi S_\psi) g'_3 Q_B\right] \\ &- iY''_\mu \left[C_\theta C_\phi g'_1 Q_{I_R} + (-C_\psi S_\phi + C_\phi S_\theta S_\psi)\, g'_4 Q_L + (C_\phi C_\psi S_\theta + S_\phi S_\psi)\, g'_3 Q_B\right] \\ &+ \ldots \end{aligned} \tag{2.1.15}$$

where the ... include gauge bosons of the non-abelian groups. By using an orthogonal matrix $\mathbb{R}$, we can find relations for the charges for the particles in the new basis.

To illustrate this point, consider the situation of a collection of $U(1)$ gauge bosons X_n and then perform a rotation on them. We can write them in a new basis Y_m

$$\begin{aligned} D_\mu &= \partial_\mu - i\sum_n g_n Q_n X_n + \ldots, \\ &= \partial_\mu - i\sum_{nm} g_n Q_n \mathbb{R}_{mn} Y_m + \ldots = \partial_\mu - i\sum_m g'_m Q'_m Y_m, \end{aligned} \tag{2.1.16}$$

where we take $X_n = \sum_m \mathbb{R}_{mn} Y_m$. This allows us to write a relation among the charges and couplings of each basis as

$$g'_m Q'_m = \sum_n g_n Q_n \mathbb{R}_{nm}. \tag{2.1.17}$$

We are motivated to enforce that $Q'_1 = \sum_n c_n Q_n$ (Q'_1 is chosen as an example and has no significance as opposed to Q'_2 or any other charge) so that the rotated basis couples to some specifically chosen charge and where c_n are real numbers. Then, for example. the coupling to the 1st gauge boson becomes

$$g'_1 Q'_1 = g'_1 \sum_n c_n Q_n = \sum_n g_n Q_n \mathbb{R}_{n1}. \tag{2.1.18}$$

We now promote Q_n to vectors $\mathbf{Q}_n$ whose components $(\mathbf{Q}_n)_p$ denote the charge Q_n for the pth

particle. In standard form this vector is

$$\mathbf{Q}_n = \begin{pmatrix} Q_{n,1} \\ Q_{n,2} \\ \vdots \\ Q_{n,p} \end{pmatrix}, \tag{2.1.19}$$

where again, for clarification, $Q_{n,1}$ is the Q_n charge of particle 1 and so on. If we ask that the $\mathbf{Q}_n$ vectors are orthogonal, then we can deduce that

$$g_1' \sum_n c_n \mathbf{Q}_n \cdot \mathbf{Q}_m = \sum_n g_n \mathbf{Q}_n \cdot \mathbf{Q}_m \mathbb{R}_{n1} \rightarrow g_1' c_m = g_m \mathbb{R}_{m1},$$
$$\mathbb{R}_{m1} = g_1' c_m / g_m. \tag{2.1.20}$$

With this result, and using the orthogonality of $\mathbb{R}$ we arrive at our final result,

$$\sum_m (\mathbb{R}_{m1})^2 = 1 \rightarrow \frac{1}{g_1^2} - \sum_m \left(\frac{c_m}{g_m} \right)^2 = 0. \tag{2.1.21}$$

This orthogonality relation of equation (2.1.21) was shown to be true to the one loop order in ref [88]. When we apply this result to the 4 brane model we have

$$\frac{1}{g_Y^2} - \sum_m \left(\frac{c_m}{g_m'} \right)^2 = 0. \tag{2.1.22}$$

We then make the identification of the hypercharge of the SM as

$$Q_Y = c_1 Q_{I_R} + c_3 Q_B + c_4 Q_L, \tag{2.1.23}$$

where $c_1 = 1/2$, $c_3 = 1/6, c_4 = -1/2$ and identify $B = Q_B/3$ and $L = Q_L$ (baryon number and lepton number respectively). The c_i are chosen such that the charges are, baryon number, lepton number, and a combination of hypercharge and baryon number minus lepton number. The specific relations for the charges are give as

$$Q_B = 3B; \ Q_L = L; \ Q_{I_R} = 2Q_Y - (B - L). \tag{2.1.24}$$

Thus in this basis we have gauged baryon number B and lepton number L. This, however, presents a problem as gauged baryon number and lepton number are anomalous charges in gauge theories. Conversely the last charge, Q_{I_R}, is a combination of Q_Y and $B - L$ which is non-anomalous. The anomalies of B and L are solved by associating the bosons with a Stückleberg [90] mass, which will be discussed in the next subsection.

Before addressing the anomalies, we consider that the charge coupling to the Y_μ gauge boson is the hypercharge, which then fixes two Euler angles θ and ψ of the rotation via

$$c_1 g_Y = -g_1' \sin(\theta), \quad c_4 g_Y = g_4' \cos(\theta) \sin(\psi). \tag{2.1.25}$$

Next we demand that Y_μ'' couples to a linear combination of anomaly-free I_R and $B - L$, that is we require the terms proportional to B and L must be equal so that they form a charge proportional to $B - L$. This can be accomplished by fixing the Euler angle ϕ as

$$\tan \phi = -\sin \theta \frac{3g_3' \cos \psi + g_4' \sin \psi}{3g_3' \sin \psi - g_4' \cos \psi}. \tag{2.1.26}$$

After fixing the angles, we have two non-anomalous gauge bosons Y_μ and Y_μ'', along with one anomalous Y_μ' gauge boson. We must rid ourselves of this anomaly in order to consider the theory self consistent.

2.1.2 Getting Rid of the Anomaly

We can rid ourselves of the anomaly associated with Y_μ' by canceling it using the 4D version [91, 92, 93, 94, 95] of the Green-Schwarz mechanism [96]. By using the Green-Schwarz mechanism, Y_μ' will acquire a mass on the order of the string scale M_s.

We use the underlying string theory to help us because in the spectrum of the closed strings there is an anti-symmetric rank 2 tensor field, the Kalb-Ramond field $B_{\mu\nu}$, from which we can construct a gauge invariant interaction with an anomalous $U(1)$ gauge field that we will call C_μ in the example below. The gauge invariant Lagrangian with the Kalb-Ramond field is

$$\mathcal{L} = -\frac{1}{12} H^{\mu\nu\rho} H_{\mu\nu\rho} - \frac{1}{4} F_{\mu\nu} F^{\mu\nu} + \frac{c}{4} \epsilon^{\mu\nu\rho\sigma} B_{\mu\nu} F_{\rho\sigma}, \tag{2.1.27}$$

where

$$H_{\mu\nu\rho} = \partial_\mu B_{\nu\rho} + \partial_\rho B_{\mu\nu} + \partial_\nu B_{\rho\mu} \tag{2.1.28}$$

is the field strength of $B_{\mu\nu}$ and c is some arbitrary constant. The anomalies associated with C_μ can be canceled by the proper choice of c, but this ends up giving mass to the gauge boson; this is the Green-Schwarz mechanism. We will re-write the Lagrangian so that the mass of the gauge boson is apparent by using

$$\frac{c}{4} \epsilon^{\mu\nu\rho\sigma} B_{\mu\nu} F_{\rho\sigma} = \frac{c}{2} \epsilon^{\mu\nu\rho\sigma} B_{\mu\nu} \partial_\rho C_\sigma \tag{2.1.29}$$

and integration by parts (remember this is part of an action and thus integrated over) of the last term of (2.1.27), which leads us to

$$\frac{c}{4}\epsilon^{\mu\nu\rho\sigma}B_{\mu\nu}F_{\rho\sigma} = -\frac{c}{2}\epsilon^{\mu\nu\rho\sigma}\left(\partial_\rho B_{\mu\nu}\right)C_\sigma = -\frac{c}{6}\epsilon^{\mu\nu\rho\sigma}H_{\rho\mu\nu}C_\sigma. \tag{2.1.30}$$

We also make use of the Bianchi identity, $\epsilon^{\mu\nu\rho\sigma}\partial_\mu H_{\nu\rho\sigma} = 0$. Adding this term to the Lagrangian doesn't change anything because it must be zero; we enforce this by adding a Lagrange multiplier field η to the Lagrangian

$$\mathcal{L} = -\frac{1}{12}H^{\mu\nu\rho}H_{\mu\nu\rho} - \frac{1}{4}F_{\mu\nu}F^{\mu\nu} - \frac{c}{6}\epsilon^{\mu\nu\rho\sigma}H_{\rho\mu\nu}C_\sigma - \frac{c}{6}\eta\epsilon^{\mu\nu\rho\sigma}\partial_\mu H_{\nu\rho\sigma}. \tag{2.1.31}$$

Again integration by parts on the final term of (2.1.31) allows us to solve the equations of motion for $H_{\mu\nu\rho}$ in the form

$$H^{\mu\nu\rho} = -c\epsilon^{\mu\nu\rho\sigma}\left(C_\sigma + \partial_\sigma\eta\right). \tag{2.1.32}$$

Inserting this solution back into the Lagrangian we arrive at the effective theory for the gauge field C_μ, which is

$$\mathcal{L} = -\frac{1}{4}F_{\mu\nu}F^{\mu\nu} - \frac{c^2}{2}\left(C_\sigma + \partial_\sigma\eta\right)^2. \tag{2.1.33}$$

An appropriate choice of gauge for C_σ can "eat" the additional η field and thus C_μ acquires a mass. Through this mechanism we give mass to the Y'_μ gauge boson of the 4 brane model, of the order of M_s, and we will eliminate the anomalies associated with it. When the Higgs fields acquire non-zero vevs will generate additional mass terms for Y'_μ, which will formally introduce mixing with the other gauge bosons, but these will be of order $(\text{TeV}/M_s)^2$. We neglect such effects and identify $Y'_\mu \approx Z'_\mu$.

2.1.3 Identifying the SM and Extension

With the anomaly of Y'_μ removed, we return to the covariant derivative in the basis of Y_μ, Y'_μ, Y''_μ and identify the photon A_μ and weak force mediators $W^+_\mu, W^-_\mu, Z^0_\mu$ by performing a Weinberg transformation on this basis of the form

$$\begin{pmatrix} A_\mu \\ Z^0_\mu \\ W^+_\mu \\ W^-_\mu \end{pmatrix} = \begin{pmatrix} C_{\theta_W} & S_{\theta_W} & 0 & 0 \\ -S_{\theta_W} & C_{\theta_W} & 0 & 0 \\ 0 & 0 & 1/\sqrt{2} & 1/\sqrt{2} \\ 0 & 0 & 1/\sqrt{2} & -i/\sqrt{2} \end{pmatrix} \begin{pmatrix} Y_\mu \\ W^3_\mu \\ W^1_\mu \\ W^2_\mu \end{pmatrix}; \tag{2.1.34}$$

this transformation then puts the covariant derivative in the form of

$$
\begin{aligned}
D_\mu &= \partial_\mu - \frac{i}{\sqrt{2}}\, g_2\, \sigma^- W_\mu^+ - \frac{i}{\sqrt{2}}\, g_2\, \sigma^+ W_\mu^- \\
&\quad - ig_2\, \cos\theta_W\, \left(\sigma^3/2 - Q_Y \tan^2\theta_W\right) Z_\mu^0 \\
&\quad - ig_2 \sin\theta_W\, \left(\sigma^3/2 + Q_Y\right) A_\mu - ig_{Y'}Q_{Y'}Z_\mu' - ig_{Y''}Q_{Y''}Y_\mu'',
\end{aligned}
\tag{2.1.35}
$$

with $\sigma^\pm = \left(\sigma^1 \pm i\sigma^2\right)/2$, and $g_Y/g_2 = \tan\theta_W$. From (2.1.15) and (2.1.35) we find

$$
\begin{aligned}
Q_Y H &= H/2\,, \\
g_{Y'}Q_{Y'}H &= (g_1' C_\theta S_\phi)H\,, \\
g_{Y''}Q_{Y''}H &= (g_1' C_\theta C_\phi)H\,, \\
Q_Y H'' &= 0\,, \\
g_{Y'}Q_{Y'}H'' &= -[g_1' C_\theta S_\phi + g_4'(C_\phi C_\psi + S_\theta S_\phi S_\psi)]H''\,, \\
g_{Y''}Q_{Y''}H'' &= -[g_1' C_\theta C_\phi + g_4'(C_\phi S_\theta S_\psi - C_\psi S_\phi)]H''\,.
\end{aligned}
\tag{2.1.36}
$$

We turn now to exploring the masses of the gauge bosons. Expanding the Higgs fields about their respective vevs, the Higgs kinetic terms of equation (2.1.10) together with the Green-Schwarz mass term, which is $\frac{1}{2}M'^2 Z_\mu' Z'^\mu$, gives

$$
\mathscr{B} = \frac{1}{2}[D_\mu^\dagger\,(0\ v)]\left[D^\mu \begin{pmatrix} 0 \\ v \end{pmatrix}\right] + \frac{1}{2}(D_\mu v'')^\dagger (D^\mu v'') + \frac{1}{2}M'^2 Z_\mu' Z'^\mu\,.
\tag{2.1.37}
$$

Expanding equation (2.1.37) gives

$$
\begin{aligned}
\mathscr{B} &= \frac{(g_2\, v)^2}{4}W_\mu^+ W^{-\mu} + \frac{(g_2 v)^2}{8\cos^2(\theta_W)}\, Z_\mu^0 Z_0^\mu \\
&\quad - \frac{v^2}{2\cos(\theta_W)}g_1' g_2\, C_\theta \left(S_\phi Z_\mu' + C_\phi Y_\mu''\right) Z_0^\mu \\
&\quad + \frac{1}{2}(g_1' v\, C_\theta)^2 \left(S_\phi Z_\mu' + C_\phi Y_\mu''\right)\left(S_\phi Z'^\mu + C_\phi Y''^\mu\right) + \frac{1}{2}M'^2 Z_\mu' Z'^\mu \\
&\quad + \frac{1}{2}v''^2 \left\{ g_1' C_\theta(S_\phi\, Z_\mu' + C_\phi\, Y_\mu'') + g_4'\left[(C_\phi C_\psi + S_\theta S_\phi S_\psi)\, Z_\mu'\right.\right. \\
&\qquad\qquad \left.\left. + (S_\psi S_\theta C_\phi - C_\psi S_\phi)\, Y_\mu''\right]\right\}^2\,. \\
&\simeq \frac{(g_2\, v)^2}{4}W_\mu^+ W^{-\mu} + \frac{(g_2 v)^2}{8\cos^2(\theta_W)}\, Z_\mu^0 Z_0^\mu - \frac{v^2}{2\cos(\theta_W)}g_1' g_2\, C_\theta C_\phi Y_\mu'' Z_0^\mu \\
&\quad + \frac{1}{2}(g_1' v\, C_\theta C_\phi)^2 Y_\mu'' Y''^\mu + \frac{1}{2}v''^2 \left(g_1' C_\theta C_\phi + g_4'\left(S_\psi S_\theta C_\phi - C_\psi S_\phi\right)\right)^2 Y_\mu'' Y''^\mu \\
&\quad + \dots
\end{aligned}
\tag{2.1.38}
$$

where the omitted terms only contain the Z' couplings, which if you recall we ignore since they will be significantly smaller than the mass term provided from the Green-Schwarz mechanism. By inspection of (2.1.38) we can see the $W^{\pm}$ masses are given by usual tree level formula, and the mass of the Z^0 particle associated with the SM is given by $M_{Z_0} = g_2 v/(2 \cos(\theta_W))$ before mixing.

Now we use the relation $g_1' S_\theta = g_4' C_\theta S_\psi$ from equation (2.1.25) to conveniently rewrite (2.1.38) as

$$
\begin{aligned}
\mathscr{B} &\simeq \frac{(g_2\, v)^2}{4} W_\mu^+ W^{-\mu} + \frac{(g_2 v)^2}{8 \cos^2(\theta_W)} Z_\mu^0 Z_0^\mu - \frac{v^2}{2\cos(\theta_W)} g_1' g_2 \, C_\theta C_\phi Y_\mu'' Z_0^\mu \\
&+ \frac{(g_1' v'')^2}{2} \left(\left(\frac{C_\phi}{C_\theta} - \frac{C_\psi S_\phi S_\theta}{C_\theta S_\psi} \right)^2 + \left(\frac{v}{v''} \right)^2 C_\theta^2 C_\psi^2 \right) Y_\mu'' Y''^\mu + \ldots \qquad (2.1.39)
\end{aligned}
$$

$$
\simeq \frac{1}{4}(g_2 v)^2\, W_\mu^+ W^{-\mu} + \left(\begin{array}{cc} Z_\mu^0 & Y_\mu'' \end{array} \right) \cdot \mathbf{M} \cdot \left(\begin{array}{c} Z_0^\mu \\ Y''^\mu \end{array} \right) + \ldots , \qquad (2.1.40)
$$

where $\mathbf{M}$ is a non-diagonal mass matrix. To identify the masses of the system we need to make another change of basis such that $\mathbf{M}$ becomes diagonal. In doing so linear combinations of Y_μ'' and Z_μ^0 become the massive bosons we observe in experiment. However, if we make the assumption that $v'' \gg v$, then the mass matrix is automatically diagonalized into the SM plus an additional massive gauge boson of the scale v'', the equation (2.1.40) becomes

$$
\begin{aligned}
\mathscr{B} &\simeq \frac{(g_2\, v)^2}{4} W_\mu^+ W^{-\mu} + \frac{(g_2 v)^2}{8 \cos^2(\theta_W)} Z_\mu^0 Z_0^\mu \\
&+ \frac{(g_1' v'')^2}{2} \left(C_\phi C_\theta^{-1} - C_\psi S_\psi^{-1} S_\phi T_\theta \right)^2 Y_\mu'' Y''^\mu + \mathcal{O}\left(\left(\frac{v}{v''} \right)^2 \right) . \qquad (2.1.41)
\end{aligned}
$$

We can see we that we preserve the SM results of the ratio of M_{Z_0} to the mass of M_W. Furthermore we make the identification that $Z'' \simeq Y'' + \text{small corrections}$.

Finally, we must check our assumption of orthogonality of charges. Table 1 shows the charges $\mathbf{Q_B}$, $\mathbf{Q_L}$, and $\mathbf{Q_{I_R}}$ are mutually orthogonal in the fermion space, *i.e.*

$$
\sum_f (\mathbf{Q}_i)_f (\mathbf{Q}_j)_f = 0 , \qquad (2.1.42)
$$

for $i \neq j$. The orthogonality relation will be satisfied to one loop [88] for the fermions. However, the charges assigned to H'' will violate the orthogonality condition. The non-orthogonality of H'' is only a minor problem, as contributions from H'' to the running of g_1' are at the 0.9%

level from the string scale to the TeV scale, and at the level of 0.3% for the running of g_4'. These are of the same order as the two loop contributions from the fermion sector, so we may ignore the nonorthogonality introduced by H'' in the context of one loop considerations.

In summary, we have constructed a model that extends the SM by using concepts introduced from string theory; by considering the symmetries of the underlying string theory, we constructed an effective field theory that has all the features of the SM plus two additional $U(1)$ gauge bosons whose masses are at the string scale and at the scale of an additional Higgs field vev. With these additional bosons, Lepton and Baryon number become gauged conservation laws. Because of the addition of two $U(1)$ gauge bosons while still retaining the SM we name this model the SM^{++}, and in the next section we look for potential signals from the SM^{++} model in LHC data.

2.1.4 The LHC Era

At the time of writing the LHC is the largest circular proton-proton collider ever constructed. With a circumference of 27 km, and with a design collision energy of 14 TeV, it will be the highest energy collider to date once full collision energy is achieved. Science runs at the LHC, which is located in the Geneva on the Swiss-French boarder, commenced during the years 2011 and 2012. To compare the model of the SM^{++}, we must first understand what is observed at the LHC experiments. One concept key to new physics discoveries is the concept of beam luminosity. The beam luminosity indicates that the number of particles crossing a unit of area per unit time may or (more likely) may not collide with the intersecting beam at the interaction points (centered around the various detectors that form the LHC). The number of a certain type of events the detectors have are capable of detecting is given by the formula

$$N_{\text{events}} = \sigma \int \mathcal{L}_{\text{I}}(t')dt', \tag{2.1.43}$$

where σ is the cross section of the process of interest and $\int \mathcal{L}_{\text{I}}(t')dt'$ is the integrated luminosity, which is typically given in units of inverse barns, where $1 \text{ bn} = 10^{-28} \text{ m}^2 = 10^2 \text{ fm}^2$. The design instantaneous luminosity of the LHC is $\mathcal{L}_{\text{I}}(t) = 10^{34} \text{ cm}^{-2}\text{s}^{-1} = 10^{-5} \text{ fb}^{-1}\text{s}^{-1}$ [97] which would give an annual integrated luminosity of 315 fb^{-1} if the LHC was to run 24 hours a day, 365 days a year however, it does not and cannot.

Detection of new physics is (like all scientific measurement) a question of statistics; the more events we observe of a rare process will make smaller the standard deviation of the null hypothesis (recall from the mean value theorem the standard deviation goes like $1/\sqrt{N}$, with N as the number of observations) and thus any deviation above 5 standard deviations of the null hypotheses is the generally accepted criteria for discovery. So a larger luminosity means better possible detection of new physics. The data we will use to compare the SM^{++} was taken during the spring of 2012 with integrated luminosities varying from 3.6 ± 0.2 fb^{-1} to 4.1 ± 0.2 fb^{-1} [98] [99]. During this time the LHC was running at collision energies of $\sqrt{s} = 8$ TeV, the highest collision energies ever produced in a lab. The s in the last equation is the common Lorentz invariant term known as a Mandelstam variable. Its value is given in the center of mass frame as

$$s = (k+p)^2 = m_1^2 + m_2^2 + 2\left(\sqrt{p^2 + m_1^2}\sqrt{k^2 + m_2^2} + p^2\right) = (E_1 + E_2)^2 = E_{\text{c.m.}}^2, \quad (2.1.44)$$

with k, p the incoming particle 4-momentum. Expressing collision energies is typically represented by $\sqrt{s} = E_{\text{c.m.}}$ with $E_{\text{c.m.}}$ as the center of mass total energy.

When searching for new particles, a common technique is looking for resonances or peaks in the cross section as a function of invariant mass. The invariant mass method is a technique that takes advantage of the conservation of momentum/energy that is enforced by Lorentz invariance. Searches can be done with multiple products in the decay of the new physics particle, however we will focus on only dilepton and dijet processes. We can see the usefulness of this method by imagining in the collision process a massive particle is produced; with a mass of M this particle then decays and produces two new particles of mass m_1' and m_2'. The conservation of energy requires

$$\sqrt{p^2 + M^2} = \sqrt{p_1'^2 + m_1'^2} + \sqrt{p_2'^2 + m_2'^2}, \quad (2.1.45)$$

where p is the initial momentum of the particle of mass M. These particles then decay, and may decay again, and so on, and the conservation of energy must then read

$$\sqrt{p^2 + M^2} = \sum_{\text{products}} E_i, \quad (2.1.46)$$

where we are summing over all the final products. We also can use the conservation of momentum to enforce

$$\mathbf{p} = \sum_{\text{products}} \mathbf{p}_i, \tag{2.1.47}$$

where $\mathbf{p}$ is the 3-momentum of the decaying particle of mass M and $\mathbf{p}_i$ the 3-momentum of the decay products. Because of this equality, equation (2.1.46) can be expressed as

$$M^2 = \left(\sum_{\text{products}} E_i \right)^2 - \left(\sum_{\text{products}} \mathbf{p}_i \right)^2. \tag{2.1.48}$$

The value of M^2 is called the invariant mass or rest mass of the particle that has undergone the decay process. In the analysis we will use to set limits on the SM^{++}, we use dilepton (detected e^+e^-, or $\mu^+\mu^-$ final states) and dijet (two nearly back-to-back jets (in transverse momentum) of multiple hadrons having nearly identical 3-momentums, can be resolved to two seed partons at the interaction point (IP)) analyses preformed by the CMS and ATLAS experiments [98] [99].

Further understanding of the experimental apparatus to compare with theory is required to understand the analysis. The two main detectors for generalized particle physics at the LHC are the Compact Muon Solenoid (CMS) and the A Toroidal LHC Apparatus (ATLAS) detectors. Both have a similar design, as both are barrel calorimeter detectors. As seen in Fig. 19 the CMS consists of several layers of detector systems. The inner-most detectors are the silicon strip and pixel detectors, which are designed to track the charged debris from collision of two partons of the colliding protons. These detectors help deduce the particles' identity and momentum, as the curvature of the track is a measurement of the particles' momentum in the magnetic field of the detector. After the inner-most tracker, the electromagnetic calorimeter (ECAL) is layered in a cylindrical fashion around the IP. This consists of 76,000 lead-tungstate scintillating crystals. The ECAL is designed to use the pair productions from near approaches of photons or of e^+e^- to the nucleus of the individual atoms of the crystal structure creating photonic showers, which are then read out by photo-multiplier tubes (PMTs) [101]. Hadrons, however, being much more massive, move through this region hardly impeded and then interact with the next layer the brass scintillator hadronic calorimeter (HCAL). This region does essentially the same as the ECAL but has the power to stop hardons. Sandwiched between the superconducting magnet that produces an axial magnetic field of 3.8 T for the CMS is the muon detection system. The muon system consists of several types of detectors, such as drift tubes and capacitive plates

CMS DETECTOR
Total weight   : 14,000 tonnes
Overall diameter : 15.0 m
Overall length   : 28.7 m
Magnetic field   : 3.8 T

STEEL RETURN YOKE
12,500 tonnes

SILICON TRACKERS
Pixel (100x150 μm) ~16m² ~66M channels
Microstrips (80x180 μm) ~200m² ~9.6M channels

SUPERCONDUCTING SOLENOID
Niobium titanium coil carrying ~18,000A

MUON CHAMBERS
Barrel: 250 Drift Tube, 480 Resistive Plate Chambers
Endcaps: 468 Cathode Strip, 432 Resistive Plate Chambers

PRESHOWER
Silicon strips ~16m² ~137,000 channels

FORWARD CALORIMETER
Steel + Quartz fibres ~2,000 Channels

CRYSTAL
ELECTROMAGNETIC
CALORIMETER (ECAL)
~76,000 scintillating PbWO₄ crystals

HADRON CALORIMETER (HCAL)
Brass + Plastic scintillator ~7,000 channels

Figure 19 : The CMS detector at the LHC cut-away shows the layering of the detector systems in the barrel calorimeter geometry. Figure taken from [100].

(these measure ionization of the internal gas like a series of Geiger counters); the muon system is the final system as the muon is so massive compared to other elementary particles (but not so massive that it decays before being detected) that it plows through the whole detector and is only finally detected when interacting in the iron yoke region of the detector (the iron yoke is the manifold the detector is built upon and used to direct the magnetic field in the CMS).

For experimental analysis a common variable, pseudo-rapidity, is used rather than the scattering angle, as it makes algorithms for jet reconstructions easier. Pseudo-rapidity is given by the equation

$$\eta = -\ln\left(\tan\left(\frac{\theta}{2}\right)\right), \tag{2.1.49}$$

with θ as the scattering angle against the beam direction (commonly taken as the z-direction). The CMS covers a region of rapidity from 0 to 2.5 as seen in Fig. 20. To find new particles we must, as in all experiments, battle against noise of the detector. Besides detector uncertainty, which ranges from trigger rates (recording proper events), to offline efficiencies (radiation can damage detectors, taking them offline), to detector acceptance (the efficiency of the detector to actually detect a particle when it is there). We have an enormous amount of background
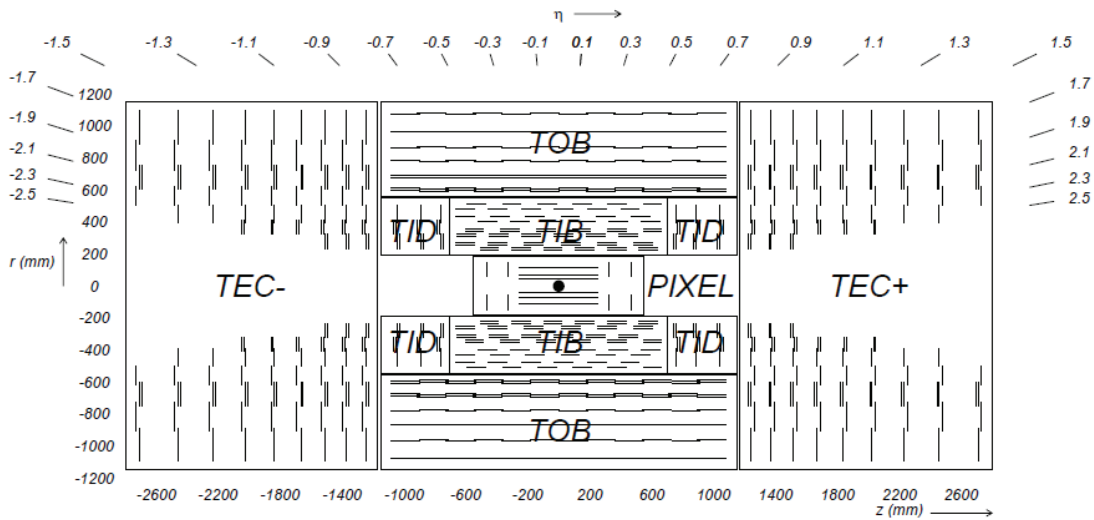
Figure 20 : The CMS detector pseudo-rapidity coverage available from the detector layout. TEC (the end caps), TOB (the outer barrel), TIB/D (the inner barrel/detector). Figure taken from [102].

events that come from well understood physics steaming from glancing interactions or other high energy interactions that have already been understood. Many of these unwanted processes are discarded by the detector itself through using a two-layer trigger system. Fast electronics make determinations if certain events are worth recording, and make the data coming from the detector more manageable to record. One way to cut down on noise events is to use selection cuts. Selection cuts correspond to only analyzing dijet, dilepton (in our case) events that correspond to having a transverse momentum (transverse to the beam direction) p_T greater than a certain value. This helps cut down on noise, as particles with high transverse momentum necessarily underwent hard collision processes rather than glancing collisions. Even with selection cuts, many processes of QCD interactions make it into the data. To understand this background noise a Monte Carlo (MC) simulation of QCD processes and the detection system is done in the invariant mass window of interest via the program PYTHIA for a certain value of integrated luminosity, as was done by the CMS Collaboration in references [98] and [103]. The MC program also determines the level of standard deviations given the integrated luminosity in order to determine if new physics is or is not found. Comparison of the MC generated background, experiment, and theory allows us to set limits on the SM^{++} model.

2.1.5 LHC Phenomenology of SM^{++}

The LHC allows us the possibility to detect the extra gauge boson Z'' if it has a mass the scale of several TeV. The SM^{++} free parameters include three new coupling strengths g'_1, g'_3, and g'_4, which are encoded into three Euler angles (θ, ϕ, ψ) of the $U(1)$ gauge field rotation.

The baryon number coupling g'_3 is fixed to be $g_3(M_s)/\sqrt{6}$ where $g_3(M_s)$ is the $SU_c(3)$ coupling from the SM at the scale of $U_B(3)$ unification which restores the underlying string theoretical symmetry at the string scale. Therefore g'_3 is determined at all energies through the renormalization group (RG) running of the $U_B(1)$ gauge field and is not a free parameter. We take the string scale to be $M_s = 10^{14}$ GeV for running down the g'_3 coupling to the TeV region that is accessible to the LHC; we take special note that we are *ignoring mass threshold effects of stringy states*, which yields $g'_3(M_s) = 0.231$. Varying the string scale does not significantly affect the running of the g'_3 within the LHC range.

To ensure perturbativity of g'_4 between the TeV scale and the string scale so that the renormalization group one loop equations are valid requires that $g'_4(M_s) \leq 1$ (in fact we would like it to be much less than 1, but this is less restrictive). Enforcing this limit in equation (2.1.22) requires that $g'_1(M_s) > 0.4845$ by knowing that the electromagnetic coupling at the mass of the Z^0 scale is $\alpha_{\mathrm{EM}}(M_{Z^0}) = 1/127.9$ [1], we can determine $g_Y(M_{Z^0})$ via

$$
\begin{aligned}
\alpha_{\mathrm{EM}} &= \frac{e^2}{4\pi} = \frac{g_2^2}{4\pi}\sin^2(\theta_W), \\
g_Y(M_{Z^0}) &= g_2(M_{Z^0})\tan(\theta_W) = \frac{\sqrt{4\pi\,\alpha_{\mathrm{EM}}(M_{Z^0})}}{\cos(\theta_W)}, \\
g_Y(M_{Z^0} = 91\text{ GeV}) &\approx 0.357, \\
g_Y(M_s) &\approx 0.429. \tag{2.1.50}
\end{aligned}
$$

In the last line, the one loop RG equations for $U_Y(1)$ are used to determine $g_Y(M_s)$, which then allows us the limit previously mentioned. Similarly we take $g'_1(M_s) \leq 1$ in order to ensure perturbativity at the string scale and all scales below (this is ensured because it is a $U(1)$ coupling). Because of the constraint of (2.1.22) and the requirement of the string scale restored symmetry of $U_B(3)$, only two free parameters are allowed the string scale M_s, which we choose to be $M_s = 10^{14}$ GeV and one coupling; we take g'_1 to be free and it must lie in the range $0.4845 < g'_1(M_s) < 1.0$.

2.1.6 Branching Ratios of Z' and Z''

Here we calculate the branching ratios ($\mathcal{B}$) of various decays types for the $U(1)$ gauge bosons of the SM^{++}. Branching ratios are defined by

$$\mathcal{B}(Z \to l) = \frac{\Gamma_{Z \to l}}{\sum_k \Gamma_{Z \to k}}, \tag{2.1.51}$$

where $\Gamma_{Z \to l}$ is the decay width of particle Z into type l. The first case we consider is setting $g_1'(M_s) \approx 1$. This leads to $\psi(M_s) = -1.245$, $\theta(M_s) = -0.217$, $\phi(M_s) = -0.0006$, $g_4'(M_s) = 0.232$, and $g_3'(M_s) = 0.231$. Substituting these values into (2.1.15), we find the vector bosons (Y, Z_μ', Z_μ'') couple to currents

$$
\begin{aligned}
J_Y &= \left(2.1 \times 10^{-1}\right) Q_{I_R} + \left(2.1 \times 10^{-1}\right) (B - L) \\
J_{Z'} &= \left(5.8 \times 10^{-4}\right) Q_{I_R} + \left(6.6 \times 10^{-1}\right) B + \left(7.4 \times 10^{-2}\right) L \\
J_{Z''} &= \left(9.8 \times 10^{-1}\right) Q_{I_R} - \left(4.7 \times 10^{-2}\right) (B - L),
\end{aligned}
\tag{2.1.52}
$$

at the string scale. To find the couplings down at the TeV region we must use $U(1)$ running equations given by

$$\frac{1}{\alpha_Y(Q)} = \frac{1}{\alpha_Y(M_s)} - \frac{b_Y}{2\pi} \ln(Q/M_s), \tag{2.1.53}$$

$$\frac{1}{\alpha_i(Q)} = \frac{1}{\alpha_i(M_s)} - \frac{b_i}{2\pi} \ln(Q/M_s), \tag{2.1.54}$$

where

$$b_i = \frac{2}{3} \sum_f Q_{i,f}^2 + \frac{1}{3} \sum_s Q_{i,s}^2, \tag{2.1.55}$$

with f and s indicating contribution from fermion and scalar loops, respectively [88]. This result can be found in many standard texts, such as Peskin and Schroeder [30]. By setting the exchange boson energy scale appropriate for current (at the time of writing) LHC data to $Q = 4$ TeV, we obtain from (2.1.54) the couplings: $g_1' = 0.406$, $g_3' = 0.196$, $g_4' = 0.218$, $\theta = -0.466$, $\psi = -1.215$, and $\phi = -0.0003$. In terms of currents, this is

$$
\begin{aligned}
J_Y &= \left(1.8 \times 10^{-1}\right) Q_{I_R} + \left(1.8 \times 10^{-1}\right) (B - L) \\
J_{Z'} &= \left(1.1 \times 10^{-4}\right) Q_{I_R} + \left(5.5 \times 10^{-1}\right) B + \left(7.6 \times 10^{-2}\right) L \\
J_{Z''} &= \left(3.6 \times 10^{-1}\right) Q_{I_R} - \left(9.2 \times 10^{-2}\right) (B - L),
\end{aligned}
\tag{2.1.56}
$$

where we have assumed that H'' has developed its vev v'' at this energy. Decay rates for a particle Z'' are calculated as

$$
\begin{aligned}
d\Gamma_{Z''\to k'p'} &= \frac{|\mathcal{M}|^2}{2M_{Z''}}\frac{d^3k'}{(2\pi)^3 2E_{k'}}\frac{d^3p'}{(2\pi)^3 2E_{p'}}(2\pi)^4\delta^{(4)}(M_{Z''}-k'-p'), \\
|\mathcal{M}|^2 &\simeq |\langle k',p'|T\{J_{Z''}^\mu Z''_\mu\}|M_{Z''}\rangle|^2 \propto J_{Z''}^2.
\end{aligned}
\tag{2.1.57}
$$

The semi equals is due to the fact that the conservation of 4 momentum is already enforced in the differential decay width formula. Due to the vector nature of these $U(1)$ couplings, each decay channel has a common kinematic term (assuming each decay product is highly relativistic so that we can ignore their individual masses), and the end results only depend on the coupling strengths as indicated in the currents. Summing over fermionic decay channels done in a generalized trace operator. We have $\mathrm{Tr}\,[Q_{I_R}B]=\mathrm{Tr}\,[Q_{I_R}L]=\mathrm{Tr}\,[BL]=0$, which give the Z' and Z'' total decay widths as

$$
\begin{aligned}
\Gamma_{Z'} &= \Gamma_{Z'\to Q_{IR}}+\Gamma_{Z'\to B}+\Gamma_{Z'\to L}, \\
&\propto \left(1.1\times 10^{-4}\right)^2\mathrm{Tr}[Q_{I_R}^2]+\left(5.5\times 10^{-1}\right)^2\mathrm{Tr}[B^2]+\left(7.6\times 10^{-2}\right)^2\mathrm{Tr}[L^2] \\
&\propto 9.7\times 10^{-8}+4.0\times 10^{-1}+2.3\times 10^{-2},
\end{aligned}
\tag{2.1.58}
$$

$$
\begin{aligned}
\Gamma_{Z''} &= \Gamma_{Z''\to Q_{I_R}}+\Gamma_{Z''\to B-L}, \\
&\propto (3.6\times 10^{-1})^2\,\mathrm{Tr}[Q_{I_R}^2]+(9.2\times 10^{-2})^2\mathrm{Tr}\left[(B-L)^2\right] \\
&\propto 1.0+4.5\times 10^{-2}\,.
\end{aligned}
\tag{2.1.59}
$$

We can determine generalized branching ratios with this information. We generalize the branching ratios into a sum over particles having a non-zero charge specified below, such as summing over all decay products with non-zero baryon number B would result in a branching ratio for, say, the Z' particle into these particles as $Z'\to B:\ 0.946$. We present the results for the remaining branching ratios as

$$
\begin{array}{ccccccc}
\mathcal{B} & Z'\to B & : & \mathcal{B} & Z'\to L & : & \mathcal{B} & Z''\to Q_{1R} & : & \mathcal{B} & Z''\to B-L \\
0.946 & : & & 0.054 & : & & 0.959 & : & & 0.041 & .
\end{array}
\tag{2.1.60}
$$

Though not relevant for LHC phenomenology due to the string scale mass, we see that Z' is very nearly all in B, with $\mathcal{B}: Z'\to B=0.946$ and $\mathcal{B}: Z'\to L=0.054$. Of course, there can be variation in decay channels particle by particle, as can be seen by the different individual
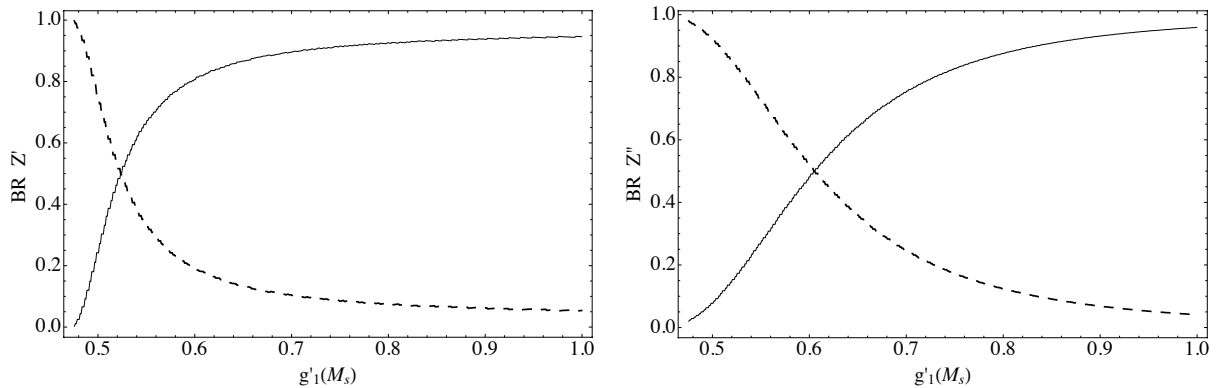
Figure 21 : Branching ratios of Z' (left) and Z'' (right) as a function of $g'_1(M_s)$. The solid lines denote the branching into B (left) and I_R (right). The dashed lines denote the branching into L (left) and B-L (right).

charges in Table 1. The physical couplings of the Z'' to fermionic fields given in Table 1 are consistent with the bounds presented in [104] from a variety of experimental constraints.

Now, we duplicate the procedure for $g'_1(M_s) = 0.4845$, for which we obtain

$$\mathcal{B}\left(Z' \to B\right) : \mathcal{B}\left(Z' \to L\right) : \mathcal{B}\left(Z'' \to Q_{1R}\right) : \mathcal{B}\left(Z'' \to B - L\right)$$
$$0.066 \quad : \quad 0.934 \quad : \quad 0.039 \quad : \quad 0.961 \; . \tag{2.1.61}$$

The chiral couplings of Z' and Z'' gauge bosons decay mostly into L and $B - L$, respectively. The individual charges in this case are given in Table 3. Figure 21 displays the branching ratios for differing values of $g'_1(M_s)$ that are allowed by perturbativity constraints.

2.1.7 Dijet and Dilepton LHC Z'' Phenomenology

Using a data set of pp collisions at $\sqrt{s} = 8$ TeV, with an integrated luminosity of 4.0 fb^{-1}, the CMS Collaboration has searched for narrow resonances in the dijet invariant mass spectrum [98]. Each event in the search is required to have its two highest p_T jets with (pseudo-rapidity) $|\eta_j| < 2.5$. The acceptance of selection requirements is reported to be $\mathcal{A} \approx 0.6$.

The invariant mass spectra fit the SM expectations and thus lower mass limits can be inferred from the cross section times branching ratio for Z'' into two jets. Similar lower mass limits have been obtained by the ATLAS Collaboration using 5.8 fb^{-1} of data collected at $\sqrt{s} = 8$ TeV [99]. These results, which are displayed in Fig. 22, extend previous exclusion limits from runs at $\sqrt{s} = 7$ TeV done in LHC7 [85, 86, 105, 106, 107].

The ATLAS Collaboration has also searched for narrow resonances in the invariant mass

spectrum of dimuon and dielectron final states at $\sqrt{s} = 7$ TeV with an integrated luminosity of 4.9 fb^{-1} and 5.0 fb^{-1}, respectively [108]. The spectra fit with SM expectations and thus upper limits on the cross section times branching ratio for Z'' into lepton pairs can be set. More recently, the CMS Collaboration updated the LHC7 results using 4.1 fb^{-1} of data collected at $\sqrt{s} = 8$ TeV [103]. The combined upper limits from LHC7 and LHC8 are shown in Fig. 23. Previous dilepton searches by the LHC experiments have been reported in [109, 110].

To set upper limits on the SM^{++} model we need to compute the dijet and dilepton cross sections along with the relevant branching ratios. The Lagrangian term for $\bar{f}\gamma^\mu f Z''_\mu$ coupling can be expressed in the traditional form of electro-weak interactions as

$$
\begin{aligned}
\mathscr{L} &= \sum_f \left((g_{Y''}Q_{Y''})_{f_L^i}\, \bar{f}_L^i \gamma^\mu f_L^i + (g_{Y''}Q_{Y''})_{f_R^i}\, \bar{f}_R^i \gamma^\mu f_R^i \right) Z''_\mu, \\
&= \frac{1}{2}\sqrt{g_Y^2 + g_2^2} \sum_f \left(\epsilon_{f_L^i}\, \bar{f}_L^i \gamma^\mu f_L^i + \epsilon_{f_R^i}\, \bar{f}_R^i \gamma^\mu f_R^i \right) Z''_\mu, \\
&= 2^{1/4}\sqrt{G_F} M_{Z^0} \sum_f \left(\epsilon_{f_L^i}\, \bar{f}_L^i \gamma^\mu f_L^i + \epsilon_{f_R^i}\, \bar{f}_R^i \gamma^\mu f_R^i \right) Z''_\mu,
\end{aligned}
\tag{2.1.62}
$$

where $f_{L(R)}^i$ are fermion chiral fields and $\epsilon_{f_L^i, f_R^i} = v_q \pm a_q$, with v_q and a_q the vector and axial couplings, respectively, and G_F is the Fermi coupling constant taken at the 4 TeV scale via

$$
G_F = \frac{1}{4\sqrt{2}} \frac{g_2^2}{M_{Z^0}^2 \cos^2\theta_W} = \frac{1}{4\sqrt{2}} \frac{g_Y^2 + g_2^2}{M_{Z^0}^2}.
\tag{2.1.63}
$$

In order to compare LHC experimental searches in dilepton and dijet events we need to consider the production cross section in the narrow Z'' width approximation of the Breit-Wigner distribution,

$$
\sigma(s) \propto \frac{\Gamma^2}{(\sqrt{s} - M_{Z''})^2 + \Gamma^2/4} \to 2\pi\,\Gamma\delta(\sqrt{s} - M_{Z''}),
\tag{2.1.64}
$$

in the limit that $\Gamma \ll M_{Z''}$. The cross-section for two quarks to Z'' is given by

$$
\hat{\sigma}(q\bar{q} \to Z'') = 2\pi \frac{K}{3} \frac{G_F M_Z^2}{\sqrt{2}} \left[v_q^2(\phi, g_1') + a_q^2(\phi, g_1') \right] \delta\left(\hat{s} - M_{Z''}^2 \right),
\tag{2.1.65}
$$

where the K-factor represents enhancements from higher order QCD processes estimated to be $K \simeq 1.3$ [111]. We include hats ($\hat{s}$, $\hat{\sigma}$) to indicate that these are the values of the partons. To understand what the detector observes we must integrate this result against the possible internal momentum configurations of the proton known as parton distribution functions (PDF). These cannot be solved by perturbation theory as they are described by QCD in the non-perturbative

regime. After folding (integration over) $\hat{\sigma}$ with the CTEQ6 parton distribution functions [112], we can determine the resonant production cross section for $\sigma(pp \rightarrow Z'')$. In Figs. 22 and 23 we compare the predicted $\sigma(pp \rightarrow Z'') \times \mathcal{B}(Z'' \rightarrow jj)$ and $\sigma(pp \rightarrow Z'') \times \mathcal{B}(Z'' \rightarrow \ell\ell)$ production rates with 95% CL upper limits as reported by the CMS and ATLAS Collaborations. We conclude that if Z'' is mostly I_R, then the predicted production rates for $M_{Z''} \approx 4$ TeV at $\sqrt{s} = 8$ TeV lie at the current dijet limits. On the other hand, if Z'' is mostly $B - L$ then the lower limit on the boson mass, $M_{Z''} \geq 3$ TeV, is determined primarily from dilepton searches.
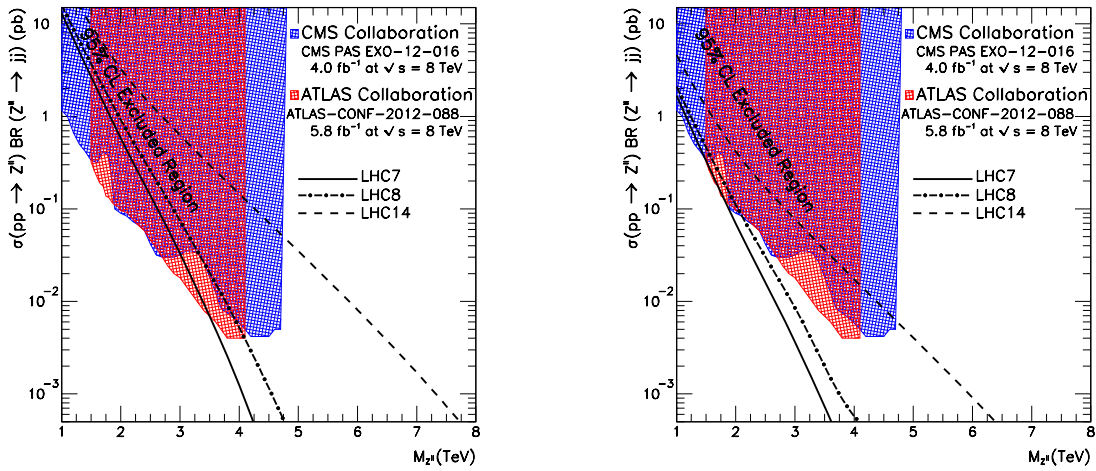
Figure 22 : Comparison of the (pre-selection cut) total cross section for the production of $pp \to Z'' \to jj$ with the 95% CL upper limits on the production of a gauge boson decaying into two jets as reported by the CMS and ATLAS Collaborations (corrected by acceptance). The case in which Z'' is mostly diagonal in I_R is shown in the left panel and the case in which it is mostly $B - L$ in the right panel.
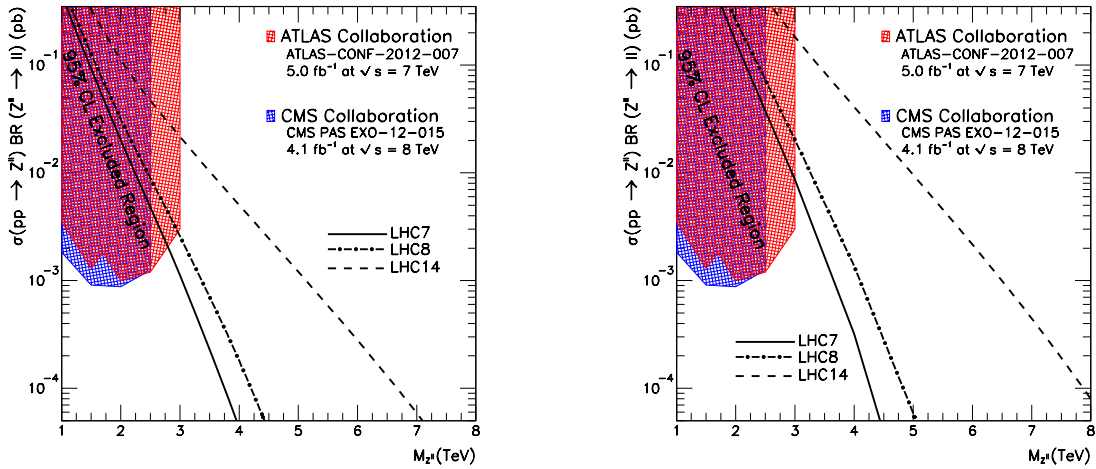
Figure 23 : Comparison of the (pre-selection cut) total cross section for the production of $pp \to Z'' \to \ell\ell$ with the 95% CL upper limits on the production of a gauge boson decaying into two leptons, as reported by the ATLAS and CMS Collaborations. The case in which Z'' is mostly diagonal in I_R is shown in the left panel and the case in which it is mostly $B - L$ in the right panel.

Table 2 : Chiral couplings of Y, Z', and Z'' gauge bosons. All fields in a given set have common $g_{Y'}Q_{Y'}$, $g_{Y''}Q_{Y''}$ couplings. We have taken Z' to be mostly B and and Z'' to be mostly I_R.

Fields	$g_Y Q_Y$	$g_{Y'} Q_{Y'}$	$g_{Y''} Q_{Y''}$
u_R	0.2434	0.1836	0.3321
d_R	-0.1214	0.1838	-0.3933
E_L	-0.1826	0.0759	0.0918
e_R	-0.3650	0.0760	-0.2709
Q_L	0.0610	0.1837	-0.0306
n_R	0.0000	0.0758	0.4545
H	0.1824	0.0000	0.3627
H''	0.0000	-0.0758	-0.4545

Table 3 : Chiral couplings of Y, Z', and Z'' gauge bosons. All fields in a given set have common $g_{Y'}Q_{Y'}$, , $g_{Y''}Q_{Y''}$ couplings. We have taken Z' to be mostly L and and Z'' to be mostly $B - L$.

Fields	$g_Y Q_Y$	$g_{Y'} Q_{Y'}$	$g_{Y''} Q_{Y''}$
u_R	0.2435	0.1101	-0.0763
d_R	-0.1217	0.1101	-0.2242
E_L	-0.1825	0.7165	0.4509
e_R	-0.3651	0.7165	0.3769
Q_L	0.0609	0.1101	-0.1503
n_R	0.0000	0.7165	0.5248
H	0.1826	-0.0000	0.0739
H''	-0.0000	-0.7165	-0.5248

2.1.8 Future Detection Possibilities

For the discovery potential in the high mass region, the dijet channel is statistically a better discriminator than lepton pairs. Therefore, we investigate at the parton level the LHC14 sensitivity for a Z'' resonance (which we take as mostly I_R) in the dijet invariant mass M. After setting selection cuts on the different jet rapidities, $|y_1|$, $|y_2| \leq 1$ and transverse momenta $p_T^{1,2} > 50$ GeV, we calculate the differential cross section as

$$\frac{d\hat{\sigma}_{ij \to kl}}{dM^2} = \frac{|\mathcal{M}|^2_{ij \to kl}}{2\hat{s}} \frac{d^3k}{(2\pi)^3 2k^0} \frac{d^3l}{(2\pi)^3 2l^0} (2\pi)^4 \delta^{(4)}(i + j - k - l)\delta(\hat{s} - M^2). \quad (2.1.66)$$

Following [81] we use the definitions $l^0 = l_\perp \cosh y_1$, $k^0 = k_\perp \cosh y_2$, and $\tau = \hat{s}/s$, where $k_\perp$, $l_\perp$ are the transverse momentum of the partons in the reaction, and we make a change of variable into rapidities via the relation

$$\frac{d^3k}{2k^0} = \frac{1}{2}d^2k_\perp dy_2 = \pi k_\perp dk_\perp dy_2. \quad (2.1.67)$$

Furthermore we use $y \equiv \frac{1}{2}(y_1 - y_2)$ and a common transverse momentum $p_\perp$ defined via $p^2 = \hat{s} = (k + l)^2 \approx 2k \cdot l = 4p_\perp^2 \cosh 2y$. This allows the expansion of the delta function $\delta(\hat{s} - M^2)$ into

$$\delta(\hat{s} - M^2) = \delta(4p_\perp^2 \cosh^2 y - M^2) = \frac{1}{4 \cosh^2 y} \delta\left(p_\perp^2 - \frac{M^2}{4 \cosh^2 y}\right). \quad (2.1.68)$$

After changing the variable yet again to $k_\perp dk_\perp l_\perp dl_\perp \to k_\perp dk_\perp p_\perp dp_\perp$, we integrate out dependence on the transverse momentum extracting from the over energy conservation delta function the perpendicular part

$$\int d^2k_\perp d^2p_\perp \delta^{(2)}(k_\perp + p_\perp)\delta(p_\perp^2 - M^2/4 \cosh^2 y) = \pi. \quad (2.1.69)$$

The parallel components of the momentum of the partons can be converted into limits on the rapidities. We must now fold the result with the PDFs for pp collisions. In terms of these variables, equation (2.1.66) folded with PDFs becomes

$$\frac{d\sigma(pp \to jj)}{dM} = \frac{1}{2}M\tau \int dy_1 dy_2 \frac{1}{\cosh^2 y} \sum_{ijkl} f_i(\sqrt{\tau}e^Y, M)f_j(\sqrt{\tau}e^{-Y}, M)\frac{d\hat{\sigma}_{ij \to kl}}{d\hat{t}}, \quad (2.1.70)$$

where we used

$$|\mathcal{M}|^2_{ij\to kl} = 16\pi\hat{s}^2 \frac{d\hat{\sigma}_{ij\to lk}}{d\hat{t}}. \tag{2.1.71}$$

We can express the cross section per interval of M as

$$
\begin{aligned}
\frac{d\sigma}{dM} &= M\tau \sum_{ijkl} \left[\int_{-Y_{\max}}^{0} dY\, f_i(x_a,\, M)\, f_j(x_b,\, M) \int_{-(y_{\max}+Y)}^{y_{\max}+Y} dy \frac{d\hat{\sigma}_{ij\to lk}}{d\hat{t}}\, \frac{1}{\cosh^2 y} \right. \\
&\quad \left. + \int_{0}^{Y_{\max}} dY\, f_i(x_a,\, M)\, f_j(x_b,\, M) \int_{-(y_{\max}-Y)}^{y_{\max}-Y} dy\, \frac{d\hat{\sigma}_{ij\to kl}}{d\hat{t}}\, \frac{1}{\cosh^2 y} \right], \tag{2.1.72}
\end{aligned}
$$

where $Y \equiv \frac{1}{2}(y_1 + y_2)$. We use for $f(x, M)$ the parton distribution functions of CTEQ6 [112]; we also have $\tau = M^2/s$, $x_a = \sqrt{\tau}e^Y$, $x_b = \sqrt{\tau}e^{-Y}$. The Y integration range in Eq. (2.1.72) is $Y_{\max} = \min\{\ln(1/\sqrt{\tau}),\ y_{\max}\}$, which comes from requiring the fraction of the total momentum of the parton to be less than one, $x_a, x_b < 1$, and the rapidity cuts $y_{\min} < |y_1|, |y_2| < y_{\max}$. The kinematics of the scattering also provides the relation $M = 2p_T \cosh y$, which, when combined with $p_T = M/2\, \sin\theta_s = M/2\sqrt{1 - \cos^2\theta_s}$, yields $\cosh y = (1 - \cos^2\theta_s)^{-1/2}$, where θ_s is the center-of-mass scattering angle. Additionally, the Mandelstam invariants are given by $\hat{s} = M^2$, $\hat{t} = -(M^2/2)\, e^{-y}/\cosh y$, and $\hat{u} = -(M^2/2)\, e^{+y}/\cosh y$.

The spin/color averaged square amplitude (for incoming quark/anti-quark pair $q\bar{q}$ and outgoing quark/anti-quark pair $q'\bar{q}'$) is given by

$$
\begin{aligned}
|\mathcal{M}(q\bar{q} \xrightarrow{Z''} q'\bar{q}')|^2 &= \frac{1}{4} \left[g_{Y''}^2 Q_{Y''}^2(q_L) + g_{Y''}^2 Q_{Y''}^2(q_R) \right] \left[g_{Y''}^2 Q_{Y''}^2(q_L') + g_{Y''}^2 Q_{Y''}^2(q_R') \right] \\
&\quad \times \left[\frac{2(u^2 + t^2)}{(s - M_{Z''}^2)^2 + (\Gamma_{Z''}\, M_{Z''})^2} \right], \tag{2.1.73}
\end{aligned}
$$

where $g_{Y''}Q_{Y''}(q_L)$ and $g_{Y''}Q_{Y''}(q_R)$ are the couplings of Z'' to quarks (note that we have not summed over the flavors).

The decay width of $Z'' \to f\bar{f}$ is given by

$$\Gamma(Z'' \to f\bar{f}) = \frac{G_F M_Z^2}{6\pi\sqrt{2}} N_c\, M_{Z''}\sqrt{1 - 4x} \left[v_f^2(1 + 2x) + a_f^2(1 - 4x) \right] \left(1 + \frac{\alpha_s}{\pi}\right), \tag{2.1.74}$$

where $\alpha_s = \alpha_s(M_{Z''})$ is the strong coupling constant at the scale $M_{Z''}$, $x = m_f^2/M_{Z''}^2$; v_f, a_f are the vector and axial couplings, and $N_c = 3$ or 1 if f is a quark or a lepton, respectively [113]. For our values of g_1' where Z'' is mostly I_R, we obtain $v_u^2 + a_u^2 = 0.396$ and $v_d^2 + a_d^2 = 0.554$.

In Table 4 we calculate prospective signal-to-noise ratios for different possible $M_{Z''}$ masses and integrated luminosity values for LHC14 data. The signal rate $\mathcal{S}$ is estimated in the invariant

mass window $[M_{Z''} - 2\Gamma,\ M_{Z''} + 2\Gamma]$ bin size, and is given as

$$\mathcal{S} = \sigma_{Z''} \int \mathcal{L}_I(t')dt',$$ (2.1.75)

where $\mathcal{S}$ is the expected number of events to be observed in the invariant mass window based on the SM^{++} cross section. To accommodate the minimal acceptance cuts on dijets from the CMS and ATLAS proposals [114], an additional kinematic cut, $|y_{\max}| < 1.0$, is included in the calculation. The noise $(\mathcal{N})$ is the square root of the expected number of QCD background events (N_{bg}) in the same dijet mass interval for the same integrated luminosity, coming from SM processes. This gives the expected signal-to-noise ratio as

$$\frac{\mathcal{S}}{\mathcal{N}} = \frac{\sigma_{Z''}}{\sqrt{\sigma_{\mathrm{bg}}}} \left(\int \mathcal{L}_I(t')dt' \right)^{1/2},$$ (2.1.76)

where σ_{bg} is the total background cross section into dijets in the invariant mass window being probed from SM processes. We conclude that the LHC provides discovery potential for Z'' which is mostly I_R for $M_{Z''} \leq 5$ TeV. The discovery potential of a Z'' that is mostly $B - L$ is controlled by the sensitivity of LHC14 to dilepton searches. For 300 fb^{-1}, the projected LHC sensitivity is again for masses $M_{Z''} \leq 5$ TeV [115].

Table 4 : Signal-to-Noise Ratio at LHC14 for Different Integrated Luminosities.

$M_{Z''}$ (TeV)	10 fb^{-1}			100 fb^{-1}			1000 fb^{-1}		
	$\mathcal{S}$	$\mathcal{B}$	$\mathcal{S}/\mathcal{N}$	$\mathcal{S}$	$\mathcal{B}$	$\mathcal{S}/\mathcal{N}$	$\mathcal{S}$	$\mathcal{B}$	$\mathcal{S}/\mathcal{N}$
4	39	579	1.62	391	5789	5.14	3910	57895	16.25
5	7	176	0.50	67	1759	1.60	670	17590	5.05
6	1	66	0.14	11	664	0.44	113	6646	1.39

2.2 Stability of Extended Higgs Mechanism

Now we turn to the stability of the SM^{++} model. For the symmetry-breaking Higgs mechanism to work, we require that the potential of the SM^{++},

$$V^{++}(H, H'') = \mu_1^2 |H|^2 + \mu_2^2 |H''|^2 + \lambda_1 |H|^4 + \lambda_2 |H''|^4 + \lambda_3 |H|^2 |H''|^2,$$ (2.2.1)

has a non-zero real minimum for all values of the interaction energies. The values of the parameters in quantum field theories change depending on the energies that the fields interact

with. Luckily, renormalizable quantum field theories allow one to compute the values of the parameters at any interaction energy (or at least tell you when the quantum field theory is no longer an accurate description of the system), or else the theory couldn't make any predictions. We say that the parameters of the theory *run* with the interaction energy; the computation of the parameters is addressed in the renormalization group equations.

2.2.1 The Renormalization Group

The renormalziation group (RG), in my opinion, can best be explained by example. Here we will use quantum electro-dynamics (QED) as our toy model. In quantum electrodynamics we have the $U(1)$ gauge invariant Lagrangian

$$\mathcal{L} = \bar{\psi}\left(iD \cdot \gamma - m\right)\psi - \frac{1}{4}F^2 = \bar{\psi}\left(i\gamma \cdot \partial + eA \cdot \gamma - m\right)\psi - \frac{1}{4}F^2 \,. \tag{2.2.2}$$

From (2.2.2) we can compute scattering cross sections of fermions undergoing interactions with the photon. At lowest order (known as tree level) we assume that the parameters in the Lagrangian are those we measure at low energies, such as for the fermion being an electron, where $m = 0.511 \text{ MeV}$ is the mass of the electron, $e = 1.6 \times 10^{-19} \text{ C}$ is the elementary charge for the electron, ψ, A are the fields for the electron and photon, respectively. However, if we want to compute observables to a higher order, then we require loops in our Feynman diagrams. One such example for QED is the correction to the photon propagator shown in Fig. 24. These
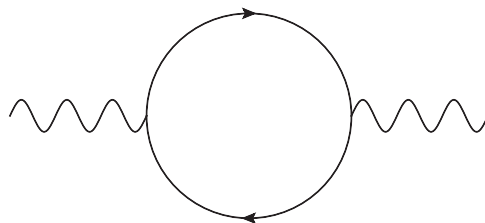
Figure 24 : Higher order terms involving photons include loops of virtual pair production of fermions particles circulating in the loop. This leads to a correction of the bare charge parameter of the Lagrangian for QED.

loops present a problem as they are formally infinite. As stated in the introduction, we can understand the infinities, by assuming the infinities arise because we extend the theory beyond its region of validity to energy scales larger than when the theory is correct. We can prevent

extending the theory beyond its reach, by introducing a cut-off scale denoted Λ. An example of this can be done by computing the value of the diagram in Fig. 24, which gives

$$-e^2 \int \frac{d^4l}{(2\pi)^4} \text{Tr} \left[\frac{\gamma^\mu((k+l)\cdot\gamma + m)\gamma^\nu(l\cdot\gamma + m)}{((k+l)^2 - m^2)(l^2 - m^2)} \right] . \tag{2.2.3}$$

We add the cut-off such that $|l| \leq \Lambda$. However, the value of Λ cannot show up in experiment and the result of the any calculation must be independent of the choice of Λ. This can only be possible if the parameters appearing the Lagrangian are themselves functions of Λ. The Eq. (2.2.2) can be put into the form

$$\mathcal{L} = \bar{\psi}(\Lambda) \left(i\gamma \cdot \partial + e(\Lambda)A(\Lambda) \cdot \gamma - m(\Lambda) \right) \psi(\Lambda) - \frac{1}{4} F(\Lambda)^2 . \tag{2.2.4}$$

Equation (2.2.4) is said to be the effective theory for energy scales $< \Lambda$. It is important to note here that in practice, we will not literally take a cut-off in the computation of the integral (2.2.3) as this creates issues for gauge invariance. We will, however, use a regularization scheme known as dimensional regularization that re-parameterized the cut-off scale Λ into a variable ϵ, which is related to the dimension in which we will calculate (2.2.3). It is still useful to discuss the RG in terms of a cut-off as it is physically more meaningful. With the understanding of (2.2.4) as an effective theory, we want to believe there is an overall field theory that describes QED from an energy scale $\Lambda = \infty$ and downward. To this end we assume there is a QED field theory for $\Lambda = \infty$ that takes the same form as the effective field theory and no extra terms (this defines a renormalizable theory as the number of divergences at the effective theory level can be absorbed into the already existing number of parameters or less; at that level, this ensures that the number of terms of the Lagrangian at the $\Lambda = \infty$ theory does not proliferate):

$$\mathcal{L} = \bar{\psi}_0 \left(i\gamma \cdot \partial + e_0 A_0 \cdot \gamma - m_0 \right) \psi_0 - \frac{1}{4} F_0^2 . \tag{2.2.5}$$

The values of the fields and parameters are now written as their *bare* values, the values valid at the highest energy scale that do not depend on Λ. We can find the values at the scale $\Lambda \neq \infty$ from the bare values by expressing the fields and parameters as

$$\begin{aligned}
\psi_0 &= Z_\psi^{1/2}(\Lambda)\psi(\Lambda) , \\
A_0^\mu &= Z_A^{1/2}(\Lambda)A^\mu(\Lambda) , \\
e_0 &= Z_e(\Lambda)Z_A^{-1/2}(\Lambda)Z_\psi^{-1}(\Lambda)\Lambda^\epsilon e(\Lambda) , \\
m_0 &= Z_m(\Lambda)Z_\psi^{-1}(\Lambda)m(\Lambda) .
\end{aligned} \tag{2.2.6}$$

The Λ^ϵ factor will be explained during explicit calculation of the running of the parameters. It is related to the dimension in which we calculate the divergent integrals, such that as $\Lambda \to \infty$, $\epsilon \to 0$. With this we can write the true or bare Lagrangian as

$$\mathcal{L} = iZ_\psi \bar{\psi}\gamma \cdot \partial\psi + Z_e \Lambda^\epsilon eA \cdot (\bar{\psi}\gamma\psi) - Z_m m\bar{\psi}\psi - \frac{Z_A}{4}F^2 \, , \tag{2.2.7}$$

where the explicit dependence on Λ is no longer displayed on Z_i, e, or m. It is easy to see, but nontrivial to prove that for gauge symmetry to be valid at all scales, that $Z_\psi = Z_e$. This is known as the Ward Identity and the proof can be found in many quantum field theory texts; we will simply assume gauge invariance is true for all scales. One other interesting note is that if there was no interaction term $eA \cdot \bar{\psi}\gamma\psi$, we would have two separate and free field theories for which $m(\Lambda) = m_0$ where the bare mass would take the physical mass of the particle. Therefore since we are calculating using perturbation theory, we can assume that the divergences of the integrals such as (2.2.3) can be expressed as a series of the coupling

$$Z_i = 1 + \sum_{n=1}^{\infty} \tilde{a}_n(e)\Lambda^n = 1 + \sum_{n=1}^{\infty} \frac{a_n(e)}{\epsilon^n} \, . \tag{2.2.8}$$

We will find it advantageous to take the logarithms of the bare values; for example, the bare charge can be written as

$$\begin{aligned} \log e_0 &= \log(Z_A^{-1/2}\Lambda^\epsilon e) = \log(Z_A^{-1/2}) + \epsilon\log(\Lambda) + \log(e) \\ &= \sum_{n=1}^{\infty} \frac{G_n(e)}{\epsilon^n} + \epsilon\log(\Lambda) + \log(e), \end{aligned} \tag{2.2.9}$$

with

$$\sum_{n=1}^{\infty} \frac{G_n(e)}{\epsilon^n} = \log(Z_A^{-1/2}). \tag{2.2.10}$$

We see in Eq. (2.2.6) that the bare values do not depend on Λ, we take advantage of this fact by taking derivatives with respect to $\log(\Lambda)$. It is advantageous to take the derivatives of the logarithms of the bare values, as this separates the dependencies of the Z_i, the result of which is

$$\begin{aligned} 0 = \frac{d\log e_0}{d\log(\Lambda)} &= \epsilon + \frac{1}{e}\frac{de}{d\log(\Lambda)} + \sum_{n=1}^{\infty}\left(\frac{\partial G_n}{\partial e}\frac{de}{d\log(\Lambda)}\frac{1}{\epsilon^n}\right) \\ 0 &= \left(1 + e\sum_{n=1}^{\infty}\frac{\partial G_n}{\partial e}\frac{1}{\epsilon^n}\right)\frac{de}{d\log(\Lambda)} + \epsilon e \, . \end{aligned}$$

$$\tag{2.2.11}$$

We now assume that if the theory is renormalizable, then $de/d\log(\Lambda)$ must be finite in the limit that $\epsilon \to 0$ and we express this as

$$\frac{de}{d\log(\Lambda)} = -\epsilon e + \beta(e) \ . \tag{2.2.12}$$

Using (2.2.12) allows us to write Eq. (2.2.11) order by order in ϵ and enforce that the coefficient of ϵ^{-n} is zero so that Eq. (2.2.11) remains true when $\epsilon \to 0$. This procedure gives the conditions

$$\begin{aligned}
\beta(e) &= e^2 \frac{\partial G_1}{\partial e} \\
\beta \frac{\partial G_n}{\partial e} &= e G_{n+1} \ .
\end{aligned} \tag{2.2.13}$$

From this we can finally express

$$\frac{de}{d\log(\Lambda)} = \beta(e) = e^2 \frac{\partial G_1}{\partial e}. \tag{2.2.14}$$

Similar expressions can be found for the other parameters of the theory as well. In the end, to know the values of the parameters at different scales Λ, one must calculate the beta function from the Z_i functions. As a note, when it was said that $\Lambda \propto \frac{1}{\epsilon}$, it was in effect choosing a regularization method of the divergent integrals known as dimensional regularization, which is the basis of the $\overline{\text{MS}}$ (MS-bar) scheme [24]. Other schemes exist but all give the same experimental values, as they must. Now we will see the RG equations in action.

2.2.2 Example Renormalization Group Use

We return to QED as our toy model, and we see from (2.2.9) that the requirement that gauge invariance at all scales makes solving the β function for QED relativity simple to calculate. We must calculate

$$\log(Z_A^{-1/2}) \approx \frac{G_1(e)}{\epsilon}. \tag{2.2.15}$$

We accomplish this again by rewriting the Lagrangian (2.2.7), this time in terms of canonically normalized fields as

$$\begin{aligned}
\mathcal{L} =\ & i\ \ \bar{\psi}\gamma \cdot \partial\psi - m\bar{\psi}\psi - \frac{1}{4}F^2 \\
& +\ \ i\delta_\psi \bar{\psi}\gamma \cdot \partial\psi - \delta_m m\bar{\psi}\psi - \frac{\delta_A}{4}F^2 \\
& +\ \ Z_e \Lambda^\epsilon e A \cdot (\bar{\psi}\gamma\psi) \ ,
\end{aligned} \tag{2.2.16}$$

where $\delta_i = Z_i - 1$. The terms containing δ_i are known as counter terms, and can be viewed as additional interactions. Let us now understand the origin of the Λ^ϵ term. In 4 dimensional QED, the elementary charge is unit-less in natural units. Generally renormalizable nontrivial theories only contain dimensionless couplings [116]. Rather than enforcing a hard cut-off Λ, we regularize the divergent integrals by using dimensional regularization. That is, we compute the loop terms in a general $D = 4 - 2\epsilon$ dimensional space-time and in the end take the result in the limit that $\epsilon \to 0$. Because we are using dimensional regularization, we like to keep the charge coupling dimensionless, so to keep that true in all dimensions, we leave e dimensionless and add in a massive multiplier that holds the units of e such that $e \to e\Lambda^\epsilon$ in D dimensions. This can be accomplished via the Feynman diagram in Fig. 24 and the additional interactions from the counter terms is given as

$$-(Z_e e)^2 \Lambda^{2\epsilon} \int \frac{d^D l}{(2\pi)^D} \text{Tr}\left[\frac{\gamma^\mu((k+l)\cdot\gamma+m)\gamma^\nu(l\cdot\gamma+m)}{((k+l)^2-m^2)(l^2-m^2)}\right] + i\delta_A\left(k^2 g^{\mu\nu} - k^\mu k^\nu\right) \ .$$

(2.2.17)

Evaluation of (2.2.17) can be done through Feynman squaring method and Wick transformations and generalized trace theorems [30], which are done below. Also we set $Z_e = 1$ since $Z_e = 1 + \mathcal{O}(e^2)$, so at lowest order for Z_A we do not include corrections to Z_e.

$$= -e^2\Lambda^{2\epsilon} \int \frac{d^D l}{(2\pi)^D} \text{Tr}\left[\frac{\gamma^\mu((k+l)\cdot\gamma+m)\gamma^\nu(l\cdot\gamma+m)}{((k+l)^2-m^2)(l^2-m^2)}\right] + i\delta_A\left(k^2 g^{\mu\nu} - k^\mu k^\nu\right)$$

$$= -De^2\Lambda^{2\epsilon} \int_0^1 dx \int \frac{d^D l}{(2\pi)^D} \frac{2l^\mu l^\nu + 2x(x-1)k^\mu k^\nu - (l^2-m^2+x(x-1)k^2)g^{\mu\nu}}{(l^2-m^2-x(x-1)k^2)^2}$$

$$+i\delta_A\left(k^2 g^{\mu\nu} - k^\mu k^\nu\right)$$

$$= -De^2\Lambda^{2\epsilon} \int_0^1 dx \int \frac{d^D l}{(2\pi)^D} \frac{(2/D-1)l^2 g^{\mu\nu} + 2x(x-1)k^\mu k^\nu - (x(x-1)k^2-m^2)g^{\mu\nu}}{(l^2-m^2-x(x-1)k^2)^2}$$

$$+i\delta_A\left(k^2 g^{\mu\nu} - k^\mu k^\nu\right)$$

$$= -iDe^2\Lambda^{2\epsilon} \int_0^1 dx \int \frac{d^D l_E}{(2\pi)^D} \frac{2x(x-1)}{(l_E^2+m^2+x(x-1)k^2)^2}\left(k^2 g^{\mu\nu} - k^\mu k^\nu\right)$$

$$+i\delta_A\left(k^2 g^{\mu\nu} - k^\mu k^\nu\right)$$

$$= -i\left(De^2\Lambda^{2\epsilon} \int_0^1 dx \int \frac{d^D l_E}{(2\pi)^D} \frac{2x(x-1)}{(l_E^2+m^2+x(x-1)k^2)^2} - \delta_A\right)\left(k^2 g^{\mu\nu} - k^\mu k^\nu\right)$$

$$= -i\left(-\frac{e^2}{12\pi^2\epsilon} + \int_0^1 dx \frac{2x(1-x)}{4\pi^2} \log\left(\frac{\overline{\Lambda}^2}{m^2+x(x-1)k^2}\right) - \delta_A\right)\left(k^2 g^{\mu\nu} - k^\mu k^\nu\right)$$

with $\overline{\Lambda}^2 = 4\pi e^{-1/2-\gamma}\Lambda^2$. The rescaling of Λ is known as the "bar" part of the $\overline{\text{MS}}$ scheme. The minimum we can do to make this finite is absorb the infinite part $e^2/12\pi^2\epsilon$ into the term δ_A; this is the minimal subtraction (MS) in the $\overline{\text{MS}}$ scheme

$$\delta_A = -\frac{e^2}{12\pi^2\epsilon} \ .$$

(2.2.18)

From this expression we can find the β function for QED as $Z_A = 1 + \delta_A$. Therefore,

$$
\begin{aligned}
\log(Z_A^{-1/2}) &\approx \frac{e^2}{24\pi^2\epsilon} \to G_1'(e) = \frac{e}{12\pi^2} \ , \\
\frac{de}{d\log\Lambda} &= \frac{de}{d\log\overline{\Lambda}} = \frac{e^3}{12\pi^2}.
\end{aligned}
\tag{2.2.19}
$$

The result of (2.2.19) is a result that can be generalized for multiple copies of the fermionic sector of the QED Lagrangian, such that each particle has a charge $Q_f e$; we can account for each particles' contribution by summing the charges so that (2.2.19) becomes

$$
\frac{de}{d\log\Lambda} = \frac{e^3}{12\pi^2} \sum_{\text{fermions}} Q_f^2.
\tag{2.2.20}
$$

Inclusion of scalar fields that interact with the $U(1)$ field (photon in this case), can also be done, however an additional diagram must be included, and in scalar abelian gauge theories, there is also a term $e^2\phi^\dagger\phi A^\mu A_\mu$. The relevant diagrams are pictured in Fig. 25. The result can be
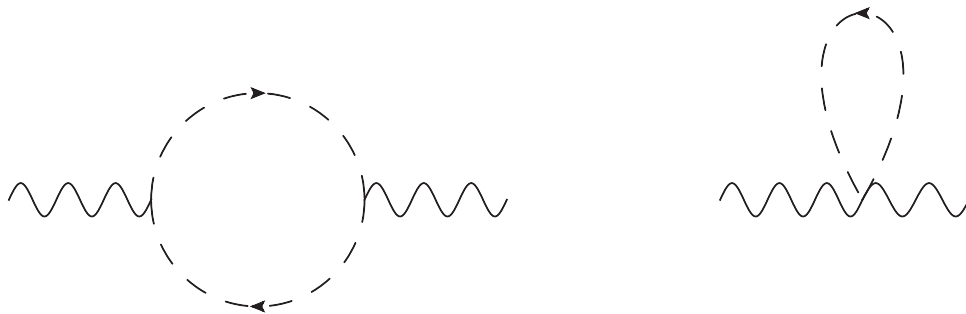
Figure 25 : Higher order terms involving photons in a theory with scalar fields includes two diagrams. This leads to a correction of the bare charge parameter of the Lagrangian for QED with scalar fields.

generalized to multiple scalar fields having couplings $Q_s e$, in which Eq. (2.2.20) becomes

$$
\frac{de}{d\log\Lambda} = \frac{e^3}{12\pi^2} \left(\sum_{\text{fermions}} Q_f^2 + \frac{1}{4} \sum_{\text{scalars}} Q_s^2 \right).
\tag{2.2.21}
$$

2.2.3 The SM Higgs Stability

On July 4th, 2012, the CERN LHC experiment reported from Higgs searches a result that indicates a Higgs boson candidate with a mass $m_H = 125$ GeV. The ATLAS [117] and CMS [118] Collaborations independently combined about 5 fb^{-1} of data collected at $\sqrt{s} = 7$ TeV and more than 5 fb^{-1} at $\sqrt{s} = 8$ TeV. The excess events at 125 GeV that was evident already in

data from the 7 TeV run [119, 120] was consistently observed by both experiments in the $\gamma\gamma$ invariant mass spectrum with a local significance of 4.5σ and 4.1σ, respectively. In addition to the photon data, an excess of events in 4 lepton final states (with $m_{4\ell} \simeq 125$ GeV) can be interpreted as a signal of the $H \to ZZ^* \to 4\ell$ decay, and is observed by both experiments with a significance of 3.4σ and 3.2σ, respectively. The CMS experiment also presented updated Higgs boson searches in W^+W^- (a broad excess in the invariant mass distribution of 1.5σ is observed), $b\bar{b}$ (no excess is observed), and $\tau\bar{\tau}$ (no excess is observed) channels. More recently, the ATLAS Collaboration reported a 2.8σ deviation in the $H \to W^+W^- \to 2\ell\nu$ decay channel [121]. When combining the data from the 7 TeV and 8 TeV runs, both experiments separately reached the sensitivity to the new boson with a local significance of 5σ [8, 9]. Additionally, the CDF and D0 Collaborations at Fermi-lab published an update on searches for the Higgs boson decaying into $b\bar{b}$ pairs using 9.7 fb^{-1} of data collected at $\sqrt{s} = 1.96$ TeV [122]. They reported a 3.3σ deviation with respect to the background-only hypothesis in the mass range between $120 - 135$ GeV.

The data seems to indicate the existence of the long sought Higgs boson. The question we address is the stability of the Higgs mechanism. That is, does Higgs field obtain a non-zero real vacuum expectation value for all energy scales. Next-to-leading order (NLO) constraints on SM vacuum stability based on two-loop renormalization group (RG) equations, one-loop threshold corrections at the electroweak scale (possibly improved with two-loop terms in the case of pure QCD corrections), and one-loop effective potential seem to indicate $m_H \approx 125 - 126$ GeV saturates the minimum value that ensures a vanishing Higgs quartic coupling around the Planck scale (M_{Pl}) (the scale we assume that quantum gravitational effects cannot be ignored, and we assume some change to the SM would be included), see *e.g.* [123, 124, 125, 126, 127, 128, 129, 130, 131, 132, 133, 134]. However, a more recent NNLO analysis [135, 136] yields a very restrictive condition of absolute stability up to the Planck scale given as

$$m_H > \left[129.4 + 1.4 \left(\frac{m_t/\text{GeV} - 173.1}{0.7} \right) - 0.5 \left(\frac{\alpha_s(m_Z) - 0.1184}{0.0007} \right) \pm 1.0_{\text{th}} \right] \text{ GeV}.$$

(2.2.22)

When combining in quadrature the theoretical uncertainty with experimental errors on the mass of the top (m_t) and the strong coupling constant (α_s), one obtains $m_H > 129 \pm 1.8$ GeV. The vacuum stability of the SM up to the Planck scale is excluded at 2σ (98% C.L. one sided) for

$m_H < 126$ GeV [135, 136]. It seems achieving stability will require some new BSM physics.

2.2.4 RG Equations of SM^{++}

In order for the Higgs mechanism to be valid for scales up to the underlying string theory of the SM^{++}, M_s, we impose the positivity conditions [137] on the parameters of SM^{++} scalar potential

$$\lambda_1 > 0, \qquad \lambda_2 > 0, \qquad \lambda_1 \lambda_2 > \frac{1}{4}\lambda_3^2. \tag{2.2.23}$$

If the conditions (2.2.23) are satisfied, we can minimize $V^{++}(H, H'')$ and find two real, non-zero, VEVs for the two Higgs fields of the SM^{++}. In the unitary gauge, the fields can be written as

$$H \equiv \frac{1}{\sqrt{2}} \begin{pmatrix} 0 \\ v_1 + h_1(x) \end{pmatrix} \quad \text{and} \quad H'' \equiv \frac{1}{\sqrt{2}} \left(v_2 + h_2(x) \right), \tag{2.2.24}$$

with v_1 and v_2 the real and non-negative VEVs. The non-zero, real solutions to the minimization of (2.2.1) are obtained for v_1 and v_2 and are given by

$$v_1^2 = \frac{-\lambda_2 \mu_1^2 + \frac{1}{2}\lambda_3 \mu_2{}^2}{\lambda_1 \lambda_2 - \frac{1}{4}\lambda_3^2} \quad \text{and} \quad v_2^2 = \frac{-\lambda_1 \mu_2^2 + \frac{1}{2}\lambda_3 \mu_1^2}{\lambda_1 \lambda_2 - \frac{1}{4}\lambda_3^2}. \tag{2.2.25}$$

To compute the scalar masses, we must expand the potential (2.2.1) around the minima (2.2.25). We denote by h and h'' the scalar fields of definite masses (mass matrix eigenstates), m_h and $m_{h''}$, respectively. After a bit of algebra, the explicit expressions for the scalar mass eigenvalues and eigenvectors are given by

$$m_h^2 = \lambda_1 v_1^2 + \lambda_2 v_2^2 - \sqrt{(\lambda_1 v_1^2 - \lambda_2 v_2^2)^2 + (\lambda_3 v_1 v_2)^2}, \tag{2.2.26}$$

$$m_{h''}^2 = \lambda_1 v_1^2 + \lambda_2 v_2^2 + \sqrt{(\lambda_1 v_1^2 - \lambda_2 v_2^2)^2 + (\lambda_3 v_1 v_2)^2}, \tag{2.2.27}$$

$$\begin{pmatrix} h \\ h'' \end{pmatrix} = \begin{pmatrix} \cos\alpha & -\sin\alpha \\ \sin\alpha & \cos\alpha \end{pmatrix} \begin{pmatrix} h_1 \\ h_2 \end{pmatrix}, \tag{2.2.28}$$

where $\alpha \in [-\pi/2, \pi/2]$ also fullfils

$$\sin 2\alpha = \frac{\lambda_3 v_1 v_2}{\sqrt{(\lambda_1 v_1^2 - \lambda_2 v_2^2)^2 + (\lambda_3 v_1 v_2)^2}}, \tag{2.2.29}$$

$$\cos 2\alpha = \frac{\lambda_1 v_1^2 - \lambda_2 v_2^2}{\sqrt{(\lambda_1 v_1^2 - \lambda_2 v_2^2)^2 + (\lambda_3 v_1 v_2)^2}}. \tag{2.2.30}$$

Now, it is convenient to invert (2.2.26), (2.2.27) and (2.2.29), to extract the parameters in the Lagrangian in terms of the physical quantities m_h, $m_{h''}$ and $\sin 2\alpha$

$$
\begin{aligned}
\lambda_1 &= \frac{m_{h''}^2}{4v_1^2}(1 - \cos 2\alpha) + \frac{m_h^2}{4v_1^2}(1 + \cos 2\alpha), \\
\lambda_2 &= \frac{m_h^2}{4v_2^2}(1 - \cos 2\alpha) + \frac{m_{h''}^2}{4v_2^2}(1 + \cos 2\alpha), \\
\lambda_3 &= \sin 2\alpha \left(\frac{m_{h''}^2 - m_h^2}{2v_1 v_2} \right).
\end{aligned}
\tag{2.2.31}
$$

One-loop corrections to (2.2.1) can be implemented by making λ_1, λ_2, and λ_3 field dependent quantities. Equation (2.2.23) then needs to be imposed in the regions where this is the case. When we talk about the stability of (2.2.1) at some energy $\Lambda = Q$ (with the use of the couplings at that scale), we are thinking that the field values are at the scale Q. For $\lambda_3 > 0$, the third condition in (2.2.23) is only invalidated for field values v_1 around $m_{h''}$, regardless of the renormalization scale Q [138]. We can find the instability regions by expressing the scalar potential as

$$
\begin{aligned}
V^{++} = \quad & \lambda_1(Q) \left(|H|^2 - \frac{v_1^2}{2} \right)^2 + \lambda_2(Q) \left(|H''| - \frac{v_2^2}{2} \right)^2 \\
+ \quad & \lambda_3(Q) \left(|H|^2 - \frac{v_1^2}{2} \right) \left(|H''|^2 - \frac{v_2^2}{2} \right).
\end{aligned}
\tag{2.2.32}
$$

The instability region ($V^{++} < 0$) is given by, $|H''| \approx 0$ and

$$
v_2 < \frac{m_{h''}}{\sqrt{2\lambda_2}}, \quad Q_- < v_1 < Q_+, \quad Q_\pm^2 = \frac{m_{h''}^2 \lambda_3}{8\lambda_1 \lambda_2} \left(1 \pm \sqrt{1 - \frac{4\lambda_1 \lambda_2}{\lambda_3^2}} \right) \Bigg|_{Q_*},
\tag{2.2.33}
$$

where Q_* is some energy scale where the third condition of (2.2.23) is violated [138]. Thus, $Q_\pm \sim m_{h''}$ when the third condition is saturated, i.e. $\lambda_1 \lambda_2 = \lambda_3^2/4$. From (2.2.33) we see that $Q_\pm \sim m_{h''}$ when all the λ_i are roughly at the same scale. If one of the $\lambda_{1,2}$ is close to zero, then Q_+ can be $\gg m_{h''}$, but this region of the parameter space is taken care of by the condition $\lambda_{1,2} > 0$. The stability for field values at $m_{h''}$ is then determined by the potential with coupling at scale $m_{h''}$ (instead of Q). Therefore, for $\lambda_3 > 0$, we impose the third condition of (2.2.23) in the vicinity of $m_{h''}$ only. Even though the potential appears to be unstable at $Q \gg m_{h''}$, it is actually stable when all the field values are at the scale Q. Note that the potential with $\lambda_i(Q)$ can only be used when the physical quantities (field values v_1, v_2) are at the scale Q.

On the other hand, the instability region for $\lambda_3 < 0$ occurs for $|H''| > v_2/\sqrt{2}$. Because of this, we can neglect the mass parameters and approximate the potential as

$$V^{++} \approx \lambda_1(Q)|H|^4 + \lambda_2(Q)|H''|^4 + \lambda_3(Q)|H|^2|H''|^2. \tag{2.2.34}$$

The instability region is then given as

$$v_2 > \frac{m_{h''}}{\sqrt{2\lambda_2}}, \quad c_- < \frac{v_1}{v_2} < c_+, \quad c_\pm^2 = \left. -\frac{\lambda_3}{2\lambda_1}\left(1 \pm \sqrt{1 - \frac{4\lambda_1\lambda_2}{\lambda_3^2}}\right)\right|_{Q_*}. \tag{2.2.35}$$

We can see in this case the ratio of v_1 and v_2 determines the instability region, which can be reached even with both v_1 and v_2 being $\gg m_{h''}$ [138]. Therefore, for $\lambda_3 < 0$, we impose the third condition at all energy scales. Note that the asymmetry in conditions on λ_3 will carry over into an asymmetry in α.

Calculations similar to the ones that lead to Eq. (2.2.21) can be done for all the parameters of the SM^{++} model. The RG equations for the five parameters in the scalar potential [139] are

$$
\begin{aligned}
\frac{d\mu_1^2}{dt} &= \frac{\mu_1^2}{16\pi^2}\left(12\lambda_1 + 6Y_t^2 + 2\frac{\mu_2^2}{\mu_1^2}\lambda_3 - \frac{9}{2}g_2^2 - \frac{3}{2}g_Y^2 - \frac{3}{2}g_{\mathcal{Y}}^2\right), \\
\frac{d\mu_2^2}{dt} &= \frac{\mu_2^2}{16\pi^2}\left(8\lambda_2 + 4\frac{\mu_1^2}{\mu_2^2}\lambda_3 - 24g_{B-L}^2\right), \\
\frac{d\lambda_1}{dt} &= \frac{1}{16\pi^2}\left(24\lambda_1^2 + \lambda_3^2 - 6Y_t^4 + \frac{9}{8}g_2^4 + \frac{3}{8}g_Y^4 + \frac{3}{4}g_2^2g_Y^2 + \frac{3}{4}g_2^2g_{\mathcal{Y}}^2 + \frac{3}{4}g_Y^2g_{\mathcal{Y}}^2 + \frac{3}{8}g_{\mathcal{Y}}^4\right. \\
&\quad \left. + 12\lambda_1 Y_t^2 - 9\lambda_1 g_2^2 - 3\lambda_1 g_Y^2 - 3\lambda_1 g_{\mathcal{Y}}^2\right), \tag{2.2.36} \\
\frac{d\lambda_2}{dt} &= \frac{1}{8\pi^2}\left(10\lambda_2^2 + \lambda_3^2 + 48g_{B-L}^4 - 24\lambda_2 g_{B-L}^2\right), \\
\frac{d\lambda_3}{dt} &= \frac{\lambda_3}{8\pi^2}\left(6\lambda_1 + 4\lambda_2 + 2\lambda_3 + 3Y_t^2 - \frac{9}{4}g_2^2 - \frac{3}{4}g_Y^2 - \frac{3}{4}g_{\mathcal{Y}}^2 - 12g_{B-L}^2\right) \\
&\quad + \frac{3}{4\pi^2}g_{\mathcal{Y}}^2 g_{B-L}^2,
\end{aligned}
$$

where $t = \ln Q$ and Y_t is the top Yukawa coupling, with

$$\frac{dY_t}{dt} = \frac{Y_t}{16\pi^2}\left(\frac{9}{2}Y_t^2 - 8g_3^2 - \frac{9}{4}g_2^2 - \frac{17}{12}g_Y^2 - \frac{17}{12}g_{\mathcal{Y}}^2 - \frac{2}{3}g_{B-L}^2 - \frac{5}{3}g_{\mathcal{Y}}g_{B-L}\right) \tag{2.2.37}$$

and $Y_t^{(0)} = \sqrt{2}\, m_t/v$. The RG running of the gauge couplings follow the standard form

$$
\begin{aligned}
\frac{dg_3}{dt} &= \frac{g_3^3}{16\pi^2}\left[-11 + \frac{4}{3}n_g\right] = -\frac{7}{16}\frac{g_3^3}{\pi^2}\,, \\
\frac{dg_2}{dt} &= \frac{g_2^3}{16\pi^2}\left[-\frac{22}{3} + \frac{4}{3}n_g + \frac{1}{6}\right] = -\frac{19}{96}\frac{g_2^3}{\pi^2}\,, \\
\frac{dg_Y}{dt} &= \frac{1}{16\pi^2}\left[A^{YY}g_Y^3\right]\,, \\
\frac{dg_{B-L}}{dt} &= \frac{1}{16\pi^2}\left[A^{(B-L)(B-L)}g_{B-L}^3 + 2A^{(B-L)Y}g_{B-L}^2 g_\mathcal{Y} + A^{YY}g_{B-L}g_\mathcal{Y}^2\right]\,, \\
\frac{dg_\mathcal{Y}}{dt} &= \frac{1}{16\pi^2}\left[A^{YY}g_\mathcal{Y}\left(g_\mathcal{Y}^2 + 2g_Y^2\right) + 2A^{(B-L)Y}g_{B-L}(g_\mathcal{Y}^2 + g_Y^2)\right. \\
&\quad + \left. A^{(B-L)(B-L)}g_{B-L}^2 g_\mathcal{Y}\right]\,,
\end{aligned}
\tag{2.2.38}
$$

where $n_g = 3$ is the number of generations and

$$
A^{ab} = A^{ba} = \frac{2}{3}\sum_f Q_{a,f}Q_{b,f} + \frac{1}{3}\sum_s Q_{a,s}Q_{b,s}\,, \qquad (a, b = Y,\ B-L)\,, \tag{2.2.39}
$$

with f and s indicating contribution from fermion and scalar loops, respectively.

For energies below the mass of the heavier Higgs H'', the effective theory is the SM. Thus the effective scalar Lagrangian in the low energy regime must take on the form appropriate for the SM

$$
\mathscr{L}_s = (\mathcal{D}^\mu H)^\dagger \mathcal{D}_\mu H - \mu^2 |H|^2 - \lambda |H|^4\,. \tag{2.2.40}
$$

The RG equations in this regime must simplify to those of SM. To obtain the matching conditions connecting the two theories so that they reflect a consistent theory, we can follow [138] and integrate out the field H'' to obtain the effective Lagrangian of the form (2.2.40). To find the effective Lagrangian is to perform the Feynman path integral over the H'' field

$$
\int \mathcal{D}H''\, e^{iS(H,H'')} = e^{iS_{\text{eff}}(H)}, \tag{2.2.41}
$$

from which you can read the potential V_{eff} of the form (2.2.40). Rather than carrying out this rather complicated task, we can approximate this integral by expanding the action $S(H, H'')$ around the field configuration that gives $\delta S/\delta H'' = 0$, which is the condition for the classical equations of motion. This gives

$$
\int \mathcal{D}H''\, e^{iS(H,H'')} \approx e^{iS(H,H_{cl})} \int \mathcal{D}H'' e^{i\int \frac{1}{2}\frac{\delta^2 S}{\delta H''^2}|_{H''_{cl}}(H''-H''_{cl})^2 + \cdots}\,, \tag{2.2.42}
$$

where above H''_{cl} is the classical solution where $\delta S/\delta H''|_{H''_{cl}} = 0$ is satisfied. From this expression we can see that S_{eff} can be approximated by $S(H, H_{cl})$ so long as $(H'' - H_{cl})$ is small

for all cases considered. Since we are in the phase where the energies of interaction are below the scale of exciting H'', we can assume the quantum corrections are small. By solving the equations of motion for H'' and neglecting the derivative terms, as we are assuming that there is little excitation of the H'' field, we have the result

$$\frac{\partial}{\partial H''}V(H, H'') = 0 \rightarrow |H''|^2 = -\frac{\mu_2^2 + \lambda_3|H|^2}{2\lambda_2}. \tag{2.2.43}$$

Replacing (2.2.43) back into $V(H, H'')$ allows you to identify the quadratic and quartic terms in the potential, which yields

$$\mu^2 = \mu_1^2 - \mu_2^2\frac{\lambda_3}{2\lambda_2} \tag{2.2.44}$$

and

$$\lambda = \lambda_1\left(1 - \frac{\lambda_3^2}{4\lambda_1\lambda_2}\right), \tag{2.2.45}$$

respectively. The matching conditions are consistent with the continuity of $v \rightleftharpoons v_1$; namely

$$v^2 = -\left.\frac{\mu^2}{\lambda}\right|_{Q=m_{h''}} = -\left.\frac{\mu_1^2 - \mu_2^2\,\lambda_3/(2\lambda_2)}{\lambda_1\left[1 - \lambda_3^2/(4\lambda_1\lambda_2)\right]}\right|_{Q=m_{h''}}, \tag{2.2.46}$$

or equivalently

$$\left.v^2\right|_{Q=m_{h''}} = \left.v_1^2\right|_{Q=m_{h''}}, \tag{2.2.47}$$

with v_1 given by (2.2.25). The quartic interaction between the heavy scalar singlet and the Higgs doublet provides an essential contribution for the stabilization the scalar field potential [138].

2.2.5 Running the Couplings

Now that we have the equations that determine how the values of the parameters of the scalar potential change with scale Q, we must solve these coupled differential equations. In order to ensure perturbativity of g_4' between the TeV scale and the string scale, we find from (2.1.22) that $g_1' > 0.232$. We also take $g_1'(M_s) \simeq 1$ in order to ensure perturbativity at the string scale. Let us first study the region of the parameter space constrained by $g_1'(M_s) \simeq 1$. The string-scale values of the other abelian couplings are fixed by previous considerations (2.1.22) and (2.1.2). The Euler angles at M_s are also fixed by (2.1.25), and (2.1.26). All the couplings and angles are therefore determined at all energies through RG running. As an illustration, we set $M_s = 10^{14}$ GeV; this leads to $g_3'(M_s) = 0.231$, $g_4'(M_s) = 0.232$, $\psi(M_s) = -1.245$, $\theta(M_s) = -0.217$, and $\phi(M_s) = -0.0006$.

Now we take $Q_{\min} = 125$ GeV and normalize $t = \ln(Q/125\,\text{GeV})$ and $t_{\max} = \ln(M_s/125\,\text{GeV})$. From the M_s scale we run the couplings and angles down to the TeV region giving $g_1' = 0.406$, $g_3' = 0.196$, $g_4' = 0.218$, $\theta = -0.466$, $\psi = -1.215$, and $\phi = -0.0003$.

We are now in a position to randomly choose v'' and $m_{h''}$ at the scale $Q = m_{h''}$. We can then use the SM relation $m_H^2 = -2\mu^2$, where $m_H \simeq 125$ GeV, and $v^2 = 246$ GeV, both taken at the same energy scale $Q = 125$ GeV to find the initial conditions for the parameters μ and λ at the $Q_{\min}$ scale. It should be noted that we take the top Yukawa coupling evaluated at the scale m_t. This introduces a small but unnoticeable error. On the other hand, m_t is taken to be the physical top mass; if we used the running mass instead, as is done in [140], the running of the quartic coupling λ would be much slower, with the instability scale pushed to almost 10^9 GeV.

Then we run the SM couplings λ, and μ from 125 GeV up to the mass scale $Q = m_{h''}$. After having done this, we then use the matching conditions to determine v, which in turns allows one to solve algebraically for m_h at the scale $Q = m_{h''}$. This process ensures that we match the SM results when $Q < m_{h''}$.

After completing this task, there is one free parameter left to be fixed at the TeV-scale: α. The initial values of g_Y, $g_{\mathcal{Y}}$ and g_{B-L} are then fixed by previous considerations as in Sec. 2.1.6.

Rather than using the parameters v'', α, and $m_{h''}'$ as the free ones, we can use the relation $M_{Z''} = g_1' \, C_\phi \, v_2 / C_\theta$ [141], so that we can take $(M_{Z''}, \alpha, m_{h''})$ as the free parameters of the model.[1]

For $M_s = 10^{14}$ GeV, we perform a scan of 10^4 random values of $(M_{Z''}, \alpha, m_{h''})$ points, and using (2.2.31) we obtain the initial conditions $(\lambda_1^{(0)}, \lambda_2^{(0)}, \lambda_3^{(0)})$ at the $Q = m_{h''}$ value, after which we integrate the RG equations (2.2.36). For each set of random points, we verify that the positivity condition (2.2.23) is fulfilled all the way to the M_s scale. The 10^4 trials are duplicated for $M_s = 10^{16}$ and $M_s = 10^{19}$ GeV. The results are encapsulated in Figs. 26 to 32. Figure 26 shows the entire scan for $M_s = 10^{14}$ GeV and $M_{Z''} = 4.5$ TeV. The points yielding a stable vacuum solution up to M_s are blue-printed, those leading to unstable vacuum solutions are red-printed, and points giving runaway solutions are purple-printed. A stable vacuum solution is one in which the positivity condition (2.2.23) is fulfilled all the way to $\Lambda = M_s$. An unstable

---

[1] For $M_s = 10^{14}$ GeV, the $v_2 \leftrightarrows M_{Z''}$ relation implies that if 7 TeV $< v_2 <$ 13 TeV, then 3.2 TeV $< M_{Z''} <$ 6.0 TeV. For a different M_s the range of $M_{Z''}$ is altered because of changes in g_1', θ, and ϕ; *e.g.* for $M_s = 10^{19}$ GeV, the range becomes 2.8 TeV $< M_{Z''} <$ 5.8 TeV.
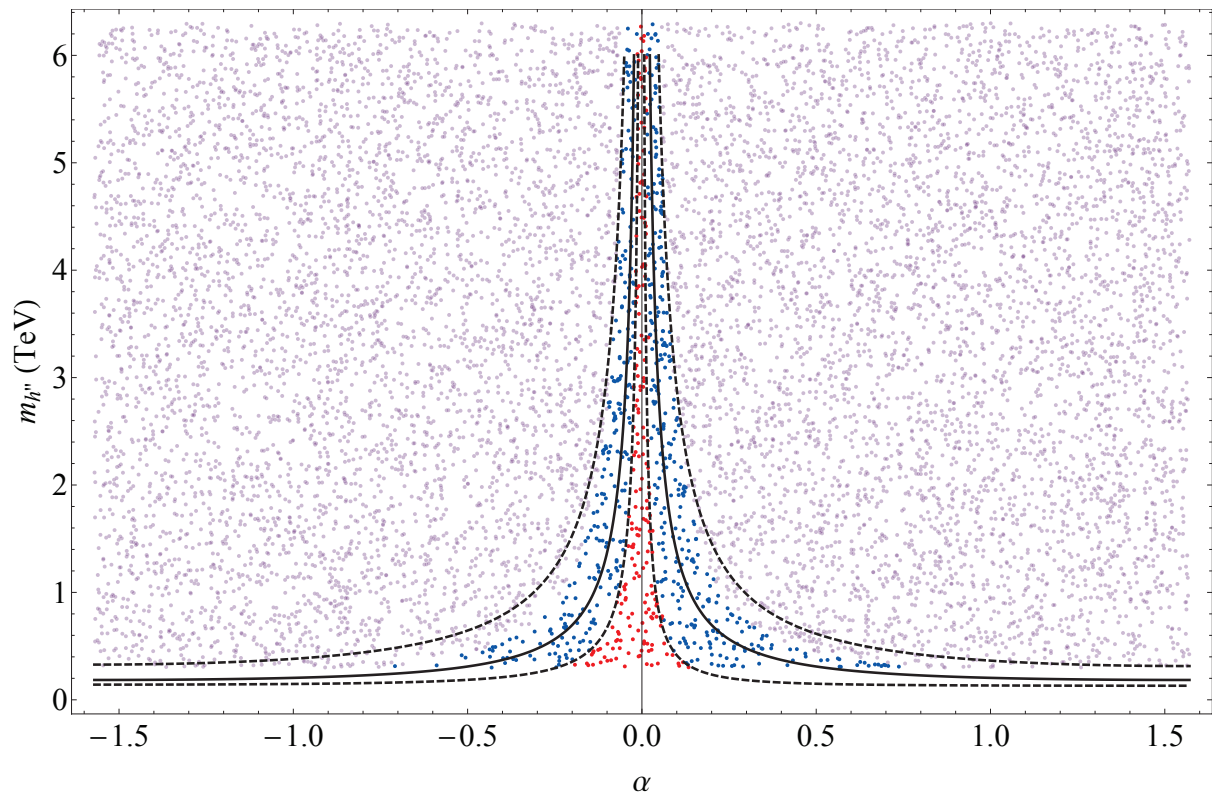
Figure 26 : The SM^{++} vacuum stability patterns in the $m_{h''}$ vs α plane, for $M_{Z''} = 4.5$ TeV. The analysis is based on a scan of 10^4 random points with $M_s = 10^{14}$ GeV. The points yielding a stable vacuum solution up to M_s are blue-printed, those leading to unstable vacuum solutions are red-printed, and points giving runaway solutions (*i.e.*, those in which the Higgs doublet self-coupling blows up) are purple-printed. Fits to the boundaries defining the region with stable vacuum solutions (dashed lines) and to the average value of the scatter points contained in that region (solid lines) are also shown [142].

solution is one in which the stability conditions of the vacuum ($\lambda_1 > 0$, $\lambda_2 > 0$, $\lambda_1\lambda_2 > \lambda_3^2/4$) are violated (recall that for the case $\lambda_3 > 0$ there is no need to impose the third condition in (2.2.23) at all scales, but only in the vicinity of $m_{h''}$). A runaway solution is one in which the RG equations drive the Higgs doublet self-coupling to non-perturbative values, thus invalidating the p-theory results. The perturbative upper bound (sometimes referred to as 'triviality' bound) is given by $\lambda_1 < 2\pi$, so that at any point in the RG evolution of the $\lambda_1(t)$ parameter, the triviality bound is violated we take λ_1 as runaway at that point [132]. The vacuum stability condition is driven by the behavior of λ_1, and actually is largely dominated by the initial condition $\lambda_1^{(0)}$. Indeed, if the extra gauge boson Z'' gets its mass through a non-Higgs mechanism and the scalar potential (2.2.1) is that of SM (*i.e.* when $v_2 = \lambda_2 = \lambda_3 = 0$), the RG evolution becomes that of SM and there are no stable solutions.[2]

To determine the range of initial conditions on $\lambda_1^{(0)}$ yielding stable vacuum solutions, we fit the boundaries of the blue band in the scatter plot. The resulting curves, which are shown as dashed lines in Fig. 26, correspond to $0.16 < \lambda_1^{(0)} < 0.96$ when $\alpha < 0$, and $0.15 < \lambda_1^{(0)} < 0.96$ when $\alpha > 0$. The lower limit of $\lambda_1^{(0)}$, which defines the boundary between stable and unstable solutions, is close to the value required for vacuum stability of the SM potential, as shown in (2.2.22). Specifically, by substituting $m_h = 130$ GeV and $\alpha = 0$ in (2.2.31) we obtain $\lambda_1^{(0)} = 0.14$. The similarities between the minimum value of m_H that allows absolute stability up to the Planck scale within SM and the minimum value of m_h in the decoupling limit of (2.2.31) reinforces the previous statement concerning the strong dependence of the RG evolution with the initial condition $\lambda_1^{(0)}$. The average value of the initial condition $\lambda_1^{(0)}$ can be performed through a fit to the blue points in the scattered plot. The result, which is shown as solid lines in Fig. 26, corresponds to $\langle \lambda_1^{(0)} \rangle = 0.28$.

The behavior of λ, together with the typical behavior of λ_1 and λ_2 for the average value of the initial condition $\langle \lambda_1^{(0)} \rangle$, are shown in Fig. 27. Note that λ_1 heads towards the instability and reaches a minimum greater than zero; thereafter it rises towards the Landau point (divergence). This behavior is characteristic of models with scalar singlets [143]. Also shown in Fig. 27 is the typical behavior of $\lambda_1\lambda_2 - \lambda_3^2/4$ for $\alpha < 0$ and $\langle \lambda_1^{(0)} \rangle = 0.28$. The asymmetry between

---

[2]Of course, even if $v_2 = \lambda_2 = \lambda_3 = 0$, with an extra gauge boson the RG evolution of λ_1 is not exactly that of SM, see (2.2.36).
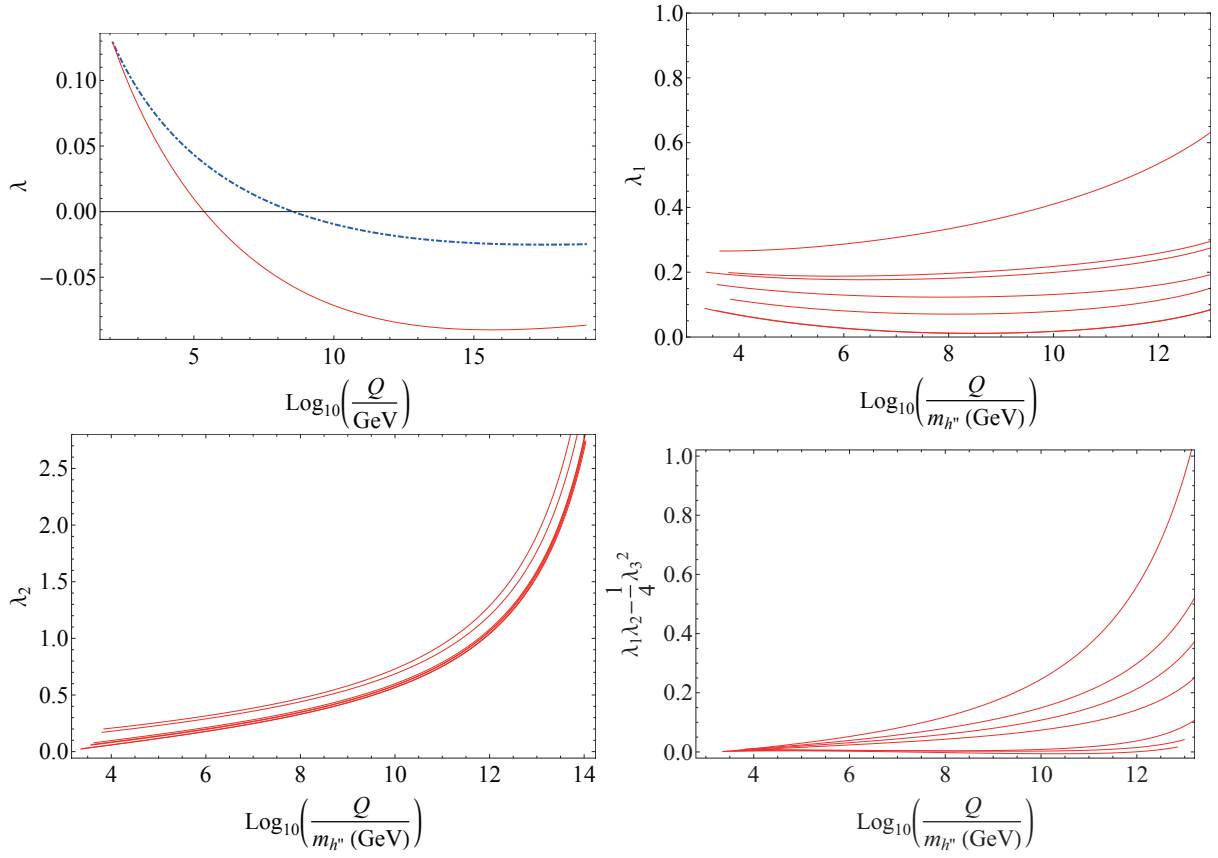
Figure 27 : From left to right downwards: the first panel shows the running of λ from its value at 125 GeV (red solid line $m_t = 172.9$ GeV and blue dot-dashed line $m_t = 164$ GeV); the second and third panels show the typical behavior of the running couplings $\lambda_1(t)$ and $\lambda_2(t)$ for the average value of the initial condition, $\langle \lambda_1^{(0)} \rangle = 0.28$ in the integration of (2.2.36); the fourth panel shows the behavior of the extra positivity condition for $\alpha < 0$. In the running of λ_i we have taken $M_s = 10^{14}$ GeV.
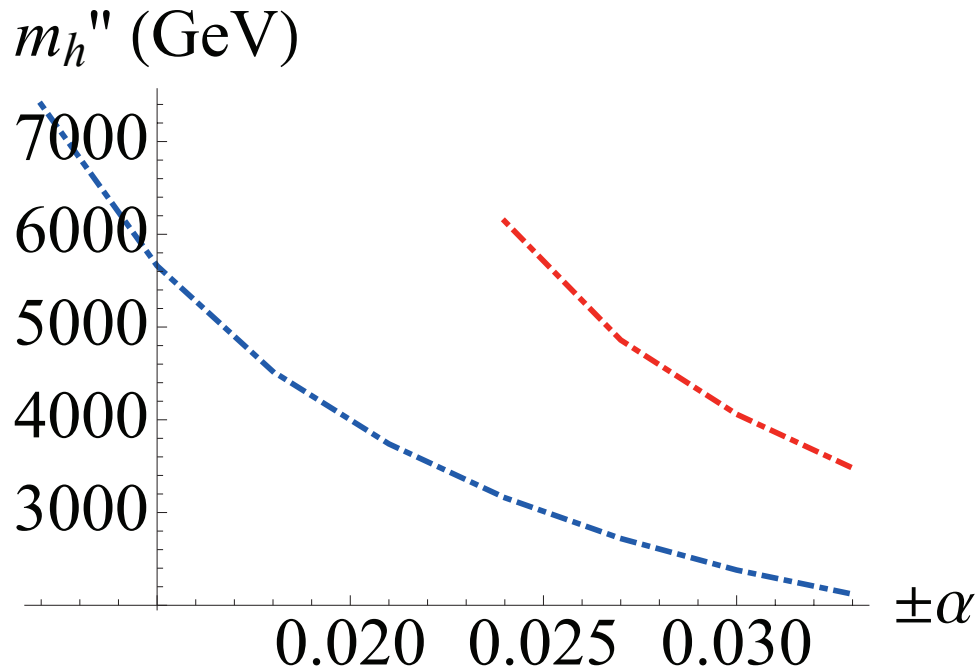
Figure 28 : The lower boundary of the allowed parameter space in the $m_{h''} - \alpha$ plane under the vacuum stability constraint of Eq. (2.2.23), for the positive alpha (blue) and negative alpha (red). We have taken $M_{Z''} = 4.5$ TeV and $M_s = 10^{14}$ GeV.

$\pm\alpha$ appears to be small on Fig. 26, but it is actually not insignificant. For a given α, the lower boundary sometimes changes by a factor of two. For example, at $\alpha = 0.24$, the lower boundary changes from $6,140$ GeV to $3,160$ GeV as seen in Fig. 28. However, the effect on the area is less noticeable. The reason is that we can only change the lower boundaries of the accepted parameter space. The upper boundary is determined by the constraint that λ_i (usually λ_2) remains perturbative. This constraint is symmetric with respect to α. So the area cannot be enlarged indefinitely. Even if somehow we can send the lower boundary to zero, the area would only increase by another 20% to 30%. To determine the sensitivity of the RG evolution with respect to the choice of the string scale, the analysis is duplicated for $M_s = 10^{16}$ GeV and $M_s = 10^{19}$ GeV. The contours displayed in Fig. 29 (for $M_{Z''} = 4.5$ TeV) show that the region of stable vacuum solutions shrinks as M_s increases. The allowed range of initial conditions with stable vacuum solutions therefore depends on the value of the string scale; e.g. for $M_s = 10^{16}$ GeV, the stability region is $0.17 < \lambda_1^{(0)} < 0.83$ when $\alpha < 0$, and $0.16 < \lambda_1^{(0)} < 0.83$ when $\alpha > 0$. For $M_s = 10^{19}$ GeV, the stability region is $0.18 < \lambda_1^{(0)} < 0.69$ when $\alpha < 0$, and $0.17 < \lambda_1^{(0)} < 0.69$ when $\alpha > 0$. The corresponding average value for $M_s = 10^{16}$ GeV is $\langle\lambda_1^{(0)}\rangle = 0.31$, and for $M_s = 10^{19}$ GeV is $\langle\lambda_1^{(0)}\rangle = 0.32$. In Fig. 30
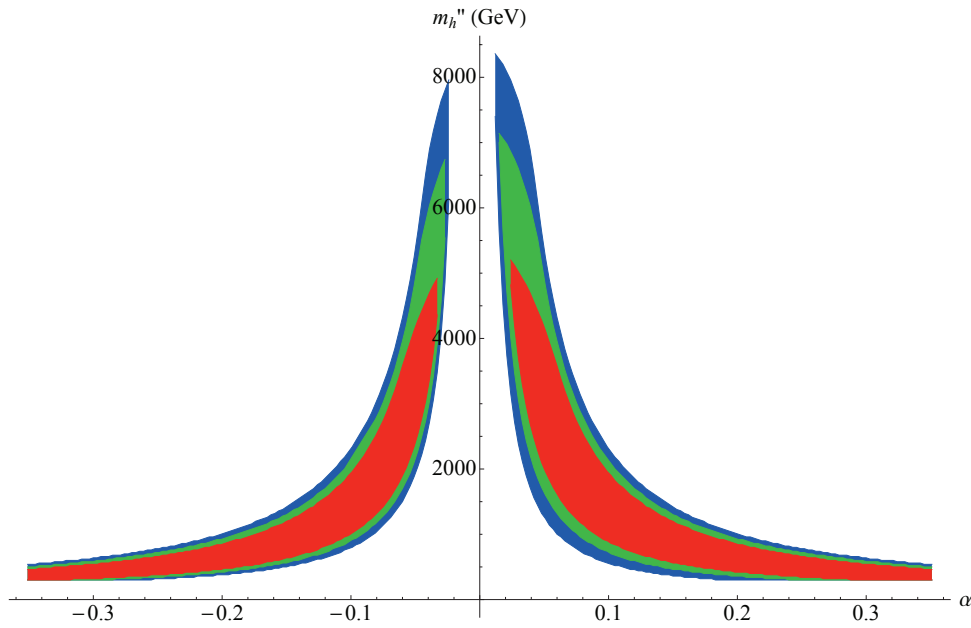
Figure 29 : The allowed SM^{++} parameter space in the $m_{h''}$ vs α plane under the vacuum stability constraint of Eq. (2.2.23), for the case $M_{Z''} = 4.5$ TeV, with $M_s = 10^{14}$ GeV (blue), $M_s = 10^{16}$ GeV (green), and $M_s = 10^{19}$ GeV (red). The perturbative upper bound is defined by $\lambda_i < 2\pi$.
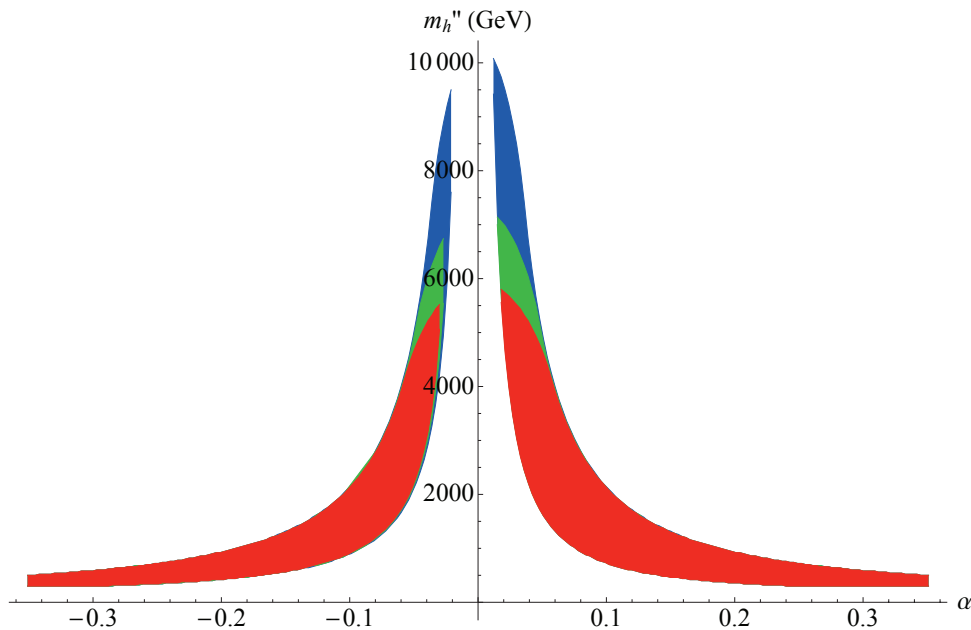
Figure 30 : Variation of SM^{++} vacuum stability regions with $M_{Z''}$. We have taken $M_s = 10^{16}$ GeV, $M_{Z''} = 3.5$ TeV (red), $M_{Z''} = 4.5$ TeV (green), and $M_{Z''} = 6.0$ TeV (blue). The perturbative upper bound is defined by $\lambda_i < 2\pi$.
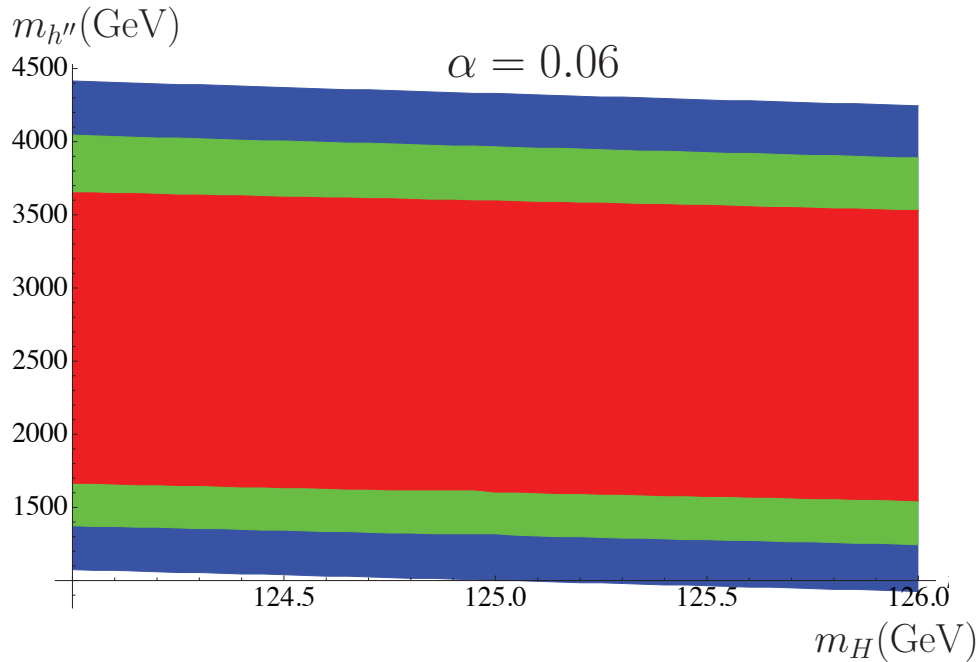
Figure 31 : Variation of SM^{++} vacuum stability regions with m_H. We have taken $\alpha = 0.06$, $M_{Z''} = 4.5$ TeV, $M_s = 10^{14}$ GeV (blue), $M_s = 10^{16}$ GeV (green), $M_s = 10^{19}$ GeV (red). The perturbative upper bound is defined by $\lambda_i < 2\pi$.

the sensitivity of the RG evolution with respect to $M_{Z''}$ is displayed. For large values of $|\alpha|$ there is no variation in the contour regions. For $\alpha > -0.05$ and $\alpha < 0.06$ there are some small variances. These small differences show the effect of the initial conditions of $\lambda_2^{(0)}$ and $\lambda_3^{(0)}$ on the evolution of the system. Figure 31 verifies that there is no significant variation of the SM^{++} vacuum stability regions within the m_H uncertainty. An example for $\alpha = 0.06$ and $M_{Z''} = 4.5$ TeV is displayed in Fig. 31. Figure 32 displays the variation of the results of the analysis with respect to varying $g_1'(M_s)$. It is clearly seen that for $0.232 < g_1'(M_s) < 1.000$ the dependence on g_1' seems to be fairly weak. The stability of SM^{++} vacuum is then nearly independent of the Z'' branching fractions [141].

While it is true that the low energy effective theory discussed in this dissertation requires a high level of fine tuning, this can be explained by applying the anthropic landscape of string theory [144, 145, 146]. Alternatively, the fine tuning can be circumvented with a more complete broken SUSY framework. Since in pure SUSY the vacuum is automatically stable, the stability analysis perforce involves the soft SUSY-breaking sector. Hence rather than simply searching for the Higgs self-coupling going negative in the ultraviolet, the stability analysis would involve finding the local and global minima of the effective potential in the multi-dimensional space of
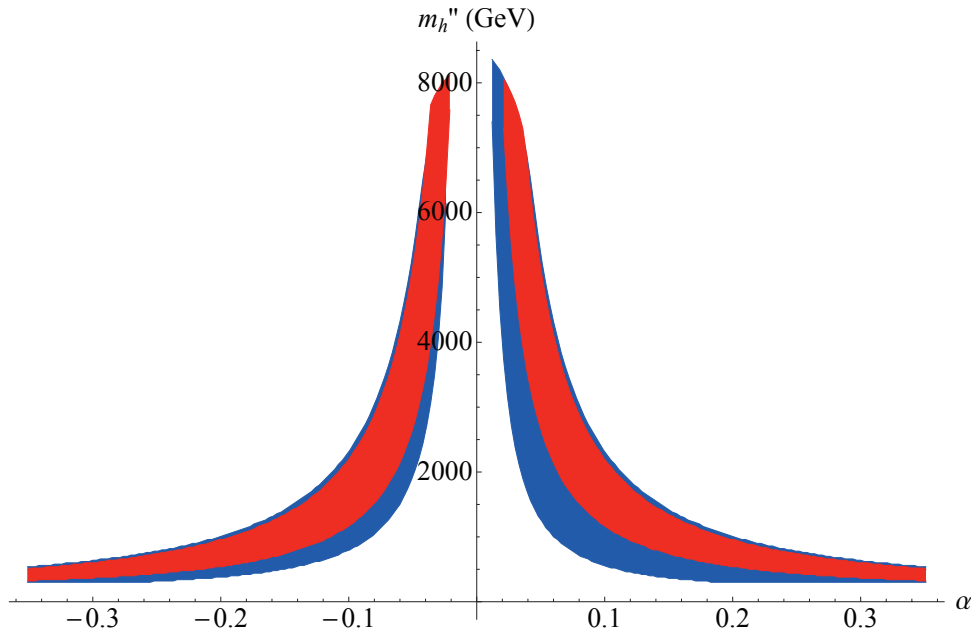
Figure 32 : Variation of SM^{++} vacuum stability regions with $g'_1(M_s)$. The stable regions correspond to $g'_1(M_s) = 1.000$ (blue), $g'_1(M_s) = 0.232$ (red). We have taken $M_s = 10^{14}$ GeV, $M_{Z''} = 4.5$ TeV, $m_H = 125$ GeV. The perturbative upper bound is defined by $\lambda_i < 2\pi$.

the soft-breaking sector [147]. However, the Higgs mass range favored by recent LHC data may be indicative of high-scale SUSY breaking [131]; perhaps near the high energy cut-off of the field theory, beyond which a string description becomes a necessity [148].

2.3   Summary of the Results and Conclusions

We have discussed the phenomenology of a Standard-like Model inspired by string theory, in which the gauge fields are localized on D-branes, whose intersection can give rise to chiral fermions. The energy scale associated with string physics is assumed to be near the Planck mass. To develop our program in the simplest way, we worked within the construct of a minimal model with gauge-extended sector $U(3)_B \times Sp(1)_L \times U(1)_{I_R} \times U(1)_L$. The resulting $U(1)$ content gauges the baryon number B, the lepton number L, and a third additional abelian charge I_R. All mixing angles and gauge couplings are fixed by rotation of the $U(1)$ gauge fields to a basis diagonal in hypercharge Y and in an anomaly free linear combination of I_R and $B - L$. The anomalous Z' gauge boson obtains a string scale Stückelberg mass via a 4D version of the Green-Schwarz mechanism. To keep the realization of the Higgs mechanism minimal, we added an extra $SU(2)$ singlet complex scalar, which acquires a VEV and gives a

TeV-scale mass to the non-anomalous gauge boson $Z"$. The model is fully predictive and can be confronted with dijet and dilepton data from LHC8 and, eventually, LHC14. We have shown that $M_{Z"} \approx 3 - 4$ TeV saturates current limits from the CMS and ATLAS Collaborations. We have also shown that for $M_{Z"} \leq 5$ TeV, LHC14 will reach discovery sensitivity $\approx 5\sigma$. After that, we derived the complete set of renormalization group equations at one loop order and we pursue a numerical study of the system to determine the triviality and vacuum stability bounds, using a scan of 10^4 random set of points to fix the initial conditions. We have shown that, if there is no mixing in the scalar sector, the top Yukawa coupling drives the quartic Higgs coupling to negative values in the ultraviolet and, as for the SM, the effective potential develops an instability below the Planck scale. However, for a mixing angle $-0.35 \leq \alpha \leq -0.02$ or $0.01 \leq \alpha \leq 0.35$, with the new scalar mass in the range $500 \text{ GeV} \leq m_{h"} \leq 8$ TeV, the SM^{++} ground state can be absolutely stable up to the string scale. Our results are largely independent of TeV-scale free parameters in the model: the mass of the non-anomalous $U(1)$ gauge boson and its branching fractions.

Part II:

Gravitational Waves From Post-Inflationary Sources

$$\ddot{h}_{ij}^{\mathrm{TT}} + 3\frac{\dot{a}}{a}\dot{h}_{ij}^{\mathrm{TT}} - \frac{1}{a^2}\nabla^2 h_{ij}^{\mathrm{TT}} = \frac{16\pi}{M_{pl}^2}T_{ij}^{\mathrm{TT}}$$

Chapter 3

Gravitational Waves from the Early Universe

3.1 Gravitational Waves Generated in the Early Universe

In section 1.2.1 we discussed how the universe on scales larger than 10^2 Mpc best described by the flat, isotropic and homogenous, represented by the metric

$$ds^2 = -dt^2 + a(t)^2 d\mathbf{x}^2. \tag{3.1.1}$$

In this section of the dissertation, we investigate what potential new discoveries can be made by observing perturbations of the FRW metric, and their sources.

Specifically we want to investigate radiative (tensor) perturbations to the FRW metric known as gravitational waves. Gravitational waves are generically predicted by GR. An excellent laboratory of GR is in the extreme locations in the universe where there are high concentrations of matter, and relativistic speeds, one such example being pulsar binaries. The 1993 Nobel Prize awarded to Hulse and Taylor was for the study of a binary pulsar system, PSR B1913+16 and it's unique properties. This particular binary system's orbital radius was found to be decaying at a rate in agreement with predictions of the decay via energy carried away by gravitational radiation with a discrepancy between observation and theory of $0.13 \pm 0.21\%$ [149]. The concept of gravitational waves is a unique resource for astronomers and cosmologists as all known data from the cosmos comes in the form of electromagnetic radiation propagating through the

universe. The disadvantage of the use of electromagnetic radiation is that it is strongly interacting compared to gravity so the information we receive has undergone secondary scatterings, effectively blurring or adding noise to what would be the most energetic and interesting sources. Gravity being a comparatively weak with interactions suppressed to by the scale M_{pl}^{-2}, gravitons[1] undergo significantly less secondary scattering events. This leaves the radiated information from energetic sources to essentially propagate un-affected, allowing a probe of some of the most interesting astrophysical sources with unprecedented clarity. Unfortunately this advantage is also its downfall as such a weak coupling to matter means it will be extremely difficult to detect. The task of direct detection is at the forefront of current physics research projects such as Advanced LIGO, VIRGO, GEO 600, and TAMA 300. These detectors are based on the concept of time of travel of light in a laser interferometer apparatus; LIGO for example, uses arm lengths of 4 km. The large length is necessary as the effect of a passing gravitational waves is proportional to the arm length of the interferometer [150]. Many excellent texts have been written regarding gravitational waves and interferometer detection systems such as [151], [150]. We will be concerned with the form of theoretical signals from stochastic sources generated in the early universe, and not on the detectors themselves.

As was stated earlier, the weak coupling of gravity allows one to detect radiation from deep within areas from which electromagnetic radiation cannot escape. One such case of interest is the opaque photon matter plasma of the early universe. Before the time of photon decoupling and the creation of the CMB ($t \approx \mathcal{O}(10^6)$ years [49]), the photons are confined by the multiple scatterings of the various constituents of the plasma. Because of this we cannot see earlier then the time of the CMB electromagnetically, similarly to why you cannot see far through a thick fog, photons originating from a further distance undergoes multiple scattering events thus not making it to your eyes. Effectively this blinds us from any direct observations of the physics before the CMB era via photons. To directly probe the physics before the CMB era we can turn to gravitational waves. We are motivated to search for clues for BSM physics at higher energies than we can produce in a lab. Specifically we saw that inflation occurs at times when the relevant energies are at the GUT scale 10^{16} GeV, therefore the time immediately following inflation presents a unique unexplored region of high energy physics that can in principle be

---

[1]The analogous particle form of gravitational waves as photons are to the particles of electromagnetic waves.

probed by gravitational waves.

The act of inflation itself is theorized to produce a stochastic background of gravitational waves [152, 153], unfortunately it is too weak to be directly detected with existing instruments. However, the possibility remains that these primordial gravitational waves can be observed via B-modes in the cosmic microwave background (CMB) [154, 155] but doing so requires precise measurement of the polarization of the CMB.

The period directly following inflation does present several mechanisms for the creation of a stochastic gravitational wave background such as the reheating and preheating phase discussed in [156, 157, 158, 159, 58, 160, 161, 162, 163, 164, 165, 166, 167, 168, 169], and cosmological phase transitions [170, 171, 172, 173, 174, 175, 176].

3.1.1 Perturbing the FRW Metric

In order to make predictions of the form and scale of the stochastic background spectrum coming from these sources, we require the Einstein field equations in the linear perturbation to the FRW metric approximation, specifically for tensor modes. The general analysis can be found in ref [4]. The qualitative answer can be described in the following manner. We make a small perturbation to the FRW metric of the form

$$g_{\mu\nu} = \bar{g}_{\mu\nu} + h_{\mu\nu}, \ \text{Min}\{\bar{g}_{\mu\nu}\} \gg h_{\mu\nu}, \tag{3.1.2}$$

where $\bar{g}_{\mu\nu}$ is the flat FRW background metric for which the over bar indicates quantities with respect to this background metric. In the above $\text{Min}\{\bar{g}_{\mu\nu}\}$ is the minimum value of the non-zero components of $\bar{g}_{\mu\nu}$. The last condition ensures that $h_{\mu\nu}$ is a small perturbation to the FRW background. The Einstein field equations,

$$R_{\mu\nu} - \frac{1}{2}g_{\mu\nu}R = \frac{8\pi}{M_{pl}^2}T_{\mu\nu}, \tag{3.1.3}$$

can be expanded to linear order in $h_{\mu\nu}$

$$\bar{R}_{\mu\nu} + R_{\mu\nu}^{(1)} - \frac{1}{2}\bar{g}_{\mu\nu}\bar{R} - \frac{1}{2}\left(h_{\mu\nu}\bar{R} + \bar{g}_{\mu\nu}R^{(1)}\right) \approx \frac{8\pi}{M_{pl}^2}\left(\bar{T}_{\mu\nu} + T_{\mu\nu}^{(1)}\right),$$

$$R_{\mu\nu}^{(1)} - \frac{1}{2}\left(h_{\mu\nu}\bar{R} + \bar{g}_{\mu\nu}R^{(1)}\right) \approx \frac{8\pi}{M_{pl}^2}T_{\mu\nu}^{(1)}, \tag{3.1.4}$$

with

$$R^{(1)}_{\mu\nu} = \frac{1}{2}\left(\bar{D}^\alpha \bar{D}_\mu h_{\nu\alpha} + \bar{D}^\alpha \bar{D}_\nu h_{\mu\alpha} - \bar{D}^2 h_{\mu\nu} - \bar{D}_\nu \bar{D}_\mu h\right),$$

$$R^{(1)} = \bar{g}^{\mu\nu} R^{(1)}_{\mu\nu} - h^{\mu\nu} \bar{R}_{\mu\nu},$$

(3.1.5)

where $\bar{D}_\alpha$ is the covariant derivative operator with respect to the background $\bar{g}_{\mu\nu}$. All terms with (1) superscript indicate the linear order perturbation of the quantity. Note that common notation for $T^{(1)}_{\mu\nu}$ is $\pi_{\mu\nu}$, and corresponds to the anisotropic energy-stress tensor perturbation to the homogenous and isotropic background matter content that governs the Friedmann equations. Following [4] the perturbations to the FRW metric are decomposed into

$$h_{00} = -E,$$

$$h_{i0} = a\left(\partial_i F + G_i\right),$$

$$h_{ij} = a^2\left(A\delta_{ij} + \partial^2_{ij} B + \partial_j C_i + \partial_i C_j + D_{ij}\right), \ (i,j = 1,2,3),$$

(3.1.6)

along with the conditions

$$\partial_i C_i = \partial_i G_i = 0, \ \partial_i D_{ij} = 0, \ D_{ii} = 0$$

(3.1.7)

This decomposition allows three separable cases of the perturbed Einstein field equations, the most important to us is the tensor perturbations h_{ij}, taking the form

$$\ddot{D}_{ij} + 3\frac{\dot{a}}{a}\dot{D}_{ij} - \frac{1}{a^2}\nabla^2 D_{ij} = \frac{16\pi}{M_{pl}^2}\pi^T_{ij},$$

(3.1.8)

where π^T_{ij} is the traceless part of the anisotropic stress. We see this is the wave equation in the FRW background of a spatially transverse ($\partial_i D_{ij} = 0$) and spatially traceless ($D_{ii} = 0$) perturbation. The question remains what are the values of the vectorial components, h_{i0}, and scalar component, h_{00} of the metric perturbation.

To answer this question we note that the Einstein field equations posses coordinate invariance, one may say gravity possesses general gauge invariance to changes in the metric. Interesting comparisons between the gauge symmetries of the SM and GR are found in [25]. We can use this gauge invariance to our advantage to find a gauge in which the scalar and vector components of the metric perturbation are zero, the so called transverse-traceless gauge. The

details of gauge transformation of the field equations can be found in ref [4]. The results are that by choosing an appropriate coordinate system $x_\mu \to x_\mu + \epsilon_\mu$ the metric perturbation is modified (gauge transformed) to

$$h_{\mu\nu} \to h_{\mu\nu} + \Delta h_{\mu\nu}, \tag{3.1.9}$$

where

$$
\begin{aligned}
\Delta h_{ij} &= -\partial_j \epsilon_i - \partial_i \epsilon_j + 2a\dot{a}\delta_{ij}\epsilon_0, \\
\Delta h_{i0} &= -\partial_0 \epsilon_i - \partial_i \epsilon_0 + 2\frac{\dot{a}}{a}\epsilon_i, \\
\Delta h_{00} &= -2\partial_0 \epsilon_0.
\end{aligned}
\tag{3.1.10}
$$

Above the system of equations (3.1.10) is written in the coordinates for which the background is expressed as

$$\bar{g}_{\mu\nu} = \text{diag}\{-1, a(t)^2, a(t)^2, a(t)^2\}. \tag{3.1.11}$$

It should be noted that a change of gauge also changes the form of π_{ij}^T as it must now be expressed in the same coordinates/gauge. Given the gauge freedom of the field equations, we choose the transverse-traceless (TT) gauge such that

$$
\begin{aligned}
h_{\mu 0} &= 0, \\
\partial_i D_{ij} &= 0, \\
D_{ii} &= 0.
\end{aligned}
\tag{3.1.12}
$$

From this another change of coordinates is used that does not effect the transverse-traceless relations to change from cosmological/comoving time to that of conformal time via

$$d\eta = \frac{dt}{a}, \tag{3.1.13}$$

allowing us to write the fully perturbed metric in the transverse-traceless gauge by use of (3.1.6) as

$$ds^2 = a(\eta)^2 \left(-d\eta^2 + (\delta_{ij} + h_{ij}^{\text{TT}})dx^i dx^j\right), \tag{3.1.14}$$

where the perturbation is governed by Eq. (3.1.8) expressed in conformal time

$$\ddot{h}_{ij}^{\text{TT}} + 2\frac{\dot{a}(\eta)}{a(\eta)}\dot{h}_{ij}^{\text{TT}} - \nabla^2 h_{ij}^{\text{TT}} = \frac{16\pi}{M_{pl}^2}\pi_{ij}^{\text{TT}}, \tag{3.1.15}$$

where over dots indicate derivatives with respect to conformal time η.

The process of finding the transverse-traceless part of any tensor is accomplished by the use of a projection operator that gives the TT part of a tensor. The TT projection operator is constructed first by forming the spatially transverse projection operator given as

$$P_{ij}(\mathbf{k}) = \delta_{ij} - \frac{k_i k_j}{k^2}, \ k_i P_{ij}(\mathbf{k}) = 0. \tag{3.1.16}$$

The transverse operator ensures that the projected tensor is transverse to the vector k_i. Applying the projection operator to a rank 2 tensor creates a transverse to the vector k_i version

$$P_{im}(\mathbf{k}) P_{pj}(\mathbf{k}) A_{jm} = A_{ip}^T, \ k_i A_{ip}^T = k_p A_{ip}^T = 0. \tag{3.1.17}$$

Subtracting out the trace of the transverse tensor allows the formation of the TT projector of the form

$$\begin{aligned} A_{ij}^{TT} &= \left(P_{im}(\mathbf{k}) P_{jn}(\mathbf{k}) - \frac{1}{2} P_{ij}(\mathbf{k}) P_{mn}(\mathbf{k}) \right) A_{mn}, \\ A_{ij}^{TT} &= P_{im,jn}(\mathbf{k}) A_{mn}. \end{aligned} \tag{3.1.18}$$

Applied to the perturbed stress-energy tensor gives

$$\begin{aligned} T_{mn}^{TT} &= P_{im,jn}(\mathbf{k}) T_{mn} = P_{im,jn}(\mathbf{k})(-a(t)^2 \delta_{mn} P + \pi_{mn}), \\ &= -a(t)^2 P_{in,jn}(\mathbf{k}) \, P + \pi_{mn}^{TT}, \\ &= \pi_{mn}^{TT}. \end{aligned} \tag{3.1.19}$$

Thus we may replace π_{ij}^{TT} in (3.1.15) by T_{ij}^{TT} as the only surviving term after the TT gauge transformation is π_{ij}^{TT}.

3.1.2 Energy From Gravitational Waves

When calculating stochastic backgrounds, it is useful to compute the energy density from the gravitational radiation in a given frequency range $k, k + dk$. In order to extract this information the covariant expression for the energy tensor in gravitational waves as given in [177] is used

$$T_{\mu\nu}^{gw} = \frac{M_{pl}^2}{32\pi} \langle \bar{D}_\mu H_{\alpha\beta}^{\mathrm{TT}} \bar{D}_\nu H^{\alpha\beta,\mathrm{TT}} \rangle \,, \tag{3.1.20}$$

where $H_{\mu\nu}^{\mathrm{TT}}$ is related to the full metric via $g_{\mu\nu} = \bar{g}_{\mu\nu} + H_{\mu\nu}^{\mathrm{TT}}$. For the case at hand $H_{ij}^{\mathrm{TT}} = a(\eta)^2 h_{ij}^{\mathrm{TT}}$. In Eq. (3.1.20) the brackets indicate a spatial average over several wavelengths of

the gravitational waves. The energy density seen by a comoving observer is given by via

$$\rho_{gw} = u^\mu u^\nu T^{gw}_{\mu\nu} \ , \tag{3.1.21}$$

with u^μ the four-velocity of a comoving observer[2]. A comoving observer of the background FRW space-time is an observer with fixed spatial coordinates and 4-velocity given by $u^\mu = (1, \mathbf{0})$ in the comoving frame, and $u^\mu = (a^{-1}, \mathbf{0})$ in the conformally flat frame. From this we find the energy density to be

$$
\begin{aligned}
\rho_{gw} &= \frac{M_{pl}^2}{32\pi a(\eta)^2} \sum_{ij} \langle \bar{D}_0 \left(a^2 h_{ij}^{\mathrm{TT}} \right) \bar{D}_0 \left(a^{-2} h_{ij}^{\mathrm{TT}} \right) \rangle, \\
&= \frac{M_{pl}^2}{32\pi a(\eta)^2} \sum_{ij} \langle \dot{h}_{ij}^{\mathrm{TT}} \dot{h}_{ij}^{\mathrm{TT}} \rangle.
\end{aligned}
\tag{3.1.22}
$$

To find the energy density per frequency interval, we make a spatial Fourier transformation

$$h_{ij}^{\mathrm{TT}}(\eta, \mathbf{x}) = \int \frac{d^3\mathbf{k}}{(2\pi)^3} h_{ij}^{\mathrm{TT}}(\eta, \mathbf{k}) e^{i\mathbf{k}\cdot\mathbf{x}} \ . \tag{3.1.23}$$

Using Parseval's theorem [178] we can express (3.1.22) as an integral over the wavevector $\mathbf{k}$ as follows

$$
\begin{aligned}
\langle \dot{h}_{ij}^{\mathrm{TT}} \dot{h}_{ij}^{\mathrm{TT}} \rangle &= \frac{1}{V} \int_V \dot{h}_{ij}^{\mathrm{TT}} \dot{h}_{ij}^{\mathrm{TT}} d^3\mathbf{x} \\
&= \frac{1}{V} \int_V \int \frac{d^3\mathbf{k}}{(2\pi)^3} \frac{d^3\mathbf{k}'}{(2\pi)^3} e^{i(\mathbf{k}'+\mathbf{k})\cdot\mathbf{x}} \dot{h}_{ij}^{\mathrm{TT}}(\eta, \mathbf{k}') \dot{h}_{ij}^{\mathrm{TT}}(\eta, \mathbf{k}) d^3\mathbf{x} \\
&= \frac{1}{L_x L_y L_z} \int \frac{d^3\mathbf{k}}{(2\pi)^3} \frac{d^3\mathbf{k}'}{(2\pi)^3} \prod_{i=1}^{3} \frac{2\sin((k'+k)_i L_i)}{(k'+k)_i} \dot{h}_{ij}^{\mathrm{TT}}(\eta, \mathbf{k}') \dot{h}_{ij}^{\mathrm{TT}}(\eta, \mathbf{k}) d^3\mathbf{x} \\
&\approx \frac{1}{V} \int \frac{d^3\mathbf{k}}{(2\pi)^3} \dot{h}_{ij}^{\mathrm{TT}}(\eta, \mathbf{k}) \dot{h}_{ij}^{\mathrm{TT}}(\eta, -\mathbf{k}), \\
&\approx \frac{1}{V} \int \frac{d^3\mathbf{k}}{(2\pi)^3} |\dot{h}_{ij}^{\mathrm{TT}}(\eta, \mathbf{k})|^2 \ ,
\end{aligned}
\tag{3.1.24}
$$

In the last line we used the fact that $h_{ij}^{\mathrm{TT}}(\eta, \mathbf{x})$ is real. The approximation in the fourth line, is valid when $(k'+k)_i << L_i$, where L_i is the length of the ith side of the volume in question (assuming a rectangular prism region). Technically this is not always true, as the range of k, k' extends from $-\infty$ to ∞, however the use of a Fourier transform in a finite volume V should be replaced by a discrete Fourier transformation for which the last result is is an exact equality,

---

[2]An observer embedded in the FRW background metric, and without motion relative to the background

and is the result of Parseval's theorem. This allows the expressions

$$\rho_{gw} = \frac{M_{pl}^2}{32\pi a(\eta)^2}\frac{1}{V}\sum_{ij}\int\frac{d^3\mathbf{k}}{(2\pi)^3}|\dot{h}_{ij}^{\mathrm{TT}}(\eta,\mathbf{k})|^2 \, ,$$

$$k\frac{d\rho_{gw}}{dk} = \frac{d\rho_{gw}}{d\log k} = \frac{M_{pl}^2}{32\pi a(\eta)^2}\frac{1}{V}\sum_{ij}\frac{k^3}{(2\pi)^3}\int|\dot{h}_{ij}^{\mathrm{TT}}(\eta,\mathbf{k})|^2 d\Omega_k. \qquad (3.1.25)$$

The use of $\exp(i\mathbf{k}\cdot\mathbf{x})$ and natural units, tells us that $k=\omega$ the angular frequency for the gravitational waves in the region $k, k+dk$. Above we should view $d\log k = dk/k$ as unit-less though technically $\log k$ does not make any physical sense. This equation will be very useful in computation of the energy spectrum. However before making use of Eq. (3.1.25) we need a method to solve Eq. (3.1.15) for $\dot{h}_{ij}^{\mathrm{TT}}$.

3.1.3   Solutions to the Field Equations

In order to solve Eq. (3.1.15) we cast it into a simplified form, by use of Fourier transformation, Eq. (3.1.23)

$$\ddot{h}_{ij}^{\mathrm{TT}}(\eta,\mathbf{k}) + 2\frac{\dot{a}(\eta)}{a(\eta)}\dot{h}_{ij}^{\mathrm{TT}}(\eta,\mathbf{k}) + k^2 h_{ij}^{\mathrm{TT}}(\eta,\mathbf{k}) = \frac{16\pi}{M_{pl}^2}T_{ij}^{\mathrm{TT}}(\eta,\mathbf{k}),\ k^2 = \mathbf{k}\cdot\mathbf{k}, \qquad (3.1.26)$$

Solving Eq. (3.1.26) can be done numerically [179], using methods such as Runge-Kutta, Leap-Frog, and Implicit Euler, or other numerical differential equation solvers. The advantage of using one of these methods, is that in a self consistent calculation the scale factor $a(\eta)$ is unknown prior to simulation. The fields that make up the matter content typically have complicated solutions that must be solved numerically. This causes the form of $a(\eta)$ to be unknown as it depends on the matter evolution. Therefore numerical methods where $a(\eta)$ is not a known quantity is useful. The use of numerical methods pervades the subject of stochastic gravitational backgrounds and is worth the time of understanding the complications within it as in Sec. 3.3 we will explore a solution to a stability issue that arrises in some numerical methods.

When using a numerical method to solve a set of differential equations, there is always a balance between accuracy and speed of a simulation. To clarify, the speed of an algorithm is not considered in actual seconds or minutes of a clock but rather how many operations are performed, when fewer operations are performed the algorithm is considered faster. Usually algorithms that are fast suffer from inaccuracies, however increasing the accuracy usually requires the use of more memory and thus increasing the number of operations. To illustrate this

trade off we will briefly review common, simple, methods of solving differential equations via numerical simulation.

In all numerical methods the full solution to some differential equation $dy/dt = f'(t, y(t))$ can be approximated by a method where you iteratively make small steps towards the final evaluation parameter, for example the final time of an evolution of a system of equations. In the simplest method, the Euler method, you advance your solution by assuming your step size is small enough that the final result error is small. You iteratively find the value of your function y by use a Taylor expansion

$$y(t + \delta t) \approx y(t) + f'(t, y(t))\delta t + \mathcal{O}\left(\frac{1}{2}f''(t, y(t))\delta t^2\right), \qquad (3.1.27)$$

Above we're now using big $\mathcal{O}$ notation that indicates the order of the dominant error comes from. Typically the terms $\frac{1}{2}f''(t, y(t))$ are dropped, and it is understood that some over all constant is involved when writing the order of the solution.

The method in (3.1.27) is the *explicit* Euler first order method. This means that each progressive step depends on the step before it *e.g.* you explicitly use the previous iteration in the next. It is first order even though each step has error $\mathcal{O}(\delta t^2)$, the accumulated error is of order $\mathcal{O}(\delta t)$. This results from dividing the interval of interest, which we will call $t : (a, b)$, into N discrete steps of size δt the accumulated error is then estimated as

$$E = \text{Max}\{\frac{1}{2}f''(t, y(t))\}N\delta t^2 = \frac{(b-a)}{2}\text{Max}\{f''(t, y(t))\}\delta t \simeq \mathcal{O}\left(\delta t\right), \qquad (3.1.28)$$

where $\text{Max}\{f''(t, y(t))\}$ is the maximal value of $f''(t, y(t))$ in the interval of (a, b). The error estimate in first order methods scales with the step size δt. Obviously to make the error smaller we should decrease the step size δt, however this requires us to increase N, requiring more computational time. To increase the accuracy with the same number of steps N, or less, methods like RK second order algorithms are used. However, by increasing the accuracy we require more storage of additional variables. Note that in terms of physical time (seconds, hours, etc.), if a computer can store additional variables more rapidly than it can run through serial operations (iterations), then there is little disadvantage to these types of methods. To quantitatively understand how second order algorithms work, we will use the example of an RK method. Runge-Kutta methods employ the concept that evaluating the term $f'(t, y(t))$ at some intermediate point(s) between t and $t + \delta t$ we decrease the error of each step. We can

generically express this idea for a RK s^{th} order term by

$$
\begin{aligned}
y(t + \delta t) &= y(t) + \sum_{m=1}^{s} b_m k_m + \mathcal{O}\left(\delta t^{s+1}\right) \\
k_1 &= \delta t f'(t, y(t)) \\
k_2 &= \delta t f'(t + c_2 \delta t, y(t) + a_{21} k_1) \\
&\vdots \\
k_s &= \delta t f'\left(t + c_s \delta t, y(t) + \sum_{m=1}^{s} a_{sm} k_m\right)
\end{aligned}
\tag{3.1.29}
$$

For the 2nd order RK algorithm we have

$$
y_{n+1} = y_n + \delta t \left(b_1 f'(t, y(t)) + b_2 f'(t + c_2 \delta t, y(t) + a_{21} k_1)\right) + \mathcal{O}\left(\delta t^3\right),
\tag{3.1.30}
$$

where the short hand $y_n = y(t)$ and $y_{n+1} = y(t + \delta t)$ is used. We solve for b_i, c_2, a_{21} via Taylor expansion to the same order and comparing the results. First expand (3.1.30) to give

$$
\begin{aligned}
y_{n+1} &= y_n + (b_1 f'_n + b_2 f'_n) \delta t \\
&+ \left(a_{21} b_2 \frac{\partial f'}{\partial y} f'_n + c_2 b_2 \frac{\partial f'}{\partial t}\right) \delta t^2 + \mathcal{O}\left(\delta t^3\right).
\end{aligned}
\tag{3.1.31}
$$

Now we expand the general solution of the Taylor series

$$
\begin{aligned}
y_{n+1} &\approx y_n + f'_n \delta t + \frac{1}{2} \frac{df'}{dt} \delta t^2 + \mathcal{O}(\delta t^3), \\
&\approx y_n + f'_n \delta t + \frac{1}{2} \left(\frac{\partial f'}{\partial t} + \frac{\partial f'}{\partial y} f'_n\right) \delta t^2 + \mathcal{O}(\delta t^3).
\end{aligned}
\tag{3.1.32}
$$

Comparing (3.1.32) and (3.1.31) allows one to solve b_i, c_2, a_{21} via

$$
\begin{aligned}
b_1 + b_2 &= 1, \\
a_{21} b_2 &= \frac{1}{2}, \\
c_2 b_2 &= \frac{1}{2}.
\end{aligned}
\tag{3.1.33}
$$

One common solution is $b_1 = 0$, $b_2 = 1$, $a_{21} = c_2 = 1/2$. This results in

$$
y_{n+1} \approx y_n + \delta t f'\left(t + \frac{\delta t}{2}, y_n + \frac{\delta t}{2} f'_n\right) + \mathcal{O}(\delta t^3).
\tag{3.1.34}
$$

Equation (3.1.34) is one solution to the RK 2nd order solutions, this particular solution is known as the mid-point method. Which has the explanation that the step term is evaluated at the mid-point between t and $t + \delta t$. From this exercise it is important to note that in (3.1.34) we require

two evaluations of $f(t, y(t))$ and thus increases the number of operations. We will continue to explore further complications with numerical methods in the next sections.

An attractive alternative to using numerical differential equation solving algorithms is the use of Green's functions solutions to (3.1.26). For known scale factors of the form

$$a(\eta) = \alpha \eta^n, \tag{3.1.35}$$

with α and n constant, it was realized in [59] that (3.1.26) has the solutions

$h_{ij}^{\mathrm{TT}}(\eta, \mathbf{k}) =$

$$\frac{16\pi}{M_{pl}^2} \frac{k}{\eta^{n-1}} \int_{\eta_i}^{\eta_f} d\eta' \, (\eta')^{n+1} \left(j_{n-1}(k\eta')y_{n-1}(k\eta) - j_{n-1}(k\eta)y_{n-1}(k\eta')\right) \, T_{ij}^{\mathrm{TT}}(\eta', \mathbf{k}).$$

$$\tag{3.1.36}$$

where $j_n(x)$ and $y_n(x)$ are spherical Bessel functions of the first and second kind, respectively. Here η_i is the starting time of the source, and η_f is the final time at which h_{ij}^{TT} is evaluated, ordinarily the time after which the emission of gravitational waves is negligible. The advantage of (3.1.36) is that it is exact. In practice we must evaluate the integral in (3.1.36) numerically, however integrals evaluated numerically do not inherently suffer from instability issues as numerical differential equation methods do. A disadvantage of using the Green's function approach is that we require the form of $a(\eta)$ before evaluation of (3.1.36). In section 3.3 it will be shown that this may present an issue when attempting to simulate physics of pre-heating.

3.1.4   Sources of Anisotropic Stress

With the equations to solve for the energy density per unit frequency, and a method for solving for $\dot{h}_{ij}^{\mathrm{TT}}$, we still need to calculate the source term $T_{ij}^{\mathrm{TT}}(\eta, \mathbf{k})$ and the scale factor $a(t)$. The scale factor is governed by the Friedmann equations for a flat background

$$\left(\frac{\dot{a}(t)}{a(t)}\right)^2 = \frac{8\pi}{3M_{pl}^2}\rho, \; \frac{\ddot{a}(t)}{a(t)} = -\frac{4\pi}{3M_{pl}^2}\left(\rho + 3P\right), \tag{3.1.37}$$

where ρ, P are the isotropic energy density, and isotropic internal pressure of the comoving perfect fluid respectively. However we do not know what the particle content of ρ and P is. In order to understand these terms in the era immediately after inflation we need to express the isotropic energy density and pressure in terms of the relevant fields. Immediately after inflation

ends, we assume we can use classical analysis of the fields in a quasi-classical setting. To find expressions for ρ and P we will use a Lagrangian for N real scalar fields assumed to be the dominant fields at the time in question. The inflaton is identified as $\Phi_0 = \phi(x, t)$ and fields $\Phi_i = \chi_i(x, t)$ represents fields which may cause pre-heating, as was outlined in Sec. 1.2.5, or be involved in phase transitions. The Lagrangian appropriate to describe gravity and these fields is given by the Hilbert action [180], note that for fields with non-integer spin it it may be more appropriate to use the Cartan-Einstein formulation of GR [181]

$$S = \int d^4x \, \sqrt{-\bar{g}} \left(\frac{M_{pl}^2}{16\pi} \bar{R} + \mathcal{L}(\Phi_i) \right), \; \mathcal{L}(\Phi_i) = \frac{1}{2} \sum_{i=1}^{N} \bar{g}^{\mu\nu} \bar{D}_\mu \Phi_i \bar{D}_\nu \Phi_i - V(\Phi_i). \quad (3.1.38)$$

Variation of (3.1.38) with respect to $\bar{g}^{\mu\nu}$ and Φ_i gives

$$\bar{R}_{\mu\nu} - \frac{1}{2}\bar{g}_{\mu\nu}\bar{R} = \frac{8\pi}{M_{pl}^2} \left(-\frac{2}{\sqrt{-\bar{g}}} \frac{\delta}{\delta\bar{g}^{\mu\nu}} \sqrt{-\bar{g}} \mathcal{L}(\Phi_i) \right),$$

$$\partial_\mu \partial^\mu \Phi_i + 3\frac{\dot{a}(t)}{a(t)}\dot{\Phi}_i = -\frac{\partial V}{\partial \Phi_i} \quad (3.1.39)$$

which then allows the identification

$$T_{\mu\nu} = -\frac{2}{\sqrt{-\bar{g}}} \frac{\delta}{\delta\bar{g}^{\mu\nu}} \sqrt{-\bar{g}} \mathcal{L}(\Phi_i) = -2\frac{\delta\mathcal{L}}{\delta\bar{g}^{\mu\nu}} + \bar{g}_{\mu\nu}\mathcal{L}. \quad (3.1.40)$$

With the given form of (3.1.38)

$$T_{\mu\nu} = -\sum_{i=1}^{N} \partial_\mu \Phi_i \partial_\nu \Phi_i + \frac{1}{2}\bar{g}_{\mu\nu} \sum_{i=1}^{N} \partial_\kappa \Phi_i \partial^\kappa \Phi_i - \bar{g}_{\mu\nu}V. \quad (3.1.41)$$

Now we can find the expressions for energy density ρ and internal pressure P by comparison with the stress-energy tensor of a perfect fluid

$$T_{\mu\nu} = (\rho + P) u_\mu u_\nu + \bar{g}_{\mu\nu}P \rightarrow T_{00} = \rho + 2P, \; T_{ii} = -a(t)^2 P \text{ (no sum on } i) \quad (3.1.42)$$

and our expression for stress-energy in terms of fields, Eq. (3.1.41), giving

$$\rho = \sum_{i=1}^{N} \left(\frac{1}{2}\dot{\Phi}_i^2 + \frac{1}{2a^2}(\nabla_x \Phi_i)^2 + V \right), \; P = \sum_{i=1}^{N} \left(\frac{1}{2}\dot{\Phi}_i^2 + \frac{1}{2a^2}(\nabla_x \Phi_i)^2 - V \right), \quad (3.1.43)$$

where above $\nabla_x \Phi_i^2$ is the spatial derivatives of the field squared, to clarify in cartesian coordinates it takes the form $\nabla_x \Phi_i^2 = \partial_x \Phi_i^2 + \partial_y \Phi_i^2 + \partial_z \Phi_i^2$. The expression for ρ and P is not in general isotropic. To separate the isotropic parts of ρ, and P and the perturbations to the perfect

fluid, we define the isotropic part as $\rho_{\mathrm{iso}} = \langle\rho\rangle$, and $P_{\mathrm{iso}} = \langle P\rangle$ where here $\langle\dots\rangle$ indicate a spatial average over a large enough volume such that perturbations resulting from the terms $\nabla_x\Phi_i$ average to zero, that is we take a course grained version of the energy density and pressure to determine the isotropic contributions. We can find the anisotropic stress, the source of gravitational waves, by applying the TT operator (3.1.18) to the field stress energy tensor (3.1.41). After the TT operator is applied terms proportional to the background metric $\bar{g}_{\mu\nu}$ will be completely zero thus the only anisotropic parts of the fields is from the term $-\sum_{i=1}^{N}\partial_\mu\phi_i\partial_\nu\phi_i$ that is fields with spatial gradients will source gravitational waves. These spatial variances in-fact grow in the pre-heating process which results in a stochastic background of gravitational waves.

It should be noted that different types of the matter fields can be included in $\mathcal{L}(\Phi_i)$ here, however, we will keep strictly to scalar fields. The evolution of the stress-energy tensor $T^{\mu\nu}$ under (3.1.39) is complicated, as is the solution to the scale factor $a(t)$. In order to make progress on these generally intractable problems we again resort to numerical methods, now for solving the field Eq. (3.1.39) and scale factor $a(t)$ evolutions.

3.1.5 Lattice Simulations

Since the matter field equations are a system of N partial differential equations one convenient method of solving these numerically is through finite differencing methods [182]. Finite differencing methods solve partial differential equations by discretizing the field on a lattice, for which in $3+1$ dimensions takes the form

$$\Phi(t, \mathbf{x}) \to \Phi(t, \mathbf{x_0} + \hat{\mathbf{n}}\Delta x), \ \hat{\mathbf{n}} = n\,\hat{\mathbf{e}}_1 + m\,\hat{\mathbf{e}}_2 + p\,\hat{\mathbf{e}}_3, \tag{3.1.44}$$

with (n, m, p) Integers denoting the 3 dimensional location on the lattice along the directions $\hat{\mathbf{e}}_i$, which are unit vectors in the separate directions comprising the lattice, finally Δx is the discrete lattice point spacing. We can solve for the field configurations at the lattice points for successive iterations of some fixed variable, typically time, in physical applications. The matter field equations we have in (3.1.39) fully expanded yield

$$\frac{\partial^2\Phi_i}{\partial t^2} - \frac{1}{a(t)^2}\nabla_{\mathbf{x}}^2\Phi_i + 3\frac{\dot{a}(t)}{a(t)}\dot{\Phi}_i = -\frac{\partial V}{\partial\Phi_i}. \tag{3.1.45}$$

We can approximate the spatial derivatives in the above as finite differences, which can be expressed in terms of a Taylor series expansion of the form

$$
\begin{aligned}
\Phi_i(t, x_1 + \Delta x, x_2, x_3) &\approx \Phi_i(t, \mathbf{x}) + \partial_1 \Phi_i(t, \mathbf{x})\Delta x + \frac{1}{2}\partial_1^2 \Phi_i(t, \mathbf{x})\Delta x^2, \\
\Phi_i(t, x_1 - \Delta x, x_2, x_3) &\approx \Phi_i(t, \mathbf{x}) - \partial_1 \Phi_i(t, \mathbf{x})\Delta x + \frac{1}{2}\partial_1^2 \Phi_i(t, \mathbf{x})\Delta x^2, \\
\partial_1 \Phi_i(t, \mathbf{x}) &\approx \frac{\Phi_i(t, x_1 + \Delta, x_2, x_3) - \Phi_i(t, x_1 - \Delta, x_2, x_3)}{2\Delta x} - \mathcal{O}(\Delta x^2),
\end{aligned}
$$

$$(3.1.46)$$

and

$$
\begin{aligned}
\partial_1^2 \Phi_i(t, \mathbf{x}) = \Delta_1^2 \Phi_i &\approx \frac{\Phi_i(t, x_1 + \Delta, x_2, x_3) - 2\Phi_i(t, x) + \Phi_i(t, x_1 - \Delta, x_2, x_3)}{\Delta x^2} \\
&- \mathcal{O}(\Delta x^2).
\end{aligned}
$$

$$(3.1.47)$$

We then use a numerical method to iteratively step forward in the fixed variable $\Phi_i(t + \delta t, \mathbf{x})$ at each lattice point $\mathbf{x}$. This must be done for each lattice point which in a $3 + 1$ dimensional field theory we have N^3 terms to evaluate $\partial^2 \Phi_i/\partial t^2$ for a lattice consisting of N points per orthogonal direction. We must update each point, and we need the first order derivatives to compute the anisotropic stress. For this reason we require storing both first and second order derivatives at each point thus doubling the number of stored points $2N^3$. In the next section we address the issues associated with lattice simulations.

3.1.6 Computational Stability and Discrete Fourier Transforms

When doing lattice simulations, there are several effects that we must account for. The first of these is we handle the finite nature of the lattice when simulating an infinite space, specifically, what do we do at the lattice boundaries? The boundaries of the lattice can be fixed, periodic, or free. For the simulation considered periodic is a natural choice, because the lattice can be viewed as a representative volume of the total universe. The isometric and homogenous assumption of the universe, allows the interpretation that effects occurring on the boundaries re-entering the lattice on the opposite side can be understood as a field configuration entering the lattice from the next identical volume element in the universe. The periodic condition can be expressed as

$$\Phi_i(t, \mathbf{x} + \hat{\mathbf{N}}_\mathbf{j}\Delta x) = \Phi_i(t, \mathbf{x}), \ \hat{\mathbf{N}}_\mathbf{j} = N\hat{\mathbf{e}}_\mathbf{j}. \tag{3.1.48}$$

Using a discrete lattice also requires careful consideration of Fourier transformations, for which we require to calculate (3.1.25). The Sampling Theorem does not allow one to find a Fourier amplitude of frequencies higher than the Nyquist critical frequency [182] given as

$$f_c = \frac{1}{2\Delta x} = \frac{N}{2}\frac{1}{L}, \tag{3.1.49}$$

with L the size of one lattice side $L = N\Delta x$. Discretizing the Fourier transform of the fields that form the stress-energy tensor perturbation gives

$$\Phi_i(t, \mathbf{k}) = \int d^3x \Phi_i(t, \mathbf{x}) e^{-i\mathbf{k}\cdot\mathbf{x}} \rightarrow \Phi_i(t, \hat{\mathbf{n}}_\mathbf{k}\Delta k) \approx \Delta x^3 \sum_{n,m,p=1}^{N} \Phi_i(t, \hat{\mathbf{n}}\Delta x) e^{-i\hat{\mathbf{n}}_\mathbf{k}\cdot\hat{\mathbf{n}}\Delta k\Delta x}, \tag{3.1.50}$$

where $\Delta k = 1/L$ and $\hat{\mathbf{n}}_\mathbf{k} = n_k\,\hat{\mathbf{e}}_{\mathbf{1k}} + m_k\,\hat{\mathbf{e}}_{\mathbf{2k}} + p_k\,\hat{\mathbf{e}}_{\mathbf{3k}}$, with $\hat{\mathbf{e}}_{\mathbf{ik}}$ is a unit vector in the k-space lattice where n_k, m_k, p_k each range over $-N/2$ to $N/2$.

It is useful to see how computationally demanding Fourier transforms are. For each k-space lattice point, of which there are N^3, we must calculate (3.1.50) which itself is an order N^3 operation. To obtain the entire discrete Fourier transformed (DFT) field it requires $N^3 \times N^3$ operations. Taking Fourier transforms and simultaneously solving the differential equations as stated previously, each step in the system is an order $2N^3 \times N^3 \times N^3$ operation, even further complicated by the fact that each Fourier mode is complex which requires us to store 2 variables for each Fourier mode, compounding the entire process by 2 leaving an overall operation of order $4N^9$. We can see even for small lattice sizes of $N = 32$ at each step we have approximately 1.4×10^{14} operations to perform! Because of this reason it is rare that someone would use a DFT. An advanced algorithm known as Fast Fourier Transforms (FFT) for which a review of the most basic form can be found in [182], allows faster execution of Fourier transformations. These algorithms change DFT from being a $(N \times N)^3$ operation to a $(N \log_2 N)^3$ operation saving us many operations. We also cut down on the number of operations with the use of symmetry relations, such as with the stress-energy tensor $T_{ij}^{\mathrm{TT}} = T_{ji}^{\mathrm{TT}}$.

The final issue we will address associated with use of simulation is stability. If a method to solve differential equations is insensitive to changes in the discrete stepping size Δx, it is said to be stable. To illustrate, consider the differential equation

$$\frac{dy}{dx} = -\alpha y, \tag{3.1.51}$$

where α is a positive real constant. The solution to (3.1.51) is $y(x) = Ae^{-\alpha x}$ with A some arbitrary constant to be fit with initial conditions. Any good numerical method should return a result near the exact solution, however this type of equation suffers from instability, for example if we use the explicit 1st order Euler method, one iteration gives

$$y(x + \delta x) = y(x)(1 - \alpha \delta x), \tag{3.1.52}$$

This result will result in a perfectly acceptable numerical solution so long as $1/\alpha < \delta x$. This condition implies that each progressive step satisfies $y(x + \delta x) < y(x)$ as the full solution agrees with. However if $1/\alpha > \delta x$ then $y(x + \delta x) > y(x)$ and each step increases the value of $y(x)$. This results in an unbounded solution that will go to infinity if the final x parameter value is sufficiently large. These are known as run away solutions. Obviously this behavior is not the intended result, we now have the surprising result that a choice of step-size can drastically alter the numerical results.

In order to combat step size sensitivity implicit methods may be used. To demonstrate, the implicit 1st Euler method, applied to (3.1.51) results in the ability to use any step size to get the correct numerical behavior, as seen below

$$\begin{aligned} y_{n+1} &= y_n + f'(x + \delta x, y_{n+1})\delta t, \\ y_{n+1} &= y_n - \alpha y_{n+1}\delta t, \\ y_{n+1} &= \frac{y_n}{1 + \alpha \delta t}. \end{aligned} \tag{3.1.53}$$

Each step gives $y_{n+1} < y_n$ as expected, regardless of step size. In implicit methods we must solve an algebraic equation for y_{n+1} which may not in general be solvable by analytical methods, nor result in a stable method.

Finite differencing methods can also be unstable, the analysis of which goes under the name von Neumann stability analysis [182]. We deduce requirements on the lattice spacing by analyzing the discrete Fourier modes of the numerical solutions. Expressing (3.1.45) with finite differencing as well as choosing the finite difference described in (3.1.47) for both the time and spatial derivatives results in

$$\Delta_t^2 \Phi_n = \frac{1}{a_n^2} \sum_{j=1}^{3} \Delta_j^2 \Phi_n - 3\frac{\dot{a}_n}{a_n}\Phi_n - \frac{\partial V}{\partial \Phi_n}, \tag{3.1.54}$$

where above it is implicitly implied that Φ is Φ_i and we now call Φ any of the fields governed by the differential Eq. (3.1.45). Again we use the short hand $\Phi_n = \Phi_i(t, \mathbf{x})$ and $\Phi_{n+1} = \Phi_i(t + \delta t, \mathbf{x})$ as well we use the notation

$$F = 3\frac{\dot{a}_n}{a_n}\Phi_n + \frac{\partial V}{\partial \Phi_n}. \tag{3.1.55}$$

Expanding and rearranging (3.1.54) gives

$$\Phi_{n+1} = 2\Phi_n - \Phi_{n-1} + \frac{\delta t^2}{a_n^2}\sum_{j=1}^{3}\Delta_j^2\Phi_n - \delta t^2 F_n. \tag{3.1.56}$$

We can analyze the stability of this method by using the spatial Fourier transformation of the numerical solutions Φ_n and expressing the numerical solution as the exact solution plus some error, which in a finite volume L^3 takes the form

$$\Phi(t, \mathbf{x}) = \Phi_{\text{exact}}(t, \mathbf{x}) + \frac{1}{V}\sum_{\mathbf{m}=-\infty}^{\infty}\xi_{\mathbf{m}}(t)e^{i\pi\mathbf{m}\cdot\mathbf{x}/\mathbf{L}^3}, \ \mathbf{m} = (n, m, p). \tag{3.1.57}$$

Applying this form of the fields on (3.1.56) gives

$$\xi_{\mathbf{m},n+1} = 2\xi_{\mathbf{m},n} - \xi_{\mathbf{m},n-1} - \frac{4\delta t^2}{a_n^2 \delta x^2}\sum_{j=1}^{3}\xi_{\mathbf{x},n}\sin^2\left(\frac{\pi\Delta x_j}{2V}\right) - \delta t^2\sum_{\mathbf{m}=-\infty}^{\infty}e^{-i\pi\mathbf{m}\cdot\mathbf{x}/\mathbf{L}^3}F_n. \tag{3.1.58}$$

The exact part of the solution has dropped from the equations since it satisfies the differential equation to all orders. For the sake of discussion we drop the possibly non-linear terms contained in F_n as this complicates the analysis. For stability we require that $|\xi_{\mathbf{m},n+1}/\xi_{\mathbf{m},n}| \leq 1$ the error does not grow unbounded step by step for any mode. For the worst case scenario the error propagates from the previous step at the same level so $\xi_{\mathbf{x},n-1} = \xi_{\mathbf{x},n}$ we then resolve

$$\left|1 - 3\frac{4\delta t^2}{a_n^2\Delta x^2}\sin^2\left(\frac{\pi\Delta x}{2V}\right)\right| \leq 1. \tag{3.1.59}$$

To ensure absolute stability in this method requires

$$\sqrt{3}\frac{\delta t}{a_n\Delta x} \leq \frac{1}{2}. \tag{3.1.60}$$

This is the famous Courant condition for wave equations [182]. We can see however in (3.1.60) that this condition cannot be satisfied at all times since $a_n \leq 1$ because of the normalization $a(\text{today}) = 1$ so this form is completely unstable! We can avoid this issue by changing coordinates and scaling the fields, so that $1/a_n$ drops for this condition.

Felder and Tkachev, created a program LATTICEEASY [183], with all statements above were addressed. The program LATTICEEASY performs self consistent calculations of the Friedmann equations and field evolutions while enforcing the Courant condition, and checking stability of the fields throughout the simulation. The fields and coordinates are scaled via

$$x_{pr} = Bx, \ \Phi_{pr} = Aa^r\Phi, \ dt_{pr} = Ba^s dt, \tag{3.1.61}$$

where B, A, r, and s are constants. These transformations change the field equations (3.1.45) into

$$\Phi_{pr}'' + (s - 2r + 3)\frac{a'}{a}\Phi_{pr}' - a^{-2s-2}\nabla_{pr}^2\Phi_{pr} - \left(r(s - r + 2)\left(\frac{a'}{a}\right)^2 + r\frac{a''}{a}\right)\Phi_{pr}$$

$$+ \frac{\partial}{\partial\Phi_{pr}}\left(\frac{A^2}{B^2}a^{-2s+2r}V\right) = 0, \tag{3.1.62}$$

where Φ', a' denote derivation with respect to program time t_{pr}. In attempts to ensure stability of the field equations the constants A, B, s, and r take specific values that depend on the dominant part of the potential which we assume takes the form

$$V = \frac{\alpha}{\beta}\Phi^\beta. \tag{3.1.63}$$

First LATTICEEASY scales the fields to their initial values to prevent unnecessarily large or small field values possibly causing over or underflows

$$A = \frac{1}{\Phi_0}, \tag{3.1.64}$$

Next LATTICEEASY removes the dampening term $a'\Phi_{pr}'/a$ by enforcing $s - 2r + 3 = 0 \rightarrow s = 2r - 3$. This allows us to check the Courant condition for stability as the matter field equations now take on the form of wave equations with a source. To avoid large sources that may drive large fluctuations in the field configuration, the dominant potential term is scaled to a similar order as the rescaled fields, such that B and r satisfy

$$B = \sqrt{\alpha}\Phi_0^{-1+\beta/2},$$

$$\frac{A^2}{B^2}a^{-2s+2r}V = \frac{a^{6-2r-\beta r}}{\beta}\Phi_{pr}^\beta,$$

$$6 - 2r - \beta r = 0 \rightarrow r = \frac{6}{2 + \beta}. \tag{3.1.65}$$

With these scalings LATTICEEASY uses a staggered-leapfrog method of progressing the evolution of the fields. Using LATTICEEASY we can calculate the anisotropic stress-energy tensor,

use a FFT, and project the TT part for sourcing the solution of the metic perturbation, for which one can use some numerical differential equation solving method, or approximate the scale factor evolution by a fixed power law and use a numerical integration of an appropriate Green's function to solve for the metric perturbation, and therefore calculate the power spectrum.

3.1.7 Numerical Solid Angle Integration on a Lattice

When we compute the power spectrum we require an integration over the solid angle in k-space of the form

$$\int \left| \dot{h}_{ij}^{\mathrm{TT}}(\eta, \mathbf{k}) \right|^2 d\Omega_k \ . \tag{3.1.66}$$

To compute this on a three dimensional rectangular lattice we must choose some k- value of which only can be evaluated on the discrete rectangular k-space values. For example if we choose some k -value along one axis as the radius to evaluate the solid angle integral. Sweeping through the solid angle sphere at that radius we will not have the value of $\left| \dot{h}_{ij}^{\mathrm{TT}}(\eta, \mathbf{k}) \right|^2$ at each point as seen in Fig. 33. To remedy this we will use a 3-dimensional interpolation method
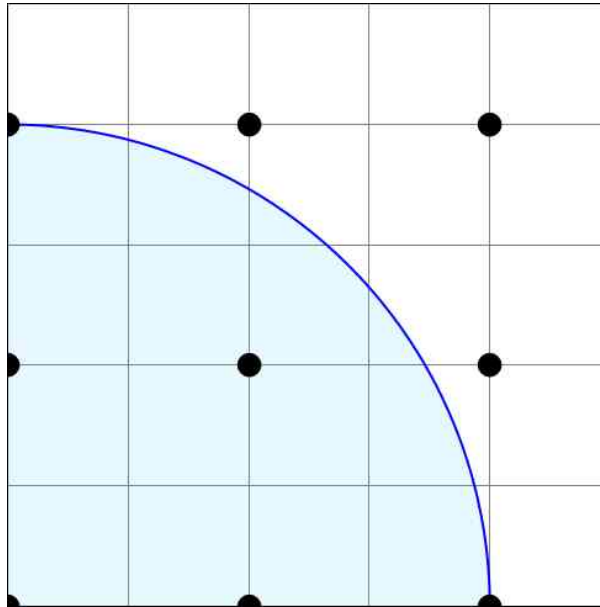
Figure 33 : Sweeping out a solid angle, as seen in blue, in a rectangular lattice requires us to use some interpolation method to find the intermediate values of the integrand function as the values of the integrand are only known at the lattice points depicted in black dots.

to obtain an approximate value of $\left| \dot{h}_{ij}^{\mathrm{TT}}(\eta, \mathbf{k}) \right|^2$ so long as the $\mathbf{k}$ value lies within the k-lattice values. Interpolation of the scalar function $\left| \dot{h}_{ij}^{\mathrm{TT}}(\eta, \mathbf{k}) \right|^2$ is done by expanding the function in a
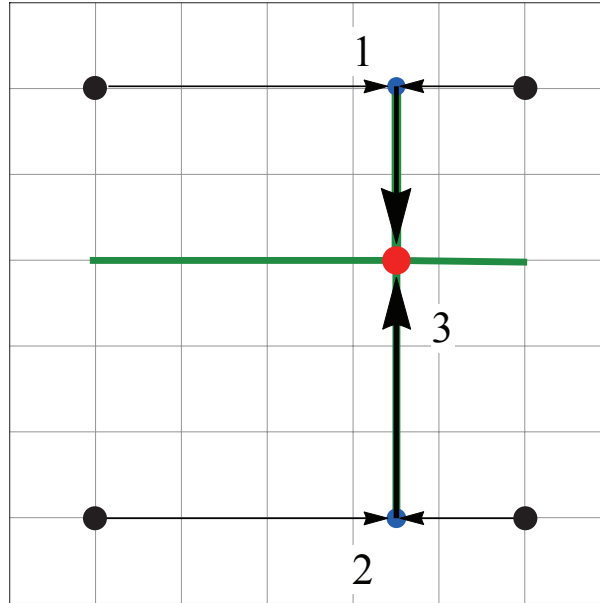
Figure 34 : First one determines the interpolated values of the function on each opposite side of the square, as seen by the arrows towards points 1 and 2. From which the the interpolated value along the y direction is found as seen by following the arrows towards point 3. This process is then repeated in the z direction to fully interpolate the value of the function in a 3 dimensional lattice.

Taylor series around each of the eight nearest lattice points that create a cube around the desired k-value. We will demonstrate this method with a scalar function $f(\mathbf{x})$ where we interpolate the function at some point $\mathbf{x}$. First we express the point $\mathbf{x}$ in component form for a rectangular coordinate system (x, y, z). To find the desired point we interpolate the value of the function on the opposite faces of the cube along the z-direction. This is done by finding the interpolated values of the function on each face by first interpolating the value of the function along the x-direction on the opposite sides of the square making in the x-y plane as depicted in Fig. 34 by the blue points 1 and 2, then finding the interpolated value in the y-direction for each face. Quantitatively the value of the function at point $1 : (x, y_1, z_1)$ of Fig. 34 is found by expanding the function at the lattice points for which we do have the value (at the lattice points which the arrows pointing towards 1 originate from)

$$
\begin{aligned}
f(\mathbf{x}_1) &= f_1 \approx f(x, y_1, z_1) + \partial_x f(x, y_1, z_1)(x_1 - x) \,, \\
f(\mathbf{x}_2) &= f_2 \approx f(x, y_1, z_1) + \partial_x f(x, y_1, z_1)(x_2 - x).
\end{aligned}
\tag{3.1.67}
$$

We approximate $\partial_x f(\mathbf{x})$ by

$$
\partial_x f(x, y_1, z_1) \approx \frac{f_2 - f_1}{\Delta x} = \frac{f_2 - f_1}{x_2 - x_1}.
\tag{3.1.68}
$$

Which then gives

$$f_1 \left(\frac{x_2 - x}{x_2 - x_1} \right) + f_2 \left(\frac{x - x_1}{x_2 - x_1} \right) \approx f(x, y_1, z_1). \tag{3.1.69}$$

This process is then repeated for the y-value, which can be visualized from following the arrows from points 1 and 2 in Fig. 34. This is done for both opposite faces of the cube and then finally interpolated along the z-axis to give the fully interpolated value at the desired point x.

3.1.8 Transfer functions

Running the program we setup the initial conditions of the field such that we are immediately following inflation at some physical comoving time t_0, corresponding to a program time $t_{pr,0}$, such that the inflaton is oscillating with small amplitude about the minimum of its self inter-action potential. This drives the amplification of various modes of the coupled scalar fields. Eventually the expansion of the universe causes oscillations of the inflaton and coupled fields to dampen, so that fluctuations are no longer large enough to source energy into gravitational waves generated by this mechanism. At this time the program stops corresponding to a final program time $t_{pr,f}$, this corresponds to some physical time in our early universe which can be solved for via

$$t_f = t_0 + \int_{t_{pr,0}}^{t_{pr,f}} a^{-s}(t_{pr}) dt_{pr}. \tag{3.1.70}$$

Once we know the result of the power spectrum at this time t_f we need to transfer these results to values we would observe today. We take advantage of the fact that gravitational waves propagate at the speed of light and red-shifts in the same way that electromagnetic radiation does. The redshift of objects moving at the speed of light can be understood because for speed of light travel $ds^2 = 0$. This along with assuming the radiation moves along a straight path (radially) from the emitted time t_e to the point of detection t_d along a coordinate distance R gives the relation

$$ds^2 = 0 = dt^2 - a(t)^2 dr^2 \rightarrow R = \int_{t_e}^{t_d} \frac{dt'}{a(t')}. \tag{3.1.71}$$

Assuming the first wave front is emitted at a comoving time t_e and detected at a time t_d and the following wave front is emitted at a time $t_e + \lambda_e$, where λ_e is the emitted wavelength in natural units, when the second wave front is detected, one would associate the time between the first wavefront and second wavefront as the wave length in natural units. The arrival of the

second wave front occurs at $t_d + \lambda_d$, where λ_d is the observed wavelength at the detection point in natural units. Since both wave fronts travel along the same coordinate distance R we find

$$\int_{t_e}^{t_d} \frac{dt'}{a(t')} = \int_{t_e+\lambda_e}^{t_d+\lambda_d} \frac{dt'}{a(t')} \quad \rightarrow \quad \int_{t_e}^{t_e+\lambda_e} \frac{dt'}{a(t')} - \int_{t_d}^{t_d+\lambda_d} \frac{dt'}{a(t')} = 0,$$

$$\frac{\lambda_e}{a(t_e)} = \frac{\lambda_d}{a(t_d)}, \tag{3.1.72}$$

where the second equality assumes that the variation of $a(t)$ time scale is much smaller than the times λ_d, λ_e allowing us to assume $a(t)$ remains constant in the integration regions. Using this relation on the frequencies for which we calculate the power spectrum, transfers the discrete frequencies calculated at the end of the simulation to the values detected today via

$$k(\text{today}) = k(t_f)\frac{a(t_f)}{a(\text{today})}. \tag{3.1.73}$$

This is simply red shifting the power in each frequency to the corresponding red-shifted frequency today. The effect of the expansion of the energy density in the gravitational waves has the same diluting effect as electromagnetic radiation such that

$$\rho_{gw}(\text{today}) = \rho_{gw}(t_f)\left(\frac{a(t_f)}{a(\text{today})}\right)^4. \tag{3.1.74}$$

We can see that the energy contained in the bin $k, k+dk$ gets redshifted and diluted.

To display these results it is common practice to display the results not in energy density per frequency but rather as $h^2 d\Omega_{gw}/d\log k$ where $\Omega_{gw} = \rho_{gw}/\rho_c$, with ρ_c the critical energy density to close the universe. Representing the data this way ensures the exact value of the Hubble constant $H = h\,100$ km/s/Mpc does not effect the final result. Take note that it is common practice to express $h^2 d\Omega_{gw}/d\log k$ as simply $h^2\,\Omega_{gw}(k)$ with the $d/d\log k$ understood, the context should make it clear.

In order to complete the transfer functions we need a method to determine the ratio $a(t_f)/a(\text{today})$. We appeal to the conservation of entropy in the universe in order to calculate this ratio. The total entropy in SM matter can be expressed normalized to the photon entropy in the form

$$S \propto a(t)^3 g_S(t) T_\gamma(t)^3 = \text{const},$$

$$g_S(t) = \sum_{\text{boson}} g_i \left(\frac{T_i^{\text{F.O.}}}{T_\gamma(t)}\right)^3 + \frac{7}{8}\sum_{\text{fermion}} g_i \left(\frac{T_i^{\text{F.O.}}}{T_\gamma(t)}\right)^3, \tag{3.1.75}$$

where g_i, $T_i^{\text{F.O.}}$ are the internal spin degeneracies of particle type i and the freeze out temperature for species i respectively. Conservation of entropy gives

$$\frac{a(t_f)}{a(\text{today})} = \left(\frac{g_S(\text{today})}{g_S(t_f)}\right)^{1/3} \frac{T_\gamma(\text{today})}{T_\gamma(t_f)}, \tag{3.1.76}$$

where $g_S(\text{today}) = 2 + \frac{7}{8} \cdot 3 \cdot 2 \cdot \left(\frac{4}{11}\right) = 3.91$ consisting of photons and three neutrino species. We can write T_γ in terms of the total energy density from SM matter. The total energy density from SM matter is dominated by particles that are relativistic at a temperature T_γ. Because of this the total energy density in SM matter is normalized to photons, and referred to as energy density in radiation (as relativistic particles behave as such) expressed as

$$\rho_{\text{rad}} = \frac{\pi^2}{30} g_\rho(T_\gamma) T_\gamma^4 \rightarrow \left(\frac{30}{\pi^2} \frac{\rho_{\text{rad}}}{g_\rho}\right)^{1/4} = T_\gamma. \tag{3.1.77}$$

where the degrees of energy freedom is given as

$$g_\rho(t) = \sum_{\text{boson}} g_i \left(\frac{T_i^{\text{F.O.}}}{T_\gamma(t)}\right)^4 + \frac{7}{8} \sum_{\text{fermion}} g_i \left(\frac{T_i^{\text{F.O.}}}{T_\gamma(t)}\right)^4. \tag{3.1.78}$$

From this it follows that

$$\frac{a(t_f)}{a(\text{today})} = \left(\frac{g_S(\text{today})}{g_S(t_f)}\right)^{1/3} \left(\frac{g_\rho(t_f)\rho_{\text{rad}}(\text{today})}{g_\rho(\text{today})\rho_{\text{rad}}(t_f)}\right)^{1/4}. \tag{3.1.79}$$

For times in the early universe $g_S \approx g_\rho$, we will extend this approximation to today, so that the final expression takes the form

$$\frac{a(t_f)}{a(\text{today})} = \left(\frac{\rho_{\text{rad}}(\text{today})}{\rho_{\text{rad}}(t_f)}\right)^{1/4} \left(\frac{g_S(\text{today})}{g_S(t_f)}\right)^{1/12}, \tag{3.1.80}$$

where $\rho_{\text{rad}}(t_f)$ is calculated in terms of the fields at final simulation time.

3.2 Gravitational Waves from Second Order Global Phase Transitions

We now apply the methods developed in the previous section to simulate the gravitational wave spectrum to be produced today from a second order global phase transition sourced from different local, non-zero, vacuum expectation values of a broken $SO(N)$ field symmetry of a scalar field ϕ_i. We are motivated to study this model because particle physicists are motivated to increase the symmetry group of the SM and thus unite the strong and electroweak forces into a GUT. The larger symmetry must become broken as the universe cools in the case the

transition is first-order, bubbles of the broken phase nucleate and coalesce. In this model the phase transition happens very rapidly—the entirety of the universe can end up in a unique state in less than a Hubble time. This process is likely to produce gravitational radiation [184, 170, 174, 185] as bubbles collide and coalesce. Another case could be the phase transition could be second-order where the fields smoothly transition to the broken phase as the temperature of the universe drops. If the broken phase has degeneracies, the effects of the existence of this phase transition can lead to observational effects. At various initially causally disconnected regions of the universe, the $SO(N-1)$ degeneracy of the minimization of the potential associated with the $SO(N)$ symmetry allows domains of space-time where the field values have different vacuum expectation values. As these domain walls collide, the differences in field value settle out, and self order, sourcing a stochastic gravitational wave background. It is worth noting that a scale-invariant spectrum of gravitational radiation is a key prediction of inflation [152, 186]. It has been noted by some authors that phase transitions of the type described above can however, mimic the scale-invariant inflationary signal [173, 169, 187]. In previous studies, authors have relied on large-N approximations to calculate the gravitational wave signal, but here we make no approximations other than those associated with numerics.

We begin with the assumptions that the universe is radiation dominated at the time when the phase transition occurs, and that the energy associated with the fields undergoing the phase transition is a small fraction, α, of the total energy density ρ_T at the time of the transition. The total energy density, at any time, is given by

$$\rho = \rho_{\text{rad}} + \rho_\phi, \ \rho_\phi = \sum_i \frac{1}{2} \left(\dot{\phi}^2 + \frac{1}{a^2} \nabla_x \phi_i^2 \right) + V(\phi_i, T) \tag{3.2.1}$$

where ρ_ϕ is the energy density associated with the scalar fields ϕ_i and

$$\rho_{\text{rad}} = (1 - \alpha)\rho \,. \tag{3.2.2}$$

Since the universe is dominated by the radiation energy-density in the relevant eras, we will only consider cases where $\alpha \ll 1$, so that the universe is well described by assuming $H^2 \propto a^{-4}$ because the potential in (3.2.1) is temperature dependent, we may simulate the phase transition by tracking the temperature throughout the simulation.

3.2.1 Statistical Mechanics of Quantum Fields

In order to arrive at the temperature dependent potential one must resort to the study of statistical mechanics of quantum fields. We can compute the potential by first expressing the fundamental quantity in quantum statistical mechanics, the partition function [188], as

$$Z_p = \text{Tr } e^{-H/T}, \tag{3.2.3}$$

with H the Hamiltonian of the system and T the temperature. The trace can be represented in field configuration space via

$$Z_p = \int \mathcal{D}\phi \, \langle \phi | e^{-H/T} | \phi \rangle = \int \mathcal{D}\phi \, \langle \phi | e^{iH(i\beta)} | \phi \rangle \, . \tag{3.2.4}$$

Equation (3.2.4) is specifically written in a form that displays the quantum propagator with the substitution $t \to i\beta = i/T$. With this in mind we can use the Feynman path integral formulation of the propagator to arrive at

$$Z_p = \int \mathcal{D}\phi \int_{\phi(0,\mathbf{x})}^{\phi(i\beta,\mathbf{x})} \mathcal{D}\chi \, e^{i \int_0^{i\beta} \mathcal{L}(\chi) d^4 x} \, . \tag{3.2.5}$$

We now make a change of variable, known as a Wick rotation, from $t \to i\tau$ such that the action for scalar fields takes the form

$$iS = -S_E = -\int \int_0^\beta \left(\frac{1}{2} \partial_\tau \phi(\bar{x})^2 + \frac{1}{2} \nabla_x \phi(\bar{x})^2 + V(\phi(\bar{x})) \right) d\tau d^3 x \, , \tag{3.2.6}$$

where now the fields are functions of $\bar{x} = (\tau, \mathbf{x})$, and we compact the notation by using the 4-dimensional Euclidean metric $\bar{\partial}^2 = \partial_\tau^2 + \nabla_x^2$ and writing $\phi(\bar{x}) = \bar{\phi}$. At this point it is worth noting that Eq. (3.2.6) takes on the form of the classical Hamiltonian with the replacement $t \to \tau$. With this notation we may now write the partition function as

$$Z_p = \int \mathcal{D}\bar{\phi} \int_{\bar{\phi}(0,\mathbf{x})}^{\bar{\phi}(\beta,\mathbf{x})} \mathcal{D}\bar{\chi} \, e^{-S_E[\bar{\chi}]} = \int \mathcal{D}\bar{\phi} \int_{\text{PBC}}^{\bar{\phi}} \mathcal{D}\chi \, e^{-S_E[\bar{\chi}]}. \tag{3.2.7}$$

In the second equality the integration limits can be taken over all field configurations with the condition that the fields $\bar{\chi}$ have periodic boundary conditions (PBC) where the period is β *i.e.*

$$\bar{\phi}(\tau, \mathbf{x}) = \bar{\chi}(\tau, \mathbf{x}) = \bar{\chi}(\tau + \beta, \mathbf{x}) = \bar{\phi}(\tau + \beta, \mathbf{x}) \, . \tag{3.2.8}$$

Equation (3.2.7) also allows identification of the probability distribution of field configurations which will be useful later on, specifically

$$Z_p = \int \mathcal{D}\bar{\phi} \, P_R[\bar{\phi}] \; \to \; P_R[\bar{\phi}] \propto e^{\beta H_{\text{eff}}[\bar{\phi}]} = \int_{\text{PBC}}^{\bar{\phi}} \mathcal{D}\chi \, e^{-S_E[\bar{\chi}]}, \tag{3.2.9}$$

where $P_R[\bar{\phi}]$ is the relative probability of the field configuration $\bar{\phi}$. From Eq. (3.2.9) we can extract the thermal potential by finding the quantum, thermal effective Euclidean action $S_E^{(\text{eff})}$ from the path integral in (3.2.9).

The effective action can be formulated by following [188] and identifying the effective Hamiltonian via

$$P_R[\bar{\phi}] = \int_{\text{PBC}}^{\bar{\phi}} \mathcal{D}\bar{\chi}\, e^{-S_E[\bar{\chi}]} = \mathcal{N}(\beta)e^{\beta H_{\text{eff}}[\bar{\phi}]}\,, \tag{3.2.10}$$

where $\mathcal{N}(\beta)$ is some temperature dependent function. We can make an approximate evaluation of (3.2.10) by expanding $S_E[\bar{\chi}]$ about the field configuration $\bar{\phi}_0$ that satisfies

$$\left.\frac{\delta S_E}{\delta \bar{\chi}}\right|_{\bar{\chi}=\bar{\phi}_0} = 0. \tag{3.2.11}$$

Now we make a change of variable and expand the action around the fixed field configuration $\bar{\phi}_0$

$$\bar{\chi} = \bar{\phi}_0 + \bar{\phi},\ \mathcal{D}\bar{\chi} = \mathcal{D}\bar{\phi}\,. \tag{3.2.12}$$

Under this change of variable, we retain the first term in the expansion of S_E to give

$$P_R \approx e^{-S_E[\bar{\phi}_0]} \int_{\text{PBC}} \mathcal{D}\bar{\phi}\, e^{-\frac{1}{2!}\bar{\phi}\cdot\frac{\delta^2 S_E}{\delta\bar{\phi}_0^2}\cdot\bar{\phi}}\,, \tag{3.2.13}$$

where above we use the shorthand

$$\bar{\phi}\cdot\frac{\delta^2 S_E}{\delta\bar{\phi}_0^2}\cdot\bar{\phi} = \int d^4\bar{x}d^4\bar{x}'\ \bar{\phi}(\bar{x}')\left.\frac{\delta^2 S_E}{\delta\bar{\phi}(x)\delta\bar{\phi}(x')}\right|_{\bar{\phi}=\bar{\phi}_0}\bar{\phi}(\bar{x})\,. \tag{3.2.14}$$

To continue with the analysis we must now choose a potential for the N scalar fields to break. We use a potential that supports a non-zero vev of the form

$$V(\phi) = \frac{\lambda}{8}\left(\phi^2 - \frac{v^2}{2}\right)^2 = -\frac{1}{2}m_0^2\phi^2 + \frac{\lambda}{8}\phi^4 + \frac{v^4\lambda}{32}, \tag{3.2.15}$$

where $\phi^2 = \sum_i \phi_i^2$ and $m_0^2 = \lambda v^2/4$. Finding the functional derivatives in (3.2.14) gives

$$\bar{\phi}\cdot\frac{\delta^2 S_E}{\delta\bar{\phi}_0^2}\cdot\bar{\phi} = \bar{\phi}\cdot\left(-\bar{\partial}^2 + m_0^2 + \frac{3\lambda}{2}\bar{\phi}_0^2\right)\cdot\bar{\phi}\,. \tag{3.2.16}$$

The integration in (3.2.13) can be shown to be proportional to

$$P_R \propto e^{-S_E[\bar{\phi}_0]} \exp\left[-\frac{1}{2}\operatorname{Tr}\ln\left(-\bar{\partial}_{\bar{x}}^2 + m_0^2 + \frac{3\lambda}{2}\bar{\phi}_0^2\right)\right]. \tag{3.2.17}$$

We evaluate the trace in Fourier space, keeping in mind the periodic behavior of $\bar{\phi}$. The periodicity is enforced by the Fourier series

$$\bar{\phi}(\bar{x}) = \frac{1}{\beta} \sum_{n=-\infty}^{\infty} \phi_n(\mathbf{x}) e^{ik_n \tau}, \ k_n = \frac{2\pi n}{\beta}. \tag{3.2.18}$$

Under this Fourier series the trace becomes

$$\frac{1}{2} \operatorname{Tr} \ln \left(-\bar{\partial}^2 + m_0^2 + \frac{3\lambda}{2} \bar{\phi}_0^2 \right) = \frac{1}{2} \int d^3x \sum_{n=-\infty}^{\infty} \int \frac{d^3k}{(2\pi)^3} \ln \left(\bar{k}^2 + \bar{m}^2 \right), \tag{3.2.19}$$

where $\bar{k}^2 = k_n^2 + \mathbf{k}^2$ and $\bar{m}^2 = m_0^2 + 3\lambda\bar{\phi}_0^2/2$. The sum over frequencies is know as *Matsubara frequency sums*. A sum of this kind is equivalent, up to an overall constant to a contour integral [188], giving a sum over residues of the form

$$\frac{1}{2} \int \frac{d^3k}{(2\pi)^3} \left(\beta\sqrt{k^2 + \bar{m}^2} + 2\ln(1 - e^{-\beta\sqrt{k^2+\bar{m}^2}}) + k \text{ independent constant}\right), \tag{3.2.20}$$

The k independent constant and integration of $\sqrt{k^2 + \bar{m}^2}$ can be absorbed into the overall temperature dependent proportionality constant, so that we only retain the $\ln$ term. Evaluation of this last term results in

$$\frac{1}{2\pi^2} \int_0^\infty k^2 \ln(1 - e^{-\sqrt{\beta^2 k^2 + \beta^2 \bar{m}^2}}) \approx -\frac{\pi^2}{90\beta^3} + \frac{\bar{m}^2}{24\beta}, \ \bar{m}\beta \ll 1. \tag{3.2.21}$$

We can now express the effective Hamiltonian as

$$\beta H_{\text{eff}} \approx S_E + \int d^3x \frac{\bar{m}^2}{24\beta} = \beta \int d^3x \ \left(\frac{1}{2}\partial_x\bar{\phi}_0^2 + V(\bar{\phi}_0) + \frac{\bar{m}^2}{24\beta} \right). \tag{3.2.22}$$

In the second equality, we assumed that $\bar{\phi}_0$ has no τ dependence. We can now find to leading order in temperature, the effective potential

$$V(\phi_i, T) \approx \frac{\lambda v^2}{8} \left(\frac{T}{2v^2} - 1 \right) \phi^2 + \frac{\lambda}{8} \left(\phi^4 + \frac{v^4}{4} \right) = m_{\text{eff}}^2(T)\phi^2 + \frac{\lambda}{8} \left(\phi^4 + \frac{v^4}{4} \right), \tag{3.2.23}$$

where the temperature dependent effective mass is parameterized by

$$m_{\text{eff}}^2 = \frac{\lambda v^2}{8} \left(\frac{T}{T_c} - 1 \right). \tag{3.2.24}$$

At temperatures higher than the critical temperature, T_c, the effective mass is positive, the potential has a unique minimum at $\phi_i = 0$, and this minimum has full $SO(N)$ symmetry. When the temperature drops to T_c where the effective mass of the field vanishes, a phase transition

occurs as the potential now allows a new stable vacuum state with an $SO(N-1)$ symmetry, a state for which the fields take non-zero vevs. The simulation can keep track of the temperature with the relations between energy and the Hubble value at the start of the simulation

$$T(t) = \frac{T_0}{a(t)}, \ \rho_0 = \frac{\pi^2}{30} g_\rho(T_0) T_0^4 = \frac{3 M_{pl}^2}{8\pi} H_0^2 \ , \tag{3.2.25}$$

where T_0 the initial temperature to be solved for as a function of the initial Hubble value H_0. We will take the number of relativistic degrees of freedom to initially be $g_\rho(T_0) = 1000$.

3.2.2 Initial Field Conditions on the Lattice

Initially the simulation will start at $T_0 = T_c$ where the field has a mean value, $\phi = 0$; however, there is a variance associated with this temperature,

$$\sigma^2 = \langle \phi^2 \rangle - \langle \phi \rangle^2 = \langle \phi^2 \rangle \ , \tag{3.2.26}$$

that sets the distribution of field values at the time of the transition. The physics of interest demand that each lattice site be assigned the average value of the field contained in one Hubble volume. We denote by $\langle \phi \rangle = \phi_v$, this average is done over one Hubble volume. Since each lattice site is causally disconnected, we select the field value at each lattice site randomly from a probability distribution of possible field values. Determining the distribution is done by using

$$P(\phi_v = \phi') = \int D\phi \mathcal{P}[\phi] \delta(\phi_v - \phi') = \langle \delta(\phi_v - \phi') \rangle. \tag{3.2.27}$$

Equation (3.2.27) finds the probability that ϕ_v has the value ϕ' by summing the probabilities of all the possible field configurations that for which $\phi_v = \phi'$, where $\mathcal{P}[\phi]$ is the probability functional of the field configuration ϕ. The volume-averaged field is given as

$$\phi_v = \frac{1}{V} \int_V d^3x \, \phi(x) = \frac{1}{V} \int_{-\infty}^{\infty} d^3x \, I(x) \phi(x), \tag{3.2.28}$$

where, for computational convenience, we have introduced a window function $I(x)$, which is a function which is 1 for x within the volume of interest and 0 outside of it. We can approximate (3.2.27) using the cumulant expansion technique, which gives a Gaussian approximation

$$P(\phi_v = \phi') \approx \sqrt{\frac{1}{2\pi\sigma^2}} \exp\left(-\frac{(\phi' - \mu)^2}{2\sigma^2} \right),$$

with $\mu = \langle \phi_v \rangle$ and $\sigma^2 = \langle \phi_v^2 \rangle - \langle \phi_v \rangle^2$. The problem is now to compute the moments of the field given by

$$
\begin{aligned}
\langle \phi_v \rangle &= \int D\phi \, \mathcal{P}[\phi] \left(\frac{1}{V} \int_V d^3x \, \phi(x) \right) , \\
\langle \phi_v^2 \rangle &= \int D\phi \, \mathcal{P}[\phi] \left(\frac{1}{V^2} \int_V d^3x \, d^3y \, \phi(x)\phi(y) \right) .
\end{aligned}
\tag{3.2.29}
$$

The full probability functional $\mathcal{P}$, can be found in, [189], but we consider only the leading order temperature dependence. We saw in (3.2.23) that leading order temperature dependence modifies the potential by replacing m with a temperature dependent term, $m_{\text{eff}}(\beta)$. For temperatures at and above T_c we are in a symmetric phase of the effective potential. We then have

$$
\mathcal{P}[\phi] = \frac{e^{-\beta H_{\text{eff}}[\phi]}}{Z} = \frac{1}{Z} \exp \left[-\beta \int d^3x \left(\frac{1}{2}\partial_x \phi^2 + V_{\text{eff}} \right) \right]
\tag{3.2.30}
$$

Note that the normalization Z is given as

$$
Z = \int \mathcal{D}\phi \, e^{-\beta H_{\text{eff}}[\phi]} .
\tag{3.2.31}
$$

We can make use of a more general expression, known as a generating functional, that is related to the moments of the field by the expression

$$
\begin{aligned}
W[J] &= \frac{1}{Z} \int \mathcal{D}\phi \, \exp \left[-\beta \int d^3x \left(\frac{1}{2}\partial_x \phi^2 + V_{\text{eff}} + J\phi \right) \right] , \\
&\approx \exp \left[-\frac{1}{2\beta} J \cdot \Delta \cdot J \right] ,
\end{aligned}
\tag{3.2.32}
$$

where in the last line we are taking using only the zeroth-order terms involving m_{eff}; that is, we are neglecting the term $\lambda\phi^4$ as it will produce higher-order corrections. As well, in (3.2.32) Δ is given as

$$
\begin{aligned}
(-\partial_x^2 + 2m_{\text{eff}}^2)\Delta(\mathbf{x}, \mathbf{x}') &= \delta^{(3)}(\mathbf{x} - \mathbf{x}') , \\
\Delta(\mathbf{x}, \mathbf{x}') &= \int \frac{d^3\mathbf{k}}{(2\pi)^3} \frac{e^{-i\mathbf{k}\cdot(\mathbf{x}-\mathbf{x}')}}{\mathbf{k}^2 + 2m_{\text{eff}}^2} .
\end{aligned}
\tag{3.2.33}
$$

With the use of (3.2.32) the moments of the field can now be expressed as

$$
\begin{aligned}
\langle \phi_v \rangle &= \frac{1}{V} \int_{-\infty}^{\infty} d^3x \, I(x) \frac{\delta}{\delta J(x)} W[J] \Big|_{J=0} , \\
\langle \phi_v^2 \rangle &= \frac{1}{V} \int_{-\infty}^{\infty} d^3x \, d^3y \, I(x)I(y) \\
&\qquad \times \frac{\delta}{\delta J(x)} \frac{\delta}{\delta J(y)} W[J] \Big|_{J=0} .
\end{aligned}
$$

We choose a Gaussian window function for which the integral $\int d^3x\, I(x) = 4\pi R^3/3 = 4\pi/3H_c^3$ is one Hubble volume at the time $T = T_c$. Evaluating the integrals of (3.2.34) at the point $T = T_c$ leads to

$$\langle \phi_v \rangle = 0 \ , \ \langle \phi_v^2 \rangle = \frac{H_c T_c}{4\pi^{3/2}} \ . \tag{3.2.34}$$

Putting this all together, we have

$$P(\phi_v = \phi') = \sqrt{\frac{H_c T_c}{8\pi^{5/2}}} \exp\left(-\frac{\phi'^2}{4\pi^{3/2}} H_c T_c\right) , \tag{3.2.35}$$

from which we draw the initial values of the initial field values.

3.2.3 Results of the Simulation

The simulation takes advantage of a 4th order RK algorithm to calculate the metric perturbation, and assumes $g_S(\text{today})/g_S(t_f) = 1/100$ for use in the transfer functions. The first major difference between the form of the gravitational-wave spectrum from self-ordering of the fields from domain interactions and that predicted by inflation is the lack of power at high-frequencies. This cut-off feature exists because second order phase transition fluctuations occur on larger than Hubble length scales.

In [161] the cut-off frequency is shown to be related to the Hubble length at the time when the gravitational wave is generated H, the result of which is

$$f_{\text{peak}} = 6 \times 10^{-10} \frac{k}{\sqrt{M_{pl}H}} \text{ Hz.} \tag{3.2.36}$$

where $k = H$ the largest possible frequency for this model. The first Friedmann equation,

$$H_c^2 = \frac{8\pi}{3} \frac{\rho_T}{M_{pl}^2}, \tag{3.2.37}$$

then implies that the cut-off should appear at

$$f_{\text{peak}} \simeq 10^{11} \frac{\rho_T^{1/4}}{M_{pl}} \text{ Hz.} \tag{3.2.38}$$

For example, with $\rho_T^{1/4} = 10^{-4} M_{pl}$ we expect the cutoff to be at $f \simeq 10^7$ Hz, which agrees with the results of the simulation shown in Fig. 35.

This model provides a probe of the energy scale of some symmetry breaking on BSM physics, as the sharp Hubble-length wall cut off can probe the era at which the symmetry
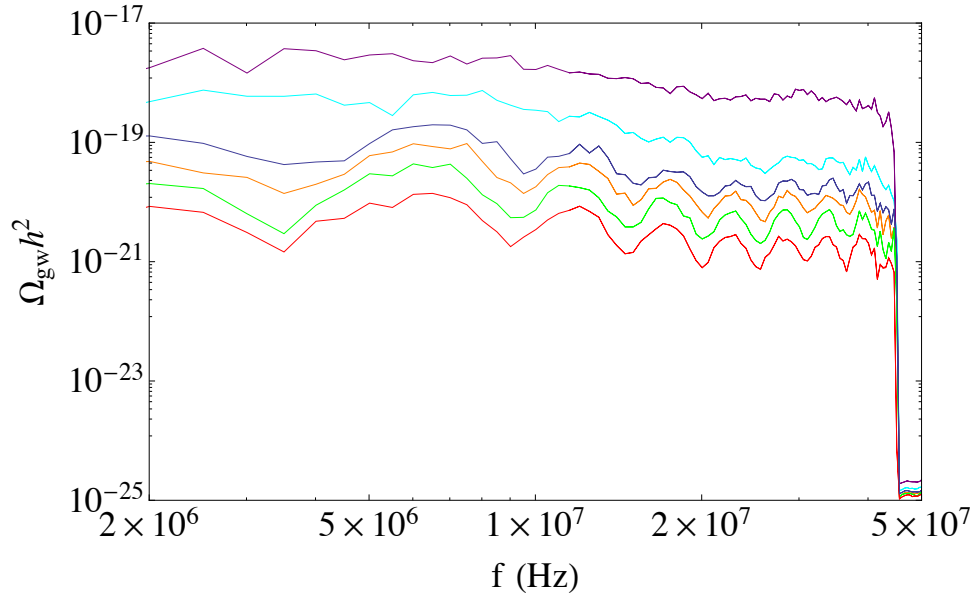
Figure 35 : The figure displays the present-day gravitational wave spectrum as calculated from the lattice simulation, from self-ordering fields on larger than Hubble volume scales. The figure displays, from top to bottom, the spectrum for N scalar fields which undergo breaking the $SO(N)$ symmetry with, $N = 2, 3, 4, 5, 8, 16$
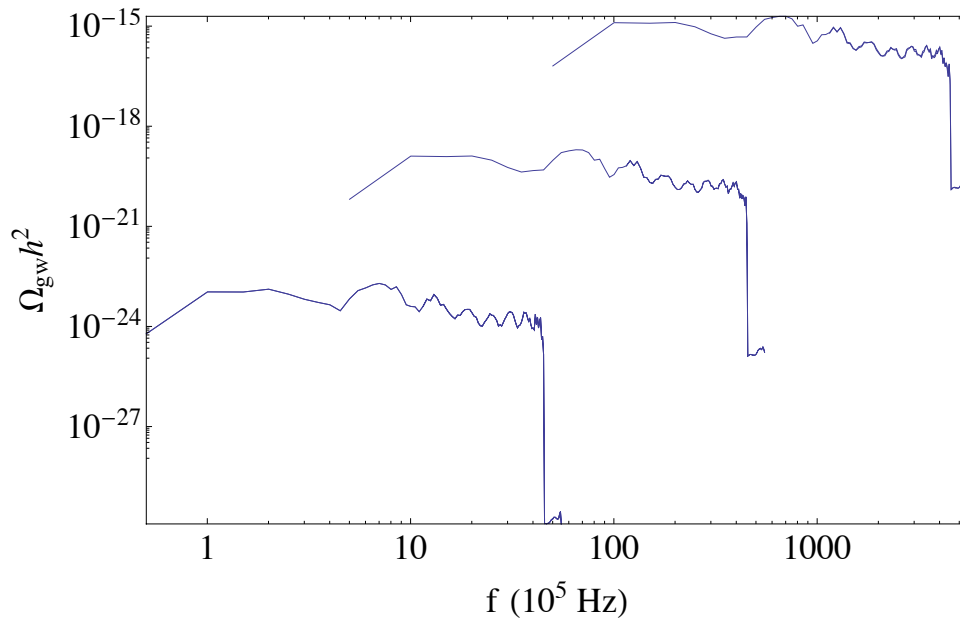
Figure 36 : The present-day gravitational wave spectrum from self-ordering. From top (rightmost) to bottom (leftmost), $\rho_T^{1/4} = 10^{-3} M_{\mathrm{pl}}$, $\rho_T^{1/4} = 10^{-4} M_{\mathrm{pl}}$, $\rho_T^{1/4} = 10^{-5} M_{\mathrm{pl}}$.

breaking occurs. A flat signal as shown in Fig. 35 could be misinterpreted as the gravitational radiation from primordial quantum fluctuations. It might, however, be possible to distinguish the two models at very high frequencies due to the Hubble length wall. The behavior of the gravitational waves can be understood as follows. Initially at the Hubble-length the gradients due to differing field values sources gravitational waves at this scale. The waves generated continue to redshift to lower frequencies. After the fields have settled from self ordering, the overall configuration of the field is the same as the initial configuration, where differing regions of the the field have different domains of vacuum values, now at a larger Hubble-length scale. The process repeats and sources gravitational waves at the scale of the new domains, and so on until the simulation ends.

The amplitude and the essentially flat nature of the spectrum were expected from the analytical approach of [169, 190] and [187]. It is interesting to note that the spectrum is flat for all the cases shown in Fig. 35, including those for $N = 2, 3$, as the analytical methods employed by [187] assumed that N is large.

In Fig. 36 we observe two important scaling effects. First, we recover the fact that the high-frequency cutoff given by equation (3.2.38) scales with $\rho_T^{1/4}$. We can also see that the amplitude of the spectrum is proportional to the energy density of the universe at the time of the transition, $\Omega_{\text{gw}}(k)h^2 \propto \rho_T$. This scaling was shown in [169, 190] and [187].

We can compare the numerical results we obtained from simulation with the analytic arguments of [169, 190] and [187], where in both cases the authors use the model presented here to estimate the gravitational wave signal from the domain interactions. The two sets of authors use slightly different parameterizations of the model; however, all authors arrive at the conclusion that there should be a flat gravitational wave spectrum from this transition.

In [169] and [190] (JKM), the authors estimated the power in gravitational waves from field reordering to be (given by equation (10) in [190] with some modification outlined in [179]) as

$$\Omega_{\text{gw}}^{\text{JKM}} h^2 = \frac{99}{N} \Omega_{\text{rad}} h^2 \left(\frac{v^4}{4NM_{pl}^4} \right) . \qquad (3.2.39)$$

This can be reduced further by using $\Omega_{\text{rad}} h^2 \approx 2 \times 10^{-5}$ and estimating the total energy density at the phase transition by

$$\langle \rho_\phi \rangle \simeq \frac{\lambda v^4}{32} = \alpha \rho = \alpha \frac{3M_{pl}^2}{8\pi} H_c^2 \to \frac{v^2}{2} = \sqrt{\frac{3\alpha}{\lambda\pi}} M_{pl} H_c. \qquad (3.2.40)$$

Table 5 : Spectral amplitudes as a function of number of fields for simulations with $\left(\rho_T^{1/4} = 10^{-4} M_{pl}, \alpha = \lambda = 0.1\right)$. The numerical values, $\Omega_{\text{gw}}^{\text{SIM}} h^2$, are an average value along the spectrum taken from the simulations, while the values in the second two columns are obtained from (3.2.39) or (3.2.43).

N	$\Omega_{\text{gw}}^{\text{SIM}} h^2$	$\alpha^2 \Omega_{\text{gw}}^{\text{JKM}} h^2$	$\alpha^2 \Omega_{\text{gw}}^{\text{FFDG}} h^2$
2	1.0×10^{-18}	9.0×10^{-21}	4.1×10^{-20}
4	3.8×10^{-20}	4.0×10^{-21}	2.1×10^{-20}
8	8.3×10^{-21}	2.0×10^{-21}	1.0×10^{-20}
16	3.1×10^{-21}	1.0×10^{-21}	5.1×10^{-21}

From Eq. 3.2.40 and the relation $H_c^2 = 8\pi\rho_T/3M_{pl}^2$, Eq. (3.2.39) becomes

$$\Omega_{\text{gw}}^{\text{JKM}} h^2 = \frac{0.016}{N} \frac{\alpha}{\lambda} \frac{\rho_T}{M_{pl}^4}. \tag{3.2.41}$$

Furthermore, in [187] (FFDG), the authors predict a scale-invariant power spectrum (Eq. (5.2) of [187])

$$\Omega_{\text{gw}}^{\text{FFDG}} h^2 \simeq \frac{511}{N} \Omega_{\text{rad}} h^2 \left(\frac{v}{\sqrt{2}M_{pl}}\right)^4, \tag{3.2.42}$$

Using Eq. (3.2.40) along with $\Omega_{\text{rad}} h^2 \approx 2 \times 10^{-5}$, the expression in (3.2.42) reduces to

$$\Omega_{\text{gw}}^{\text{FFDG}} h^2 \simeq \frac{0.082}{N} \frac{\alpha}{\lambda} \frac{\rho_T}{M_{pl}^4}. \tag{3.2.43}$$

Both of these estimates assume the universe is comprised only of the scalar fields. However, we diluted the source by a factor of α, to preserve a radiation-dominated phase during and after the phase transition; this dilutes the analytic estimates (3.2.39,3.2.43) by a factor of α^2.

It is worth pointing out that some of the phase transitions we have simulated result in the production of global topological defects: global strings for $N = 2$, global monopoles $N = 3$, and global textures for $N > 3$. Surprisingly, we find that the gravitational radiation produced is consistent with the large N approximation even for low values of N, where the approximation is not valid (see the analytic estimates above). The results of the estimates and simulation data are summarized in Tables 5 and 6. The numerical results suggest a large value of N is not needed to make a scale invariant spectrum. Since the results of [169, 190, 187] are derived using a large N approximation for the amplitude, one does not expect these estimates to accurately approximate the amplitude of the gravitational waves in the low-N limit. It can be seen the simulations differ from analytic estimates by an order of magnitude and are more accurate at large N, consistent with the fact that analytic methods are derived from a large N expansion.

Table 6 : Spectral amplitudes as a function of ρ_T for simulations with $N = 4, \alpha = \lambda = 0.1$. The numerical values $\Omega_{\text{gw}}^{\text{SIM}} h^2$ are an average of the spectral values taken from the simulations, while the values in the second two columns are obtained from (3.2.39) or (3.2.43).

$\rho_T^{1/4}(M_{pl})$	$\Omega_{\text{gw}}^{\text{SIM}} h^2$	$\alpha^2 \Omega_{\text{gw}}^{\text{JKM}} h^2$	$\alpha^2 \Omega_{\text{gw}}^{\text{FFDG}} h^2$
10^{-3}	4.7×10^{-16}	4.0×10^{-17}	2.1×10^{-16}
10^{-4}	3.8×10^{-20}	4.0×10^{-21}	2.1×10^{-20}
10^{-5}	4.0×10^{-24}	4.0×10^{-25}	2.1×10^{-24}

3.3 Adaptive Green's Function Method

In Sec. 3.2, the simulation of the metric perturbation was done via a 4th order RK algorithm (RK4). In Sec. 3.1.6 however, we saw that in general explicit numerical differential equation solving methods suffer from stability issues, including the RK4 method. As the system is iterated, the instability of the solution can typically be suppressed at the step where it occurs by increasing the accuracy of the method; in particular, changing from a 2nd-order method to a 4th-order method can move the instability by a power of 2 in the number of iterations. However, we saw that using implicit methods can remove stability issues, so by choosing a different algorithm the instability in numerical calculations can disappear entirely.

An easy fix to an instability associated with the method of solving the metric perturbation is to use a method that numerically integrates an exact expression that only depends on the stability of the source. For example we saw in Eq. (3.1.36) that the metric perturbation has an exact solution in terms of Green's functions (repeated here for connivence)

$$h_{ij}^{\text{TT}} = \frac{16\pi}{M_{pl}^2} \frac{k}{\eta^{n-1}} \int_{\eta_i}^{\bar{\eta}} d\eta' \, (\eta')^{n+1} \left(j_{n-1}(k\eta') y_{n-1}(k\eta) - j_{n-1}(k\eta) y_{n-1}(k\eta') \right) T_{ij}^{\text{TT}}(\eta', \mathbf{k}),$$

$$(3.3.1)$$

where the scale factor is assumed to have the form $a(\eta) = \alpha \, \eta^n$ and again η is the conformal time coordinate. To understand the computational advantage of this expression, let us consider the solution with $n = 1$ appropriate for radiation dominated expansion. Under this assumption Eq. (3.1.36) takes the form

$$h_{ij}^{\text{TT}}(\eta, \mathbf{k}) = \frac{16\pi}{M_{pl}^2} \int_{\eta_i}^{\bar{\eta}} d\eta' \, \frac{\eta' \sin\left[k(\eta - \eta')\right]}{k\eta} T_{ij}^{\text{TT}}(\eta', \mathbf{k}),$$

$$(3.3.2)$$

This expression can be approximately evaluated by any number of numerical integration methods, the simplest being the rectangular sum method (Riemann sum), which simply cuts the
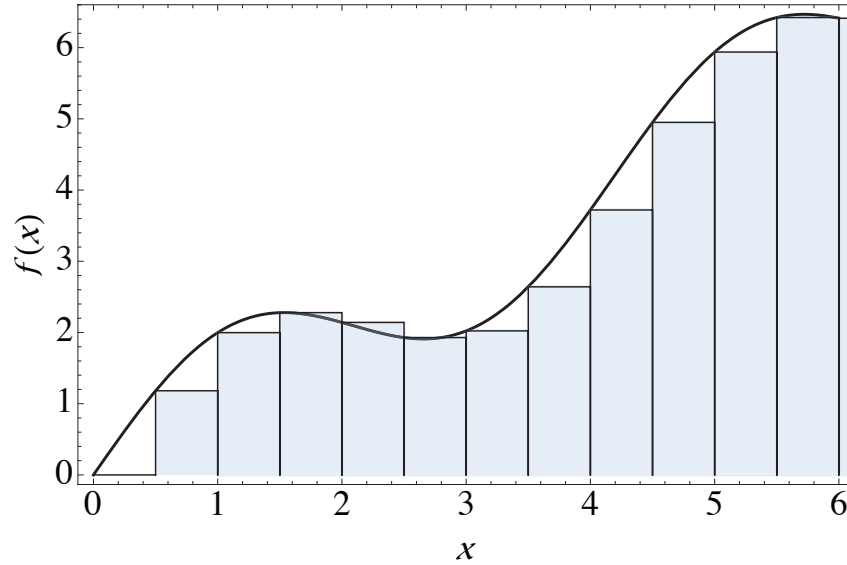
Figure 37 : The integral $\int_0^6 f(x)dx$ can be approximated in the rectangular sum method by summing the areas of the rectangular regions under the curve as seen in the figure above.

integration region into N segments of length $\Delta\eta$ and approximates the area under the curve as a sum of the values of integrand evaluated at $n\Delta\eta$ multiplied by the width $\Delta\eta$, where n ranges from 0 to N, thus approximating the integration as a sum of the areas of rectangles making the area under the curve as seen in Fig. 37 In such a simple approximation the error associated with this method can be extracted by examining the integration over one of the rectangular regions

$$
\begin{aligned}
\int_a^{a+\Delta\eta} f(\eta)d\eta &\approx \int_a^{a+\Delta\eta} \left(f(a) + f'(a)(\eta - a) + \ldots\right) d\eta \\
&= f(a)\Delta\eta + f'(a)\frac{\Delta\eta^2}{2} + \ldots
\end{aligned}
\tag{3.3.3}
$$

adding up all the rectangular regions takes the form

$$
\int_a^b f(\eta)d\eta \approx \sum_{n=0}^{N-1} f(a + n\Delta\eta)\Delta\eta + \mathcal{O}\left(\Delta\eta\right) ,
\tag{3.3.4}
$$

thus the rectangular method is a 1st order approximation. The equation (3.3.2) under this method takes the form

$$
h_{ij}^{\text{TT}}(\eta, \mathbf{k}) \approx \frac{16\pi\Delta\eta}{M_{pl}^2} \sum_{n=0}^{N-1} \frac{\eta_n \sin\left[k(\eta - \eta_n)\right]}{k\eta} T_{ij}^{\text{TT}}(\eta_n, \mathbf{k}) , \quad \eta_n = \eta_i + n\Delta\eta.
\tag{3.3.5}
$$

We can see the advantage of this form as the only source of instability comes from $T_{ij}^{\text{TT}}(\eta_n, \mathbf{k})$, so long as $T_{ij}^{\text{TT}}(\eta_n, \mathbf{k})$ is within machine sized numbers the method is absolutely stable, and
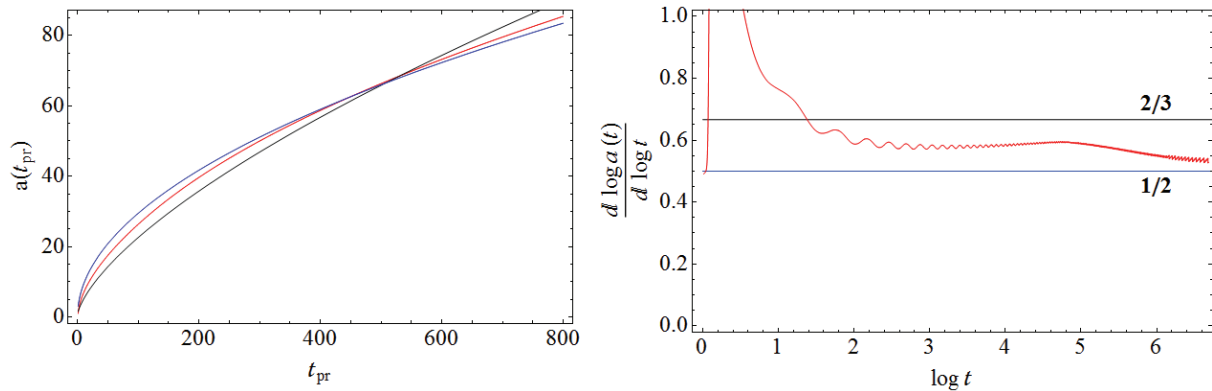
Figure 38 : (Left) The scale factor (red) initially starts in a state of close to that of a matter dominated form $a \propto t^{2/3}$ (black) but as the system evolves, the scale factor tends toward the scale factor for a radiation dominated universe $a \propto t^{1/2}$ (blue). (Right) The expression $d \log a / d \log t$ gives the power of the scale factor for a form $a = \alpha t^n \rightarrow \log a = \log \alpha + n \log t$. In red is the value for the scale factor $d \log a / d \log t$ under self consistant evolution. We can see the scale factor tends toward the form for matter domination $n = 2/3$ after which the scale factor falls towards a radiation dominated universe $n = 1/2$.

furthermore much more computationally rapid. This method was employed by [59] to calculate the spectrum associated with pre-heating mechanisms.

Unfortunately we've given up the flexibility of using the exact form of $a(\eta)$ for an approximate $a(\eta) = \alpha \eta^n$ form. This can present issues with this formulation, such as the case when the potential for pre-heating cases is taken as

$$V(\phi, \chi) = \frac{1}{2} m^2 \phi^2 + \frac{g^2}{2} \chi^2 \phi^2 \,, \tag{3.3.6}$$

where ϕ is the inflaton and χ is the field that will undergo pre-heating. In this quadratic form of the potential LATTICEEASY can self consistently evolve the fields and scale factor. Interestingly from this model the scale factor undergoes a transition, from an initially matter dominated scale factor (in comoving coordinates $a \propto t^{2/3}$) to a radiation dominated system (in comoving coordinates $a \propto t^{1/2}$), as is seen in Fig. 38. In such a case it is not clear when to choose one scale factor form and exclude the other. Unfortunately we have to make some approximation which naively the differential equation solving methods do not. We do not want to sacrifice the numerical stability associated with the analytic method, but want to make as few approximations as possible.
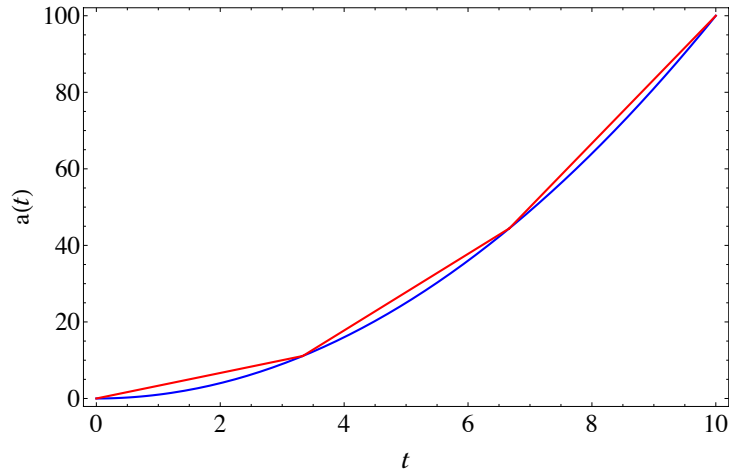
Figure 39 : The scale factor $a(t)$ as seen in blue, can be approximated as a piece-wise function of linear segments, as seen in red. The approximation becomes better and better as the line segments become shorter and shorter.

3.3.1 Stability With No Scale Factor Assumption

We retain both the stability of the numerical integration methods and have the flexibility of an arbitrary scale factor, by examining the form of the scale factor on the scale η, $\eta + \Delta\eta$. On this scale every scale factor can be approximated as linear segment. In fact, because all numerical methods must calculate the scale factor at discrete times in self consistent simulation; in numerical methods the scale factor is exactly a series of linear segments. To develop the method we take any scale factor and approximate its form as a piece wise function of linear segments as seen in Fig. 39. With the explicit form

$$a(\eta) = \begin{cases} \alpha_1 \eta + \beta_1 & \eta_i \le \eta < \eta_i + \Delta\eta \\ \alpha_2 \eta + \beta_2 & \eta_i + \Delta\eta \le \eta < \eta_i + 2\Delta\eta \\ \vdots & \\ \alpha_N \eta + \beta_N & \eta_i + (N-1)\Delta\eta \le \eta < \eta_f \ . \end{cases} \qquad (3.3.7)$$

Continuity of the scale factor is enforced by the conditions

$$\alpha_n \eta_{n-1} + \beta_n = \alpha_{n-1}\eta_{n-1} + \beta_{n-1} \ , \ \eta_m = \eta_i + m\Delta\eta \ . \qquad (3.3.8)$$

We can build up a solution of the metric perturbation h_{ij}^{TT}. To accomplish this, first assume that there is no source of gravitational waves before the time η_i, that $h_{ij}^{\mathrm{TT}}(\eta_i, \mathbf{k}) = 0$. From the time η_i to $\eta_i + \Delta\eta$ the scale factor is $\alpha_1 \eta + \beta_1$. The solution to the field equations (3.1.15) with this

form of a scale factor is given by

$$
\begin{aligned}
h_{ij}^{\mathrm{TT}} = \quad & \frac{1}{\alpha_1 \eta + \beta_1} \left(A_1(k) \cos(k\eta) + B_1(k) \sin(k\eta) \right) \\
+ \quad & \frac{16\pi}{M_{pl}^2 \, k(\alpha_1 \eta + \beta_1)} \int_{\eta_i}^{\bar{\eta}} d\eta' (\alpha_1 \eta' + \beta_1) \sin[k(\eta - \eta')] T_{ij}^{\mathrm{TT}}(\eta', \mathbf{k}) \,,
\end{aligned}
$$

$$(3.3.9)$$

where

$$
\bar{\eta} = \mathrm{Min}\left\{ \eta_1, \eta \right\}, \ \eta_i \leq \eta \leq \eta_1. \tag{3.3.10}
$$

Examining (3.3.9) we see we have a purely radiative part, which corresponds to the free prop-agation solution $T_{ij}^{\mathrm{TT}} = 0$, where A_1, B_1 are in general complex values that depend on k. We also we have a source term that generates the gravitational waves in this era. To solve for the values A_1 and B_1 we use the initial conditions of the previous era. For this particular era of $\eta_i \leq \eta < \eta_i + \Delta\eta$, the conditions are $h_{ij}^{\mathrm{TT}}(\eta_i, \mathbf{k}) = 0$ and $\partial_\eta h_{ij}^{\mathrm{TT}}(\eta_i, \mathbf{k}) = 0$. Computationally we are only interested in evaluating h_{ij}^{TT} at the endpoints of each era, *e.g.* $\eta_i + \Delta\eta$, $\eta_i + 2\Delta\eta$ and so on. We need only to express (3.3.9) at these points where the scale factor for era n (conformal time given by $\eta_{n-1} \leq \eta < \eta_n$) is $a_n = \alpha_n \eta + \beta_n$. With this notation the general solution for era n of the metric perturbation becomes

$$
\begin{aligned}
h_{ij}^{\mathrm{TT}}(\eta_n, \mathbf{k}) = \quad & \frac{1}{a_n} \left(A_n(k) \cos(k\eta_n) + B_n(k) \sin(k\eta_n) \right) \\
+ \quad & \frac{16\pi}{M_{pl}^2 \, k a_n} \int_{\eta_{n-1}}^{\eta_n} d\eta' (\alpha_n \eta' + \beta_n) \sin[k(\eta_n - \eta')] T_{ij}^{\mathrm{TT}}(\eta', \mathbf{k}) \,,
\end{aligned}
$$

$$(3.3.11)$$

where continuity of the metric perturbation is used to solve for A_n and B_n as described for the first era. To make this clear, we adopt a more compact notation denoting $h_n(\eta)$ as the metric perturbation evaluated at the time η during the era n. By demanding the continuity of the metric perturbation via

$$
\begin{aligned}
h_{n-1}(\eta_{n-1}) &= h_n(\eta_{n-1}) \,, \\
\partial_\eta h_{n-1}(\eta_{n-1}) &= \partial_\eta h_n(\eta_{n-1}) \,,
\end{aligned}
\tag{3.3.12}
$$

we can solve for A_{n+1} and B_{n+1} in terms of the values of the generated gravitational waves generated from the previous era. This can be understood as the generation of gravitational

waves which then freely propagate from the source under the expansion of the universe, while the source generates new gravitational waves as well.

By evaluating (3.3.11) and its derivative with respect to η with the rectangular method, we have

$$
\begin{aligned}
h_n(\eta_n) &\approx \frac{1}{a_n} \left(A_n(k) \cos[k\eta_n] + B_n(k) \sin[k\eta_n] \right) , \\
h'_n(\eta_n) &\approx -\frac{\alpha_n}{a_n^2} \left(A_n(k) \cos[k\eta_n] + B_n(k) \sin[k\eta_n] \right) \\
&\quad + \frac{k}{a_n} \left(B_n(k) \cos[k\eta_n] - A_n(k) \sin[k\eta_n] \right) \\
&\quad + \frac{16\pi}{M_{pl}^2} T_{ij}^{\mathrm{TT}}(\eta_n, \mathbf{k}) .
\end{aligned}
\tag{3.3.13}
$$

The solution of the continuity conditions in this approximation give

$$
\begin{aligned}
B_n &= \frac{a_{n-1}}{k \sec(k\eta_{n-1})} \left[h'_{n-1}(\eta_{n-1}) + \left(\frac{\alpha_n}{a_{n-1}} + k \tan(k\eta_{n-1}) \right) h_{n-1}(\eta_{n-1}) \right] , \\
A_n &= \frac{a_{n-1}}{\cos(k\eta_{n-1})} h_{n-1}(\eta_{n-1}) - B_n \tan(k\eta_{n-1}) .
\end{aligned}
\tag{3.3.14}
$$

With this method we can build up the solution of h'_n for each step throughout the program, for any scale factor evolution, while retaining the stability inherent in the numerical integration method. Since this method uses a Green's function approach to solving the field equations, while adapting the solution for differing regions of time it is dubbed the *adaptive Green's function approach* (AGF).

3.3.2 Example Use of Adaptive Green's Functions

To show the effectiveness of the AGF approach we will simulate the motivating problem for a pre-heating simulation with the quadratic inflaton potential (3.3.6), and will compare the results of the AGF method with that of the Green's function methods assuming scale factors of definite matter and radiation form. We will then compare the AGF method with a trapezoidal implicit numerical differential equation solver as a secondary check of the validity of the method.

The inherent scaling of the variables in LATTICEEASY for this particular potential enforces the condition $t_{pr} \propto t$. Since the source term is a function of the t_{pr} the AGF method must be re-derived in terms of the solution to the field equation in comoving time, which results in a similar set of equations.

We use a 3-dimensional lattice of size $N = 256$ points along each edge, along with a value $L_{pr} = 2.75$ which simulates a physical size of $L_{ph} = 2.8 \times 10^6 \, l_{pl}$. The final program time is taken to be $t_f = 800$ and is the time in which the spectrum no longer receives large additions to its spectrum. As was seen in Sec. 3.1.6 the use of FFT causes the simulations to have many operations to perform. In an attempt to decrease the computation time, we use parallel processing. specifically we used Open MP [191] to split the lattice in multiple segments to perform any operation on the lattice points in parallel so long as the operation did not depend on values being updated simultaneously in other lattice segments. Even with this added improvement and attempts at optimization of calculations to avoid unnecessary repetitive calculations, the AGF calculation took 7.96 days on a computer with specifications: Intel Xeon X5680 12 core CPU at 3.33Ghz and 96 GB of 1333MHz RAM. The simulations were computed with a metric perturbation step size of $\Delta t = 0.025$ and field step size of $dt = 0.005$ to satisfy Courant conditions. The length of the calculation can be attributed to the fact that in comoving time the AGF method becomes twice as complicated, as the complex nature of the constants A_n, B_n must be carefully handled. The method of Green's functions with the same parameters for matter and radiation dominated scale factor forms took 4.81 days and 2.67 days respectively. To make a comparison of the AGF with a numerical differential equation solving method we used an implicit trapezoidal method to solve the scaled equation

$$\mathcal{H}_{ij}^{\mathrm{TT}}(t, \mathbf{k}) = a^r h_{ij}^{\mathrm{TT}}(t, \mathbf{k}), \ s = 2r - 3 \ , \ r = 3/2 \ ,$$

$$\ddot{\mathcal{H}}_{ij}^{\mathrm{TT}}(t, \mathbf{k}) + \left[\frac{k^2}{a^{2(s+1)}} - r\frac{\ddot{a}}{a} + r(1-r)\left(\frac{\dot{a}}{a}\right)^2 \right] \mathcal{H}_{ij}^{\mathrm{TT}}(t, \mathbf{k}) = \frac{16\pi}{M_{pl}^2 a^{2(s+1)-r}} T_{ij}^{\mathrm{TT}}(t, \mathbf{k}) \ .$$

$$(3.3.15)$$

The scaling is necessary as many numerical methods are unstable without the scaling procedure. In fact, 3 other possible methods were attempted without scaling (Implicit Euler, 2nd order RK , and Leap-frog Method) all of which developed instabilities under the evolution of the system. After the simulation ends, we return to the metric perturbation via the relation

$$\dot{h}_{ij}^{\mathrm{TT}}(t, \mathbf{k}) = a^{-r}\dot{\mathcal{H}}_{ij}^{\mathrm{TT}}(t, \mathbf{k}) - ra^{-(r+1)}\dot{a}\mathcal{H}_{ij}^{\mathrm{TT}}(t, \mathbf{k}) \ . \tag{3.3.16}$$

The trapezoidal method with the same parameters took 3.04 days to complete. In Fig. 40 the comparison of the four different methods is shown to demonstrates that the AGF gives
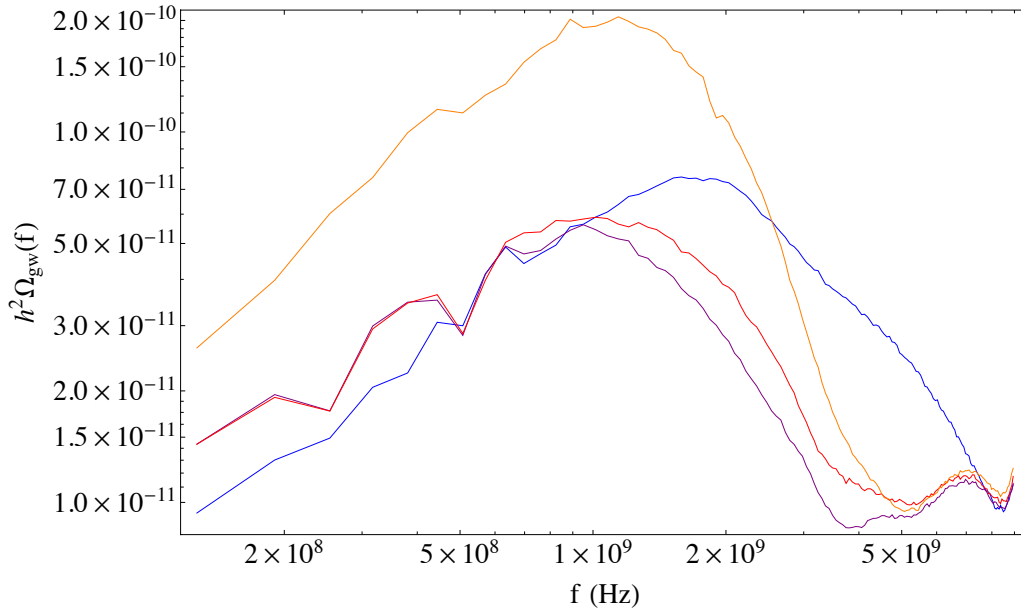
Figure 40 : The gravitational wave spectrum from pre-heating calculated from four different methods. The orange curve is calculated from numerical integration for the Green's function method assuming a radiation dominated scale factor. The Blue curve is calculated from numerical integration for the Green's function method assuming a matter dominated scale factor. The red curve is the spectrum calculated from the AGF method, and finally the purple curve is calculated from the trapezoidal method. It is easy to see that the AGF method and that of the trapezoidal method agree very well, while the matter and radiation methods tend to over estimate the spectrum.

the same value as the implicit trapezoidal method, while the radiation and matter scale factor Green's function methods over estimate the result.

The requirement for re-deriving the AGF equations for each unique potential because of the scaling of the time coordinate in LATTICEEASY is unfortunate as a general algorithm would be preferable. The problem lies in the fact that T_{ij}^{TT} is calculated internally as function of t_{pr}. In the metric perturbation equation $h_{ij}^{\text{TT}} \propto \int d\eta' \ldots T_{ij}^{\text{TT}}(t_{pr})$ we need to numerically integrate a function which we do not have the form of in the appropriate coordinate system. In order to circumvent this we can attempt to either transform $T_{ij}^{\text{TT}}(t_{pr}) \to T_{ij}^{\text{TT}}(\eta')$ at each step, which at this time has been left unexplored, or attempt to derive the AGF for $h_{ij}^{\text{TT}}(t_{pr})$ that is a function of program time t_{pr}. In program time, the field equations (3.1.15) take the form

$$\ddot{h}_{ij}^{\text{TT}}(t_{pr},\mathbf{k}) + (3+s)\frac{\dot{a}(t_{pr})}{a(t_{pr})}\dot{h}_{ij}^{\text{TT}}(t_{pr},\mathbf{k}) + \frac{k^2}{a(t_{pr})^{2(s+1)}B^2}h_{ij}^{\text{TT}}(t_{pr},\mathbf{k}) = \frac{16\pi}{M_{pl}^2}\frac{T_{ij}^{\text{TT}}(t_{pr},\mathbf{k})}{B^2 a(t_{pr})^{2s}} ,$$
$$(3.3.17)$$

where the over dot indicates a derivative with respect to t_{pr}. Taking the AGF approximation of

linear segments gives

$$
\begin{aligned}
\ddot{h}_{ij}^{\mathrm{TT}}(t_{pr}, \mathbf{k}) \quad &+ \frac{(3+s)\alpha_n}{(\alpha_n t_{pr} + \beta_n)} \dot{h}_{ij}^{\mathrm{TT}}(t_{pr}, \mathbf{k}) + \frac{k^2}{(\alpha_n t_{pr} + \beta_n)^{2(s+1)} B^2} h_{ij}^{\mathrm{TT}}(t_{pr}, \mathbf{k}) \\
&= \quad \frac{16\pi}{M_{pl}^2} \frac{T_{ij}^{\mathrm{TT}}(t_{pr}, \mathbf{k})}{B^2 a(t_{pr})^{2s}} \; .
\end{aligned}
\tag{3.3.18}
$$

Unfortunately there seems to be no known general solution to this equation due to the $a^{2(s+1)}$ factor . Even a change of variable of the form $h \rightarrow A a^r h$ does not help finding a general solution. Therefore a general AGF method at this point is not possible to derive by using LATTICEEASY, though the method of transforming the stress-energy tensor may result in some usefulness. The AGF method may still be viable if one uses a different method to solve the field equations rather than the method implemented in LATTICEEASY which forces $s = 2r - 3$, If another method is used to solve the field equations where we can set $s = -1$ permanently, then the AGF method should be able to be used with out problem. The AGF method can certainly be many times slower than an alternative method, it does offer a stable method of calculating stochastic gravitational wave backgrounds that other numerical methods cannot.

3.4 Summary of the Results and Conclusions

The study of stochastic backgrounds reveals that it is possible to extract information on the scales and types of processes we associate with originating from the post inflationary era. The sources studied here: pre-heating and global second order phase transitions generate energy in gravitational waves on the scales $h^2 \Omega_{gw} \simeq 10^{-11}$, 10^{-19}, respectively. For pre-heating and second order phase transitions, the frequency of gravitational waves ranges of order $f \simeq 10^9$, 10^6 Hz, respectively. In studying global second order phase transitions flat spectra are produced with a Hubble wall like feature. This Hubble-wall feature can be used to determine the scales at which the self ordering of the fields takes place, thus giving us knowledge of where we should expect new physics. It was also investigated how the use of Green's functions methods can hope to improve the task of computing such stochastic backgrounds. The use of numerical integration results in a more stable method of calculating the backgrounds, but it requires prior knowledge of the scale factor evolution. Even in a more accurate self consistent solution, where the scale factor evolution is numerically solved for, the scale factor will be

a series of linear segments due to the finite nature of numerical methods. Motivated by the finite nature of the numerical process, one may assume that the scale factor truly is a linear piece-wise function. This allows one to generate an algorithm for calculation of a stochastic background that makes use of the Green's functions and does not require prior knowledge of the form of the scale factor. We name this algorithm the adaptive Green's function method. This method generates a stochastic background for the troublesome process of a pre-heating with one additional scalar field and a quadratic inflaton potential, that agrees well with the result of the numerical differential equation solving methods. The use of LATTICEEASY is not straight forward when combined with the AGF method for general potentials. For this reason we are forced to abandon the use of LATTICEEASY's field evolution methods and require further study into methods more compatible with the AGF method.

Part III:

Dark Sector Physics

$$N_{\text{eff}} = 3.62 \pm 0.25 \; , \; \bar{\text{f}}\text{f} \to H^*/h^* \to \bar{w}w$$

Chapter 4

Dark Sector Physics

Beyond standard model (SM) physics models to be probed at the Large Hadron Collider (LHC) often include the concept of a hidden sector, consisting of $SU(3) \times SU(2) \times U(1)$ singlet fields. Independent of any model, the standard sector and the hidden sector are coupled by interactions of gauge-invariant operators which illuminate the path for exploring structures in the hidden sector by observing phenomena in the visible standard sector. A tantalizing realization of this idea is provided by the Higgs portal, which connects the Higgs fields in the two sectors by an elementary quartic interaction [192, 193, 194, 137, 195, 196, 197, 64]. Such a construct moves a precision study of the Higgs sector into a central position of new physics searches at the LHC. Likewise, astrophysical observations open the gates for complementary information to further test the Higgs portal hypothesis and to improve our understanding of the physics in the hidden sector.

4.1 Extra Relativistic Degrees of Freedom

Precision cosmology has been primarily driven by measurements of the CMB temperature anisotropies [198]. The anisotropies can be decomposed into spherical harmonics via

$$\delta T(\hat{n}) = T(\hat{n}) - T_{\mathrm{CMB}} = \sum_{l,m} a_{lm} Y_l^m(\hat{n}) \,, \tag{4.1.1}$$

where T_{CMB} is the average temperature across the sky observed today as $T_{\mathrm{CMB}} \simeq 2.7255(6)$ K [1], and $\hat{n}$ a unit vector towards some point in the sky parameterized by polar and azimuthal angle.

From this decomposition, the angular power spectrum may be constructed in terms of the variance, C_l, of the CMB fluctuations as a function of multipole number l given by

$$\langle \frac{\delta T}{T}(\hat{n}) \frac{\delta T}{T}(\hat{n}') \rangle_{\hat{n} \cdot \hat{n}' = \cos\theta} = \frac{1}{4\pi} \sum_{l=0}^{\infty} (2l+1) C_l P_l(\cos\theta), \tag{4.1.2}$$

where $P_l(x)$ are the Legendre polynomials, θ is the angle between two different directions in the sky $\hat{n}$, $\hat{n}'$, and $\langle \ldots \rangle$ denote an average across the entire sky. The most recent observational result for C_l is given in Fig. 9. The cause of the peaks and troughs of the CMB power spectrum is the compression due to gravitational potentials and resistance to this compression due to pressure gradients in the early universe. The angular scales, θ_s, of the acoustic peaks are highly sensitive to the angular size of the sound horizon (the distance pressure waves of speed c_s can travel in the early universe plasma since the big bang), and are given by $\theta_s = r_s/D$, where the distance to the last scattering surface of the CMB is $D = \int_{\text{last scattering}}^{\text{today}} dt/a(t)$. The angular size θ_s is very precisely determined by the data, however, D cannot be precisely determined because the density of the dark energy as a function of the scale factor is unknown. Therefore, another angular scale, which can be measured, must be used to eliminate D.

The diffusion angular scale can be used for this purpose. Peaks of temperature anisotropy on scales smaller than the photon diffusion length become Silk dampened, which is associated with random walks of photons on the small scale in the plasma. This blurs out (weakens) correlations amongst small scale anisotropies. Diffusion causes a drop in power toward high l and makes the CMB power spectrum sensitive to the angular scale of the diffusion length r_{d} given by $\theta_{\text{d}} = r_{\text{d}}/D$. For a random walk process, the diffusion distance increases as the square root of time, thus

$$t^{1/2} \propto a \rightarrow t \propto \frac{1}{H} \rightarrow r_d \propto H^{-1/2}. \tag{4.1.3}$$

Since the sound horizon $r_s = c_s\, t = c_s/2H$, we can form the relation

$$\frac{\theta_{\text{d}}}{\theta_{\text{s}}} = \frac{r_d}{r_s} \propto H^{1/2}, \tag{4.1.4}$$

where H is the Hubble parameter at the time the angular scales θ_{d} and θ_{s} froze into the CMB. At this time $t \simeq t_{\text{EQ}}$, from which we can assume the energy density is dominated equally by

ρ_{rad} and ρ_{mat}. The Friedmann equation then allows

$$H^{1/2} = \left(\frac{8\pi}{3M_{pl}^2}(\rho_{\text{rad}} + \rho_{\text{mat}}) \right)^{1/4} = \left(\frac{8\pi}{3M_{pl}^2}\frac{2\pi^2}{30}g_\rho(T_{\text{EQ}})T_{\text{EQ}}^4 \right)^{1/4},$$

$$g_\rho(T_{\text{EQ}}) = 2 + \frac{7}{8}\cdot 2\cdot N_{\text{eff}}\left(\frac{4}{11}\right)^{4/3} \qquad (4.1.5)$$

where g_ρ is the effective degrees of relativistic species at the time of the formation of the angular scales. The effective degrees from the concordance model of cosmology would suggest that g_ρ consists of a photon with 2 spin degeneracies, and $N_{\text{eff}} = 3$ left-handed neutrinos with 2 spin degeneracies each. The factor $7/8$ reflects the fermi statistical nature of the neutrinos and $(4/11)^{4/3}$ reflects the difference in temperatures of the neutrinos to the photon plasma and can be derived from conservation of entropy. The precise measurements of (4.1.4) along with (4.1.5) should give a consistency check of $N_{\text{eff}} \approx 3$ for the effective number of relativistic species normalized to that of a left-handed neutrino at the time t_{EQ}. Currently, high-resolution observations of the CMB temperature anisotropy are providing a precise measurement of the damping tail of CMB power spectrum, shedding light on N_{eff}, and over the past few years evidence has been accumulating for a possible excess on the number of "equivalent" light neutrino species above SM expectation, $N_{\text{eff}} \approx 3 + \Delta N > 3$. A selection of the most recent cosmological N_{eff} measurements and the 1σ confidence intervals from various combinations of models and data sets are shown in Fig. 41.

At the time of this writing, the Planck spacecraft has measured the CMB to an unprecedented precision [7]. One of the most striking results of the mission is that the best-fit Hubble constant has the value $h = 0.674 \pm 0.012$, with a dark energy density parameter $\Omega_\Lambda = 0.686 \pm 0.020$, and matter density parameter $\Omega_{\text{M}} = 0.307 \pm 0.019$. This result is at more than 2.3σ deviations of the value obtained with the Hubble Space Telescope, $h = 0.738 \pm 0.024$ [12]. The impact of the new h determination is particularly complex in the investigation of the effective number of relativistic degrees of freedom (as the times which the angular scales θ_s, θ_r change with h). From the CMB data alone, the Planck Collaboration reported $N_{\text{eff}} = 3.36 \pm 0.34$. Adding baryon acoustic oscillation (BAO) data yields $N_{\text{eff}} = 3.30 \pm 0.27$. Both of these values are consistent with the SM value of 3.046 (slightly larger than 3 as the neutrino decoupling from photons is not an abrupt process [199]). Adding the H_0 measurement to the CMB data
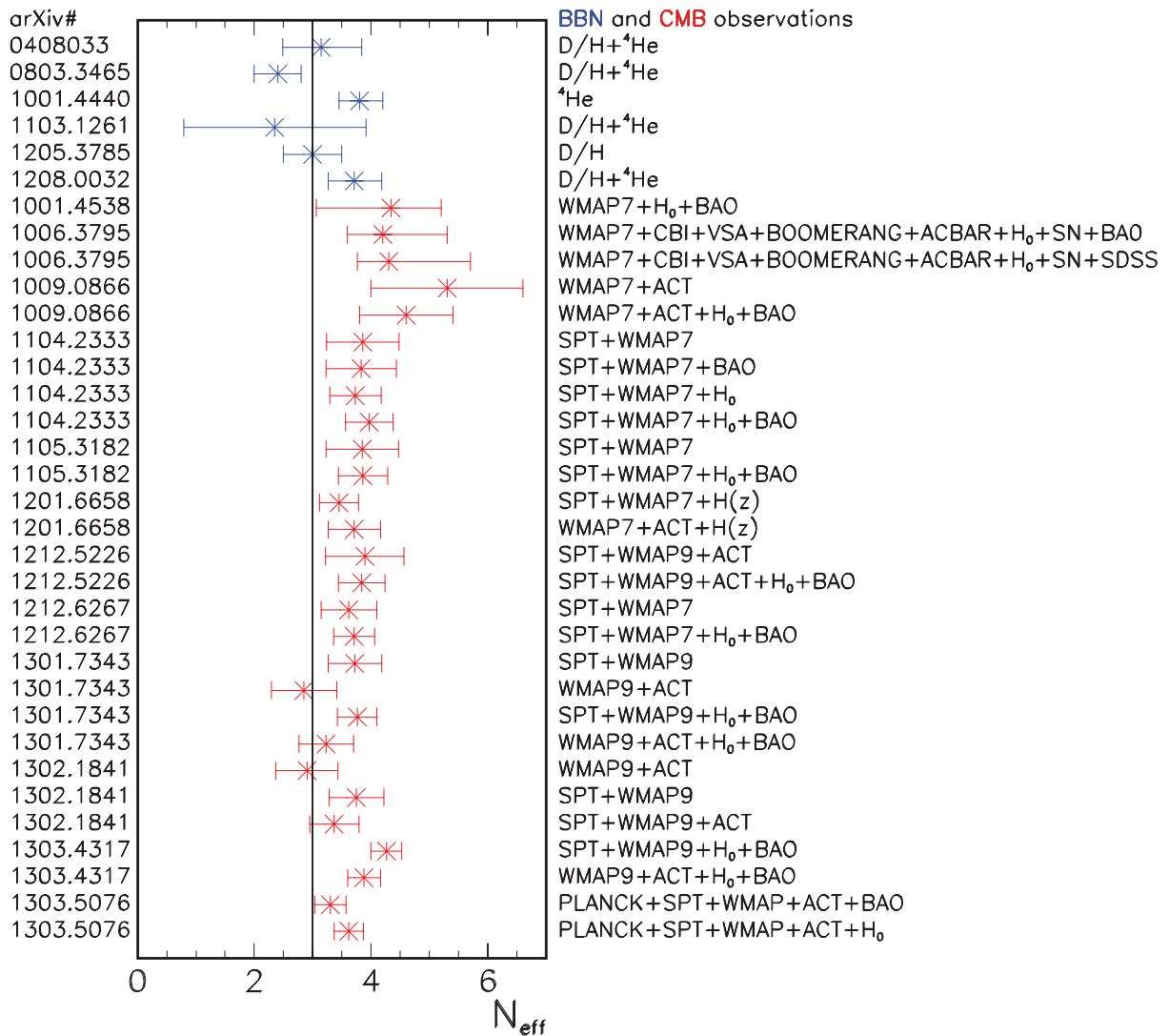
Figure 41 : A selection of the most recent cosmological N_{eff} measurements and the 1σ confidence intervals from various combinations of models and data sets. The first five measurements correspond to BBN observations [203, 204, 205, 206, 207, 208]. The other intervals result from a combination of the latest distance measurements from the baryon acoustic oscillations (BAO) in the distribution of galaxies [209], precise measurements of H_0 by the Hubble Space Telescope [12], and CMB data collected by the Wilkinson Microwave Anisotropy Probe (WMAP), the South Pole Telescope (SPT), the Atacama Cosmology Telescope (ACT), the Cosmic Background Imager (CBI), the Very Small Array (VSA), BOOMERANG, the Arcminute Cosmology Bolometer Array Receiver (ACBAR), and the Planck mission [210, 211, 212, 213, 214, 215, 216, 217, 218, 219, 220, 7]. Image from [221] .

gives $N_{\text{eff}} = 3.62 \pm 0.25$ and relieves the tension between the CMB data and H_0 at the expense of new neutrino-like physics (at around the 2.3σ level). In other words, it is possible to alleviate the tensions between the CMB, BAO, and H_0 data by invoking an increase in N_{eff}. It should be noted, however, that any preference for new physics comes almost entirely from the astrophysical data sets.

The CMB data can also be complemented by big bang nucleosynthesis (BBN) data, which offers the deepest reliable probe of the early universe, being based on well-understood SM physics [200, 201, 202]. The expansion rate of the universe at early times increases with the number of relativistic particle species in thermal equilibrium, and this in turn sets timescales for BBN. One can then use predictions of the abundances of light nuclei (D, ^{3}He, ^{4}He, ^{7}Li) synthesized at the end of the "first three minutes" to constrain the number of light species. For instance, in SM cosmology the neutron-proton interconversion rate $n \leftrightharpoons p$ drops out of equilibrium at $T \sim 1$ MeV. Nearly all the surviving neutrons when nucleosynthesis begins end up bound in the most stable light element ^{4}He. Therefore, the primordial mass fraction of ^{4}He, conventionally referred to as Y_{p}, can be estimated by the simple counting argument: $Y_{\text{p}} = 2n/p(1+n/p)^{-1}$. If $N_{\text{eff}} > 3$, the expansion rate at fixed temperature is increased and the neutron-proton ratio freezes out at a higher temperature, leaving more free neutrons, and thus a larger primordial abundance of ^{4}He. By measuring N_{eff} we may be able to detect some new physics BSM.

4.1.1   Adding New Species

To account for $N_{\text{eff}} > 3$, we must add some particles to the concordance model of cosmology that predicts the evolution of a spatially-flat expanding universe filled with dark energy (Λ), dark matter (DM), baryons (b), photons (γ), and and three flavors of left-handed (*i.e.* one chiral state ν_L) neutrinos (along with their right-handed, antineutrinos $\bar{\nu}_R$). The Hubble parameter H is determined by the total energy density

$$H^2(t) = \left(\frac{\dot{a}(t)}{a(t)}\right)^2 = \frac{8\pi}{3M_{pl}^2}\left[\rho_\Lambda(t) + \rho_{\text{DM}}(t) + \rho_{\text{b}}(t) + \rho_\gamma(t) + 3\rho_{\nu_L}(t)\right]. \tag{4.1.6}$$

The quantities of importance can be expressed in units of h to avoid uncertainties in H, *e.g.* $\Omega_M = \Omega_{\text{DM}} + \Omega_{\text{b}} \simeq [0.111(6) + 0.0226(6)]h^{-2}$ [1].

In the early universe, the energy density is dominated by radiation from extremely relativistic particles. When the temperature drops below the electron mass, the standard model of particle physics constrains the relativistic particle content to photons and neutrinos. As a result, the radiation energy density then is $\rho_{\mathrm{R}} = \rho_\gamma + 3\,\rho_{\nu_L}$. To accommodate new physics in the form of extra relativistic degrees of freedom, it is convenient to account for the extra contribution to the SM energy density by normalizing it to that of an "equivalent" neutrino species. The number of "equivalent" light neutrino species can then be expressed as

$$N_{\mathrm{eff}} \equiv \frac{\rho_{\mathrm{R}} - \rho_\gamma}{\rho_{\nu_L}} \,, \tag{4.1.7}$$

which quantifies the total "dark" relativistic energy density (including the three left-handed SM neutrinos) in units of the energy density of a single Weyl neutrino [222]. Any relativistic degree of freedom originating from BSM physics is then included in N_{eff}.

If neutrinos are fully decoupled prior to $e^\pm$ annihilation, they do not share in the energy transferred from annihilating $e^\pm$ pairs to photons. In this very good approximation, the photons are hotter than the neutrinos in the post-$e^\pm$ annihilation universe by a factor $T_\gamma / T_{\nu_L} = (11/4)^{1/3}$ and so

$$\rho_{\nu_L} = \frac{7}{8} \left(\frac{4}{11} \right)^{4/3} \rho_\gamma \,, \tag{4.1.8}$$

yielding

$$N_{\mathrm{eff}} = \frac{8}{7} \left(\frac{11}{4} \right)^{4/3} \frac{\rho_{\mathrm{R}} - \rho_\gamma}{\rho_\gamma} \,. \tag{4.1.9}$$

Since the temperature of the CMB is $T_{\mathrm{CMB}} \simeq 2.7255(6)$ K [1], we can determine the energy density in photons as measured today to be

$$\Omega_\gamma = \frac{\pi^2 (k_B T_{\mathrm{CMB}})^4}{15 \hbar^2 c} \frac{8\pi G}{3 \times 10^4 \,(\mathrm{km\ s^{-1}\ Mpc^{-1}})^2} \frac{1}{h^2} \simeq 2.471 \times 10^{-5} \, h^{-2} \,. \tag{4.1.10}$$

On the other hand, the energy density of the cosmic neutrino background (CνB) is found to be

$$\Omega_{\nu_L} = \frac{3\rho_{\nu_L}}{\rho_c} = \frac{\sum_i m_{\nu_i}}{93.14 \, h^2 \, \mathrm{eV}} \,, \tag{4.1.11}$$

where now we have included the fact that neutrinos are massive and $3\rho_{\nu_L} \approx \sum_i m_{\mu_i}$, indicating the neutrino species are non-relativistic today. We know from neutrino oscillation experiments that at least two of the neutrino states are non-relativistic today because both $(\Delta m_{31}^2)^{1/2} \simeq 0.05$ eV and $(\Delta m_{21}^2)^{1/2} \simeq 0.009$ eV [223] are larger than the temperature $T_{\mathrm{C}\nu\mathrm{B}} \simeq 1.96$ K $\simeq$

1.7×10^{-4} eV. If the third neutrino state is very light and still relativistic, its relative contribution to Ω_{ν_L} is negligible and (4.1.11) remains an excellent approximation of the total neutrino energy density.

One finds that Ω_{ν_L} is restricted to the approximate range $0.000637(0.001078) < \Omega_{\nu_L} h^2 < 0.0637$, and therefore, the radiation energy density today, $\Omega_{\rm rad} \approx \Omega_\gamma$, is completely negligible. It follows from (4.1.6) that new physics contributions to $\rho_{\rm rad}$ alter cosmology through the effect on the scale factor and since $\rho_{\rm rad}$ is negligible today, the early universe becomes the sole laboratory in which one can measure $N_{\rm eff}$.

Several explanations have been proposed to explain a possible ΔN excess. These include:
(i) models based on milli-weak interactions of right-handed partners of three Dirac neutrinos such as the SM^{++} model among others [224, 225, 226].
(ii) models based on active-sterile mixing of neutrinos in a heat bath [227, 228].
(iii) models in which the extra relativistic degrees of freedom are related to possible dark matter candidates produced via decay of heavy relics [229, 230, 231, 232, 233, 234, 235, 236].

An interesting consequence of such a non-thermal DM scenario is that if the lifetime of the decaying particle X is longer than about 10^3 seconds, the expansion history of the universe during the era of BBN will not have ΔN_X contributions to number of "equivalent" light neutrino species. Moreover, if there is a light DM particle that annihilates to photons after the ν_L have decoupled, the photons are heated beyond their usual heating from $e^\pm$ annihilation, reducing the late time ratio of neutrino and photon temperatures (and number densities), leading to $N_{\rm eff} < 3$ [237, 238, 239]. This opens the window for the addition of one or more ν_R neutrino flavors while remaining consistent with $N_{\rm eff} = 3$. A thorough study of the various possibilities listed above has been pursued in ref [240].

We will use the possibility that both right-handed Dirac neutrinos and non-thermal dark matter particles can contribute to the number of "equivalent" light neutrino species, *i.e.* $\Delta N = \Delta N_\nu + \Delta N_X$.

4.1.2 Non-Thermal Dark Matter

A series of independent observations involving galaxies and clusters of galaxies as well as the CMB seem to indicate that the most successful structure-formation models have been those

in which most of the mass in the universe comes in the form of cold dark matter (CDM), *i.e.* particles that were moving non-relativisticly in the early universe [241, 242, 243]. A mixture of about 80% CDM and 20% hot dark matter would only reproduce the data on nearby galaxies and clusters if the average density of matter in the universe were at or close to the critical density, $\Omega_{\mathrm{M}} = 1$. However, like all such critical-density models, cold plus hot dark matter models require that galaxies and clusters must have formed fairly recently, which disagrees with observations. The evidence increasingly favors ΛCDM models, in which CDM and baryons make up about a third of the critical density, with a cosmological constant or some other form of dark energy contributing the remainder. We now address adding non-thermal matter to the standard history of the universe.

Relativistic Constraint on X

First we will address adding in non-thermal dark matter to the concordance model of cosmology by assuming that the total DM in existence today is conceived of a small fraction of particles of type X, which have cooled due to expansion of the universe and are non-relativistic today, but were relativistic at the CMB epoch, and a larger fraction of type χ that constitute the primordial CDM, which is cold today and has always been cold. We assume the particles of type X are produced via decay of a heavy relic particle of type X', which allows the particle X to be relativistic at the CMB epoch so that these particles can add to N_{eff}. However, to do this we must ensure that during the CMB epoch the X particles are relativistic. We can set a limit on this by assuming the progenitor particle X' is initially non-relativistic and unstable with a lifetime τ. When X' decay to $X' \to X + \gamma$ (at present, we do not consider the more complicated scenario in which high energy neutrinos are among the decay products [244]) in the center-of-mass frame of X' (this should also be a good approximation of any frame, as we assume that X' is non-relativistic so its mass energy dominates) we have from the conservation of energy

$$M_{X'} = E_\tau + p_\tau = \sqrt{p_\tau^2 + M_X^2} + p_\tau \Rightarrow p_\tau = \frac{M_{X'}{}^2 - M_X^2}{2M_{X'}}, \qquad (4.1.12)$$

where $E_\tau = M_X \gamma_\tau$, p_τ is the energy and momentum, respectively, of the particle X at the time τ when X', with mass $M_{X'}$ decays. The Lorentz boost factor γ_τ at time τ can be expressed as

$$\gamma_\tau = \frac{E_\tau}{M_X} = \frac{M_{X'}}{2M_X} + \frac{M_X}{2M_{X'}}. \qquad (4.1.13)$$

As the universe expands and cools, the X momentum and thus energy will red shift, giving [49]

$$E^2(t) = p_\tau^2 \left(\frac{a(\tau)}{a(t)}\right)^2 + M_X^2 = M_X^2 \gamma(t)^2 \,. \tag{4.1.14}$$

Using the redshift, we can express the Lorentz boost factor γ as a function of time as

$$\gamma^2(t) = 1 + \left(\frac{p_\tau \, a(\tau)}{M_X \, a(t)}\right)^2 = 1 + \left(\frac{a(\tau)}{a(t)}\right)^2 \left(\frac{E_\tau^2 - M_X^2}{M_X^2}\right) = 1 + \left(\frac{a(\tau)}{a(t)}\right)^2 \left(\gamma_\tau^2 - 1\right) \,. \tag{4.1.15}$$

For $[a(t)/a(\tau)]^2 \left(\gamma_\tau^2 - 1\right) \ll 1$, the Lorentz boost factor takes the approximate form

$$\gamma(t) \approx 1 + \frac{1}{2}\left(\frac{a(\tau)}{a(t)}\right)^2 \left(\gamma_\tau^2 - 1\right) - \frac{1}{8}\left(\frac{a(\tau)}{a(t)}\right)^4 \left(\gamma_\tau^2 - 1\right)^2 + \cdots \,. \tag{4.1.16}$$

From this we can determine the non-relativistic limit by demanding the magnitude of the second term in the expansion to be greater than the third term to consider the X particle non-relativistic, which results in

$$\left(\frac{a(\tau)}{a(t)}\right)^2 \left(\gamma_\tau^2 - 1\right) < 4 \,. \tag{4.1.17}$$

Therefore, by this criteria the particle X is relativistic if $\gamma(t) > \sqrt{5}$, and so if this condition is met during the CMB epoch, then the X particles can contribute to N_{eff}.

Adding the Relativistic DM to ρ_{rad}

Continuing, we must add the proper dark matter evolution into the Friedmann equations, so we now examine the time dependence of the DM energy density (the components being the type χ and the type X). At any time after the decay of X' the total energy density in DM is

$$\rho_{\text{DM}}(t) = \rho_X(t) + \rho_\chi(t) = \gamma(t) M_X n_X(t) + \rho_\chi(t) \,, \tag{4.1.18}$$

where $\rho_X(t)$ is the energy density in the DM particles of type X (and may or may not be cold) and $\rho_\chi(t)$ is the energy density in the primordial CDM. The second equality comes from the fact that we take $n_X(t)$ to be the number density of particles of type X and each particle has energy $M_X \gamma(t)$.

Now, since ρ_χ is made entirely of dust-like (cold) particles, it becomes diluted as

$$\rho_\chi(t) = \frac{\rho_\chi(\text{today})}{a^3(t)} \,, \tag{4.1.19}$$

where we have used the convention $a(\text{today}) = 1$. Likewise, any number density of particles in an expanding universe will scale as $a^{-3}(t)$ and so we can write

$$\rho_X(t) = \frac{M_X n_X(\text{today})}{a^3(t)} \gamma(t). \tag{4.1.20}$$

At this point we make an assumption that the total dark matter today is entirely in the form of cold dark matter (CDM),

$$\rho_{\text{DM}}(\text{today}) = \rho_{\text{CDM}}(\text{today}), \tag{4.1.21}$$

and so the energy density for particles of type X make up some fraction f of the total CDM today

$$\rho_X(\text{today}) = f \rho_{\text{CDM}}(\text{today}). \tag{4.1.22}$$

By evaluating (4.1.20) at $t = \text{today}$ along with (4.1.22), and (4.1.20) we obtain

$$M_X \, n_X(\text{today}) \, \gamma(\text{today}) = f \, \rho_{\text{CDM}}(\text{today}) \rightarrow \rho_X(t) = f \, \frac{\rho_{\text{CDM}}(\text{today})}{a^3(t)} \, \gamma(t). \tag{4.1.23}$$

Giving the full expression for the dark matter as a function of time as

$$\rho_{\text{DM}}(t) = f \, \frac{\rho_{\text{CDM}}(\text{today})}{a^3(t)} \, \gamma(t) + \rho_\chi(t). \tag{4.1.24}$$

This can be reduced even further by evaluating (4.1.24) at $t = \text{today}$ to obtain

$$\rho_{\text{CDM}}(\text{today}) = f \, \rho_{\text{CDM}}(\text{today}) + \rho_\chi(\text{today}) \rightarrow \rho_\chi(\text{today}) = (1-f)\rho_{\text{CDM}}(\text{today}). \tag{4.1.25}$$

Finally, the dark matter content as a function of time is given as

$$\rho_{\text{DM}}(t) = f \frac{\rho_{\text{CDM}}(\text{today})}{a^3(t)} \gamma(t) + (1-f) \frac{\rho_{\text{CDM}}(\text{today})}{a^3(t)}. \tag{4.1.26}$$

Calculating N_{eff} from ρ_{rad}

Now that we can identify a potentially relativistic part of the DM energy density, we can add its contribution to ρ_{rad} at this point we can also add in the right chiral neutrino states and their assumed relativistic contribution to the energy density of the universe. Taking the dominate energy density component at t_{EQ} gives

$$\rho_{\text{R}}(t_{\text{EQ}}) = \rho_\gamma(t_{\text{EQ}}) + 3 \, \rho_{\nu_L}(t_{\text{EQ}}) + 3 \, \rho_{\nu_R}(t_{\text{EQ}}) + \rho_X(t_{\text{EQ}}) + \rho_{\text{s}}(t_{\text{EQ}}), \tag{4.1.27}$$

where $\rho_{\nu_R}(t_{\text{EQ}})$ is the energy density contained in one flavor of right chiral neutrinos and ρ_{s} is the energy density in sterile neutrinos. From Eq. (4.1.27) we can calculate the effective number of neutrinos at the time of radiation-matter equality from (4.1.7) as

$$N_{\text{eff}} = 3 + 3\frac{\rho_{\nu_R}}{\rho_{\nu_L}} + \frac{\rho_X}{\rho_{\nu_L}} + \frac{\rho_{\text{s}}}{\rho_{\nu_L}} = 3 + \Delta N = 3 + \Delta N_\nu + \Delta N_X \,, \tag{4.1.28}$$

where we take all the energy densities evaluated at t_{EQ} and, unless otherwise specified for this point, all the quantities are evaluated at t_{EQ}.

To separate the effect of the additional particles we use $\Delta N_\nu = (3 \, \rho_{\nu_R} + \rho_{\text{s}})/\rho_{\nu_L}$ and $\Delta N_X = \rho_X/\rho_{\nu_L}$ for the additional effect from right chiral neutrinos and X particles, respectively.

To remove ρ_{ν_L} from ΔN, we make use of (4.1.8) to obtain

$$\Delta N_X = \frac{8}{7}\left(\frac{11}{4}\right)^{4/3}\frac{\rho_X}{\rho_\gamma} \,, \tag{4.1.29}$$

where we have assumed that particles of type X decouple from the plasma prior to ν_L decoupling, conserving the ratio T_γ/T_{ν_L} from SM cosmology. Substituting (4.1.23) into (4.1.29) we finally obtain

$$\Delta N_X = \frac{8}{7}\left(\frac{11}{4}\right)^{4/3}\frac{\Omega_{\text{CDM}}}{\Omega_\gamma}\, a(t_{\text{EQ}})\, \gamma(t_{\text{EQ}})\, f \,, \tag{4.1.30}$$

where we used the standard relation $\rho_\gamma(t_{\text{EQ}}) = \rho_c\, \Omega_\gamma/a^4(t_{\text{EQ}})$. The contribution from the right chiral neutrinos will be left to the next subsection.

Scale Factor Consistant Reaction

Because we add new particles to the thermal history of the universe, the history of $a(t)$ and thus $\gamma(t)$ also changes. To make corrections to the scale factor, we will neglect the accelerating phase of the scale factor and assume that we are still in a matter dominated universe. The matter phase was preceded by the phase of radiation domination, and for our calculations we will make the approximation of instantaneous phase change. That is, we assume at the time of radiation-matter equality t_{EQ} the scale factor instantaneously changes from a radiation dominated phase to a matter dominated phase, with continuity ensured. With these considerations, the scale factor can be expressed in a piece-wise form as

$$a(t) = \begin{cases} \left(\frac{3}{2}\, H_0\, t\right)^{2/3} & \text{if } t > t_{\text{EQ}} \\ \left(\frac{3}{2}\, H_0\, t_{\text{EQ}}^{1/4}\right)^{2/3} t^{1/2} & \text{if } t_{\text{EQ}} > t \end{cases} \,, \tag{4.1.31}$$

where H_0 is the Hubble parameter today. Substituting (4.1.31) in (4.1.30), we obtain

$$\Delta N_X = \frac{8}{7} \left(\frac{11}{4}\right)^{4/3} \frac{\Omega_{\rm CDM}}{\Omega_\gamma} \gamma(t_{\rm EQ}) \left(\frac{300 \text{ km s}^{-1} \text{ Mpc}^{-1}}{2}\right)^{2/3} (ht_{\rm EQ})^{2/3} f. \qquad (4.1.32)$$

Next, we calculate the radiation-matter equality time t_{EQ}, *i.e.*, the time in which

$$\rho_{\rm M}(t_{EQ}) = \rho_{\rm R}(t_{EQ}) \Rightarrow \frac{\rho_{\rm R}}{\rho_{\rm M}} = \frac{\rho_\gamma(t_{\rm EQ}) \left\{1 + \frac{7}{8} \left(\frac{4}{11}\right)^{4/3} [3 + \Delta N_\nu + \Delta N_X(t_{\rm EQ})]\right\}}{\rho_M(t_{\rm EQ})} = 1\,, \qquad (4.1.33)$$

and by scaling the quantities with their respective powers of the scale factor, we arrive at

$$\frac{1}{a(t_{\rm EQ})} \frac{\Omega_\gamma}{\Omega_{\rm M}} \left[1 + \frac{7}{8} \left(\frac{4}{11}\right)^{4/3} (3 + \Delta N_\nu + \Delta N_X)\right] = 1\,. \qquad (4.1.34)$$

Using the piece-wise form of the scale factor from (4.1.31), we can determine the radiation-matter equality time as

$$ht_{EQ} = \frac{1}{150} \left(\frac{\Omega_\gamma}{\Omega_{\rm M}}\right)^{3/2} \left[1 + \frac{7}{8} \left(\frac{4}{11}\right)^{4/3} (3 + \Delta N_\nu + \Delta N_X)\right]^{3/2} \text{km}^{-1}\text{s Mpc}\,. \qquad (4.1.35)$$

Note that the combination $ht_{\rm EQ}$ is independent of h.

As a constancy check, we can set $\Delta N_\nu = \Delta N_X = 0$, make use of (4.1.10), and take the central values recently reported by the Planck Collaboration: $\Omega_{\rm M} \simeq 0.315$ and $h \simeq 0.673$ [7], which gives $t_{\rm EQ} = 1.19 \times 10^{12}$ s, which is in very good agreement with the concordance model of cosmology.

Proceeding to insert (4.1.35) into (4.1.32) then gives

$$\Delta N_X = \frac{8}{7} \left(\frac{11}{4}\right)^{4/3} \frac{\Omega_{\rm CDM}}{\Omega_{\rm M}} \gamma(t_{\rm EQ}) \left[1 + \frac{7}{8} \left(\frac{4}{11}\right)^{4/3} (3 + \Delta N_\nu + \Delta N_X)\right] f\,, \qquad (4.1.36)$$

for which we must solve for ΔN_X, however at this point it is worth exploring the quantity $\gamma(t_{\rm EQ})$ and its dependence on h. By taking $R = M_{X'}/M_X$ and τ occurring in the radiation dominated era, $\gamma(t)$ becomes

$$\gamma(t_{\rm EQ}) = \sqrt{1 + \left(\frac{\tau}{t_{\rm EQ}}\right) \frac{(R^2 - 1)^2}{4R^2}}\,, \qquad (4.1.37)$$

which does have some h dependence, $t_{\rm EQ} \propto h^{-1}$. To make our analysis completely independent of h (which we have seen has large systematic uncertainties), we can rewrite the decay time as a fraction of the time of the radiation matter equality, $\mathcal{T} = \tau/t_{\rm EQ}$, *e.g.*, for $\mathcal{T} = 0.1$, the X

particle is produced at a time which is 1% of t_{EQ}. This new variable allows expressing (4.1.36) independently of h:

$$\Delta N_X = \frac{\Omega_{\text{CDM}}}{\Omega_{\text{M}}} \sqrt{1 + \mathcal{T}\frac{(R^2 - 1)^2}{4R^2}} \left[\frac{8}{7}\left(\frac{11}{4}\right)^{4/3} + 3 + \Delta N_\nu + \Delta N_X\right] f. \qquad (4.1.38)$$

Note that (4.1.38) scales with the ratio $\Omega_{\text{CDM}}/\Omega_{\text{M}} \simeq 1.19$, which does not depend on the Hubble parameter. Solving for ΔN_X gives

$$\Delta N_X = \left[\frac{8}{7}\left(\frac{11}{4}\right)^{4/3} + 3 + \Delta N_\nu\right] \mathscr{Y} \left(\frac{\Omega_{\text{M}}}{\Omega_{\text{CDM}} f} - \mathscr{Y}\right)^{-1}, \qquad (4.1.39)$$

where

$$\mathscr{Y} = \sqrt{1 + \mathcal{T}\frac{(R^2 - 1)^2}{4R^2}} . \qquad (4.1.40)$$

Note that (4.1.39) develops a pole if

$$\rho_{\text{M}}(t_{\text{EQ}}) = \frac{\rho_{\text{M}}(\text{today})}{a^3(t_{\text{EQ}})} = \frac{\rho_{\text{CDM}}(\text{today})}{a^3(t_{\text{EQ}})}\gamma(t_{\text{EQ}})f = \rho_X(t_{\text{EQ}}), \qquad (4.1.41)$$

which implies $\rho_{\text{R}}(t_{\text{EQ}}) = \rho_X(t_{\text{EQ}})$. This saturates the regime for validity of (4.1.36).

Results

In Fig. 4.1.2 we can see contours of constant ΔN_X in the R *vs.* $\mathcal{T}$ plane, for the case in which $\Delta N_\nu = 0$. As expected, to produce a given ΔN_X contribution, the required ratio of masses diminishes with increasing lifetime. We can see that, for $h = 0.647$, a fraction of X particles larger than 3.8% yields a contribution to N_{eff} that is outside the 1σ region allowed by Planck data. The preceding discussion can be easily generalized to more complex models endowed with a dynamical dark sector. In a fashion similar to [245], we assume there are n different decay possibilities/channels for DM particles of the type $X'_j \to X_i + \gamma$. We further assume that each decay process occurs instantaneously at a time τ_i and that of the total fraction of dark matter particles coming from each decay process is f_i. For N particle species, this gives the relation

$$f\rho_{\text{CDM}}(\text{today}) = \sum_{i=1}^{N} \rho_{X_i}(\text{today}) \Rightarrow \frac{\rho_{X_i}(\text{today})}{\rho_{\text{CDM}}(\text{today})} = f_i, \qquad (4.1.42)$$

with $\sum_{i=1}^{N} f_i = f$. Provided each particle in the ensemble X_i meets the criteria for being relativistic, it will contribute

$$\Delta N_{X_i} = \frac{\rho_{X_i}}{\rho_{\nu_L}} = \frac{8}{7}\left(\frac{11}{4}\right)^{4/3} \frac{\Omega_{\text{CDM}}}{\Omega_\gamma} a(t_{\text{EQ}}) \gamma_i f_i, \qquad (4.1.43)$$
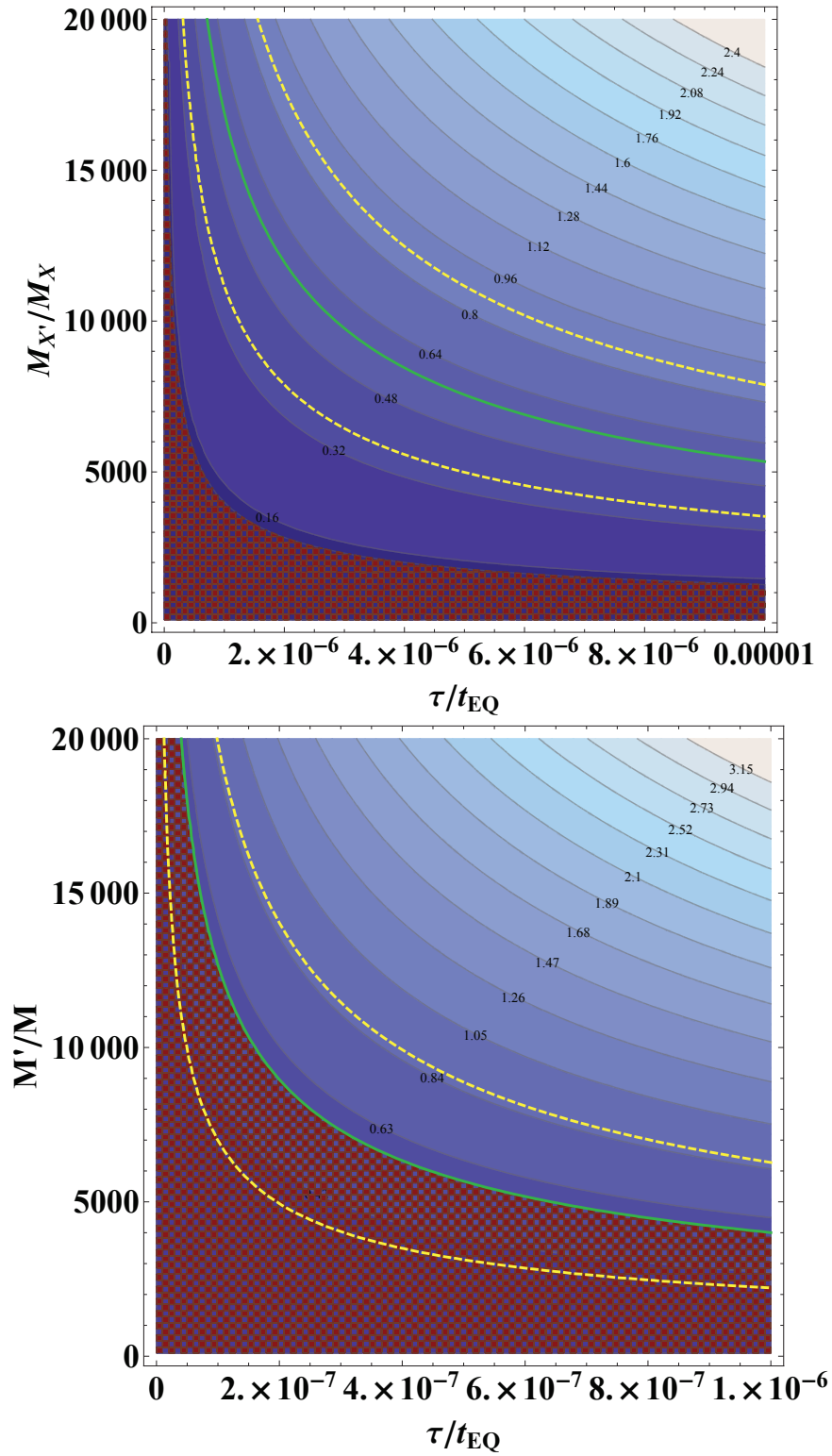
Figure 42 : Contours of constant ΔN in the R *vs.* $\mathcal{T}$ plane, with $f = 1\%$ (top) and $f = 3.8\%$ (bottom), for the case in which $\Delta N_\nu = 0$. The (green) solid line indicates the upper limit on ΔN (with $h \simeq 0.674$) as reported by the Planck Collaboration. The band between the dashed (yellow) lines corresponds to the allowed ΔN region reported by Planck Collaboration using $h \simeq 0.738$. The crosshatched area pertains to the region of the parameter space for which the X particles are not relativistic at the CMB epoch, and should therefore not be taken under consideration.

where ρ_{X_i} and ρ_{ν_L} are again taken at the time of matter-radiation equality, and $\gamma_i(t)$ is the Lorentz factor of each particle X_i. As stated earlier, each particle may decay from some particle X_j' at a time τ_i such that each γ_i is given by

$$\gamma_i = \sqrt{1 + \mathcal{T}_i \frac{(R_i^2 - 1)}{4R_i^2}}, \tag{4.1.44}$$

where $\mathcal{T}_i = \tau_i/t_{\text{EQ}}$ and $R_i = M_j'/M_{X_i}$. Once more we assume that the decays occur prior to the time of matter-radiation equality. We denote the total X_i contribution to the effective number of neutrinos by $\Delta N_{\Sigma X} = \sum_{i=1}^{N} \Delta N_{X_i}$, so that $\Delta N = \Delta N_\nu + \Delta N_{\Sigma X}$, with

$$\Delta N_{X_i} = \frac{8}{7} \left(\frac{11}{4}\right)^{4/3} \frac{\Omega_{\text{CDM}}}{\Omega_\gamma} \, \gamma_i(t_{\text{EQ}}) \left(\frac{300 \text{ km s}^{-1} \text{ Mpc}^{-1}}{2}\right)^{2/3} (ht_{\text{EQ}})^{2/3} \, f_i \,. \tag{4.1.45}$$

Duplicating the procedure for a single X particle, with the change of $\Delta N_X \rightarrow \Delta N_{\Sigma X}$ we obtain

$$ht_{\text{EQ}} = \frac{1}{150} \left(\frac{\Omega_\gamma}{\Omega_M}\right)^{3/2} \left[1 + \frac{7}{8} \left(\frac{4}{11}\right)^{4/3} (3 + \Delta N_\nu + \Delta N_{\Sigma X})\right]. \tag{4.1.46}$$

All in all the total contribution to the number of "equivalent" light neutrino species is

$$\Delta N_{\Sigma X} = \left[\frac{8}{7} \left(\frac{11}{4}\right)^{4/3} + 3 + \Delta N_\nu\right] \left(\sum_{i=1}^{N} f_i \gamma_i\right) \left(\frac{\Omega_M}{\Omega_{\text{CDM}}} - \sum_{i=1}^{N} f_i \gamma_i\right)^{-1}. \tag{4.1.47}$$

It should be noted that the parent particle X_j' can be the same for multiple particles X_i, as is the case for multiple decay channels.

4.1.3 Right-Handed Neutrinos with Milli-Weak Interactions

In addition to the $(2.984 \pm 0.009)\nu_L$ species measured from the width for invisible decays of the Z_0 boson [246], there could also exist ν_R states that are sterile, *i.e.* singlets of the SM gauge group, and therefore insensitive to weak interactions. Such sterile states are predicted in models involving additional TeV-scale Z' gauge bosons, which allow for milli-weak interactions of the ν_R. If the ν_R carry a non-zero $U(1)'$ charge, then the $U(1)'$ symmetry forbids them from obtaining a Majorana mass much larger than the $U(1)'$-breaking scale. Therefore, in most of these models there are no Majorana mass terms and the ν_R states, which are almost massless, become the Dirac partners of the SM ν_L species.

Here we will add in the right-handed neutrino species to study the expected increase in N_{eff} due to the presence of such light Dirac neutrinos with ongoing searches of Z' gauge bosons at

the LHC. A critical input for such an analysis is the relation between the relativistic degrees of freedom (r.d.o.f.) and the temperature of the primordial plasma. This relation is complicated because the temperature which is of interest for right-handed neutrino decoupling from the heat bath may lay in the vicinity of the quark-hadron cross-over transition, which offers problems as the exact form of $g_S(T)$ is in a non-perturbative regime of QCD and thus requires high statistics lattice simulations of a QCD (LQCD) plasma in this phase.

We begin by first establishing ΔN_ν as a function of the ν_R decoupling temperature. By taking into account the conservation of entropy of the rest of the plasma between the temperature from ν_R decoupling, $T_{\nu_R}^{\text{dec}}$, and the ν_L decoupling temperature, $T_{\nu_L}^{\text{dec}}$, we can arrive at an equation for ΔN_ν. First we express the total entropy of the universe at the ν_R decoupling as

$$S(T_{\nu_R}^{\text{dec}}) \propto a(t_{\nu_R})^3 g_S(T_{\nu_R}^{\text{dec}}) \left(T_{\nu_R}^{\text{dec}}\right)^3 = \text{const} , \qquad (4.1.48)$$

where t_{ν_R} is the ν_R decoupling time after which particles may annihilate and thus add energy to the photon matter plasma, which corresponds to an increase in temperature and change in $g_S(T)$. The particles that decoupled have their thermal distribution temperature simply scale with a^{-1}; because of this, after ν_R decoupling the effective entropy density is

$$a(t_{\nu_R})^3 g_S(T_{\nu_R}^{\text{dec}}) \left(T_{\nu_R}^{\text{dec}}\right)^3 = a(t)^3 g_S(T)T^3 + a(t)^3 g_{S,\nu_R} \left(\frac{T_{\nu_R}^{\text{dec}} a(t_{\nu_R})}{a(t)}\right)^3 , \qquad (4.1.49)$$

where g_{S,ν_R} is the entropy degrees of freedom from ν_R, which is now freely streaming. Simplifying this expression results in

$$\left(\frac{a(t_{\nu_R})T_{\nu_R}^{\text{dec}}}{a(t)}\right)^3 \left(g_S(T_{\nu_R}^{\text{dec}}) - g_{S,\nu_R}\right) = g_S(T)T^3 , \qquad (4.1.50)$$

but since $T_{\nu_R}(t) = a(t_{\nu_R})T_{\nu_R}^{\text{dec}}/a(t)$ for $t > t_{\nu_R}$, this expression simplifies to

$$\left(g_S(T_{\nu_R}^{\text{dec}}) - g_{S,\nu_R}\right) T_{\nu_R}(t)^3 = g_S(T)T^3. \qquad (4.1.51)$$

By redefining $g_S(T^{\text{dec}})$ at decoupling temperatures to not include the particles which are decoupling, we can drop the $-g_{S,\nu_R}$ from above. With Eq. (4.1.51), we can construct the contribution to N_{eff} by Eq. (4.1.28) where we have the relation

$$\Delta N_\nu = 3\frac{\rho_{\nu_R}}{\rho_{\nu_L}} = 3\left(\frac{T_{\nu_R}(t_{\text{EQ}})}{T_{\nu_L}(t_{\text{EQ}})}\right)^4 = 3\left(\frac{g_S(T_{\nu_L}^{\text{dec}})}{g_S(T_{\nu_R}^{\text{dec}})}\right)^{4/3} , \qquad (4.1.52)$$

where standard cosmology gives $g_s(T_{\nu_L}^{\text{dec}}) = 43/4$ [49]. For the particle content of the SM, there is a maximum of $g_s(T_{\nu_R}^{\text{dec}}) = 427/4$ (with $T_{\nu_R}^{\text{dec}} > m_{\text{top}}$), which corresponds to a minimum value of $\Delta N_\nu = 0.14$.

If $T_{\nu_R}^{\text{dec}}$ occurs during the QCD phase transition, then the value of $g_S(T_{\nu_L}^{\text{dec}})$ is very complicated as the degrees of freedom are undergoing rapid changes. At energies above the deconfinement transition towards the quark gluon plasma, quarks and gluons are the relevant degrees of freedom for the QCD sector, such that the total number of SM r.d.o.f. consisting of $\left(\gamma,\ 8G,\ 3\nu_L,\ e_{L,R},\ \mu_{L,R},\ u_{L,R}^{r,g,b}, d_{L,R}^{r,g,b}, s_{L,R}^{r,g,b}\right)$

$$g_S = 2(1+8) + \frac{7}{8}\left[3\cdot 2 + 2\cdot 2 + 2\cdot 2 + 3(2\cdot 2 + 2\cdot 2 + 2\cdot 2)\right] = 61.75\ . \qquad (4.1.53)$$

As the universe cools down, the SM plasma transitions to a regime where mesons and baryons are the pertinent degrees of freedom confining the quarks and gluons within. Precisely, the relevant hadrons present in this energy regime are pions and charged kaons, such that $g_S = 19.25$ [240]. This significant reduction in the degrees of freedom results from the rapid annihilation or decay of any more massive hadrons which may have formed during the transition. The quark-hadron crossover transition therefore corresponds to a large redistribution of entropy into the remaining degrees of freedom. We express the effective number of interacting r.d.o.f. in the plasma at temperature T by

$$g_S(T) \simeq r(T)\left(\sum_{\text{bosons}} g_{\text{b}} + \frac{7}{8}\sum_{\text{fermions}} g_{\text{f}}\right), \qquad (4.1.54)$$

with $g_{\text{b}} = 2$ for each real vector field and $g_{\text{f}} = 2$ for each spin-$\frac{1}{2}$ Weyl field. The coefficient $r(T)$ is unity for the lepton and photon contributions and is the ratio $s(T)/s_{\text{SB}}$ for the quark-gluon plasma, where $s(T)$ is the actual entropy and s_{SB} is the ideal Stefan-Bolzmann entropy. We must now examine LQCD simulations and radiative correction analyses to obtain the function $r(T)$.

QCD Confinement Phase Transition Fitting

Two complementary approaches that describe high temperature QCD phenomena result in similar expressions for $r(T)$. We will compare their predictions during the de-confinement transition.

The first approach relies on next-to-leading order (NLO) radiative corrections to the non-interacting Stefan-Boltzmann law within the $\overline{\text{MS}}$ scheme [247]. The second approach is based on high statistics lattice simulations of the QCD plasma during the changeover phase [248]. In either case, all thermodynamic quantities can be obtained from the QCD partition function $Z_p(T, V)$. The need for LQCD comes from the fact that perturbative calculations are no longer valid as the strong coupling becomes large at these temperatures. In LQCD the basic outline is to calculate Z_p via the path integration method we saw in Sec. 3.2.1 on a lattice. The idea is that from the form

$$Z_p \propto \int \mathcal{D}\phi \; e^{-S_E[\phi]} \;, \tag{4.1.55}$$

a field configuration ϕ can be discretized on a lattice (just like in Sec. 3.1.6), and expectation values $\langle \phi(x_1) \dots \phi(x_n) \rangle$ can be calculated by treating $\exp(-S_E[\phi])$ as the relative probability of a field configuration with many degrees of freedom. The many degrees of freedom offers a computational challenge that is typically solved by a Markov-Chain Monte Carlo (MCMC) method [249]. Lattice field theories are further complicated by the use of Weyl fields and gauge symmetry on a lattice, which is the subject of Wilson loops [24] and a discrete lattice spacing RG analysis. However the partition function is calculated it can be used for various quantities. For instance, its logarithm defines the free energy density,

$$\mathcal{F} = -\frac{T}{V} \ln \; Z_p \;. \tag{4.1.56}$$

The energy density and pressure are derivatives of $\ln \; Z_p$ with respect to T and V, respectively,

$$\rho = \frac{T^2}{V} \; \frac{\partial \ln \; Z_p}{\partial T} \qquad \text{and} \qquad p = T \; \frac{\partial \ln \; Z_p}{\partial V} \;. \tag{4.1.57}$$

However, for sufficiently large volumes, T is the only intensive parameter controlling the thermodynamics and the pressure can be directly derived from the free energy density,

$$p = -\mathcal{F} \;. \tag{4.1.58}$$

To obtain the entropy density, recall that from (1.2.7) we can express the entropy density in an isotropic, homogenous universe as

$$s = \rho + p = T \; \frac{\partial p}{\partial T}. \tag{4.1.59}$$

In practice, the quantity most convenient to calculate on the lattice is the trace anomaly in units of the fourth power of the temperature $\Theta^{\mu\mu}/T^4$, where the QCD trace anomaly is given by

$$\Theta^{\mu\mu} \equiv \rho - 3p = T^5 \frac{\partial(p/T^4)}{\partial T}\,. \tag{4.1.60}$$

Using (4.1.60), the pressure is obtained by integrating $\Theta^{\mu\mu}/T^5$ over the temperature

$$\frac{p(T)}{T^4} - \frac{p(T_0)}{T_0^4} = \int_{T_0}^{T} dT' \frac{\Theta^{\mu\mu}(T')}{T'^5}\,, \tag{4.1.61}$$

where T_0 is an arbitrary temperature that is generally chosen in the low temperature regime where the pressure and other thermodynamical quantities are suppressed exponentially by Boltzmann factors associated with the lightest hadronic states; the convenient extrapolation $T_0 \to 0$ yields $p/T_0^4 \to 0$. After p/T^4 is obtained, we can calculate the entropy density. The increasing entropy curve from LQCD can be fit by

$$\frac{s}{T^3} \simeq 18.62 \left(\frac{175.41}{T_{\mathrm{MeV}} - 148.46}\right)^2 \frac{e^{175.41/(T_{\mathrm{MeV}} - 148.46)}}{\left[e^{175.41/(T_{\mathrm{MeV}} - 148.46)} - 1\right]^2} + \frac{42.82}{\sqrt{392\,\pi}}\, e^{-\frac{(T_{\mathrm{MeV}} - 169.88)^2}{392}}\,, \tag{4.1.62}$$

where T_{MeV} is the temperature in units of MeV and T_{MeV} satisfies $150\,\mathrm{MeV} < T_{\mathrm{MeV}} < 1\,\mathrm{GeV}$. We compare the rise of $g_S(T)$ as given in (4.1.63) with the LQCD result shown in Fig. 43, as well as a comparison of $g_S(T)$ as obtained using LQCD and the NLO approach is shown. Finally, we obtain the relevant degrees of entropy as

$$g_S(T) \simeq 47.5\, r(T) + 19.25\,, \tag{4.1.63}$$

which reflects the particle content in (4.1.53) as well as 3 species of right-handed neutrinos along with $r(T)$ determined from (4.1.62).

If relativistic particles are present that have decoupled from the photons, it is necessary to distinguish between two kinds of r.d.o.f.: those associated with the total energy density g_ρ, and those associated with the total entropy density g_S. Since the quark-gluon energy density in the plasma has a similar T dependence to that of the entropy (see Fig. 7 in [248]), we take $g_\rho(T) \approx g_S(T)$.

Calculating the ν_R Decoupling Temperature

We can solve for the right-handed neutrino decoupling temperature by reason that the right-handed neutrino decouples from the plasma when its mean free path becomes greater than the
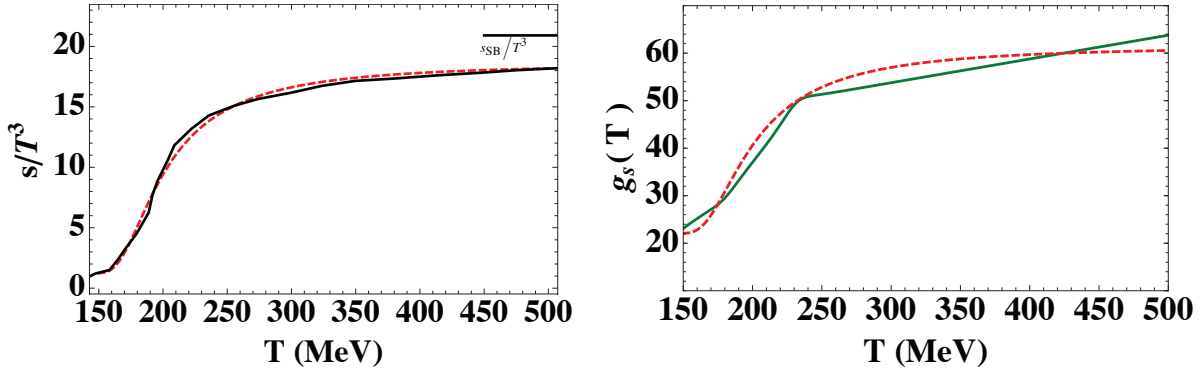
Figure 43 : Left: The (black) solid line is the entropy density as obtained from high statistics lattice simulations [248] (we used the results obtained using the p4-action [250]). The (red) dashed line is the fit given in Eq. (4.1.62). Right: The effective number of interacting relativistic degrees of freedom, g_S, as a function of the temperature for $150 \text{ MeV} \leq T \leq 500 \text{ MeV}$. The solid line is obtained from the NLO correction result given in [251] (adapted from [247]). The red dashed curve is the result from the fit of LQCD calculations.

Hubble radius at that time. To do this, we first calculate the ν_R interaction rate given by

$$\Gamma(T) = \mathcal{K} \frac{1}{8} \left(\frac{\bar{g}}{M_{Z'}} \right)^4 T^5 \sum_{i=1}^{6} \mathcal{N}_i \,, \tag{4.1.64}$$

where $\mathcal{N}_i$ is the number of chiral states that are available to scatter with ν_R, with groupings as given in Table 1, such that $\mathcal{N}_1$ is the number of chiral states in u_R ($\sum_{i=1}^{6} = 28$). The effective coupling $\bar{g}$ is

$$\bar{g} \equiv \left(\frac{\sum_{i=1}^{6} \mathcal{N}_i g_i^2 g_6^2}{\sum_{i=i}^{6} \mathcal{N}_i} \right)^{1/4} \,, \tag{4.1.65}$$

with g_i the chiral couplings of the Z' gauge boson for species i, and the constant $\mathcal{K} = 0.5$ (2.5) for annihilation (annihilation + scattering) [224].

To illustrate, we calculate $\bar{g}$ for two candidate models. The first is a set of variations on D-brane constructions which do not have coupling constant unification. The second are two $U(1)$ models, $U(1)_\psi$ and $U(1)_\chi$, which are embedded in a grand unified exceptional E_6 group, with breaking pattern

$$E_6 \to SO(10) \times U(1)_\psi \to SU(5) \times U(1)_\psi \times U(1)_\chi \,. \tag{4.1.66}$$

The latter two are interesting because they have long been suspected to contribute to N_{eff} [254, 255, 256, 257] and provide a test basis for Z' searches at ATLAS [258] and CMS [110, 259]. For each of the E_6 models we may write g_i in (4.1.65) as $g_i = g_0 Q_i$, where in conformity with

Table 7 : The charges of the $U(1)_\chi$ and the $U(1)_\psi$.

bin	Fields	Q_χ	Q_ψ
1	U_r	$1/(2\sqrt{10})$	$-1/(2\sqrt{6})$
2	D_R	$-3/(2\sqrt{10})$	$-1/(2\sqrt{6})$
3	L_L	$3/(2\sqrt{10})$	$1/(2\sqrt{6})$
4	E_R	$1/(2\sqrt{10})$	$-1/(2\sqrt{6})$
5	Q_L	$-1/(2\sqrt{10})$	$1/(2\sqrt{6})$
6	N_R	$5/(2\sqrt{10})$	$-1/(2\sqrt{6})$

grand unification we follow [257] and choose

$$g_0 = \sqrt{\frac{5}{3}}\, g_2\, \tan\theta_W \sim 0.46\,, \qquad (4.1.67)$$

with g_2 the $SU(2)_L$ coupling. The charges Q_i for the different fermions in this model are given in Table 7 [257]. In the D-brane construction of the SM^{++} outlined in Sec. 2.1 or any D-brane construct the Weyl fermions live at the brane intersections of a particular 4-stack quiver configuration: $U(3)_C \times SU(2)_L \times U(1)_{I_R} \times U(1)_L$ [260]. We consider here two possibilities in which the Z'' gauge boson of the SM^{++} is taken at TeV scales and has branching ratio that is mostly into I_R or mostly $B - L$ (the specific definition is found in the section 4.2.2). The chiral couplings (g_i) of these gauge bosons are given in Tables 2 and 3 [141, 88].

With (4.1.64) we can determine $T_{\nu_R}^{\rm dec}$ via

$$\Gamma(T_{\nu_R}^{\rm dec}) = H(T_{\nu_R}^{\rm dec})\,, \qquad (4.1.68)$$

where H can be retrieved from the Friedmann equations in the era of radiation dominance

$$H(T_{\nu_R}^{\rm dec}) = 1.66\sqrt{g_\rho(T_{\nu_L}^{\rm dec})}\,\frac{(T_{\nu_R}^{\rm dec})^2}{M_{\rm Pl}}\,\left(\frac{3}{\Delta N_\nu}\right)^{3/8}\,, \qquad (4.1.69)$$

where above we have used (4.1.52) to replace $g_\rho(T_{\nu_R}^{\rm dec})$ for $g_\rho(T_{\nu_L}^{\rm dec})$. Solving (4.1.68) results in

$$
\begin{aligned}
\Delta N_\nu &= 3\left(\frac{13.28\,\sqrt{g(T_{\nu_L}^{\rm dec})}\,M_{Z''}^4}{M_{\rm Pl}\,\mathcal{K}\,(T_{\nu_R}^{\rm dec})^3\,\bar{g}^4\,\sum_{i=1}^{6}\mathcal{N}_i}\right)^{8/3} \\
&= \left[\frac{5.39\times10^{-6}}{\mathcal{K}\,\sum_{i=1}^{6}\mathcal{N}_i}\left(\frac{M_{Z''}/{\rm TeV}}{\bar{g}}\right)^4\frac{1}{(T_{\nu_R}/{\rm GeV})^3}\right]^{8/3}\,. \qquad (4.1.70)
\end{aligned}
$$

In Fig. 44 we show the region of the parameter space allowed from the decoupling Eq. (4.1.70) to accommodate contributions of ΔN_ν within the 1σ region of Planck data.
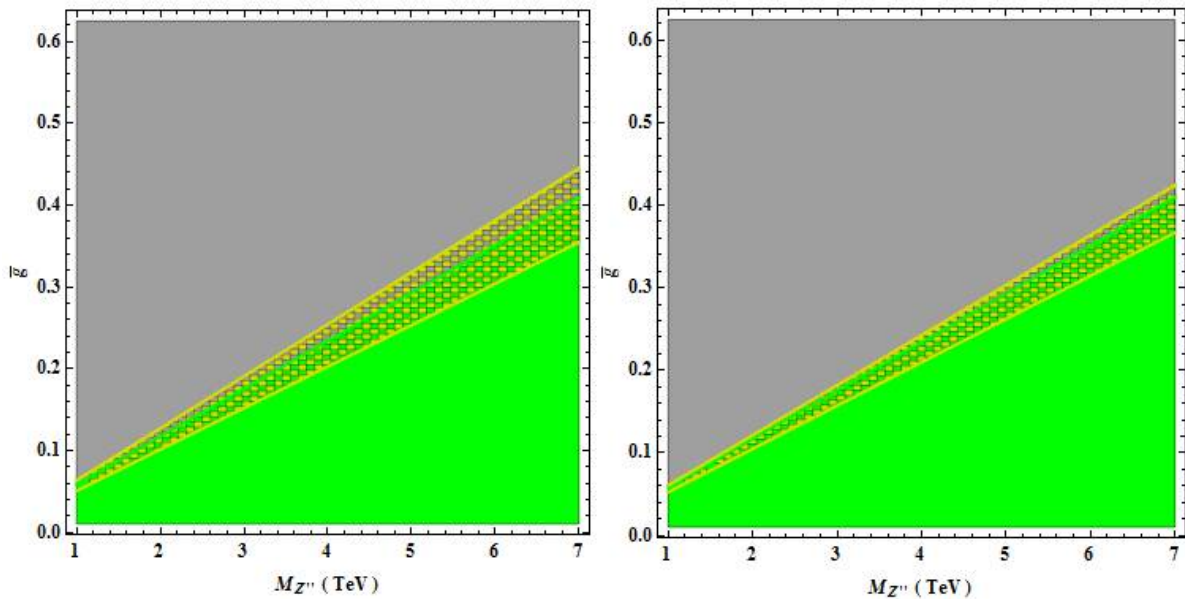
Figure 44 : The green area shows the region allowed from decoupling requirements to accommodate $3.03 < N_{\rm eff} < 3.57$, and the yellow cross-hatched area shows the region allowed from decoupling requirements to accommodate $3.37 < \Delta N_{\rm eff} < 3.87$, respectively. We have taken $\mathcal{K} = 0.5$ (left) and $\mathcal{K} = 2.5$ (right).

Substituting (4.1.70) into (4.1.39), we obtain an expression for ΔN for cases with a single non-thermal DM particle and right-handed neutrinos adding to the contribution of $N_{\rm eff}$. In Fig. 45 we show contours of constant ΔN in the $M_{Z''}/(K\overline{g})$ $vs.$ $\mathcal{T}(R^2-1)^2/(2R)^2$ plane, with $f = 1\%$. For all cases in Fig. 45, $T^{\rm dec}_{\nu_R} \ll m_{\rm charm}$, so our use of (4.1.63) is validated.

For $\overline{g} \simeq 0.3$, there is a region of the parameter space inside the 1σ interval of Planck data (with $h \simeq 0.674$) that can accommodate contributions to ΔN from both DM and ν_R with a Z'' gauge boson[1] within the LHC discovery reach. It is important to stress that for the E_6 Z'_ψ model, the LHC experimental limits on $M_{Z'}$ for null signals for enhancements in dilepton searches entail $M_{Z'} > 2.3\,{\rm TeV}$ at the 95 %CL [258, 110, 259]. In some of the models with $\overline{g} \approx 0.3$, the Z' may have large couplings to quarks (e.g., I_R and $B-L$ models) and the LHC experimental limits are dominated by dijet final states which imply $M_{Z'} < 4\,{\rm TeV}$ at 95% CL [261, 262, 263]. For all the cases there is a region of the parameter space inside the 1σ interval of Planck data (with $h \simeq 0.674$) that can accommodate contributions to ΔN from both DM and ν_R, and be in agreement with LHC limits.

---

[1]In the general cases where we are not referring to the SM^{++} model, one can interchange Z' and Z'' as the TeV scale gauge boson.

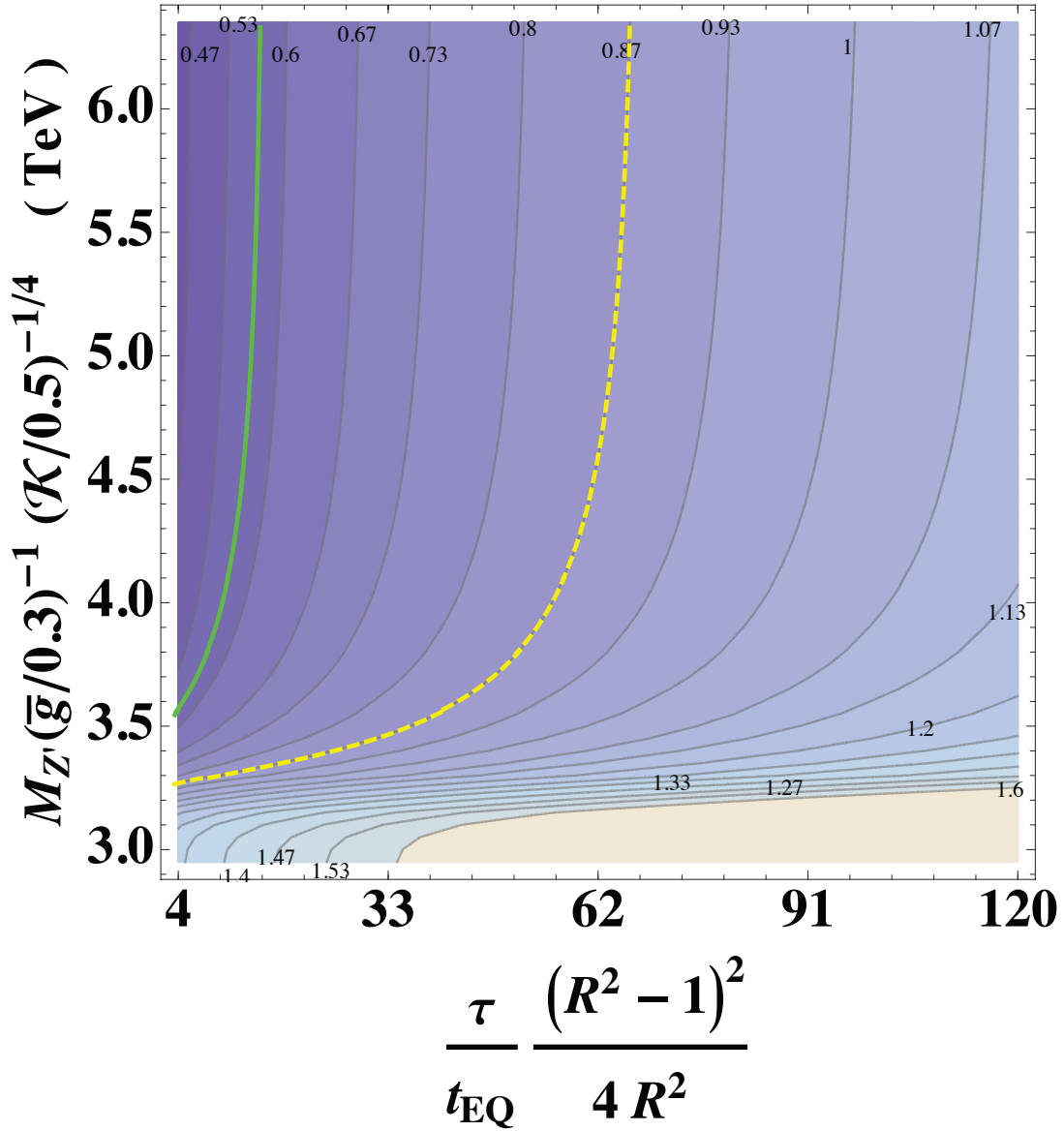Figure 45 : Contours of constant ΔN in the $M_{Z'}/(K\bar{g})$ vs. $\mathcal{T}(R^2-1)^2/(2R)^2$ plane, with $f = 1\%$. The (green) solid line indicates the upper limit on ΔN (with $h \simeq 0.674$) as reported by the Planck Collaboration. The band between the dashed (yellow) lines corresponds to the allowed ΔN region reported by Planck Collaboration using $h \simeq 0.738$.

4.1.4 Big Bang Nucleosynthesis Limits

As a final constraint we now verify that $X' \to X + \gamma$ does not drastically alter any of the light elemental abundances synthesized during BBN. By following [264], we can assume that the photons injected into the plasma rapidly redistribute their energy through scattering with background photons and through inverse Compton scattering. As a consequence, the constraints from BBN are (almost) independent of the initial energy distribution of the injected photons and are only sensitive to the total energy released in the decay process. In the spirit of [265], we conveniently write the electromagnetic energy release as $\varepsilon_\gamma \equiv E_\gamma Y_{X'}$, where $E_\gamma = (M_{X'}^2 - M_X^2)/(2M_{X'})$ is the initial electromagnetic energy release in each X' decay and $Y_{X'} \equiv n_{X'}/n_\gamma^{\mathrm{BG}}$ is the number density of X' before the decay, normalized to the number density of background photons $n_\gamma^{\mathrm{BG}} = 2\,\zeta(2)\,T_\gamma^3/\pi^2$. For $Y_{X'}$, each X' decay produces one X, and so the X' abundance may be expressed in terms of the present X abundance through

$$
\begin{aligned}
Y_{X'}(\tau) = Y_{X,\tau} = Y_{X,\mathrm{today}} &= \frac{\Omega_X \rho_c}{M_X\, n_\gamma^{\mathrm{BG}}(\mathrm{today})} \\
&\simeq 2.26 \times 10^{-14} \left(\frac{\mathrm{TeV}}{M_X}\right) \frac{\Omega_{\mathrm{CDM}} h^2}{0.1199} \frac{f}{0.01}\,,
\end{aligned}
\tag{4.1.71}
$$

yielding

$$
\varepsilon_\gamma = 1.13 \times 10^{-11}\, \frac{\Omega_{\mathrm{CDM}} h^2}{0.1199}\, \frac{f}{0.01} \left(\frac{M_{X'}}{M_X} - \frac{M_X}{M_{X'}}\right)\,\mathrm{GeV}\,.
$$

The thorough analysis of electromagnetic cascades reported in [264] reveals that the shaded regions of Fig. 46 are ruled out by considerations of light elemental abundances produced during BBN. The various regions are disfavored by the following conservative criteria: *(i)* D/H $< 10^{-4.9}$ (low); *(ii)* D/H $> 10^{-4.3}$ (high); *(iii)* ^{7}Li/H $< 10^{-10.05}$; *(iv)* primordial ^{4}He abundance < 0.227. The straight lines represent several combinations of R and τ/t_{EQ} producing the ΔN_X indicated in the labels. All straight lines intersect the BBN bounds at about $\log_{10}(\tau/t_{EQ}) = -8.2$. The constraints from BBN are weak for early decays because at early times the universe is hot and thus the X' secondary photon spectrum is rapidly thermalized, leaving just a few extra high-energy photons that cannot alter the light elemental abundances. However, for $\tau/t_{\mathrm{EQ}} > 10^{-8.2}$, BBN excludes most of the relevant parameter space.
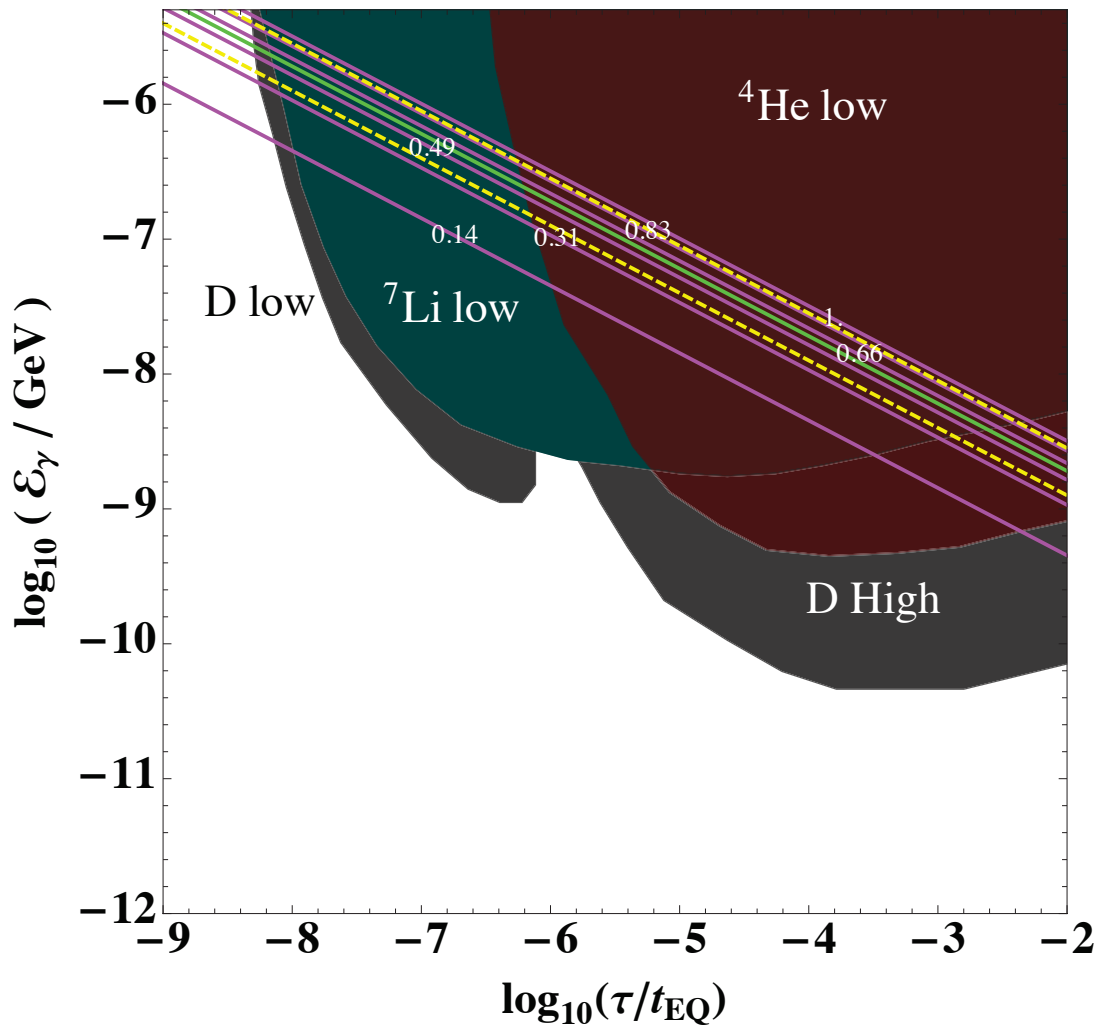
Figure 46 : The released electromagnetic energy are represented via the lines labeled by ΔN_X varying from $0.14 - 1.0$ as a function of $\log_{10}(\tau/t_{\text{EQ}})$. In order to avoid destroying the BBN results, these lines must not intersect any regions where any elemental abundance has been established. Generically, the only parameter space available is for $\log_{10}(\tau/t_{\text{EQ}}) < -9$. The (green) solid line indicates the upper limit on ΔN (with $h \simeq 0.674$) as reported by the Planck Collaboration. The band between the dashed (yellow) lines corresponds to the allowed ΔN region reported by Planck Collaboration using $h \simeq 0.738$.

4.2   Higgs Portal to the Dark Sector and WIMPS

Recent dark matter direct detection research has found that hints of a WIMP of mass 10 GeV has been seen by various collaborations reported by the DAMA/LIBRA [68], CoGeNT [69, 70], CRESST [71], and CDMS [72] Collaborations, each of which report signals consistent with a dark matter particle of similar mass. These four experiments make use of different technologies, target materials, and detection strategies, but each reports results that are not compatible with known backgrounds, but which can be accommodated by a dark matter particle with a mass of about 10 GeV and an elastic scattering cross section with nucleons of $1 - 2 \times 10^{-41}$ cm^2 [266, 267, 268, 269].

Furthermore it is observed that around the Galactic Center (GC), there exists a bright and spatially extended source of γ-ray emission peaking at energies of a few GeV. The spectrum and morphology of this signal is consistent with one originating from dark matter annihilations [270, 271, 272, 273]. Very recently, evidence of this signal has been found from regions outside of the GC [274] in the directions of the sky coincident with the *Fermi* Bubbles: two
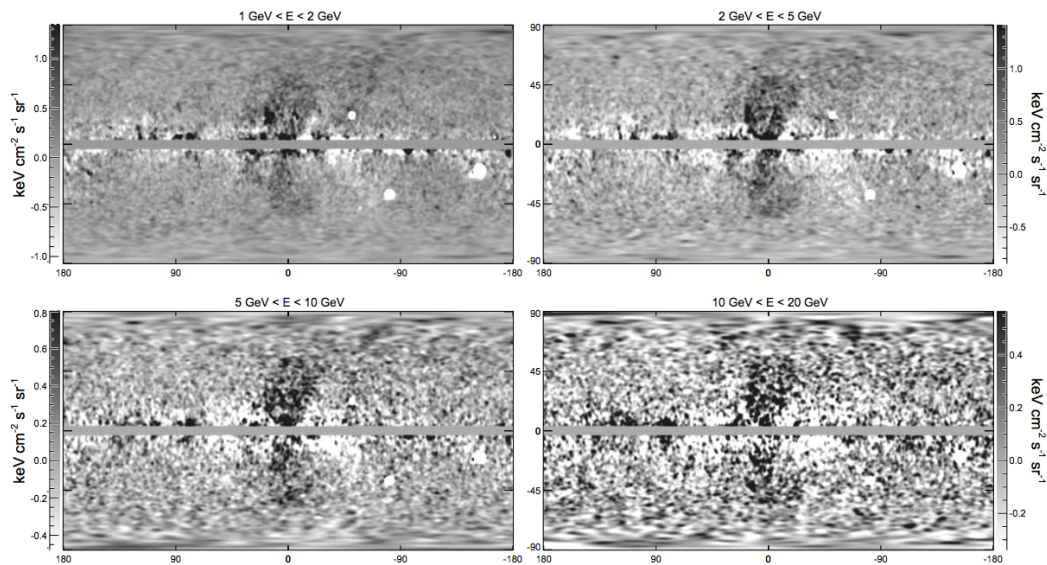
Figure 47 : After subtracting the away the *Fermi* diffuse galactic model from 1.6 years of LAT data two nearly symmetric bubble structures appear extending out from the galactic center know as *Fermi* bubbles (image adopted from [275]).

bilateral γ-ray lobes centered at the core of the Galaxy and extending to around $50°$ above and below the Galactic plane (*i.e.*, $r = \pm 10$ kpc, where r is the distance from the GC) [276, 275] as

seen in Fig. 47. At lower Galactic latitudes these structures are coincident with a non-thermal microwave 'haze' found in WMAP 23-33 GHz data [277] (confirmed recently by the Planck space mission [278]) and the thermal X-ray emission seen by ROSAT [279].

Far from the Galactic plane ($|b| \geq 30°$), the observed energy-weighted γ-ray spectrum is nearly invariant with latitude and fairly flat ($d\Phi_\gamma/dE_\gamma \propto E_\gamma^{-2}$) over the energy range observed by *Fermi*. The correlation found in the multi-wavelength observations seems to indicate that the Bubbles (measured in the range of $E_\gamma \sim 1 - 100$ GeV) are produced by a population of $\mathrm{GeV} - \mathrm{TeV}$ electrons (with an approximately power-law spectrum $d\Phi_e/dE_e \propto E_e^{-3}$) via inverse Compton scattering of ambient low-energy photons, as the same electrons can also simultaneously produce radio synchrotron radiations in the presence of magnetic fields [276, 280]. The transparency of this elementary and self-consistent framework provides strong support for a leptonic origin of the high-latitude emission from the *Fermi* Bubbles.

Conversely, at latitudes closer to the disk ($|b| \geq 20°$), the spectrum of the emission correlated with the Bubbles possesses a pronounced spectral feature in $E_\gamma^2 d\Phi_\gamma/dE_\gamma$ peaking at $E_\gamma \sim 1 - 4$ GeV, which cannot be produced by any realistic spectrum of electrons [274]. This implies that a second (non-inverse-Compton) emission mechanism must be responsible for the bulk of the low-energy, low-latitude emission. The spectral shape of this second component is similar to the one reported from the GC. The intrinsic non-inverse-Compton emission appears spatially consistent with a luminosity per volume falling approximately as $r^{-2.4} - r^{-2.8}$. As a consequence, the spectral feature visible in the low-latitude Bubbles is most likely the extended counterpart of the GC excess, now detected out to at least $r \sim 2 - 3$ kpc. Even though millisecond pulsars possess a spectral cutoff at approximately the required energy, these sources exhibit a spectral shape that is much too soft at sub-GeV energies to accommodate this signal [281].

The spectrum and angular distribution of the signal is broadly consistent with one predicted from ~ 10 GeV dark matter particles annihilating to leptons, or from ~ 50 GeV dark matter particles annihilating to quarks, following a distribution similar to, but slightly steeper than, the canonical Navarro-Frenk-White profile. In either case, the morphology of the γ-ray signal requires a dark matter distribution that scales approximately as $\rho_{\mathrm{DM}} \propto r^{-1.2} - r^{-1.4}$, that is the annihilation rate per volume is proportional to the square of the dark matter density. Such a dark matter distribution is in good agreement with current observational constraints [282].

For the 10 GeV dark matter candidate, the normalization of the observed signal requires a velocity average annihilation cross section on the order of

$$\langle \sigma_\tau v \rangle \sim 2 \times 10^{-27}~\text{cm}^3/\text{s} = 1.7 \times 10^{-10}~\text{GeV}^{-2}\,, \qquad (4.2.1)$$

up to overall uncertainties in the normalization of the halo profile [283].

Moreover dark matter particles can also elastically scatter with nuclei in the Sun, leading to their gravitational capture and subsequent annihilation. Electrons and muons produced in such annihilations quickly lose their energy to the Solar medium and produce no observable effects. Annihilations to taus, on the other hand, produce neutrinos which, for a 10 GeV, can be observed by Super-Kamiokande. For the required branching into $\tau^+\tau^-$ of about 10% – as given by (4.2.1) – existing data constrain the dark matter spin-independent elastic scattering cross section with protons to be less than $4 \times 10^{-41}~\text{cm}^2$ [284, 285].

For the 50 GeV dark matter particle, the normalization of the observed signal requires a velocity average annihilation cross section on the order of

$$\langle \sigma_b v \rangle \sim 8 \times 10^{-27}~\text{cm}^3/\text{s} = 6.7 \times 10^{-10}~\text{GeV}^{-2}\,. \qquad (4.2.2)$$

The XENON-100 Collaboration reported a 90% CL bound on the elastic scattering cross section with nuclei of $\mathcal{O}(10^{-44}~\text{cm}^2)$ [286]. A later analysis has arrived at alternative conclusions allowing for a signal of two events with a favored mass of 12 GeV and large error contour extending to about 50 GeV [74].

It is worthwhile to point out that the bounds from the combined analysis of 10 dwarf spheroidals [287, 288], galaxy clusters [289], or diffuse γ-ray emission [290, 291] are not sensitive enough to probe the velocity average annihilation cross sections (4.2.1) and (4.2.2).

With this recent (at the time of this writing) observations a minimal hidden sector Higgs portal model has been suggested by Weinberg [15].

It has attractive qualities to explain these observations, and we will examine to what extent its free parameters can be adjusted to fit, experimental searches for new physics at the LHC, constraints from cosmological observations, constraints from direct detection searches, and a possible explanation of the low-latitude γ-ray emission from the *Fermi* Bubbles.

4.2.1 Constructing Weinberg's WIMPs

Let us start by examining the Weinberg Higgs portal model. It is based on a broken global $U(1)$ symmetry associated with the dark matter charge W: the number of weakly-interacting massive particles (WIMPs) minus the number of their antiparticles. The hidden sector contains a Dirac field ψ (carrying WIMP quantum number $W = +1$) and a complex scalar field (with $W = 2$, so that its expectation value leaves an unbroken reflection symmetry $\psi \to -\psi$). All SM fields are assumed to have $W = 0$.

The scalar potential consists of the SM component $[s]$, the isomorphic component in the hidden sector $[h]$, and the quartic interaction coupling between the two sectors with strength η_χ. The Lagrangian density for the scalar sector reads

$$\mathscr{L} = |\partial\Phi_h|^2 + |\partial\Phi_s|^2 + \mu_h^2|\Phi_h|^2 - \lambda_h|\Phi_h|^4 + \mu_s^2|\Phi_s|^2 - \lambda_s|\Phi_s|^4 - \eta_\chi|\Phi_h|^2|\Phi_s|^2\,,$$

(4.2.3)

where Φ_s is the SM scalar doublet and Φ_h is a complex scalar field. We separate a massless Goldstone boson field $\alpha(x)$ and a massive radial field $r(x)$ by defining

$$\Phi_h(x) = \frac{1}{\sqrt{2}}\,r(x)\,e^{i\,2\alpha(x)}\,,$$

(4.2.4)

where $r(x)$ and $\alpha(x)$ are real, with the phase of $\Phi_h(x)$ adjusted to make the vacuum expectation value (VEV) of $\alpha(x)$ zero. The $SU(2) \times U(1)$ symmetry of the SM is (of course) broken by a non-vanishing VEV of the neutral component ϕ of the scalar doublet,

$$\Phi_s = \frac{1}{\sqrt{2}}\begin{pmatrix} G^\pm \\ v_\phi + \phi' + iG^0 \end{pmatrix},$$

(4.2.5)

where $v_\phi \simeq 246$ GeV. The G fields are the familiar Goldstone bosons, which are eaten by the vector bosons (*i.e.* the $G^\pm$ become the longitudinal components of the charged W-boson and G^0 becomes the longitudinal component of the Z-boson). In terms of real fields the Lagrangian density (4.2.3) takes the form

$$\mathscr{L} = \frac{1}{2}\partial r^2 + \frac{1}{2}\partial\phi^2 + 2r^2\partial\alpha^2 + \frac{\mu_h^2}{2}r^2 - \frac{\lambda_h}{4}r^4 + \mu_s^2|\phi|^2 - \lambda_s|\phi|^4 - \frac{\eta_\chi}{2}r^2|\phi|^2\,.$$

(4.2.6)

The $U(1)$ symmetry of W conservation is also broken and r gets a VEV

$$r(x) = v_r + r'(x)\,,$$

(4.2.7)

with v_r real and non-negative. We demand the scalar potential obtains its minimum value at

$$\mathcal{V} = -\frac{\mu_h^2}{2}v_r^2 + \frac{\lambda_h}{4}v_r^4 - \frac{\mu_s^2}{2}v_\phi^2 + \frac{\lambda_s}{4}v_\phi^4 + \frac{\eta_\chi}{4}v_r^2 v_\phi^2 \,. \tag{4.2.8}$$

Physically, the most interesting solutions to the minimization of (4.2.8),

$$\partial_{v_r}\mathcal{V} = -\mu_h^2 v_r + \lambda_h v_r^3 + \frac{\eta_\chi}{2}v_r v_\phi^2 = 0 \tag{4.2.9}$$

and

$$\partial_{v_\phi}\mathcal{V} = -\mu_s^2 v_\phi + \lambda_s v_\phi^3 + \frac{\eta_\chi}{2}v_r^2 v_\phi = 0 \,, \tag{4.2.10}$$

are obtained for v_r and v_ϕ both non-vanishing

$$v_\phi^2 = \frac{1}{\lambda_s}\left(\mu_s^2 - \frac{\eta_\chi v_r^2}{2}\right) \tag{4.2.11}$$

and

$$v_r^2 = \frac{1}{\lambda_h}\left(\mu_h^2 - \frac{\eta_\chi v_\phi^2}{2}\right) \,, \tag{4.2.12}$$

respectively. To compute the scalar masses, we must expand the potential around the minima

$$
\begin{aligned}
\mathcal{L} &= \frac{1}{2}(\partial r')^2 \\
&+ 2v_r^2\partial\alpha^2 + 4v_r r'\partial\alpha^2 + 2r'^2\partial\alpha^2 \\
&- \lambda_h v_r^2 r'^2 - \lambda_s v_\phi^2 \phi'^2 - \eta_\chi v_r v_\phi r'\phi' + \cdots \,,
\end{aligned}
\tag{4.2.13}
$$

where the dots indicate 3-point and 4-point interactions, as well as the SM interactions. There is a mixing term present for r' and ϕ'. We find the fields of definite mass by diagonalizing the mass matrix for r' and ϕ'. We denote by H and h the scalar fields of definite masses, $m_H = 125$ GeV and m_h, respectively. After a bit of algebra, the explicit expressions for the scalar mass eigenvalues and eigenvectors are given by

$$m_h^2 = \lambda_h v_r^2 + \lambda_s v_\phi^2 - \sqrt{(\lambda_s v_\phi^2 - \lambda_h v_r^2)^2 + (\eta_\chi v_r v_\phi)^2} \tag{4.2.14}$$

and

$$m_H^2 = \lambda_h v_r^2 + \lambda_s v_\phi^2 + \sqrt{(\lambda_s v_\phi^2 - \lambda_h v_r^2)^2 + (\eta_\chi v_r v_\phi)^2} \,, \tag{4.2.15}$$

with

$$\begin{pmatrix} h \\ H \end{pmatrix} = \begin{pmatrix} \cos\chi & -\sin\chi \\ \sin\chi & \cos\chi \end{pmatrix} \begin{pmatrix} r' \\ \phi' \end{pmatrix} \,, \tag{4.2.16}$$

where $\chi \in [-\pi/2, \pi/2]$ also fulfills

$$\sin 2\chi = \frac{\eta_\chi v_\phi v_r}{\sqrt{(\lambda_s v_\phi^2 - \lambda_h v_r^2)^2 + (\eta_\chi v_r v_\phi)^2}} = \frac{2\eta_\chi v_\phi v_r}{m_H^2 - m_h^2}, \tag{4.2.17}$$

and

$$\cos 2\chi = \frac{\lambda_s v_\phi^2 - \lambda_h v_r^2}{\sqrt{(\lambda_s v_\phi^2 - \lambda_h v_r^2)^2 + (\eta_\chi v_r v_\phi)^2}}, \tag{4.2.18}$$

yielding

$$\tan 2\chi = \frac{\eta_\chi v_r v_\phi}{\lambda_s v_\phi^2 - \lambda_h v_r^2}. \tag{4.2.19}$$

The Goldstone boson in (4.2.13) has to be be re-normalized so that it resumes the standard canonical form. This is achieved through scaling $\alpha \to \alpha' = 2v_r\alpha$, giving

$$2v_r^2 \partial\alpha^2 + 4v_r r' \partial\alpha^2 + 2r'^2 \partial\alpha^2 \to \frac{1}{2}\partial\alpha'^2 + \frac{1}{v_r}r'\partial\alpha'^2 + \frac{1}{2v_r^2}r'^2\partial\alpha'^2. \tag{4.2.20}$$

Adding in the dark matter sector requires at least one Dirac field

$$\mathscr{L}_\psi = i\bar{\psi}\gamma \cdot \partial\psi - m_\psi \bar{\psi}\psi - \frac{f}{\sqrt{2}}\bar{\psi}^c\psi\Phi_h^\dagger - \frac{f^*}{\sqrt{2}}\bar{\psi}\psi^c\Phi_h. \tag{4.2.21}$$

We assign ψ a charge $W = 1$, so that the Lagrangian is invariant under the global transformation $e^{iW\alpha}$. Applying a phase change allows us to express ψ as

$$\psi(x) = \psi'(x)e^{i\alpha(x)}. \tag{4.2.22}$$

We can now rewrite (4.2.21) in terms of ψ', α, and r

$$\mathscr{L}_\psi = i\bar{\psi}'\gamma \cdot \partial\psi' - (\bar{\psi}'\gamma\psi') \cdot \partial\alpha - m_\psi\bar{\psi}'\psi' - \frac{f}{2}\bar{\psi}'^c\psi'r - \frac{f}{2}\bar{\psi}'\psi'^c r, \tag{4.2.23}$$

where we have taken f to be real. Once r achieves a VEV we can expand the dark matter sector to get

$$\begin{aligned}
\mathscr{L}_\psi &= \frac{i}{2}\left(\bar{\psi}'\gamma \cdot \partial\psi' + \bar{\psi}'^c\gamma \cdot \partial\psi'^c\right), \\
&- \frac{m_\psi}{2}\left(\bar{\psi}'\psi' + \bar{\psi}'^c\psi'^c\right) - \frac{fv_r}{2}\bar{\psi}'^c\psi' - \frac{fv_r}{2}\bar{\psi}'\psi'^c, \\
&- \frac{1}{2}(\bar{\psi}'\gamma\psi' - \bar{\psi}'^c\gamma\psi'^c) \cdot \partial\alpha, \\
&- \frac{f}{2}r'\left(\bar{\psi}'^c\psi' + \bar{\psi}'\psi'^c\right). \tag{4.2.24}
\end{aligned}$$

Note that we have made the Lagrangian explicitly symmetric via relations like

$$\psi^c \;=\; C\bar{\psi}^T \tag{4.2.25}$$

$$\bar{\psi}^c\psi^c \;=\; (-\psi^T C^{-1} C\bar{\psi}^T) = \bar{\psi}\psi \tag{4.2.26}$$

$$\bar{\psi}_c \gamma \cdot \partial \psi_c \;=\; -\psi^T C^{-1}\gamma C \cdot \partial \bar{\psi}^T$$

$$\;=\; \psi^T \gamma^T \cdot \partial \bar{\psi}^T = -(\partial \bar{\psi} \cdot \gamma\psi) \to \bar{\psi}\gamma \cdot \partial\psi \,. \tag{4.2.27}$$

In (4.2.26) we used the Grassman nature of the spinor fields; in the second line of (4.2.27) we used integration by parts to transfer the derivative onto the ψ field. Similar results can be found for the other expressions.

Diagonalization of the ψ' mass matrix generates the mass eigenvalues,

$$m_{\pm} = m_{\psi} \pm f v_r, \tag{4.2.28}$$

for the two mass eigenstates

$$\psi_- = \frac{i}{\sqrt{2}}\left(\psi'^c - \psi'\right) \quad \text{and} \quad \psi_+ = \frac{1}{\sqrt{2}}\left(\psi'^c + \psi'\right). \tag{4.2.29}$$

In this basis, the act of charge conjugation on $\psi_{\pm}$ results in

$$\psi^c_{\pm} = \psi_{\pm}. \tag{4.2.30}$$

This tells us that the fields $\psi_{\pm}$ are Majorana fermions. The Lagrangian is found to be

$$\begin{aligned}
\mathscr{L}_{\psi} \;=\;& \frac{i}{2}\bar{\psi}_+ \gamma \cdot \partial \psi_+ + \frac{i}{2}\bar{\psi}_- \gamma \cdot \partial \psi_- - \frac{1}{2}m_+\bar{\psi}_+\psi_+ - \frac{1}{2}m_-\bar{\psi}_-\psi_-, \\
&- \frac{i}{4v_r}(\bar{\psi}_+\gamma\psi_- - \bar{\psi}_-\gamma\psi_+)\cdot \partial\alpha', \\
&- \frac{f}{2}r'(\bar{\psi}_+\psi_+ - \bar{\psi}_-\psi_-).
\end{aligned} \tag{4.2.31}$$

We must now put r' into its massive field representation, for which the interactions of interest are

$$-\frac{f\sin\chi}{2}H(\bar{\psi}_+\psi_+ - \bar{\psi}_-\psi_-) - \frac{f\cos\chi}{2}h(\bar{\psi}_+\psi_+ - \bar{\psi}_-\psi_-). \tag{4.2.32}$$

This leads to 3-point interactions between the W-WIMPs and the Higgs boson of the SM.

In summary, instead of one Dirac W-WIMP, there are two Majorana W-WIMPs of different masses. However, the heavier W-WIMP will decay into the lighter one by emitting a Goldstone

boson, while the lighter one is kept stable by an unbroken reflection symmetry. Therefore in this model we can expect that the universe today will contain only one type of Majorana W-WIMP, the lighter one w, with mass m_w equal to the smaller of $m_\pm$. Throughout, $\Delta m = |m_+ - m_-| = 2|fv_r|$ denotes the mass splitting of the W-WIMP states. (The most common variables used in this discussion are summarized in Table 8.)

A cautionary note is worth taking on board at this juncture. It has long been known that the spontaneous breaking of a global $U(1)$ symmetry have several disconnected and degenerate vacua (the phase of the vacuum expectation value $\langle 0|\Phi_h|0\rangle$ can be different in different regions of space, and actually we expect it to be different in casually disconnected regions), leading to catastrophic domain-wall structure in the early universe [292, 293]. In the spirit of [292], it may be possible to introduce a small explicit breaking of the symmetry, such that the domain walls disappear before dominating the matter density of the universe, while leaving (pseudo-)Goldstone bosons and the same dark matter phenomenology.[2]

The absence of new physics signals at the LHC place constraints on the model. We discuss this next.

---

[2]Other approaches, if exceedingly fine-tuned, may offer alternative solutions [294, 295, 296, 297, 298].

Table 8 : Definition of Most Common Variables of W-WIMP Model.

Φ_s	SM Scalar Doublet
Φ_h	Complex Scalar Field
ϕ	Neutral Component of the Scalar Doublet
r	Massive Radial Field
α	Goldstone Boson
v_ϕ	Vacuum Expectation Value of ϕ
v_r	Vacuum Expectation Value of r
H	SM Higgs Boson
h	Hidden Scalar
η_χ	Quartic Interaction Coupling Between SM and Hidden Sectors
χ	H-h Mixing Angle
w	lightest W-WIMP
Δm	W-WIMP Mass Splitting
f	Coupling Between Hidden Majorana Fermions and Complex Scalar Field

4.2.2 Constraints from Collider Experiments

As was stated previously the recent discovery [8, 299] SM Higgs boson like particle suggests that with measurements of branching ratios in various channels, a study of the properties of the Higgs-like state has the potential for revealing whether or not the Higgs sector is as simple as envisioned in the SM. Since invisible decays reduce the branching fraction to the (visible) SM final states, it is to be expected that $\mathcal{B}(H \to \text{invisible})$ is strongly constrained. Indeed $\mathcal{B}(H \to \text{invisible})$ is known to be less than about 19% at 95%CL [300, 301, 302]. Thus, the mixing of the SM with the hidden sector must be weak. Note that for $\eta_\chi \ll 1$ the relations between masses and angles then becomes

$$m_h^2 \approx 2\lambda_h v_r^2, \qquad m_H^2 \approx 2\lambda_s v_\phi^2, \qquad \tan 2\chi \approx \frac{2\eta_\chi v_r v_\phi}{m_H^2 - m_h^2}, \qquad (4.2.33)$$

where we have assumed $\lambda_s v_\phi^2 > \lambda_h v_r^2$. For a Higgs width of about 4 MeV, the partial width for decay into unobserved particles is found to be

$$\Gamma_{H \to \text{invisible}} < 0.8 \text{ MeV}. \qquad (4.2.34)$$

The phenomenology of a Higgs portal to the hidden sector depends on whether the SM Higgs particle is lighter or heavier than the new companion. In this study we take $m_H > m_h$. The decay rate into invisible stuff, $\Gamma_{H \to \text{invisible}}$, has two distinct contributions: $\Gamma_{H \to \text{invisible}}^{\text{SM}}$ and $\Gamma_{H \to \text{hidden}}$. The former is dominated by $H \to 2Z \to 4\nu$, with an invisible Z branching ratio of 4%. The 4ν rate can be predicted from observed decays $H \to 2Z \to 4l$. For the sake of simplicity, hereafter we will omit the contribution of $\Gamma_{H \to \text{invisible}}^{\text{SM}}$. Unless expressly stated otherwise herein, we assume $m_w + \Delta m > m_H/2$ and thus H decays (invisibly) into the hidden sector via three channels: $H \to 2\alpha'$, $H \to 2h$, and $H \to 2w$. From the event rates for visible Higgs production and decay channels we could derive upper bounds on non-SM admixtures in the wave-function of the Higgs boson and on the new three invisible decay channels. To this end we now compute the decay rates for these three processes.

$\underline{\mathbf{\Gamma_{H \to 2\alpha'}}}$

Substituting in (4.2.20) r' by the field of definite mass, $r' = h \cos \chi + H \sin \chi$, we can write the Higgs–Goldstone boson interaction term as

$$\frac{1}{v_r} r' \partial \alpha'^2 \to \frac{\sin \chi}{v_r} H (\partial \alpha')^2 + \frac{\cos \chi}{v_r} h (\partial \alpha')^2 \,. \tag{4.2.35}$$

Using (4.2.35) we write the Feynman rule for interactions of the type H, α', α' as

$$-i \frac{2 \sin \chi}{v_r} k \cdot k', \tag{4.2.36}$$

where $k \, (k')$ is the 4-momentum of the incoming (outgoing) α' particle, and the factor of 2 is a symmetry factor, as one can exchange incoming-outgoing α' twice. From this 3-point interaction we can calculate the decay width of the SM Higgs H into 2 Goldstone bosons α'. In the rest frame of the Higgs, the differential decay probability per unit time is given by

$$d\Gamma_{H \to 2\alpha'} = \frac{1}{2m_H} \left(\frac{2 \sin \chi}{v_r} k_1 \cdot k_2 \right)^2 dQ \,, \tag{4.2.37}$$

where

$$\begin{aligned}
dQ &= \frac{1}{2!} \frac{d^3 k_1}{(2\pi)^3 2k_1} \frac{d^3 k_2}{(2\pi)^3 2k_2} (2\pi)^4 \delta(m_H - k_1 - k_2) \delta^{(3)}(\mathbf{k}_1 + \mathbf{k}_2) \\
&= \frac{1}{16} \frac{d\Omega_{k_1}}{(2\pi)^2} \bigg|_{k_1 = m_H/2}
\end{aligned} \tag{4.2.38}$$

is the phase space for a two-body final state (the factor of $1/2!$ is included because of identical particles in the final state). After some algebra (4.2.37) can be re-written as

$$d\Gamma_{H \to 2\alpha'} = \frac{d\Omega_{k_1}}{128 \, \pi^2 m_H} \left[\frac{2 \sin \chi}{v_r} 2 \left(\frac{m_H}{2} \right)^2 \right]^2 \,. \tag{4.2.39}$$

The partial decay width can now be expressed as

$$\Gamma_{H \to 2\alpha'} = \frac{1}{32\pi} \left(\frac{\sin \chi}{v_r} \right)^2 m_H^3 \,. \tag{4.2.40}$$

For $m_H \gg m_h$ and $m_H^2 \gg 2 \eta_\chi v_r v_\phi$, we can use the small angle approximation

$$\sin \chi \approx \chi = \eta_\chi v_r v_\phi / (m_H^2 - m_h^2) \,. \tag{4.2.41}$$

In this very good approximation the decay width becomes

$$\Gamma_{H \to 2\alpha'} = \frac{1}{32\pi} \left(\frac{\eta_\chi v_\phi}{m_H^2 - m_h^2} \right)^2 m_H^3. \tag{4.2.42}$$

$\underline{\Gamma_{\mathbf{H}\to\mathbf{2h}}}$

We begin by expanding the scalar potential $\mathcal{V}$ around the VEVs of r and ϕ after which we diagonalize the mass matrix. Together this requires that we expand around the fields

$$
\begin{aligned}
r(x) &= v_r + h\cos\chi + H\sin\chi\,, \\
\phi(x) &= v_\phi + H\cos\chi - h\sin\chi\,,
\end{aligned}
\tag{4.2.43}
$$

which puts $\mathcal{V}$ in the form

$$
\begin{aligned}
\mathcal{V} =\ & \frac{1}{2}m_H^2 H^2 + \frac{1}{2}m_h^2 h^2 \\
& - \frac{1}{16}\left(\eta_\chi + 3(\lambda_h + \lambda_s) + 3(\eta_\chi - \lambda_h - \lambda_s)\cos 4\chi\right)H^2 h^2 \\
& - \frac{1}{4}v_\phi \cos\chi[6\lambda_s - \eta_\chi + 3(\eta_\chi - 2\lambda_s)\cos 2\chi]Hh^2 \\
& + \frac{1}{4}v_r \sin\chi[\eta_\chi - 6\lambda_h + 3(\eta_\chi - 2\lambda_h)\cos 2\chi]Hh^2 \\
& - \frac{1}{4}\left(\lambda_s \cos^4\chi + \eta_\chi \cos^2\chi \sin^2\chi + \lambda_h \sin^4\chi\right)H^4 \\
& - \frac{1}{4}\left(\lambda_h \cos^4\chi + \eta_\chi \cos^2\chi \sin^2\chi + \lambda_s \sin^4\chi\right)h^4 \\
& + \frac{1}{2}\left(v_\phi \sin\chi(\eta_\chi \cos^2\chi + 2\lambda_s \sin^2\chi) - v_r(2\lambda_h \cos^3\chi + \eta_\chi \cos\chi \sin^2\chi)\right)h^3 \\
& - \frac{1}{2}\left(v_r \sin\chi(\eta_\chi \cos^2\chi + 2\lambda_h \sin^2\chi) + v_\phi(2\lambda_s \cos^3\chi + \eta_\chi \cos\chi \sin^2\chi)\right)H^3 \\
& + \frac{1}{4}\left(\lambda_h - \lambda_s + (\lambda_s + \lambda_h - \eta_\chi)\cos 2\chi\right)\sin 2\chi\,Hh^3 \\
& + \frac{1}{4}\left(\lambda_s - \lambda_h + (\lambda_s + \lambda_h - \eta_\chi)\cos 2\chi\right)\sin 2\chi\,H^3 h \\
& + \frac{1}{2}v_\phi \sin\chi[2(3\lambda_s - \eta_\chi)\cos^2\chi + \eta_\chi \sin^2\chi]H^2 h \\
& + \frac{1}{2}v_r(\eta_\chi \sin\chi \sin 2\chi - 6\lambda_h \cos\chi \sin^2\chi - \eta_\chi \cos^3\chi)H^2 h\,.
\end{aligned}
\tag{4.2.44}
$$

Since $\chi < 1$, we first expand the potential around $\chi = 0$, and then using (4.2.17) we further expand around $\eta_\chi = 0$ retaining only the terms of first order in η_χ; this results in

$$
\begin{aligned}
\mathcal{V} \approx\ & \frac{1}{2}m_H^2 H^2 + \frac{1}{2}m_h^2 h^2 \\
& - \frac{\eta_\chi}{4}H^2 h^2 - \frac{\lambda_h}{4}h^4 - \frac{\lambda_s}{4}H^4 - \frac{\eta_\chi \lambda_h v_r v_\phi}{m_H^2 - m_h^2}Hh^3 + \frac{\eta_\chi \lambda_s v_r v_\phi}{m_H^2 - m_h^2}H^3 h \\
& - \lambda_h v_r h^3 - \lambda_s v_\phi H^3 - \frac{\eta_\chi v_\phi}{2}\left(\frac{6\lambda_h v_r^2}{m_H^2 - m_h^2} + 1\right)Hh^2 \\
& + \frac{\eta_\chi v_r}{2}\left(\frac{6\lambda_s v_\phi^2}{m_H^2 - m_h^2} - 1\right)H^2 h\,.
\end{aligned}
$$

Using (4.2.33) we can manipulate this expression to write the scalar potential as

$$
\begin{aligned}
\mathcal{V} \approx\ & \frac{1}{2}m_H^2 H^2 + \frac{1}{2}m_h^2 h^2 \\
& - \frac{\eta_\chi}{4}H^2 h^2 - \frac{\lambda_h}{4}h^4 - \frac{\lambda_s}{4}H^4 - \frac{\eta_\chi \lambda_h v_r v_\phi}{m_H^2 - m_h^2}Hh^3 + \frac{\eta_\chi \lambda_s v_r v_\phi}{m_H^2 - m_h^2}H^3 h \\
& - \frac{m_h^2}{2v_r}h^3 - \frac{m_h^2}{2v_\phi}H^3 - \frac{\eta_\chi v_\phi}{2}\left(\frac{m_H^2 + 2m_h^2}{m_H^2 - m_h^2}\right)Hh^2 \\
& + \frac{\eta_\chi v_r}{2}\left(\frac{2m_H^2 + m_h^2}{m_H^2 - m_h^2}\right)H^2 h \, .
\end{aligned} \tag{4.2.45}
$$

Under the approximations taken previously, $m_H \gg m_h$ and $m_H^2 \gg 2\eta_\chi v_r v_\phi$, the relevant Hhh interaction term results in

$$
-\frac{\eta_\chi v_\phi}{2}\left(\frac{m_H^2 + 2m_h^2}{m_H^2 - m_h^2}\right)Hh^2. \tag{4.2.46}
$$

The differential decay probability per unit time is given by

$$
\begin{aligned}
d\Gamma_{H\to 2h} =\ & \\
\frac{1}{2m_H}\ & \left(\frac{\eta_\chi v_\phi}{m_H^2 - m_h^2}\right)^2 (m_H^2 + 2m_h^2)^2 \frac{1}{2!}\frac{k^2\,dk\,d\Omega}{(2\pi)^2 4E_k}\frac{1}{2k}\,\delta\left(m_h - 2\sqrt{k^2 + m_H^2}\right)\, .
\end{aligned} \tag{4.2.47}
$$

The partial $H \to 2h$ decay width can now be expressed as

$$
\Gamma_{H\to 2h} = \frac{1}{32\,\pi\,m_H^2}\left(\frac{\eta_\chi v_\phi}{m_H^2 - m_h^2}\right)^2 (m_H^2 + 2m_h^2)^2 \sqrt{m_H^2 - 4m_h^2}\,. \tag{4.2.48}
$$

In the limit $m_H \gg m_h$ we obtain

$$
\Gamma_{H\to 2h} = \frac{1}{32\pi}\left(\frac{\eta_\chi v_\phi}{m_H^2 - m_h^2}\right)^2 m_H^3\,. \tag{4.2.49}
$$

$\mathbf{\Gamma_{H\to 2w}}$

For $m_w < m_H/2$, the $r - \phi$ mixing allows the Higgs boson to decay into pairs of the lightest W-WIMP. We obtain the invariant amplitude for this process (a description of Feynman rules for Majorana fermions can be found in Ref. [24]),

$$
i\mathcal{M} = if\sin\chi\,\bar{u}(p)v(p')\,, \tag{4.2.50}
$$

where $u(p)$ and $v(p)$ are Dirac spinors. The spin average rate is given by

$$
\sum_s |\mathcal{M}|^2 = 4f^2 \sin^2\chi(p\cdot p' - m_w^2). \tag{4.2.51}
$$

The partial H-decay rate into $2w$ is

$$
\begin{aligned}
d\Gamma_{H\to 2w} &= \frac{|\mathcal{M}|^2}{2m_H}\frac{d^3p'}{(2\pi)^3 2E_{p'}}\frac{d^3p}{(2\pi)^3 2E_p}(2\pi)^4\delta^{(3)}(\mathbf{p'}+\mathbf{p})\delta(m_H - p' - p), \\
&= \frac{1}{2!}\frac{d\Omega}{64\pi^2 m_H^2}\sqrt{m_H^2 - 4m_w^2}\,|\mathcal{M}|^2_{\mathbf{p'}=-\mathbf{p},\ p=\sqrt{(m_H/2)^2 - m_w^2}},
\end{aligned}
\tag{4.2.52}
$$

and so the partial width for this decay is given by

$$
\Gamma_{H\to 2w} = \frac{2(m_H^2 - 4m_w^2)}{32\pi m_H^2}\left(\frac{f\eta_\chi v_r v_\phi}{m_H^2 - m_h^2}\right)^2\sqrt{m_H^2 - 4m_w^2}.
\tag{4.2.53}
$$

For $m_H \gg 2m_w$, (4.2.53) becomes

$$
\Gamma_{H\to 2w} = \frac{1}{16\pi}\left(\frac{f\eta_\chi v_r v_\phi}{m_H^2 - m_h^2}\right)^2\sqrt{m_H^2 - 4m_w^2}.
\tag{4.2.54}
$$

$\Gamma_{H\to \text{ hidden}}$

All in all, the decay width of the Higgs into the hidden sector is given by

$$
\Gamma_{H\to\text{hidden}} = \frac{1}{16\pi}\left(\frac{\eta_\chi\, v_\phi}{m_H^2 - m_h^2}\right)^2 m_H^3 + \frac{1}{16\pi}\left(\frac{f\,\eta_\chi\,v_r\,v_\phi}{m_H^2 - m_h^2}\right)^2\sqrt{m_H^2 - 4m_w^2}.
\tag{4.2.55}
$$

Assuming $m_H \gg m_h$, this decay width is

$$
\Gamma_{H\to\text{hidden}} = \frac{\eta_\chi^2 v_\phi^2}{16\pi m_H} + \frac{\eta_\chi^2\Delta m^2 v_\phi^2}{64\pi m_H^3}.
\tag{4.2.56}
$$

Comparing (4.2.34) and (4.2.56) we obtain

$$
|\Delta m| > 2m_H\sqrt{\frac{8.3\times 10^{-5}}{\eta_\chi^2} - 1},
\tag{4.2.57}
$$

which is satisfied if $|\eta_\chi| < 0.009$.

4.2.3 Constraints from Direct Detection Experiments

Direct detection experiments attempt to observe the recoil from the elastic scattering of dark matter particles interacting with nuclei in the detector. Since the late 90's the DAMA/NaI Collaboration [303] has been claiming to observe the expected annual modulation of the dark matter induced nuclear recoil rate due to the rotation of the Earth around the Sun [304, 305]. The upgraded DAMA/LIBRA detector confirmed [306] the earlier result adding many more statistics, and it has reached a significance of 8.9σ for the cumulative exposure [68]. In 2010,

the CoGeNT Collaboration reported an irreducible excess in the counting rate [69], which may also be ascribed to a dark matter signal. One year later, the same collaboration reported further data analyses showing that the time-series of their rate is actually compatible with an annual modulation effect [70]. In CoGeNT data the evidence for the annual modulation is at the 2.8σ level. In the summer of 2011, the CRESST Collaboration also reported an excess of low energy events that are not consistent with known backgrounds [71]. In particular, 67 counts were found in the dark matter acceptance region and the estimated background from leakage of e/γ events, neutrons, α particles, and recoiling nuclei in α decays is not sufficient to account for all the observed events. The CRESST Collaboration rejected the background-only hypothesis at more than 4σ. Of particular interest here, the DAMA (after including the effect of channeling in the NaI crystal scintillators [307]) and CoGeNT results appear to be compatible with a relatively light dark matter particle, in the few GeV to tens of GeV mass range, with a scattering cross section against nucleons of about 7×10^{-41} cm^2 [266, 267, 268, 269]. The central value favored by CRESST data points to somewhat larger dark matter masses, but it is still compatible at the 1σ level with the range determined by the other two experiments.

Very recently, CDMS II Collaboration reported three candidate events with an expected background of 0.7 events [72]. If interpreted as a signal of elastically scattering dark matter, the central value of the likelihood analysis of the measured recoil energies favors a mass of 8.6 GeV and a scattering cross section on nucleons of

$$\sigma_{wN}^{m_w \approx 10 \text{ GeV}} \approx 1.9 \times 10^{-41} \text{ cm}^2 \,. \tag{4.2.58}$$

The 68% confidence band is somewhat large and overlaps with previous signal claims.

Alongside these "signals" stands the series of null results from the XENON-100 [286] and XENON-10 [308] experiments, which at present have the world's strongest exclusion limit. Some authors have pointed out that uncertainties in the response of liquid xenon to low energy nuclear recoil may be significant, particularly in the mass region of interest [309, 310]. In light of these suspicions, a recent re-analysis of XENON data suggests candidates in fact may have been observed [74]. The data favor a mass of 12 GeV, though the 90% error contours extend from 7 to 30 GeV with the cross section varying between 6×10^{-41} cm^2 and 4×10^{-45} cm^2. Taken together, these different arguments suggest that the existing data set is not inconsistent with a dark matter candidate of about 10 GeV.

The wN cross section for elastic scattering is given by

$$\sigma_{wN} = \frac{4}{\pi} \frac{m_w^2 m_N^2}{(m_w + m_N)^2} \frac{f_p^2 + f_n^2}{2}, \qquad (4.2.59)$$

where $N \equiv \frac{1}{2}(n + p)$ is an isoscalar nucleon, in the renormalization group-improved parton model [311, 312]. The effective couplings to protons f_p and neutrons f_n are given by

$$f_{p,n} = \sum_{q=u,d,s} \frac{G_q}{\sqrt{2}} f_{Tq}^{(p,n)} \frac{m_{p,n}}{m_q} + \frac{2}{27} f_{TG}^{(p,n)} \sum_{q=c,b,t} \frac{G_q}{\sqrt{2}} \frac{m_{p,n}}{m_q}, \qquad (4.2.60)$$

where G_q is the W-WIMP's effective Fermi coupling for a given quark species,

$$\mathscr{L} = \frac{G_q}{\sqrt{2}} \bar{\psi}_- \psi_- \bar{\psi}_q \psi_q, \qquad (4.2.61)$$

with ψ_q the SM quark field of flavor q. The first term in (4.2.60) reflects scattering with light quarks, whereas the second term accounts for interaction with gluons through a heavy quark loop. The terms $f_{Tq}^{(p,n)}$ are proportional to the matrix element, $\langle \bar{q}q \rangle$, of quarks in a nucleon, and are given by

$$f_{Tu}^p = 0.020 \pm 0.004, \quad f_{Td}^p = 0.026 \pm 0.005, \quad f_{Ts}^p = 0.118 \pm 0.062,$$

$$f_{Tu}^n = 0.014 \pm 0.003, \quad f_{Td}^n = 0.036 \pm 0.008, \quad f_{Ts}^n = 0.118 \pm 0.062. \qquad (4.2.62)$$

We also have $f_{TG}^{(p,n)} = 1 - \sum_{u,d,s} f_{Tq}^{(p,n)}$, which is $f_{TG}^p \approx 0.84$ and $f_{TG}^n \approx 0.83$ [311].

To establish the value of G_q/m_q we look back at (4.2.32) along with the SM Yukawa interaction term, which involves the mixing of both scalar fields, H and h. For interactions of W-WIMPs with SM quarks, the relevant terms are

$$\mathscr{L} = \frac{m_q \cos \chi}{v_\phi} H \bar{\psi}_q \psi_q - \frac{m_q \sin \chi}{v_\phi} h \bar{\psi}_q \psi_q + \cdots + \frac{f \sin \chi}{2} H \bar{\psi}_- \psi_- + \frac{f \cos \chi}{2} h \bar{\psi}_- \psi_-. \quad (4.2.63)$$

The scattering of a w particle off a quark then gives

$$\begin{aligned}
\mathcal{M} &= i \frac{f m_q \sin \chi \cos \chi}{v_\phi} \bar{u}_q(p') u_q(p) \left(\frac{1}{t - m_H^2} - \frac{1}{t - m_h^2} \right) \bar{u}(k') u(k) \\
&\approx i \frac{f m_q \eta_\chi v_r}{m_H^2 m_h^2} \bar{u}_q(p') u_q(p) \bar{u}(k') u(k) \\
&\approx i \frac{m_q \eta_\chi \Delta m}{2 m_H^2 m_h^2} \bar{u}_q(p') u_q(p) \bar{u}(k') u(k).
\end{aligned} \qquad (4.2.64)$$

This leads to the identification of the effective coupling

$$\frac{2 G_q}{\sqrt{2}} = \frac{m_q \eta_\chi \Delta m}{2 m_H^2 m_h^2} \Rightarrow \frac{G_q}{m_q} = \frac{\eta_\chi \Delta m}{2 \sqrt{2} \, m_H^2 m_h^2}. \qquad (4.2.65)$$

Insertion of (4.2.65) and (4.2.60) into (4.2.59) yields

$$\sigma_{wN} \approx 3 \times 10^{-7} \left[\frac{226.27 \, \eta_\chi \Delta m \, \text{GeV}}{m_h^2} \right]^2 \text{pb} \,. \tag{4.2.66}$$

Combining (4.2.66) with the signals/bounds on elastic scattering of dark matter particles on nucleons we obtain a constraining relation for $\eta_\chi \Delta m$. For $m_w = 10 \text{ GeV}$, we use the cross section reported by CDMS Collaboration (4.2.58) to obtain

$$\eta_\chi \Delta m = \frac{3.5 \times 10^{-2}}{\text{GeV}} \, m_h^2 \,. \tag{4.2.67}$$

For $m_w = 50 \text{ GeV}$, we adopt the 90% CL upper limit reported by the XENON-100 Collaboration [286] to obtain

$$\eta_\chi \Delta m < \frac{3.6 \times 10^{-4}}{\text{GeV}} \, m_h^2 \,. \tag{4.2.68}$$

4.2.4 Constraints from Cosmological Observations

As noted in [15] the Goldstone boson α is a natural candidate for an impostor equivalent neutrino. The contribution of α to N_{eff} is $\Delta N = \rho_\alpha / \rho_{\nu_L}$, which can also be expressed as

$$\Delta N = \frac{4}{7} \left(\frac{g(T_{\nu_L}^{\text{dec}})}{g(T_\alpha^{\text{dec}})} \right)^{4/3} \,, \tag{4.2.69}$$

where $g(T) = g_S(T) \approx g_\rho(T)$ is the effective number of interacting (thermally coupled) relativistic degrees of freedom at temperature T [49].

We now turn to calculating the interaction rate for Goldstone bosons,

$$\Gamma(T) = \sum_{\text{fermions}} n_{\text{f}}(T) \langle \sigma v \rangle \,, \tag{4.2.70}$$

where

$$n_{\text{f}}(T) = \frac{g_{\text{f}}}{2\pi^2} \int_0^\infty \frac{k^2}{e^{\beta\sqrt{k^2+m_{\text{f}}^2}} + 1} dk \tag{4.2.71}$$

is the number density of an interacting fermion of type f (with mass m_{f}) in thermal equilibrium with, $\beta = (k_B T)^{-1}$, and g_{f}, the number of chiral states. The average in (4.2.70), indicates an average over the statistical distribution for a given temperature. For $T \gg m_{\text{f}}$, we obtain

$$n_{\text{f}}(T) \approx g_{\text{f}} \frac{3\zeta(3)}{4\pi^2} \left(\frac{k_B T}{\hbar c} \right)^3 \,. \tag{4.2.72}$$

This results in a simplification of (4.2.70)

$$\Gamma(T) \approx \frac{3\zeta(3)}{4\pi^2} \left(\frac{k_B T}{\hbar c}\right)^3 \sum_{\text{fermions}} g_{\text{f}} \langle \sigma v \rangle. \tag{4.2.73}$$

Since the Goldstone boson only interacts with the SM fields via the Higgs, we can have scatterings of the type $\alpha\psi \to \alpha\psi$, with ψ a generic SM fermion. The α scattering off fermions is described by SM Yukawa interaction terms that can be written as

$$
\begin{aligned}
Y_{\text{f}} \phi \bar{\psi} \psi \quad &\to \quad Y_{\text{f}} v_\phi \bar{\psi} \psi + Y_{\text{f}} \phi' \bar{\psi} \psi, \\
&= \quad m_{\text{f}} \bar{\psi} \psi + \frac{m_{\text{f}}}{v_\phi} H \bar{\psi} \psi \, \cos\chi - \frac{m_{\text{f}}}{v_\phi} h \bar{\psi} \psi \, \sin\chi \, ,
\end{aligned}
\tag{4.2.74}
$$

where Y_{f} is the Yukawa coupling of the fermion in question.

We proceed to calculate the scattering cross section. The invariant amplitude follows from the Feynman rules

$$
\begin{aligned}
i\mathcal{M} \quad = \quad & \frac{2m_f \sin\chi \cos\chi}{v_r v_\phi} (k \cdot k') \frac{i}{t - m_H^2} \bar{u}(p') u(p) \\
& - \frac{2m_f \cos\chi \sin\chi}{v_r v_\phi} (k \cdot k') \frac{i}{t - m_h^2} \bar{u}(p') u(p).
\end{aligned}
\tag{4.2.75}
$$

The momenta of incoming and outgoing (outgoing primed) particles are defined by

$$
\begin{aligned}
p^\mu \quad &= \quad (p, p \sin\varphi, 0, -p \cos\varphi) \\
k^\mu \quad &= \quad (k, 0, 0, k) \\
k'^\mu \quad &= \quad (k', k' \sin\vartheta, 0, k' \cos\vartheta) \\
p'^\mu \quad &= \quad (p', -p' \sin\vartheta', 0, -p' \cos\vartheta') \, ,
\end{aligned}
\tag{4.2.76}
$$

with $t = p' - p$. To obtain the (unpolarized) cross section, we have to take the square of the modulus of $\mathcal{M}$ and then carry out the spin and color (if appropriate) sums

$$\frac{1}{2} \sum_{\text{spins, colors}} |\mathcal{M}|^2 = 8N_c \left(\frac{m_f \sin\chi \cos\chi}{v_r v_\phi}\right)^2 \left(\frac{m_H^2 - m_h^2}{(t - m_H^2)(t - m_h^2)}\right)^2 (k \cdot k')^2 (p \cdot p' + m_f^2), \tag{4.2.77}$$

where $N_c = 3$ for quarks and $N_c = 1$ for leptons. The cross section in the center-of-mass frame (c.m.) in the highly relativistic approximation is given by

$$\frac{d\sigma}{d\Omega} \approx \frac{N_c}{8\pi^2 s} \left(\frac{m_f \eta_\chi}{(t - m_H^2)(t - m_h^2)}\right)^2 (k \cdot k')^2 (p \cdot p') \, , \tag{4.2.78}$$

where $s = (k + p)^2 \approx 4k^2$ and finally $\eta_\chi \ll 1$. To make progress on this problem we take the effective coupling form

$$\sigma(s) \approx \frac{N_c}{64\pi} \left(\frac{m_f \eta_\chi}{m_H^2 m_h^2}\right)^2 s^2 . \tag{4.2.79}$$

Non-equilibrium thermal physics tells us that the way to do thermal averaging within Boltzmann's approximation is

$$
\begin{aligned}
\langle \sigma v \rangle &= \int d\Pi_{p'} d\Pi_{k'} d\Pi_k d\Pi_p |\mathcal{M}(k + p \to k' + p')|^2 f_{\mathrm{f}}(p, T) f_\alpha(k, T) \\
&\times (2\pi)^4 \delta^{(4)}(p + k - p' - k'),
\end{aligned}
\tag{4.2.80}
$$

with $d\Pi_p = d^3 p' / [(2\pi)^3 2 E_{p'}]$ and likewise for the other parameters. Here, f_{f} and f_α are Fermi and Bose equilibrium normalized distributions, corresponding to the f fermion and α boson, respectively. The expression from non-equilibrium thermal physics [Eq. (4.2.80)] is approximated by

$$\langle \sigma v \rangle \approx \int \frac{d^3 k}{(2\pi)^3} \frac{d^3 p}{(2\pi)^3} f_{\mathrm{f}}(p, T) f_\alpha(k, T) \, v_M \, \sigma(s) , \tag{4.2.81}$$

where $v_M \approx k \cdot p/(pk) = 2(1 + \cos\varphi)$ is the Möller velocity in the ultra-relativistic limit [313, 314] and $s = 2kp(1 + \cos\varphi)$ is the c.m. energy of two interacting particles with initial momenta not necessarily co-linear. The velocity average cross section then is found to be

$$
\begin{aligned}
\langle \sigma v \rangle &\approx \frac{1}{8\pi^4} \int_0^\infty p^2 dp \int_0^\infty k^2 dk \int_0^\pi \sin\varphi \, d\varphi \, f_{\mathrm{f}}(p, T) f_\alpha(k, T) \\
&\times 2(1 + \cos\varphi) \, \sigma_{\mathrm{c.m.}}[2kp(1 + \cos\varphi)], \\
&= N_c \frac{15 \zeta^2(5)}{\pi \zeta^2(3)} \left(\frac{m_f \eta_\chi}{m_H^2 m_h^2}\right)^2 (k_B T)^4, \\
&\approx 3.55 N_c \left(\frac{m_f \eta_\chi}{m_H^2 m_h^2}\right)^2 (k_B T)^4.
\end{aligned}
\tag{4.2.82}
$$

Putting this all together, we obtain

$$\Gamma(T) \approx 0.32 \left(\frac{\eta_\chi}{m_H^2 m_h^2}\right)^2 (k_B T)^7 \sum_{\mathrm{fermions}} g_{\mathrm{f}} \, N_c \, m_{\mathrm{f}}^2. \tag{4.2.83}$$

Now, since we can approximate the energy density (at high temperatures) by including only particles species i with $T \gg m_i$, it follows that

$$\rho_{\mathrm{R}} = \left(\sum_{\mathrm{bosons}} g_{\mathrm{b}} + \frac{7}{8} \sum_{\mathrm{fermions}} g_{\mathrm{f}}\right) \frac{\pi^2}{30} (k_B T)^4 = \frac{\pi^2}{30} g(T) (k_B T)^4 \tag{4.2.84}$$

and therefore the Hubble parameter (4.1.69) becomes

$$H(T) \simeq \frac{1.66}{M_{\mathrm{Pl}}} \sqrt{g(T)} \, (k_B T)^2 , \tag{4.2.85}$$

where $g_{b(f)}$ is the number of degrees of freedom of each boson (fermion) and the sum runs over all boson and fermion states with $T \gg m_i$. The factor of 7/8 is due to the difference between the Fermi and Bose integrals.

The Goldstone boson decouples from the plasma when its mean free path becomes greater than the Hubble radius at that time

$$\Gamma(T_\alpha^{\text{dec}}) = H(T_\alpha^{\text{dec}}) \,. \tag{4.2.86}$$

The most interesting thermodynamics originates if α goes out of thermal equilibrium while T is still above the mass of the muons but below the mass of all other particles of the SM, a time when neutrinos are still in thermal equilibrium. For instance, with $\eta_\chi = 0.005$ and $m_h \approx 500$ MeV we obtain [15]

$$\Delta N = (4/7)(43/57)^{4/3} = 0.39 \,. \tag{4.2.87}$$

This corresponds to a number of equivalent light neutrino species that is consistent at the 1σ level with both the estimate of N_{eff} using Planck + BAO data as well as the estimate using Planck + H_0 data.

However, of particular interest here is the case where the mass of the Goldstone boson companion field is $m_h \approx 98$ GeV and $\eta_\chi = 0.0003$. For such set of parameters, α decouples when

$$0.32 \left(\frac{\eta_\chi}{m_H^2 m_h^2} \right)^2 (k_B T)^7 \, 12 \, m_b^2 = \frac{1.66}{M_{\text{Pl}}} \sqrt{86.25} \, (k_B T)^2 \,, \tag{4.2.88}$$

where we have approximated $\sum_{\text{fermions}} N_c \, g_f \, m_f^2 \approx 12 m_b^2$. This gives $T \approx 5$ GeV, and so the α contribution to N_{eff} is found to be

$$\Delta N \approx 0.036. \tag{4.2.89}$$

The corresponding value of N_{eff} is within the 1σ interval of the value reported by the Planck Collaboration using Planck + BAO data, but far out from the value derived using Planck + H_0 data. Should future data point towards the Planck + H_0 value, one should find a different origin to explain the extra relativistic degrees of freedom (if $m_h \approx 98$ GeV). One interesting possibility is to include the right-handed partners of the three left-handed, SM neutrinos. It was shown elsewhere [224, 141, 225, 226, 221] that milli-weak interactions of these Dirac states

(through their coupling to a TeV-scale Z' gauge boson) may allow the ν_R's to decouple during the course of the quark-hadron crossover transition, just so that they are partially reheated compared to the ν_L's. Remarkably, the required mass for the Z' gauge boson is within the range of discovery of LHC.

4.2.5 Fitting Fermi data and the Observed Dark Matter Density

Next, in line with our stated plan, we use *Fermi* data and the observed relic density to determine the free parameters of the model. To this end we first calculate the annihilation rate into SM fermions and Goldstone bosons.

4.2.6 W-WIMP Annihilation into SM Fermions

The W-WIMP can annihilate into SM fermions via $\bar{\psi}_-\psi_- \to \phi^*/r^* \to \bar{\psi}\psi$, with an s-channel Higgs or h mediator. The matrix element of this process is given by

$$i\mathcal{M} = if \sin\chi \, \cos\chi \, \bar{v}(p')u(p) \left(\frac{i}{s - m_H^2} - \frac{i}{s - m_h^2} \right) \frac{im_{\rm f}}{v_\phi} \bar{u}(k')v(k) \,. \tag{4.2.90}$$

The minus sign in the second propagator is necessary because the r couples with a negative sign to fermions compared to the Higgs; see (4.2.74). The spin-averaged invariant amplitude reads

$$\frac{1}{4}\sum|\mathcal{M}|^2 = N_c \left(\frac{fm_{\rm f}\sin\chi \, \cos\chi}{v_\phi} \right)^2 \frac{4 \, (m_h^2 - m_H^2)^2 \, (p\cdot p' - m_w^2)(k\cdot k' - m_{\rm f}^2)}{(s - m_h^2)^2(s - m_H^2)^2} \,. \tag{4.2.91}$$

Now, let's calculate the cross section for $f\bar{f}$-pair production

$$\begin{aligned}
d\sigma &= \frac{1}{8E_p|p|}|\mathcal{M}|^2 \frac{d^3k}{(2\pi)^3 2E_k} \frac{d^3k'}{(2\pi)^3 2E_{k'}}(2\pi)^4\delta^{(3)}(\mathbf{k}' + \mathbf{k}) \\
&\quad \times \quad \delta(2E_p - E_k - E_{k'}),
\end{aligned} \tag{4.2.92}$$

and so

$$\begin{aligned}
\sigma &= \frac{|\mathcal{M}|^2}{64\pi} \frac{|k'|}{|p|E_p^2} \\
&= \frac{N_c}{16\pi} \left(\frac{fm_{\rm f}\sin\chi \, \cos\chi}{v_\phi} \right)^2 \frac{|k'|}{|p|} \frac{(m_h^2 - m_H^2)^2}{(s - m_h^2)^2(s - m_H^2)^2} \frac{(p\cdot p' - m_w^2)\,(k\cdot k' - m_{\rm f}^2)}{E_p^2} \\
&\approx \frac{N_c}{16\pi} \left(\frac{\eta_\chi m_{\rm f}\Delta m}{2(s - m_h^2)(s - m_H^2)} \right)^2 \sqrt{\frac{|s - 4m_{\rm f}^2|}{|s - 4m_w^2|}} \frac{(s - 4m_w^2)(s - 4m_{\rm f}^2)}{s} \,. \tag{4.2.93}
\end{aligned}$$

In this case the out state does not consist of identical particles. For phenomenological purposes, the h pole needs to be softened to a Breit-Wigner form by obtaining and utilizing the correct total widths Γ_h of the resonance. This is accomplished by modification of the s-channel propagator for h via

$$\frac{i}{s - m_h^2} \rightarrow \frac{i}{s - m_h^2 - im_h\Gamma_h} . \tag{4.2.94}$$

It should be noted that we could also do the same analysis on the H pole which may also have some phenomenological interest as an independent analysis of the *Fermi* bubbles resulted in a best fit annihilation of dark matter of a particle with mass $m_w \approx 61$ GeV into $b\bar{b}$ [315]. After this is done, the contribution of the $f\bar{f}$ channel is as follows:

$$
\begin{aligned}
\sigma &= \frac{N_c}{16\pi} \left(\frac{\eta_\chi m_{\mathrm{f}} \Delta m}{2(m_H^2 - m_h^2)(s - m_H^2)} \right)^2 \frac{(m_H^2 - m_h^2)^2 + m_h^2 \Gamma_h^2}{(s - m_h^2)^2 + m_h^2 \Gamma_h^2} \sqrt{\frac{|s - 4m_{\mathrm{f}}^2|}{|s - 4m_w^2|}} \\
&\quad \times \frac{(s - 4m_w^2)(s - 4m_{\mathrm{f}}^2)}{s} , \\
&\approx \frac{N_c}{16\pi} \left(\frac{\eta_\chi m_{\mathrm{f}} \Delta m}{2(s - m_H^2)} \right)^2 \frac{1}{(s - m_h^2)^2 + m_h^2 \Gamma_h^2} \sqrt{\frac{|s - 4m_{\mathrm{f}}^2|}{|s - 4m_w^2|}} \frac{(s - 4m_w^2)(s - 4m_{\mathrm{f}}^2)}{s} .
\end{aligned}
\tag{4.2.95}
$$

For $\Delta m > m_H/2$, the decay channels of the h field are: $h \rightarrow f\bar{f}$, $h \rightarrow w\bar{w}$, and $h \rightarrow 2\alpha'$. The corresponding decay widths are given by

$$
\begin{aligned}
\Gamma_{h \rightarrow f\bar{f}} &= \sum_{\text{fermions}} \frac{N_c}{8\pi m_h^2} \left(\frac{m_{\mathrm{f}} \sin \chi}{v_\phi} \right)^2 (m_h^2 - 4m_{\mathrm{f}}^2)^{3/2} \\
&\approx \sum_{\text{fermions}} \frac{N_c}{8\pi m_h^2} \left(\frac{m_{\mathrm{f}} \eta_\chi v_r}{m_H^2 - m_h^2} \right)^2 (m_h^2 - 4m_{\mathrm{f}}^2)^{3/2} \\
&\approx \sum_{\text{fermions}} \frac{N_c}{8\pi m_h^2 f^2} \left(\frac{m_{\mathrm{f}} \eta_\chi \Delta m}{2(m_H^2 - m_h^2)} \right)^2 (m_h^2 - 4m_{\mathrm{f}}^2)^{3/2} \\
&\approx \frac{3}{8\pi m_h^2 f^2} \left(\frac{m_{\mathrm{b}} \eta_\chi \Delta m}{2(m_H^2 - m_h^2)} \right)^2 (m_h^2 - 4m_{\mathrm{f}}^2)^{3/2}
\end{aligned}
\tag{4.2.96}
$$

(in the last line we have taken $m_b < m_w < m_t$),

$$
\begin{aligned}
\Gamma_{h \rightarrow w\bar{w}} &= \frac{2 \left(m_h^2 - 4m_w^2 \right) f^2 \cos^2 \chi}{32\pi m_h^2} \sqrt{m_h^2 - 4m_w^2} \\
&\approx \frac{f^2}{16\pi m_h^2} (m_h^2 - 4m_w^2)^{3/2}
\end{aligned}
\tag{4.2.97}
$$

(inclusion of this channel requires $2m_w < m_h$), and

$$
\begin{aligned}
\Gamma_{h \to 2\alpha'} &= \frac{1}{32\pi} \left(\frac{\cos\chi}{v_r} \right)^2 m_h^3 \\
&\approx \frac{f^2}{8\pi\Delta m^2} m_h^3 .
\end{aligned}
\tag{4.2.98}
$$

The dominant terms of the total decay width come from the hidden sector. Hence, in what follows we neglect terms accounting for h decay into the visible sector and consider $m_h < 2m_w$ (so that the decay $h \to w\bar{w}$ is closed). Under these assumptions the decay width takes a particularly simple form

$$
\Gamma_h = \frac{f^2}{8\pi\Delta m^2} m_h^3 .
\tag{4.2.99}
$$

Next, we compute the averaged cross section for thermal interactions. In the cosmic co-moving frame (the frame where the gas is assumed to be at rest as a whole) we have

$$
\langle \sigma v \rangle = \frac{\int d^3p\, d^3p'\, f_w(p, T) f_w(p', T)\, \sigma v_M}{\int d^3p\, d^3p'\, f_w(p, T) f_w(p', T)} ,
\tag{4.2.100}
$$

where $\mathbf{p}$ and $\mathbf{p}'$ are the three-momenta of the colliding particles, whose equilibrium distribution function at temperature T is Maxwell-Boltzmann,

$$
f_w(p, T) \approx e^{-\beta\sqrt{p^2 + m_w^2}} ,
\tag{4.2.101}
$$

with $p = |\mathbf{p}|$ and $p' = |\mathbf{p}'|$. The Maxwell-Boltzmann distribution remains a good approximation provided $3\,m_w\,\beta > 1$. The Möller velocity can be expressed as

$$
v_M = \frac{1}{EE'}\sqrt{(p \cdot p')^2 - m_w^4} = \frac{1}{2EE'}\sqrt{s(s - 4m_w^2)} ,
\tag{4.2.102}
$$

where E and E' are the energies of the scattering particles. Note that in the c.m. frame the velocity of the colliding W-WIMPs is half the Möller velocity, $v = \sqrt{1 - 4m_w^2/s} = v_M/2$.

For $s \gg m_{\mathrm{f}}$, from (4.2.93) and (4.2.102) we obtain

$$
\sigma v_M = \frac{N_c}{8\pi} \left(\frac{\eta_\chi m_{\mathrm{f}} \Delta m}{2(s - m_h^2)(s - m_H^2)} \right)^2 (s - 4m_w^2) .
\tag{4.2.103}
$$

We evaluate (4.2.100) by expanding σv_M around

$$
s = 4E^2 = \frac{4m_w^2}{1 - v^2} \approx 4m_w^2(1 + v^2 + \dots)
\tag{4.2.104}
$$

to obtain a series solution in powers of v of which the leading order term is

$$
\langle \sigma v \rangle \approx \frac{N_c}{2\pi} \left(\frac{\eta_\chi m_{\mathrm{f}} m_w \Delta m}{2(4m_w^2 - m_h^2)(4m_w^2 - m_H^2)} \right)^2 \langle v^2 \rangle ,
\tag{4.2.105}
$$

where $\langle v^2 \rangle$ is the W-WIMP thermally averaged velocity.

All in all, the total average annihilation cross section into SM particles (labelled by subindex i) is given by

$$\sum_{\text{fermions}} \langle \sigma_i v \rangle \approx \frac{3}{2\pi} \left(\frac{\eta_\chi m_b m_w \Delta m}{2(4m_w^2 - m_H^2)} \right)^2 \frac{\langle v^2 \rangle}{(4m_w^2 - m_h^2)^2 + m_h^2 \Gamma_h^2} , \qquad (4.2.106)$$

where we have assumed that the overwhelming contribution into $b\bar{b}$ dominates the process.

Provided the theory is not strongly coupled, (4.2.106) is generally a good approximation for relativistic particles, but for low velocities and in the presence of a long-range force (classically, when the potential energy due to the long-range force is comparable to the particles' kinetic energy), the perturbative approach breaks down. In the non-relativistic limit, the question of how the long-range potential modifies the cross section for short-range interactions can be formulated as a scattering problem in quantum mechanics, with significant modifications to the cross sections occurring when the particle wavefunctions are no longer well approximated by plane waves (so the Born expansion is not well-behaved). The deformation of the wavefunctions due to a Coulomb potential was calculated by Sommerfeld [316], yielding a $\sim 1/v$ enhancement to the cross section for short-range interactions (where the long-range behavior due to the potential can be factorized from the relevant short-range behavior). Along these lines, for low-velocity ($v \sim 10^{-3}$) W-WIMPs in our Galactic halo, we expect interactions with the H and h fields to enlarge the cross section, as the attractive Yukawa potential

$$V_w(r) = -\frac{f^2 \cos^2(\chi)}{4\pi} \frac{e^{-m_h r}}{r} - \frac{f^2 \sin^2(\chi)}{4\pi} \frac{e^{-m_H r}}{r} \approx -\frac{f^2}{4\pi} \frac{e^{-m_h r}}{r} \simeq -\frac{f^2}{4\pi} \frac{1}{r} . \qquad (4.2.107)$$

cause passing W-WIMPS to be drawn toward each other [317]. For p-wave scattering, $\langle v^2 \rangle \rightarrow \langle S(v) v^2 \rangle$, where

$$S(v) \approx \frac{\pi \tilde{\alpha}}{v} \frac{1}{1 - e^{-\pi \tilde{\alpha}/v}} \left(1 + \frac{\pi^2 \tilde{\alpha}^2}{4v^2} \right) , \qquad (4.2.108)$$

is the Sommerfeld enhancement factor in the Coloumb approximation, with $\tilde{\alpha} = f^2/(4\pi)$ [318]. Following [319] we compute the thermally averaged Sommerfeld enhancement factor by approximating $\left(1 - e^{-\pi \tilde{\alpha}/v} \right)^{-1}$ with $\tilde{\alpha} \ll 1$

$$\langle S(v) v^2 \rangle \approx 6x^{-1} + 4\sqrt{\pi} \tilde{\alpha} x^{-1/2} + \frac{4\pi^2 \tilde{\alpha}^2}{3} + \pi^{5/2} \tilde{\alpha}^3 x^{1/2} + \frac{\pi^4 \tilde{\alpha}^4}{6} x, \qquad (4.2.109)$$

where $x = m_w/T$. Figure 4.2.6 shows the effect of the Sommerfeld enhancements at low temperatures. For interactions in the Galactic halo (G.h.), we have $\langle v^2 \rangle \sim 10^{-6}$, and therefore
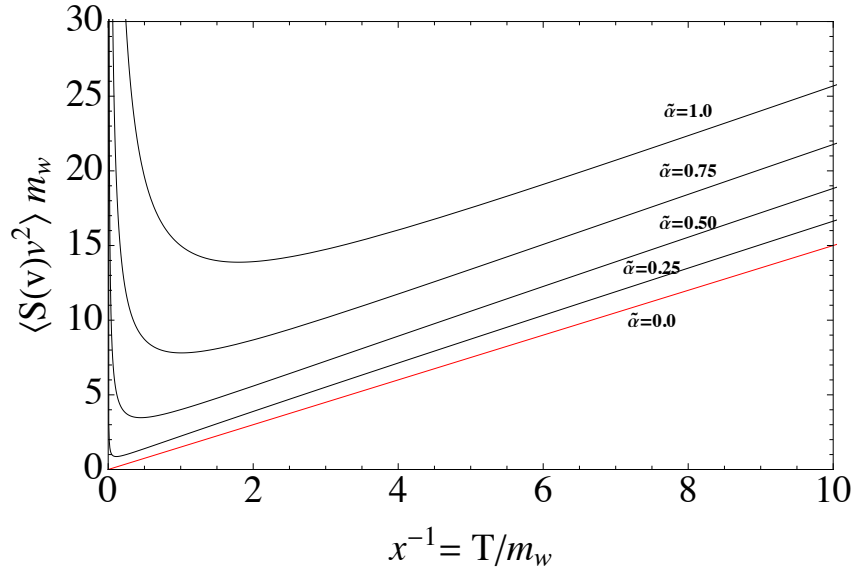
Figure 48 : Sommerfeld enhancements allow the thermally averaged cross section to increase at low temperatures T. The figure shows varying values of $\tilde{\alpha}$ and the red curve is the result with no Sommerfeld enhancement.

the thermally average annihilation cross section into $b\bar{b}$ becomes

$$
\begin{aligned}
\langle \sigma_b v \rangle &\approx \frac{3}{2\pi} \left(\frac{\eta_\chi m_b m_w \Delta m}{2(4m_w^2 - m_H^2)} \right)^2 \frac{1}{(4m_w^2 - m_h^2)^2 + m_h^2 \Gamma_h^2} \\
&\times \frac{1}{4} \left(6 x_{\text{G.h.}}^{-1} + 4\sqrt{\pi}\tilde{\alpha} x_{\text{G.h.}}^{-1/2} + \frac{4\pi^2 \tilde{\alpha}^2}{3} + \pi^{5/2}\tilde{\alpha}^3 x_{\text{G.h.}}^{1/2} + \frac{\pi^4 \tilde{\alpha}^4}{6} x_{\text{G.h.}} \right),
\end{aligned}
$$
(4.2.110)

with $x_{\text{G.h.}} \approx 3 \times 10^6$.

4.2.7   W-WIMP Annihilation into Pairs of Goldstone Bosons

In addition to the annihilation into SM fermions we must consider the $w\bar{w} \to 2\alpha'$ annihilation channel. The invariant amplitude for this process is given by

$$
i\mathcal{M} = \frac{2if}{v_r} \bar{v}(p) u(p') \left(\frac{\sin^2 \chi}{s - m_H^2} - \frac{\cos^2 \chi}{s - m_h^2} \right) k \cdot k'.
$$
(4.2.111)

We then average over the in state spins to obtain

$$
\frac{1}{4} \sum_{s,s'} |\mathcal{M}|^2 = \frac{f^2 s^2 [(s - m_h^2)\sin^2 \chi - (s - m_H^2)\cos^2 \chi]^2}{2v_r^2 (s - m_h^2)^2 (s - m_H^2)^2} (s - 4m_w^2).
$$

The general expression for the cross section reads

$$
\sigma = \frac{1}{16\pi\sqrt{s}\sqrt{|s - 4m_w^2|}} \frac{f^4 s^2 [(s - m_h^2)\sin^2 \chi - (s - m_H^2)\cos^2 \chi]^2}{\Delta m^2 (s - m_h^2)^2 (s - m_H^2)^2} (s - 4m_w^2).
$$
(4.2.112)

Using the small angle approximation, *i.e.* $\cos\chi \approx 1$, we obtain

$$\sigma \approx \frac{f^2 s^2 \sqrt{|s - 4m_w^2|}}{16\pi\sqrt{s}(s - m_h^2)^2} \left(\frac{f^2}{\Delta m^2} + \frac{(m_h^2 + m_H^2 - 2s)}{2(s - m_H^2)^2} \frac{\eta_\chi^2 v_\phi^2}{(m_H^2 - m_h^2)^2} \right) . \qquad (4.2.113)$$

Taking a thermal average gives

$$\langle \sigma_{\alpha'} v \rangle \approx \frac{2f^4 m_w^4}{\pi \Delta m^2 [(m_h^2 - 4m_w^2)^2 + m_h^2 \Gamma_h^2]} \langle v^2 \rangle . \qquad (4.2.114)$$

If the W-WIMPs are highly non-relativistic we have to correct (4.2.114) to account for the Sommerfeld enhancement

$$\langle \sigma_{\alpha'} v \rangle \approx \frac{2f^4 m_w^4}{\pi \Delta m^2 [(m_h^2 - 4m_w^2)^2 + m_h^2 \Gamma_h^2]} \langle S(v) v^2 \rangle . \qquad (4.2.115)$$

4.2.8 W-WIMP Parameter Fits

The total flux of γ-rays per solid angle from W-WIMP annihilation into SM particles (labelled by subindex i) is given by

$$\frac{d\Phi_\gamma}{dE_\gamma} = \sum_{\text{fermions}} \frac{\langle \sigma_i v \rangle}{2} \frac{\mathcal{J}_{\Delta\Omega}}{J_0} \frac{1}{\Delta\Omega_{\text{obs}} m_w^2} \left. \frac{dN_\gamma}{dE_\gamma} \right|_i , \qquad (4.2.116)$$

where $\mathcal{J}/J_0$ is the normalized integral of mass density squared of the dark matter in the line of sight, dN_γ/dE_γ is the γ-ray spectrum per annihilation into particle species i, $\Delta\Omega_{\text{obs}}$ is the observational solid angle in steradians, and the sum runs over all possible annihilation channels. It is noteworthy that $d\Phi_\gamma/dE_\gamma$ is the total photon number flux per unit energy per unit steradian for a full sky observation and, when compared to the total photon count of the Fermi-LAT observation with $|b| > 10°$, must be scaled to the field of view of that observation, $\Delta\Omega_{\text{obs}} = 10.4$ sr. From (4.2.106) we see that, for 10 GeV $< m_w < 50$ GeV, the dominant annihilation channel is $b\bar{b}$. Annihilation into $c\bar{c}$ and $\tau^+\tau^-$ are suppressed by about an order of magnitude. Hereafter we make the case for a w with a mass of about 50 GeV, which annihilates into $b\bar{b}$. The photon flux expected from the *Fermi* Bubbles is shown in Fig. 4.2.8. Comparing (4.2.2) and (4.2.106) we obtain

$$\begin{aligned}
\langle \sigma_b v \rangle &\approx \frac{3}{2\pi} \left(\frac{\eta_\chi m_b m_w \Delta m}{2(4m_w^2 - m_H^2)} \right)^2 \frac{1}{(4m_w^2 - m_h^2)^2 + m_h^2 \Gamma_h^2} \\
&\quad \frac{1}{4} \left(6x_{\text{G.h.}}^{-1} + 4\sqrt{\pi}\tilde{\alpha} x_{\text{G.h.}}^{-1/2} + \frac{4\pi^2 \tilde{\alpha}^2}{3} + \pi^{5/2} \tilde{\alpha}^3 x_{\text{G.h.}}^{1/2} + \frac{\pi^4 \tilde{\alpha}^4}{6} x_{\text{G.h.}} \right) \\
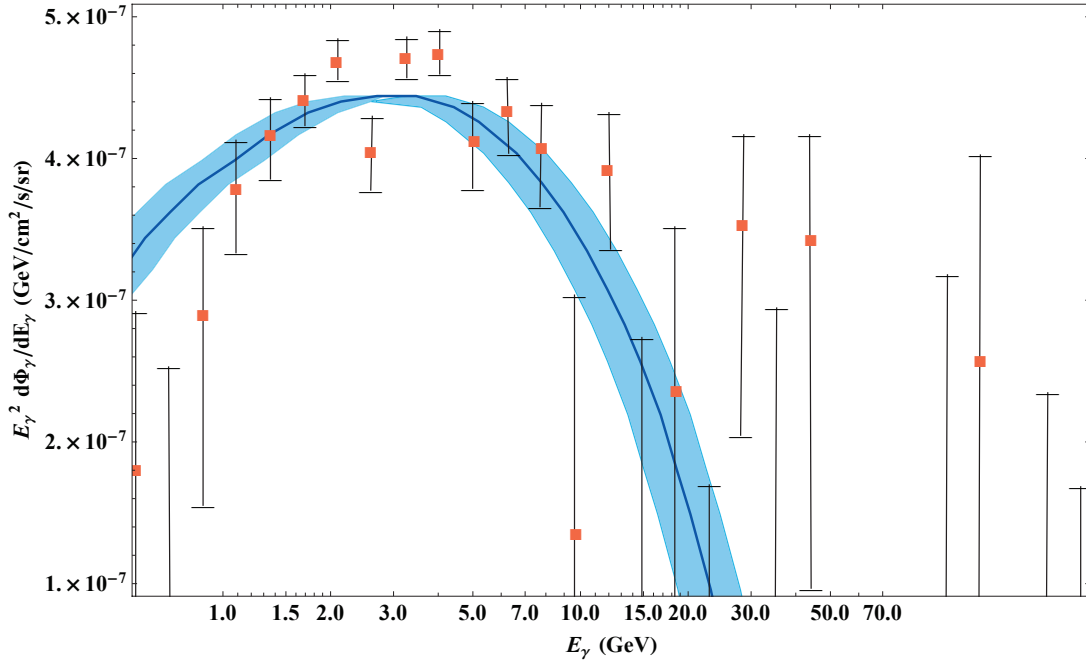&= 6.7 \times 10^{-10} \text{GeV}^{-2} .
\end{aligned}$$

$$(4.2.117)$$

Figure 49 : Comparisons of the observed γ-ray spectrum of the low-latitude ($|b| = 10° - 20°$) emission, after subtracting the contribution from inverse Compton scattering to that predicted from 50 GeV W-WIMPs annihilating to $b\bar{b}$. We have adopted a generalized NFW profile with an inner slope of $\gamma = 1.2$, and normalized the signal to a local density of 0.4 GeV/cm^3 and an annihilation cross section of $\langle \sigma_b v \rangle = 8 \times 10^{-27}$ cm^3/s. The band shows the variation in the mass range 45 GeV $< m_w < 55$ GeV for the same normalization. Adapted from Fig. 14 of Ref. [274].

To be produced thermally in the early universe in an abundance equal to the measured dark matter density, $\Omega_{\mathrm{DM}} h^2 = 0.1120 \pm 0.0056$ [1], the 50 GeV w-particle must have an annihilation cross section of

$$\sum_{\mathrm{all\,species}} \langle \sigma_i v \rangle \sim 3 \times 10^{-26} \text{ cm}^3/\text{s} = 2.5 \times 10^{-9} \text{ GeV}^{-2}, \tag{4.2.118}$$

when thermally averaged over the process of freeze-out, $x_{\mathrm{f.o.}} \sim 20$ [320, 251]. It is noteworthy that for $\tilde{\alpha} \lessapprox 0.01$ the effect of the Sommerfeld enhancement on the final relic particle abundance is negligible [321, 322]. Herein we will work on the range of the coupling $\tilde{\alpha}$ over which Sommerfeld annihilation can be neglected in the calculation of relic densities. Because *a priori* we do not know whether $\langle \sigma_{\alpha'} v \rangle$ or $\langle \sigma_b v \rangle$ dominates the total annihilation cross section at freeze-out, we combine (4.2.106) and (4.2.114) evaluated at $v(x_{\mathrm{f.o.}})$ together with (4.2.118) to

Table 9 : Best fit parameters for $\Delta m = 6000$ GeV.

Δm	6000 GeV
m_h	98.8 GeV
f	0.34
$\tilde{\alpha}$	0.009
η_χ	1.8×10^{-4}
χ	0.049
$\Gamma_{H \to \text{invisible}}$	0.65 MeV
$\langle \sigma_{\alpha'} v(x_{\text{f.o.}}) \rangle$	2.7×10^{-26} cm^{3}s^{-1}
$\langle \sigma_b v(x_{\text{f.o.}}) \rangle$	0.3×10^{-26} cm^{3}s^{-1}
$\langle \sigma_{\alpha'} v(x_{\text{G.h.}}) \rangle$	7.8×10^{-26} cm^{3}s^{-1}

obtain

$$\left[\frac{2f^4 m_w^4}{\pi \Delta m^2} + \frac{3}{2\pi} \left(\frac{\eta_\chi m_b m_w \Delta m}{2(4m_w^2 - m_H^2)} \right)^2 \right] \frac{1}{(4m_w^2 - m_h^2)^2 + m_h^2 \Gamma_h^2} \frac{3}{2x_{\text{f.o.}}} \approx 2.5 \times 10^{-9} \text{GeV}^{-2}.$$
(4.2.119)

To determine the allow region of the parameter space, for $m_w = 50$ GeV, we solve (4.2.117) and (4.2.119) while simultaneously demanding that $\tilde{\alpha} \lessgtr 0.01$, and that the upper limit on the invisible decay width for the SM Higgs (4.2.34) is not violated by (4.2.55). The best fit parameters are given in Table 9, for an example with $\Delta m = 6000$ GeV. We can see that the annihilation into pairs of Goldstone bosons is dominating the $w\bar{w}$ interactions at freeze-out by a factor of about 9. Precise determination of the parameters is at present hampered by the large uncertainties in the dark matter halo profile. Interestingly, the W-WIMP-nucleon cross section is within the reach of the XENON1T experiment [323], providing a strong motivation for the ideas discussed in this section. Again I reiterate that the fine tuned nature of the dark sector may be avoidable by the use of the result of $m_w = 61$ GeV [315] we may fit the result to the Higgs pole.

Duplicating the procedure described above, we have scanned the mass range of the parameter space that is consistent with Fermi data: 45 GeV $< m_w < 55$ GeV; see Fig. 4.2.8. Our

results are encapsulated in Figs. 4.2.8, 4.2.8 and 4.2.8. In particular, Fig. 4.2.8 and 4.2.8 display, for $\Delta m = 5500$ GeV, the region of the parameter space of m_w vs. σ_{wN} not yet excluded by current direct detection experiments or the LHC. Future LHC data will either more tightly constrain this parameter space or will turn up evidence for a signal. Note that the region excluded by nonexistence of a solution ($\Gamma_{H \to \text{invisible}} \approx 0.3$ MeV) up to the current LHC bound will be very tightly constrained after the LHC coming upgrade, assuming no signal appears. In the case that a signal does appear, the combination of relations shown in Figs. 4.2.8 and 4.2.8 will constrain model parameters providing the XENON1T experiment with the specific cross section required to confirm this model. As an illustration, in Fig. 4.2.8 we show contours of constant η_χ in the $\Delta m - m_w$ plane for the case in which $\mathcal{B}(H \to \text{invisible})$ saturates the current limit, $\Gamma_{H \to \text{invisible}} = 0.8$ MeV. The direct detection cross section sampling this sub-region of the parameter space varies between 1.8×10^{-46} cm^2 and 2.2×10^{-46} cm^2, with an average of 1.9×10^{-46} cm^2.

4.2.9 W-WIMP Interpretation for Hints of Light Dark Matter

Signals broadly compatible with ~ 10 GeV dark matter have been observed in four direct detection experiments: DAMA/LIBRA [68], CoGeNT [69, 70], CRESST [71], and CDMS-II [72]. In this section we explore the compatibility with one particular region of the W-WIMP parameter space. The features of this region of the parameter space has bearing on the evidence for extra-relativistic degrees of freedom at the CMB epoch.

In order to elaborate on the case for $m_w \sim 10$ GeV, we consider $m_h \approx 500$ MeV and $\eta_\chi \approx 0.005$. Substituting these values in (4.2.67), it is straightforward to see that to comply with the elastic cross section "signal" reported by the CDMS Collaboration [72], we must set $\Delta m \approx 1.75$ GeV. This in turn determines via (4.2.106) a thermal average annihilation cross section into quarks: $\langle \sigma_b v(x_{\text{G.h.}}) \rangle \approx 1.3 \times 10^{-39}$ cm^3 s^{-1}. Note that this is more than ten orders of magnitude smaller than current limits on light dark matter from anti-proton data [324, 325, 326].

The observed dark matter density is obtained again through dominant W-WIMP annihilation into the hidden sector. To demonstrate this point, we must first compute the $w\bar{w} \to 2h$ annihilation cross section, as this channel is now open. We consider the relevant terms of
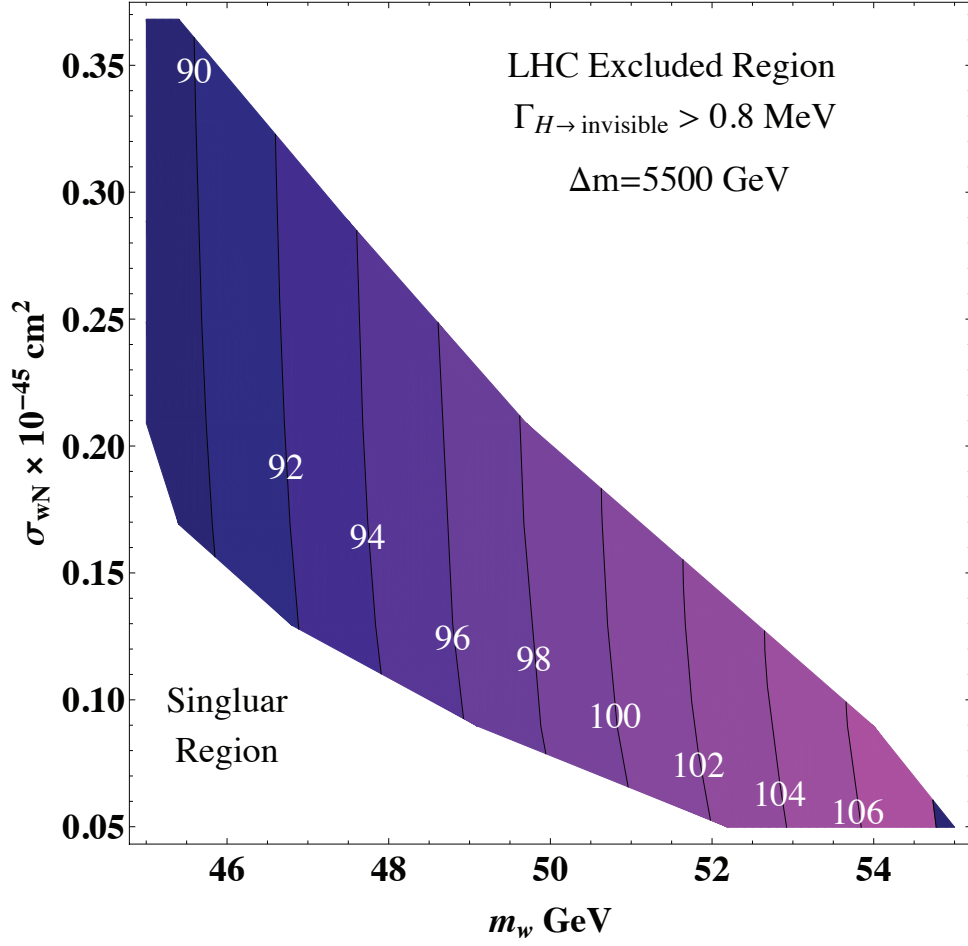
Figure 50 : Contours of constant m_h/GeV in the $\sigma_{wN} - m_w$ plane. The contours satisfy *Fermi* data, the relic density requirement, and the LHC bound $\mathcal{B}(H \to \text{ invisible})$. We have required $\tilde{\alpha} \lessgtr 0.01$ and taken $\Delta m = 5500$ GeV.

(4.2.32),

$$\frac{f \cos \chi}{2} h \bar{\psi}_- \psi_- + \frac{f \sin \chi}{2} H \bar{\psi}_- \psi_- \;, \tag{4.2.120}$$

as well as the relevant terms of the scalar potential

$$\mathcal{V} \approx \cdots - \frac{m_h^2}{2 v_r} h^3 - \frac{\eta_\chi v_\phi}{2} \left(\frac{m_H^2 + 2m_h^2}{m_H^2 - m_h^2} \right) H h^2 \;; \tag{4.2.121}$$

together this gives the total reaction matrix element

$$\begin{aligned}
\mathcal{M} &= if\bar{v}(p)u(p') \frac{i}{s - m_h^2} \left(\frac{-i3! m_h^2}{2 v_r} \right) + if \frac{\eta_\chi v_r v_\phi}{m_H^2 - m_h^2} \bar{v}(p)u(p') \frac{i}{s - m_H^2} \\
&\times \left(\frac{-i\eta_\chi v_\phi (m_H^2 + 2m_h^2)}{m_H^2 - m_h^2} \right) .
\end{aligned} \tag{4.2.122}$$

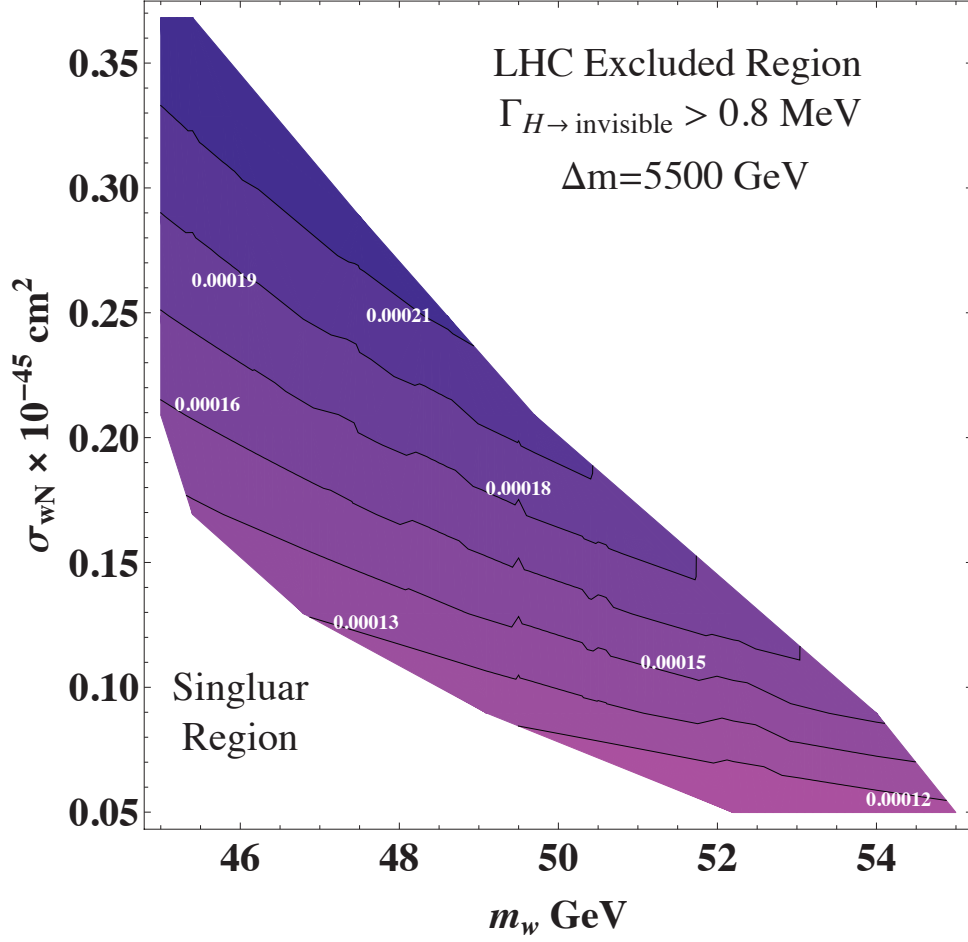Assuming $\eta_\chi \ll 1$ and $m_h \ll m_H$, we arrive at a manageable form of the spin-averaged

Figure 51 : Contours of constant η_χ in the $\sigma_{wN} - m_w$ plane. Again the contours satisfy *Fermi* data, the relic density requirement, and the LHC bound $\mathcal{B}(H \to \text{ invisible})$. We have required $\tilde{\alpha} \lesssim 0.01$ and taken $\Delta m = 5500$ GeV.

$w\bar{w} \to 2h$ amplitude

$$\frac{1}{4} \sum_{\text{spins}} |\mathcal{M}|^2 \approx f^2 \left(\frac{9m_h^4}{v_r^2(s - m_h^2)^2} + \frac{6m_h^2 \eta_\chi^2 v_\phi^2 (m_H^2 + 2m_h^2)}{(s - m_h^2)(s - m_H^2)} \right) (p \cdot p' - m_w^2) ,$$

$$\approx f^2 \left(\frac{18f^2 m_h^4}{\Delta m^2 (s - m_h^2)^2} + \frac{3m_h^2 \eta_\chi^2 v_\phi^2 m_H^2}{(s - m_h^2)(s - m_H^2)} \right) (s - 4m_w^2) ,$$

$$\tag{4.2.123}$$

and the scattering cross section

$$\sigma \approx \frac{f^2}{32\pi s} \sqrt{\frac{s - 4m_h^2}{s - 4m_w^2}} \left(\frac{18f^2 m_h^4}{\Delta m^2 (s - m_h^2)^2} + \frac{3m_h^2 \eta_\chi^2 v_\phi^2 m_H^2}{(s - m_h^2)(s - m_H^2)} \right) (s - 4m_w^2) . \tag{4.2.124}$$

We take the thermal average in the low temperature limit, that is $T \ll m_w$,

$$\langle \sigma_h v \rangle \approx \left(\frac{9f^4 m_h^4}{8\pi \Delta m^2 (m_h^2 - 4m_w^2)^2} + \frac{3f^2 v_\phi^2 \eta_\chi^2 m_h^2}{16\pi (m_h^2 - 4m_w^2)} \right) \langle v^2 \rangle . \tag{4.2.125}$$
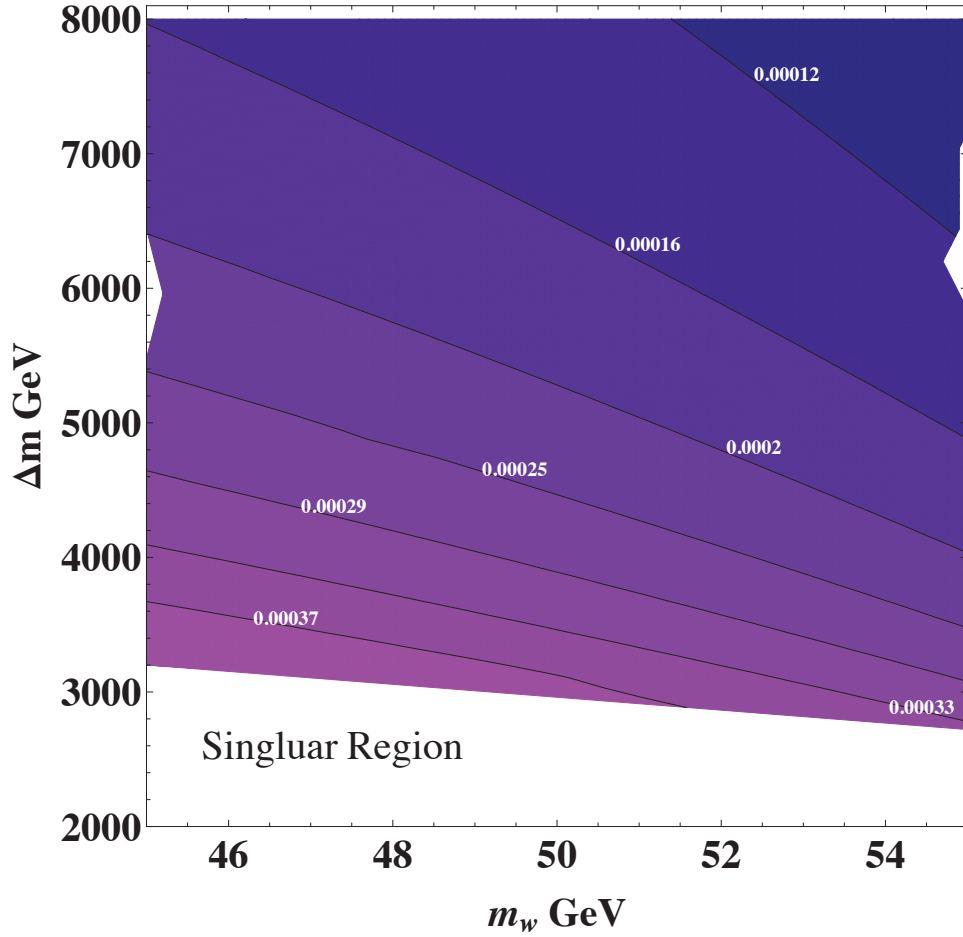
Figure 52 : Contours of constant η_χ in the $\Delta m - m_w$ plane. The contours satisfy *Fermi* data, the relic density requirement, and saturates the LHC bound $\mathcal{B}(H \to \text{ invisible})$. We have required $\tilde{\alpha} \lessapprox 0.01$ and we have verified that the XENON-100 upper limit [286] is not violated.

By demanding the total annihilation cross section to comply with the relic density requirement [251] we obtain

$$\langle \sigma_{\alpha'} v \rangle_+ \langle \sigma_h v \rangle + \sum_{\text{fermions}} \langle \sigma_i v \rangle \sim 3 \times 10^{-26} \text{ cm}^3/s \,, \qquad (4.2.126)$$

and so

$$f \approx 0.070 \,, \qquad (4.2.127)$$

yielding $\chi \approx 10^{-3}$. The latter is consistent with the upper bound on the mixing angle $\chi < 10^{-2}$ [252] derived from the invisible Higgs search by the OPAL Collaboration [253]. In addition, the production of pion pairs plus a large missing energy carried away by the Goldstone boson, α', could become a smoking gun at the LHC [252]. As a final check we ensure that the LHC upper limit on the hidden decay width of the Higgs is satisfied; taking note that the decay

channel $H \to \bar{\psi}_+\psi_+$ is now open, we have

$$\frac{\eta_\chi^2 v_\phi^2}{16\pi m_H} + \frac{\eta_\chi^2 \Delta m^2 v_\phi^2}{32\pi m_H^3} = 0.24 \text{ MeV} < 0.8 \text{ MeV} . \tag{4.2.128}$$

In Fig. 4.2.9 we exhibit the range of parameters consistent with the 95% CL upper limit on $\mathcal{B}(H \to \text{invisible})$ [300, 301, 302] together with possible signal regions associated with data from CDMS-II [72]. For $m_w = 10$ GeV, the best-fit intervals at the 68% CL and the 90% CL are $3 \times 10^{-42} < \sigma_{wN}/\text{cm}^2 < 2.5 \times 10^{-41}$ and $2 \times 10^{-42} < \sigma_{wN}/\text{cm}^2 < 3 \times 10^{-41}$, respectively. The horizontal lines preserve the constant η_χ/m_h ratio that allows decoupling of α' at $T \approx m_\mu$, yielding $N_{\text{eff}} = 3.39$.
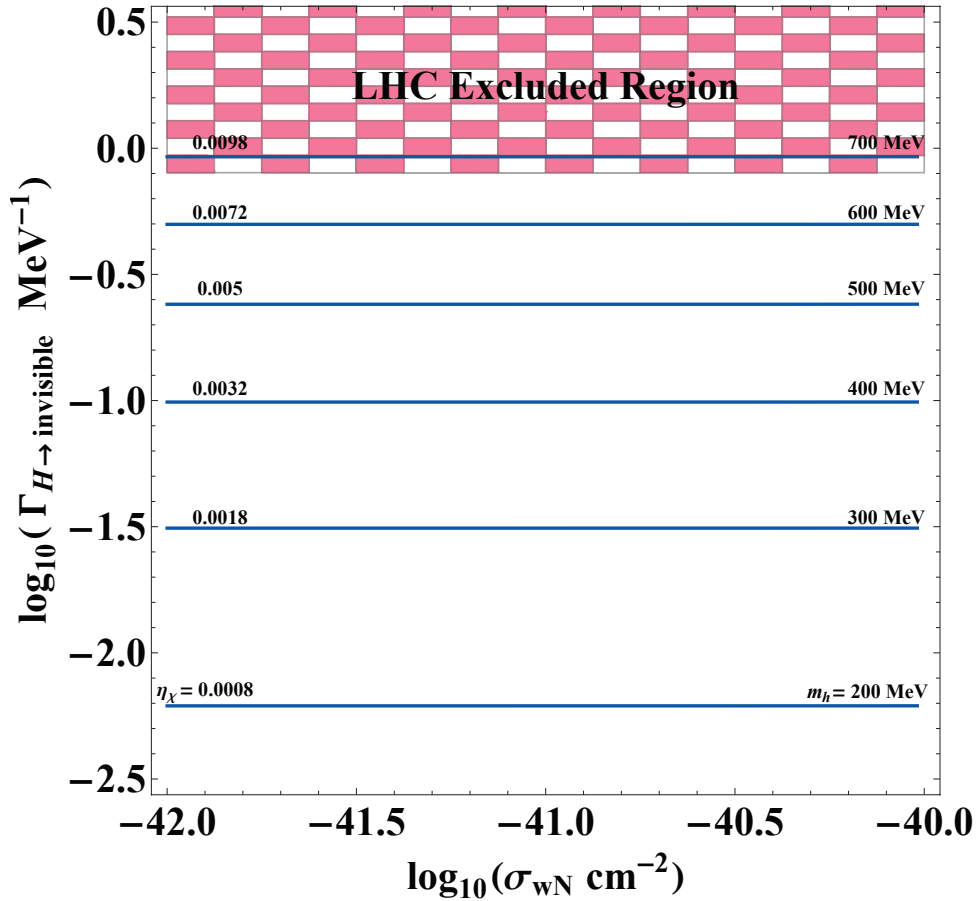

Figure 53 : $\Gamma_{H\to\text{invisible}}$ for varying values of σ_{wN}. The plotted values are nearly constant as the terms from $\Gamma_{H\to\alpha,h}$ dominate the decay width, and thus there is weak dependence on the direct detection cross section. For varying values of m_h we adjust the value of η_χ so that the Goldstone bosons decouple from the primordial plasma at $k_B T \approx m_\mu$, yielding $N_{\text{eff}} = 3.39$. For $200 \text{ MeV} \leq m_h \leq 700 \text{ MeV}$, the Higgs decay width into the hidden sector varies between $(0.006 - 0.92)$ MeV. The constant η_χ/m_h contours shown here are independent of m_w, and therefore span the mass range $7 \text{ GeV} \lesssim m_w/\text{GeV} \lesssim 10$.

In summary, we have shown that W-WIMPs of about 10 GeV can simultaneously explain

the observed relic density and the possible signals observed by direct detection experiments, while avoiding limits from indirect detection experiments. In the near future, the Large Underground Xenon (LUX) dark matter experiment [327] will collect enough statistics to probe the $\sim 10\,\mathrm{GeV}$ dark matter hypothesis. Concurrent with LUX observations will be precise measurements of the Higgs branching fractions by the LHC ATLAS and CMS experiments (operating at $\sqrt{s} = 14$ TeV). This new arsenal of data, when combined with observations the Phased IceCube Next Generation Upgrade (PINGU) [328], will have the potential to single out this distinctive Higgs portal light dark matter model.[3]

4.3 Summary of the Results and Conclusions

Light-element abundances probing big bang nucleosynthesis and precision data from cosmology probing the CMB decoupling epoch have hinted at the presence of extra relativistic degrees of freedom. This is widely referred to as "dark radiation", suggesting the need for new light states in the UV completion of the SM. We provided a brief and concise overview of the current observational status of such dark radiation and we investigated the interplay between two possible interpretations of the extra light states: the right-handed partners of three Dirac neutrinos (which interact with all fermions through the exchange of a new heavy vector meson) and dark matter particles that were produced through a non-thermal mechanism, such us late time decays of massive relics. Interestingly, the first scenario ties together cosmological indications of the extra light states in SM^{++} and the production of the heavy vector particle Z'' at the LHC.

We have also studied the minimal hidden sector recently introduced by Weinberg, which communicates with the visible sector via the Higgs portal. We have re-examined the possibility that the Goldstone boson associated with the hidden scalar may be masquerading as a fractional cosmic neutrino. The broken symmetry associated with this Goldstone boson could regulate the conservation of the particles in the dark matter sector. We have studied the implications of this model for direct and indirect detection experiments. In particular we have shown that W-WIMPs (with $m_w \approx 50$ GeV) are capable of accommodating the desired effective annihilation into $b\bar{b}$ to reproduce the photon spectrum of the *Fermi* Bubbles. We have

---

[3]Since the annihilation rate into SM particles is largely suppressed compared to annihilations into the hidden sector, this particular model predicts null results at PINGU.

also demonstrated that the thermal cross section required to account for the relic dark matter abundance can easily be obtained if $w\bar{w} \to 2\alpha$ is the dominant annihilation channel. However, given that the Goldstone bosons would decouple at 5 GeV (i.e. in the very early universe), the contribution to the effective number of neutrinos for the described parameter space is negligible, and thus cannot explain the evidence for dark radiation. In the near future, the upgraded LHC together with the new XENON1T experiment will further whittle down the parameter space, or else make a discovery. On the other hand, if $m_w \approx 10$ GeV, Weinberg's hidden sector does not provide a viable explanation of the *Fermi* Bubbles. However, there remains an interesting region of the parameter space which can account for the alleged signals recently reported by direct detection experiments. In this region, the Goldstone bosons decouple from the primordial plasma near the 100 MeV temperature, consistent with the two measurements of the effective number of neutrinos reported by the Planck Collaboration. In this region of the parameter space, W-WIMP annihilation into Goldstone bosons is also sufficient for consistency of the observed dark matter abundance. Furthermore, future LHC measurements will further constrain this sector of the Higgs portal (or better, find a signal), while LUX will close the deliberations on the alleged direct signals.

Chapter 5

Future Prospects on Beyond the Standard Model Physics

In 2012, the LHC entered its first long shutdown for upgrades. Starting as early as 2015 the LHC beams will attain collisions at an energy $\sqrt{s} = 13$ TeV [329], in an effort to prepare for design collision energy of $\sqrt{s} = 14$ TeV at a luminosity of 10^{34} cm^{-2} s^{-1}. In addition to the 2015 run of the LHC, there are also plans for high luminosity-LHC (HL-LHC) in 2023, which has the prospective goal of accumulating 3000 pb^{-1} of data. With this exciting future nearly here, beyond the standard model physics may soon become experimental fact.

The Higgs-like boson discovery [8, 9] of 2012 seems to be more and more likely the actual Higgs boson of the standard model, as evidenced in Fig. 54. As discussed in Sec. 2.1, it may be possible in the future for the LHC to detect additional gauge bosons, which may reflect an underlying symmetry that can be supported by a D-brane construct [141]. The additional bosons may also help to solve the vacuum stability problem of the standard model as shown in Sec. 2.2.5 [142]. Furthermore, in Sec. 4.1, it was shown that it may be possible to bring collider physics and cosmological observations together by explaining the possible additional relativistic degrees of freedom inferred from CMB anisotropy analysis, with the addition of extra gauge bosons and the right chiral components of neutrinos [221]. The latter also solves the neutrino oscillation problem outlined in Sec. 1.1.4.

Further investigation into the Higgs boson particle can result in a portal to BSM physics. In Sec. 4.2 we have explored the minimal hidden sector recently introduced by Weinberg [15].
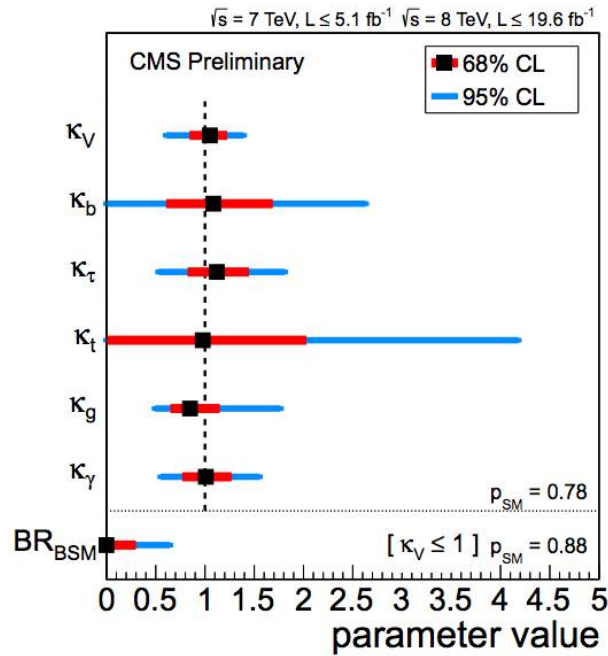
Figure 54 : The best fit to observation couplings for the Higgs-like boson detected at CMS, along with corresponding confidence intervals. The couplings are for $\kappa_V, \kappa_b, \kappa_\tau, \kappa_t, \kappa_g, \kappa_\gamma$ for the vector bosons $(W_\pm, Z_0)$, bottom, τ, top, gluon, and photon couplings assuming no BSM physics. This results in a p-value of $p_{SM} = 0.78$, allowing BSM physics while restricting the vector boson coupling to $\kappa_V \leq 1.0$ results in an upper limit on the branching ratio for the Higgs into invisibles (image from [329]).

This model can explain the γ-ray emission from the low-latitude regions of the *Fermi* Bubbles, for which the spectral shape is consistent with an approximately 50 GeV dark matter particle annihilating into $b\bar{b}$, with a normalization corresponding to $\langle \sigma_b v \rangle \sim 8 \times 10^{-27}$ cm^3/s. Moreover, in a separate region of the parameter space, $m_w \approx 10$ GeV the model has the potential to explain recent hints from dark matter direct detection experiments and at the same time it provides predictions for LHC [330]. In the near future, the upgraded LHC, together with the new XENON1T experiment, will further whittle down the parameter space, or else make a discovery.

Far from the particle physics experiments lies another method of discovery of BSM physics, that of gravitational wave astronomy. As of 2011, the LIGO detectors at Hanford, WA, and Livingston, LA, are undergoing upgrades to Advanced LIGO, whose prospective noise curve can be seen in Fig. 55. Advanced LIGO is expected to be completed in 2015, which should allow unprecedented detection ability of gravitational waves [331]. The study of gravitational wave astronomy opens the door to probes of matter densities that are far from obtainable in
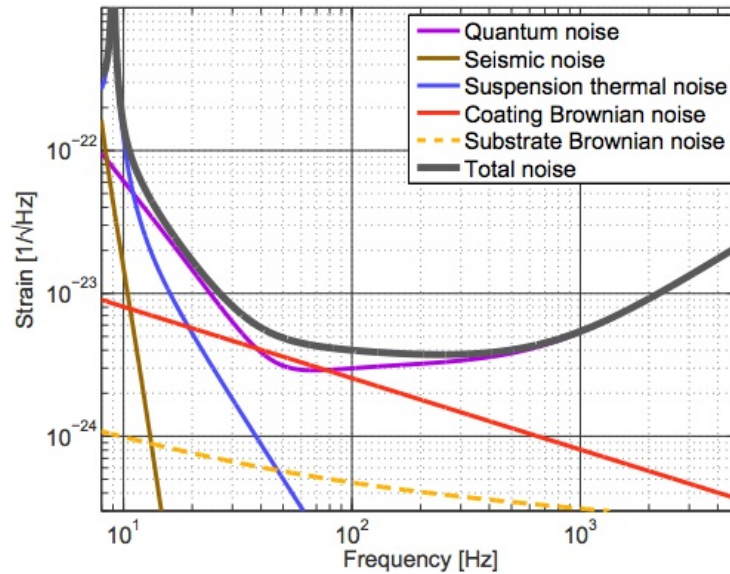
Figure 55 : The prospective noise curve for Advanced LIGO results in a spectral strain sensitivity of order $\sqrt{\text{Noise}} \sim 10^{-23}$ Hz$^{-1/2}$, allowing for better noise suppression and possible direct detection of gravitational waves. Image from [331].

a lab, such as that found in pulsars [150]. It is a new set of eyes on the sky as everything we have received from the cosmos has been in the form of photons. The field of gravitational wave astronomy may even reveal a pathway to probing physics of the GUT scale as discussed in Sec. 3.2, though detection of a signal of the strength $\Omega_{gw}h^2 \sim 10^{-24} - 10^{-15}$ [179] lies out of reach of even possible future detectors except the possible future big bang observer (BBO) [332] (see Fig. 56); the possibility is exciting that far in the future, it may be possible.

Whatever lies beyond the SM whether it be SUSY, a Higgs portal, a GUT theory, or string theory, it may soon be within reach with as the discovery of the Higgs, future upgrades of the LHC, and Advanced LIGO hold in store an exciting future for all.
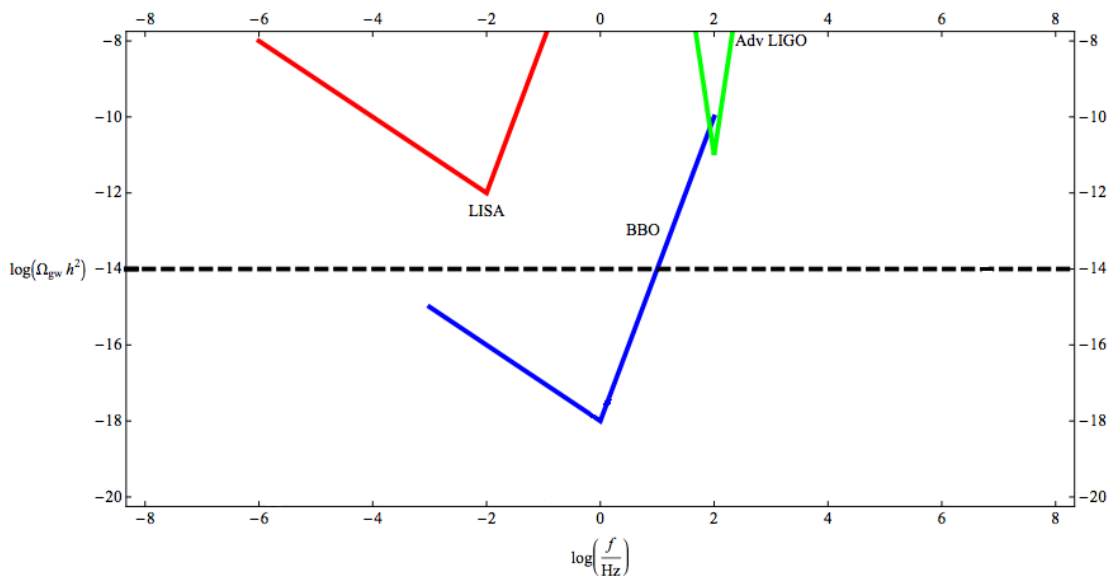
Figure 56 : The future detection of a gravitational wave stochastic background with the projected sensitivity curves of possible future detectors such as Advanced LIGO and BBO. The spectra of gravitational waves from second order global phase transitions may be detected in the far future if BBO is actually completed, but in the near future seems to be out of reach for detection. Image modified from [167].

Bibliography

[1] J. Beringer *et al.* [Particle Data Group Collaboration], Phys. Rev. D **86**, 010001 (2012).

[2] S. Weinberg, Eur. Phys. J. C **34**:5-13, 2004 [arXiv: hep-ph/0401010].

[3] A. Einstein, Annalen Phys. **49**, 769 (1916) [Annalen Phys. **14**, 517 (2005)].

[4] S. Weinberg. *Cosmology*, (Oxford University Press, New York, USA 2009).

[5] A. Einstein, Annalen Phys. **17**, 891 (1905) [Annalen Phys. **14**, 194 (2005)].

[6] A. Einstein, Sitzungsber. Press. Akad. Wiss. Berlin (Math. Phys.) **1917**, 142 (1917).

[7] P. A. R. Ade *et al.* [Planck Collaboration], [arXiv:1303.5076 [astro-ph.CO]].

[8] G. Aad *et al.* [ATLAS Collaboration], [arXiv:1207.7214 [hep-ex]].

[9] S. Chatrchyan *et al.* [CMS Collaboration], [arXiv:1207.7235 [hep-ex]].

[10] Alan H. Guth, Phys. Rev. D **23**, 347-356 (1981).

[11] Image from ESA (URL: http : //spaceinimages.esa.int/var/esa/storage/images/esa$_m$ultimedia/imag
accessed on 2 Aug 2013.

[12] A. G. Riess, L. Macri, S. Casertano, H. Lampeitl, H. C. Ferguson, A. V. Filippenko,
S. W. Jha and W. Li *et al.*, Astrophys. J. **730**, 119 (2011) [Erratum-ibid. **732**, 129 (2011)]
[arXiv:1103.2976 [astro-ph.CO]].

[13] M. Markevitch, A. H. Gonzales, D. Clowe, A. Vikhlinin, L. David, W. Forman, C. Jones,
S. Murray, W. Tucker, Astrophys. J. **606**, 819-824 (2004) [arXiv:astro-ph/0309303].

[14] R. C. Rubin, F. W. Kent, Jr., Astrophys. J. **158**, 379 (1970).

[15] S. Weinberg, Phys. Rev. Lett. 110, **241301** (2013) [arXiv:1305.1971 [astro-ph.CO]].

[16] S. L. Glashow, Nucl. Phys. **22**, 579-588 (1961).

[17] J. Goldstone, A. Salam, S. Weinberg, Phys. Rev. **127**, 965-970 (1962).

[18] S. Weinberg, Phys. Rev. Lett. **19**, 1264-1266 (1967).

[19] P. W. Higgs, Phys. Rev. Lett. **13**, 508-509 (1964).

[20] D. J. Gross and F. Wilczek, Phys. Rev. Lett. **30**, 1343 (1973).

[21] D. J. Gross and F. Wilczek, Phys. Rev. D **8**, 3633 (1973).

[22] H. D. Politzer, Phys. Rev. Lett. **30**, 1346 (1973).

[23] H. D. Politzer, Phys. Rept. **14**, 129-180 (1974).

[24] M. Srednicki, *Quantum Field Theory*, (University Press, Cambridge, UK 2007).

[25] L. H. Ryder, *Quantum Field Theory: second edition*, (Cambridge University Press, Cambridge UK, 1996).

[26] R. J. Davis, D. S. Harmer, and K. C. Hoffman, Phys. Rev. Lett. **20**, 1205 (1968).

[27] M. C. Gonzalez-Garcia and M. Maltoni, Phys. Rept. **460**, 1 (2008) [arXiv:0704.1800 [hep-ph]].

[28] S. F. Novaes, [arXiv:hep-ph/0001283v1].

[29] H. Nishino *et al.* [Super-Kamiokande Collaboration], Phys. Rev. Lett. **102**, 141801 (2009) .

[30] M. E. Peskin, and D. V. Schroeder. *An Introduction to Quantum Field Theory*, (Westview Press, 1995).

[31] M. Kobayashi, and T. Maskawa. Progress of Theoretical Physics **49** (2) 652.

[32] B. Zwiebach. *A First Course in String Theory second edition*. (Cambridge University Press, Cambridge, UK, 2009).

[33] S. Cullen and M. Perelstein, Phys. Rev. Lett. **83**, 268 (1999) [arXiv: hep-ph/9903422].

[34] C. D. Hoyle, U. Schmidt, B. R. Heckel, E. G. Adelberger, J. H. Gundlach, D. J. Kapner and H. E. Swanson, Phys. Rev. Lett. **86**, 1418 (2001) [arXiv:hep-ph/0011014].

[35] S. Hannestad and G. Raffelt, Phys. Rev. Lett. **87**, 051301 (2001) [arXiv:hep-ph/0103201].

[36] S. Hannestad and G. G. Raffelt, Phys. Rev. Lett. **88**, 071301 (2002) [arXiv:hep-ph/0110067].

[37] L. A. Anchordoqui, J. L. Feng, H. Goldberg and A. D. Shapere, Phys. Rev. D **65**, 124027 (2002) [arXiv:hep-ph/0112247].

[38] L. A. Anchordoqui, J. L. Feng, H. Goldberg and A. D. Shapere, Phys. Rev. D **66**, 103002 (2002) [arXiv:hep-ph/0207139].

[39] S. Chatrchyan *et al.* [CMS Collaboration], Phys. Rev. Lett. **108**, 111801 (2012) [arXiv:1112.0688 [hep-ex]].

[40] S. Chatrchyan *et al.* [CMS Collaboration], Phys. Rev. Lett. **108**, 261803 (2012) [arXiv:1204.0821 [hep-ex]].

[41] G. Aad *et al.* [ATLAS Collaboration], Phys. Lett. B **716**, 122 (2012) [arXiv:1204.4646 [hep-ex]].

[42] S. Chatrchyan *et al.* [CMS Collaboration], JHEP **1209**, 094 (2012) [arXiv:1206.5663 [hep-ex]].

[43] A. Friedmann, Z. Phys. **10**, 377 (1922).

[44] A. Friedmann, Z. Phys. **21**, 326 (1924).

[45] H. P. Robertson, Astrophys. J. **82**, 284 (1935).

[46] H. P. Robertson, Astrophys. J. **83**, 187, 257 (1936).

[47] A. G. Walker, Proc. Lond. Math. Soc. (2) **42**, 90 (1936).

[48] E. Hubble, Proc. Nat. Acad. Sci. **15**, 168 (1927).

[49] E. W. Kolb and M. S. Turner, *The Early Universe,* (Front. Phys. **69**, 1 1990).

[50] A. A. Penzias and R. W. Wilson, Astrophys. J. **142**, 419 (1965).

[51] G. F. Smoot, *et al.* Astrophys. J. **420**, 450-456 (1994).

[52] W. Hu. [arXiv: astro-ph/0210696].

[53] P. A. R. Ade *et al.* (Planck Collaboration) [arXiv:astro-ph/1303.5075].

[54] C.L. Bennett, D. Larson, J.L. Weiland [arXiv:astro-ph/1212.5225v2].

[55] A. G. Riess *et al.* [Supernova Search Team Collaboration], Astron. J. **116**, 1009 (1998) [arXiv:astro-ph/9805201].

[56] S. Perlmutter *et al.* [Supernova Cosmology Project Collaboration], Astrophys. J. **517**, 565 (1999) [astro-ph/9812133].

[57] S. Perlmutter and B. P. Schmidt, Lect. Notes Phys. **598**, 195 (2003) [arXiv:astro-ph/0303428].

[58] J. Garcia-Bellido, A. D. Linde, Phys. Rev. **D** 57, 6075 (1998) [arXiv:hep-ph/9711360].

[59] L. R. Price and X. Siemens, Phys. Rev. D **78**, 063541 (2008) [arXiv:0805.3570 [astro-ph]].

[60] M. Milgrom, Astrophys. J. **270**, 365-370 (1983).

[61] R. S. Ellis, Phil. Trans. R. Soc. A **368**, 967987 (2010).

[62] G. Steigman and M. S. Turner, Nucl. Phys. B **253**, 375-386 (1985).

[63] H. Goldberg, Phys. Rev. Lett. **50**, 1419 (1983) [Erratum-ibid. **103**, 099905 (2009)].

[64] C. Englert, T. Plehn, D. Zerwas and P. M. Zerwas, Phys. Lett. B **703**, 298 (2011) [arXiv:1106.3097 [hep-ph]].

[65] Image from (URL: http : //apod.nasa.gov/apod/ap060824.html) accessed 2 Aug 2013. Composite credit: (X-ray) NASA/CXC/CFa/M. Markevitch *et al.* [arXiv:astro-ph/0511345]. (Lensing Map) NASA/STScI;ESO WFI; Magellan/U.Arizona/D. Clowe *et al.* Astrophys J. **648**, L109-L113 (2006) [arXiv:astro-ph/0608407]. (Optical) NASA/STScI; Magellan/U.Arizona/D.Clowe, *et al.*

[66] B. Lee, and S. Weinberg, Phys. Rev. Lett. **39**, 165 (1977).

[67] Images from P. Gagnon (URL: http : //www.quantumdiaries.org/2013/07/12/can − the − lhc − solv and (URL: http : //www.quantumdiaries.org/2013/07/01/getting − our − hands − on − dark − mat Accessed on 2 Aug 2013.

[68] R. Bernabei, *et al.* Eur. Phys. J. C **67**, 39 (2010) [arXiv:1002.1028 [astro-ph.GA]].

[69] C. E. Aalseth *et al.* [CoGeNT Collaboration], Phys. Rev. Lett. **106**, 131301 (2011) [arXiv:1002.4703 [astro-ph.CO]].

[70] C. E. Aalseth *et al.* [CoGeNT Collaboration], Phys. Rev. Lett. **107**, 141301 (2011) [arXiv:1106.0650 [astro-ph.CO]].

[71] G. Angloher *et al.* Eur. Phys. J. C **72**, 1971 (2012) [arXiv:1109.0702 [astro-ph.CO]].

[72] R. Agnese *et al.* [CDMS Collaboration], [arXiv:1304.4279 [hep-ex]].

[73] XENON 100 Collaboration, Phys. Rev. Lett. **109**, 181301 (2012) [arXiv:1207.5988].

[74] D. Hooper, [arXiv:1306.1790 [hep-ph]].

[75] D. J. Kapner, T. S. Cook, E. G. Adelberger, J. H. Gundlach, B. R. Heckel, C. D. Hoyle, H. E. Swanson, Phys. Rev. Lett. **98**, 021101 (2007). [arXiv: hep-ph/0611184].

[76] J. Polchinski, Phys. Rev. Lett. **75**, 4724 (1995) [arXiv:hep-th/9510017].

[77] J. Polchinski, [arXiv:hep-th/9611050].

[78] I. Antoniadis, N. Arkani-Hamed, S. Dimopoulos and G.R. Dvali, Phys. Lett. B **436**, 257 (1998) [arXiv:hep-ph/9804398].

[79] S. Cullen, M. Perelstein and M. E. Peskin, Phys. Rev. D **62**, 055012 (2000) [arXiv:hep-ph/0001166].

[80] L. A. Anchordoqui, H. Goldberg, S. Nawata and T. R. Taylor, Phys. Rev. Lett. **100**, 171603 (2008) [arXiv:0712.0386 [hep-ph]].

[81] L. A. Anchordoqui, H. Goldberg, S. Nawata and T. R. Taylor, Phys. Rev. D **78**, 016005 (2008) [arXiv:0804.2013 [hep-ph]].

[82] D. Lüst, S. Stieberger and T. R. Taylor, Nucl. Phys. B **808**, 1 (2009) [arXiv:0807.3333 [hep-th]].

[83] L. A. Anchordoqui, H. Goldberg, D. Lüst, S. Nawata, S. Stieberger and T. R. Taylor, Phys. Rev. Lett. **101**, 241803 (2008) [arXiv:0808.0497 [hep-ph]].

[84] L. A. Anchordoqui, H. Goldberg, D. Lüst, S. Nawata, S. Stieberger and T. R. Taylor, Nucl. Phys. B **821**, 181 (2009) [arXiv:0904.3547 [hep-ph]].

[85] V. Khachatryan *et al.* [CMS Collaboration], Phys. Rev. Lett. **105**, 211801 (2010) [Phys. Rev. **106**, 029902 (2011)] [arXiv:1010.0203 [hep-ex]].

[86] S. Chatrchyan *et al.* [CMS Collaboration], Phys. Lett. B **704**, 123 (2011) [arXiv:1107.4771 [hep-ex]].

[87] D. Lust and T. R. Taylor, [arXiv:1308.1619 [hep-ph]].

[88] L. A. Anchordoqui, I. Antoniadis, H. Goldberg, X. Huang, D. Lüst and T. R. Taylor, Phys. Rev. D **85**, 086003 (2012) [arXiv:1107.4309 [hep-ph]].

[89] L. A. Anchordoqui, H. Goldberg, X. Huang, D. Lüst and T. R. Taylor, Phys. Lett. B **701**, 224 (2011) [arXiv:1104.2302 [hep-ph]].

[90] H. Ruegg and M. Ruiz-Altaba, Int. J. Mod. Phys. A **19**, 3265 (2004) [arXiv:hep-th/0304245].

[91] E. Witten, Phys. Lett. B **149**, 351 (1984).

[92] M. Dine, N. Seiberg and E. Witten, Nucl. Phys. B **289**, 589 (1987).

[93] J. J. Atick, L. J. Dixon and A. Sen, Nucl. Phys. B **292**, 109 (1987).

[94] W. Lerche, B. E. W. Nilsson, A. N. Schellekens and N. P. Warner, Nucl. Phys. B **299**, 91 (1988).

[95] L. E. Ibanez and F. Quevedo, JHEP **9910**, 001 (1999) [arXiv:hep-ph/9908305].

[96] M. B. Green and J. H. Schwarz, Phys. Lett. B **149**, 117 (1984).

[97] P. Vankov, *ATLAS Upgrade for the HL-LHC: meeting the challenges of a five-fold increase in collision rate* ATL-UPGRADE-PROC-2012-003 [arXiv:1201.5469].

[98] CMS Collaboration, *Search for narrow resonances using the dijet mass spectrum in pp collisions at $\sqrt{s} = 8$ TeV*, CMS PAS EXO-12-016.

[99] ATLAS Collaboration, *Search for new phenomena in dijet mass and angular distributions using 5.8 fb^{-1} of pp collisions at $\sqrt{s} = 8$ TeV collected by the ATLAS detector*, ATLAS-CONF-2012-088.

[100] L. Taylor, *CMS detector design* Image retrieved from (URL: $http://cms.web.cern.ch/news/cms-detector-design$) access 3 Aug 2013.

[101] C. G. Tully, *Elementary Particle Physics in a Nutshell* (Princeton University Press, 2011).

[102] M. Krammer, *Instrumentation at the LHCThe silicon tracking systems,Nuclear Instruments and Methods in Physics Research Section A: Accelerators, Spectrometers, Detectors and Associated Equipment*, Vol **699**,134-138, 21 Jan 2013. Proceedings of the 8th International Hiroshima Symposium on the Development and Application of Semiconductor Tracking Detectors, Academia Sinica, Taipei, Taiwan, December 5 8, 2011.

[103] CMS Collaboration, *Search for resonances in dilepton mass spectra in pp collisions at $\sqrt{s} = 8$ TeV*, CMS PAS EXO-12-015.

[104] M. Williams, C. P. Burgess, A. Maharana and F. Quevedo, [arXiv:1103.4556 [hep-ph]].

[105] G. Aad *et al.* [ATLAS Collaboration], Phys. Lett. B **708**, 37 (2012) [arXiv:1108.6311 [hep-ex]].

[106] CMS Collaboration, *Search for narrow resonances using the dijet mass spectrum in pp collisions at $\sqrt{s} = 7$ TeV*, CMS PAS EXO-11-094.

[107] ATLAS Collaboration, *Search for new phenomena in dijet mass and angular distributions using 4.8 fb^{-1} of pp collisions at $\sqrt{s} = 7$ TeV collected by the ATLAS detector*, ATLAS-CONF-2012-038.

[108] ATLAS Collaboration, *Search for high mass dilepton resonances with 5 fb^{-1} of pp collisions at $\sqrt{s} = 7$ TeV with the ATLAS experiment*, ATLAS-CONF-2012-007.

[109] G. Aad *et al.* [ATLAS Collaboration], Phys. Rev. Lett. **107**, 272002 (2011) [arXiv:1108.1582 [hep-ex]].

[110] S. Chatrchyan *et al.* [CMS Collaboration], [arXiv:1206.1849 [hep-ex]].

[111] V. Barger and R. J. N. Phillips, *Collider Physics*, (Addison-Wesley, 1987).

[112] J. Pumplin, D. R. Stump, J. Huston, H. L. Lai, P. Nadolsky and W. K. Tung, JHEP **0207**, 012 (2002) [arXiv:hep-ph/0201195].

[113] D. Feldman, Z. Liu and P. Nath, JHEP **0611**, 007 (2006) [arXiv:hep-ph/0606294].

[114] A. Bhatti *et al.*, J. Phys. G **36**, 015004 (2009) [arXiv:0807.4961 [hep-ex]].

[115] C. -W. Chiang, N. D. Christensen, G. -J. Ding and T. Han, Phys. Rev. D **85**, 015023 (2012) [arXiv:1107.5830 [hep-ph]].

[116] A. Zee. *Quantum Field Theory in a Nutshell*. (Princeton University Press, 2003).

[117] F. Gianotti, CERN Seminar: *Update on the SM Higgs Searches in ATLAS*, 4 July 2012.

[118] J. Incandela, CERN Seminar: *Update on the SM Higgs Searches in CMS*, 4 July 2012.

[119] G. Aad *et al.* [ATLAS Collaboration], Phys. Lett. B **710**, 49 (2012) [arXiv:1202.1408 [hep-ex]].

[120] S. Chatrchyan *et al.* [CMS Collaboration], Phys. Lett. B **710**, 26 (2012) [arXiv:1202.1488 [hep-ex]].

[121] O. Arnaez (on behalf of the ATLAS Collaboration), *Searches for the SM scalar boson in the $H \to W^+W^-$ channels with the ATLAS detector*, talk given at Higgs Hunting 2012, Orsay, France, 18-20 July, 2012.

[122] T. Aaltonen *et al.* [CDF and D0 Collaborations], [arXiv:1207.6436 [hep-ex]].

[123] M. Lindner, M. Sher and H. W. Zaglauer, Phys. Lett. B **228**, 139 (1989).

[124] M. Sher, Phys. Rept. **179**, 273 (1989).

[125] M. A. Diaz, T. A. ter Veldhuis and T. J. Weiler, Phys. Rev. Lett. **74**, 2876 (1995) [arXiv:hep-ph/9408319].

[126] J. A. Casas, J. R. Espinosa and M. Quiros, Phys. Lett. B **342**, 171 (1995) [arXiv:hep-ph/9409458].

[127] M. A. Diaz, T. A. ter Veldhuis and T. J. Weiler, Phys. Rev. D **54**, 5855 (1996) [arXiv:hep-ph/9512229].

[128] J. A. Casas, J. R. Espinosa and M. Quiros, Phys. Lett. B **382**, 374 (1996) [arXiv:hep-ph/9603227].

[129] G. Isidori, G. Ridolfi and A. Strumia, Nucl. Phys. B **609**, 387 (2001) [arXiv:hep-ph/0104016].

[130] G. Isidori, V. S. Rychkov, A. Strumia and N. Tetradis, Phys. Rev. D **77**, 025034 (2008) [arXiv:0712.0242 [hep-ph]].

[131] L. J. Hall and Y. Nomura, JHEP **1003**, 076 (2010) [arXiv:0910.2235 [hep-ph]].

[132] J. Ellis, J. R. Espinosa, G. F. Giudice, A. Hoecker and A. Riotto, Phys. Lett. B **679**, 369 (2009) [arXiv:0906.0954 [hep-ph]].

[133] J. Elias-Miro, J. R. Espinosa, G. F. Giudice, G. Isidori, A. Riotto and A. Strumia, Phys. Lett. B **709**, 222 (2012) [arXiv:1112.3022 [hep-ph]].

[134] Z. -z. Xing, H. Zhang and S. Zhou, [arXiv:1112.3112 [hep-ph]].

[135] F. Bezrukov, M. Y. .Kalmykov, B. A. Kniehl and M. Shaposhnikov, [arXiv:1205.2893 [hep-ph]].

[136] G. Degrassi, S. Di Vita, J. Elias-Miro, J. R. Espinosa, G. F. Giudice, G. Isidori and A. Strumia, [arXiv:1205.6497 [hep-ph]].

[137] V. Barger, P. Langacker, M. McCaskey, M. Ramsey-Musolf and G. Shaughnessy, Phys. Rev. D **79**, 015018 (2009) [arXiv:0811.0393 [hep-ph]].

[138] J. Elias-Miro, J. R. Espinosa, G. F. Giudice, H. M. Lee and A. Strumia, JHEP **1206**, 031 (2012) [arXiv:1203.0237 [hep-ph]].

[139] L. Basso, S. Moretti and G. M. Pruna, Phys. Rev. D **82**, 055018 (2010) [arXiv:1004.3039 [hep-ph]].

[140] J. A. Casas, J. R. Espinosa, M. Quiros and A. Riotto, Nucl. Phys. B **436**, 3 (1995) [Erratum-ibid. B **439**, 466 (1995)] [arXiv:hep-ph/9407389].

[141] L. A. Anchordoqui, I. Antoniadis, H. Goldberg, X. Huang, D. Lüst, T. R. Taylor, B. Vlcek Phys. Rev. D **86**, 066004 (2012) [arXiv:1206.2537 [hep-ph]].

[142] L. A. Anchordoqui, I. Antoniadis, H. Goldberg, X. Huang, D. Lüst, T. R. Taylor, B. Vlcek JHEP **1302**, 074 (2013) [arXiv:1208.2821 [hep-ph]].

[143] M. Kadastik, K. Kannike, A. Racioppi and M. Raidal, JHEP **1205**, 061 (2012) [arXiv:1112.3647 [hep-ph]].

[144] R. Bousso and J. Polchinski, JHEP **0006**, 006 (2000) [arXiv:hep-th/0004134].

[145] L. Susskind, [arXiv:hep-th/0302219].

[146] M. R. Douglas, JHEP **0305**, 046 (2003) [arXiv:hep-th/0303194].

[147] M. Claudson, L. J. Hall and I. Hinchliffe, Nucl. Phys. B **228**, 501 (1983).

[148] A. Hebecker, A. K. Knochel and T. Weigand, JHEP **1206**, 093 (2012) [arXiv:1204.2551 [hep-th]].

[149] R. A. Hulse, J. H. Taylor. Astrophys. J. **195**, L51-L53, pt 2 (1975).

[150] M. Maggiore. *Gravitational Waves Vol 1*. (Oxford University Press, 2008).

[151] J. D. E. Creighton and W. G. Anderson. *Gravitational-Wave Physics and Astronomy 1st ed*. (Wiley-VCH, 2011)

[152] A. A. Starobinsky, JETP Lett. **30**, 682 (1979) [Pisma Zh. Eksp. Teor. Fiz. **30**, 719 (1979)].

[153] B. Allen, Phys. Rev. **D37**, 2078 (1988).

[154] D. N. Spergel *et al.* (WMAP), Astrophys. J. Suppl. **170**, 377 (2007) [arXiv:astro-ph/0603449].

[155] H. Peiris and R. Easther, JCAP **0610**, 017 (2006) [arXiv: astro-ph/0609003].

[156] L. Kofman, A. D. Linde, and A. A. Starobinksy, Phys. Rev. Lett. **73**, 3195 (1994) [arXiv: hep-th/9405187].

[157] S. Y. Khlebnikov and I. I. Tkachev, Phys. Rev. D **56**, 653 (1997) [arXiv:hep-ph/9701423].

[158] P. B. Greene, L. Kofman, A. D. Linde, and A. A. Starobinksy, Phys. Rev. D **56**, 6175 (1997) [arXiv:hep-ph/9705347].

[159] L. Kofman, A. D. Linde, and A. A. Starobinksy, Phys. Rev. D **56**, 3258 (1997) [arXiv:hep-ph/9704452].

[160] J. Garcia-Bellido, [arXiv:hep-ph/9804205].

[161] R. Easther, E. A. Lim, JCAP **0604**, 010 (2006). [arXiv:astro-ph/0601617].

[162] R. Easther, J. T. Giblin, Jr and E. A. Lim, Phys. Rev. Lett. **99**, 221301 (2007) [arXiv:astro-ph/0612294].

[163] J. Garcia-Bellido, D. G. Figueroa, and A. Sastre, Phys. Rev. D **77**, 043517 (2008) [arXiv:0707.0839].

[164] J. Garcia-Bellido, D. G. Figueroa, and A. Sastre, Phys. Rev. Lett. **98**, 061301 (2007) [arXiv: astro-ph/0701014].

[165] J. F. Dufaux, A. Bergman, G. N. Felder, L. Kofman, J. P. Uzan, Phys. Rev. D76, 123517 (2007) [arXiv:0707.0875].

[166] R. Easther, J. T. Giblin, Jr. and E. A. Lim, Phys. Rev. D **77**, 103519 (2008) [arXiv:0712.2991 [astro-ph]].

[167] R. Easther, J. T. Giblin, E. A. Lim, W. I. Park, and E. D. Stewart, JCAP **0805**, 013 (2008) [arXiv:0801.4197].

[168] C. Caprini, R. Durrer, and G. Servant, Phys. Rev. D **77**, 124015 (2008) [arXiv:0711.2593].

[169] K. Jones-Smith, L. M. Krauss and H. Mathur, Phys. Rev. Lett. **100**, 131302 (2008) [arXiv:0712.0778 [astro-ph]].

[170] A. Kosowsky, M. S. Turner and R. Watkins, Phys. Rev. D **45**, 4514 (1992).

[171] A. Kosowsky, M. S. Turner, and R. Watkins, Phys. Rev. Lett. **69**, 2026 (1992).

[172] A. Kosowsky and M. S. Turner, Phys. Rev. D **47**, 4372 (1993), [arXiv: astro-ph/9211004].

[173] L. M. Krauss, Phys. Lett. B **284**, 229 (1992).

[174] M. Kamionkowski, A. Kosowsky, and M. S. Turner, Phys. Rev. **D49**, 2837-2851 (1994) [arXiv:astro-ph/9310044].

[175] G. Felder, J. Garcia-Bellido, P. B. Green, L. Kofman, A. Linde, and I. Tkachev, Phys. Rev. Lett. **87**, 011601 (2001).

[176] A. Kosowsky, A. Mack, and T. Kahniashvilil, Phys. Rev. D **66**, 024030 (2002) [arXiv: astro-ph/0111483].

[177] C. W. Misner, K. S. Thorne, and J. A. Wheeler, *Gravitation* (Freeman, San-Francisco, CA USA, 1973).

[178] I. S. Gradshteyn and I. M. Ryzhik. *Tables of Integrals, Series, and Products 6th ed.* (Academic Press, 2000).

[179] J. T. Giblin, Jr, L. R. Price, X. Siemens, and B. Vlcek. JCAP **1211**, 006 (2012) [arXiv: 1111.4014 [astro-ph.CO]].

[180] D. Hilbert, Konigl. Gesell. d. Wiss. Gottingen, Nachr. Math.-Phys. Kl. 395-407 1915.

[181] F. W. Hehl, P. Von Der Heyde, G. D. Kerlick and J. M. Nester, Rev. Mod. Phys. **48**, 393 (1976).

[182] W. H. Press, S. A. Tenkolsky, W. T. Vetterling, and B. P. Flannery, *Numerical Recipes 3rd ed.* (Cambridge University Press, New York, NY USA 2007).

[183] G. N. Felder and I. Tkachev, [arXiv:hep-ph/0011159].

[184] E. Witten, Phys. Rev. D **30**, 272 (1984).

[185] H. C. Child and J. T. Giblin, Jr. (to appear) as referenced in JCAP **1211**, 006 (2012) [arXiv: 1111.4014 [astro-ph.CO]].

[186] V. A. Rubakov, M. V. Sazhin and A. V. Veryaskin, Phys. Lett. B **115**, 189 (1982).

[187] E. Fenu, D. G. Figueroa, R. Durrer and J. Garcia-Bellido, JCAP **0910**, 005 (2009) [arXiv:0908.0425 [astro-ph.CO]].

[188] D. Bailin and A. Love, *Introduction to Gauge Field Theory Rev ed.* (Institute of Physics Publishing, Bristol and Philadelphia, in association with University of Sussex Press, 1993).

[189] M. Hindmarsh, R. J. Rivers, Nucl. Phys. **B417**, 506-526 (1994). [arXiv:hep-ph/9307253].

[190] L. M. Krauss, K. Jones-Smith, H. Mathur and J. Dent, Phys. Rev. D **82**, 044001 (2010) [arXiv:1003.1735 [astro-ph.CO]].

[191] J. Simons, S. Shah, K. Hotta, A. Fritsch, P. Tirumalai *et al. OpenMP API.* (URL: http : //openmp.org/wp/).

[192] R. Schabinger and J. D. Wells, Phys. Rev. D **72**, 093007 (2005) [arXiv:hep-ph/0509209].

[193] B. Patt and F. Wilczek, [arXiv:hep-ph/0605188].

[194] V. Barger, P. Langacker, M. McCaskey, M. J. Ramsey-Musolf and G. Shaughnessy, Phys. Rev. D **77**, 035005 (2008) [arXiv:0706.4311 [hep-ph]].

[195] S. Andreas, C. Arina, T. Hambye, F. -S. Ling and M. H. G. Tytgat, Phys. Rev. D **82**, 043522 (2010) [arXiv:1003.2595 [hep-ph]].

[196] H. E. Logan, Phys. Rev. D **83**, 035022 (2011) [arXiv:1010.4214 [hep-ph]].

[197] S. Bock, R. Lafaye, T. Plehn, M. Rauch, D. Zerwas and P. M. Zerwas, Phys. Lett. B **694**, 44 (2010) [arXiv:1007.2645 [hep-ph]].

[198] S. Dodelson, *Modern Cosmology*. (Academic Press, 2003).

[199] G. Mangano, G. Miele, S. Pastor, T. Pinto, O. Pisanti and P. D. Serpico, Nucl. Phys. B **729**, 221 (2005) [arXiv:hep-ph/0506164].

[200] S. Sarkar, Rept. Prog. Phys. **59**, 1493 (1996) [arXiv:hep-ph/9602260].

[201] K. A. Olive, G. Steigman and T. P. Walker, Phys. Rept. **333**, 389 (2000) [arXiv:astro-ph/9905320].

[202] G. Steigman, Ann. Rev. Nucl. Part. Sci. **57**, 463 (2007) [arXiv:0712.1100 [astro-ph]].

[203] R. H. Cyburt, B. D. Fields, K. A. Olive and E. Skillman, Astropart. Phys. **23**, 313 (2005) [arXiv:astro-ph/0408033].

[204] V. Simha and G. Steigman, JCAP **0806**, 016 (2008) [arXiv:0803.3465 [astro-ph]].

[205] Y. I. Izotov and T. X. Thuan, Astrophys. J. **710**, L67 (2010) [arXiv:1001.4440 [astro-ph.CO]].

[206] G. Mangano and P. D. Serpico, Phys. Lett. B **701**, 296 (2011) [arXiv:1103.1261 [astro-ph.CO]].

[207] M. Pettini and R. Cooke, [arXiv:1205.3785 [astro-ph.CO]].

[208] G. Steigman, Adv. High Energy Phys. **2012**, 268321 (2012) [arXiv:1208.0032 [hep-ph]].

[209] W. J. Percival *et al.* [SDSS Collaboration], Mon. Not. Roy. Astron. Soc. **401**, 2148 (2010) [arXiv:0907.1660 [astro-ph.CO]].

[210] E. Komatsu *et al.* [WMAP Collaboration], Astrophys. J. Suppl. **192**, 18 (2011) [arXiv:1001.4538 [astro-ph.CO]].

[211] M. C. Gonzalez-Garcia, M. Maltoni and J. Salvado, JHEP **1008**, 117 (2010) [arXiv:1006.3795 [hep-ph]].

[212] J. Dunkley *et al.*, Astrophys. J. **739**, 52 (2011) [arXiv:1009.0866 [astro-ph.CO]].

[213] Z. Hou, R. Keisler, L. Knox, M. Millea and C. Reichardt, [arXiv:1104.2333 [astro-ph.CO]].

[214] R. Keisler *et al.*, Astrophys. J. **743**, 28 (2011) [arXiv:1105.3182 [astro-ph.CO]].

[215] M. Moresco, A. Cimatti, R. Jimenez, L. Pozzetti, G. Zamorani, M. Bolzonella, J. Dunlop and F. Lamareille *et al.*, JCAP **1208**, 006 (2012) [arXiv:1201.3609 [astro-ph.CO]].

[216] G. Hinshaw, D. Larson, E. Komatsu, D. N. Spergel, C. L. Bennett, J. Dunkley, M. R. Nolta and M. Halpern *et al.*, [arXiv:1212.5226 [astro-ph.CO]].

[217] Z. Hou, C. L. Reichardt, K. T. Story, B. Follin, R. Keisler, K. A. Aird, B. A. Benson and L. E. Bleem *et al.*, [arXiv:1212.6267 [astro-ph.CO]].

[218] E. Di Valentino, S. Galli, M. Lattanzi, A. Melchiorri, P. Natoli, L. Pagano and N. Said, [arXiv:1301.7343 [astro-ph.CO]].

[219] E. Calabrese, R. A. Hlozek, N. Battaglia, E. S. Battistelli, J. R. Bond, J. Chluba, D. Crichton and S. Das *et al.*, [arXiv:1302.1841 [astro-ph.CO]].

[220] M. Benetti, M. Gerbino, W. H. Kinney, E. W. Kolb, M. Lattanzi, A. Melchiorri, L. Pagano and A. Riotto, [arXiv:1303.4317 [astro-ph.CO]].

[221] L. A. Anchordoqui, H. Goldberg and B. Vlcek, *Tracing the Interplay between Non-Thermal Dark Matter and Right-Handed Dirac Neutrinos with LHC Data,* in Proceedings of the 33rd International Cosmic Ray Conference (ICRC 2013), Rio de Janeiro, Brazil, 2 - 9 July; [arXiv:1305.0146 [astro-ph.CO.]].

[222] G. Steigman, D. N. Schramm and J. E. Gunn, Phys. Lett. B **66**, 202 (1977).

[223] M. C. Gonzalez-Garcia, M. Maltoni, J. Salvado and T. Schwetz, JHEP **1212**, 123 (2012) [arXiv:1209.3023 [hep-ph]].

[224] L. A. Anchordoqui and H. Goldberg, Phys. Rev. Lett. **108**, 081805 (2012) [arXiv:1111.7264 [hep-ph]].

[225] A. Solaguren-Beascoa and M. C. Gonzalez-Garcia, Phys. Lett. B **719**, 121 (2013) [arXiv:1210.6350 [hep-ph]].

[226] L. A. Anchordoqui, H. Goldberg and G. Steigman, Phys. Lett. B **718**, 1162 (2013) [arXiv:1211.0186 [hep-ph]].

[227] J. Hamann, S. Hannestad, G. G. Raffelt, I. Tamborra and Y. Y. Y. Wong, Phys. Rev. Lett. **105**, 181301 (2010) [arXiv:1006.5276 [hep-ph]].

[228] L. M. Krauss, C. Lunardini and C. Smith, [arXiv:1009.4666 [hep-ph]].

[229] K. Ichikawa, M. Kawasaki, K. Nakayama, M. Senami and F. Takahashi, JCAP **0705**, 008 (2007) [arXiv:hep-ph/0703034].

[230] J. Hasenkamp, Phys. Lett. B **707**, 121 (2012) [arXiv:1107.4319 [hep-ph]].

[231] J. L. Menestrina and R. J. Scherrer, Phys. Rev. D **85**, 047301 (2012) [arXiv:1111.0605 [astro-ph.CO]].

[232] J. L. Feng, V. Rentala and Z. 'e. Surujon, Phys. Rev. D **85**, 055003 (2012) [arXiv:1111.4479 [hep-ph]].

[233] D. Hooper, F. S. Queiroz and N. Y. Gnedin, Phys. Rev. D **85**, 063513 (2012) [arXiv:1111.6599 [astro-ph.CO]].

[234] O. E. Bjaelde, S. Das and A. Moss, JCAP **1210**, 017 (2012) [arXiv:1205.0553 [astro-ph.CO]].

[235] J. Hasenkamp and J. Kersten, [arXiv:1212.4160 [hep-ph]].

[236] P. Di Bari, S. F. King and A. Merle, [arXiv:1303.6267 [hep-ph]].

[237] C. M. Ho and R. J. Scherrer, Phys. Rev. D **87**, 023505 (2013) [arXiv:1208.4347 [astro-ph.CO]].

[238] C. M. Ho and R. J. Scherrer, Phys. Rev. D 87, **065016** (2013) [arXiv:1212.1689 [hep-ph]].

[239] G. Steigman, [arXiv:1303.0049 [astro-ph.CO]].

[240] C. Brust, D. E. Kaplan and M. T. Walters, [arXiv:1303.5379 [hep-ph]].

[241] G. Jungman, M. Kamionkowski and K. Griest, Phys. Rept. **267**, 195 (1996) [arXiv:hep-ph/9506380].

[242] G. Bertone, D. Hooper and J. Silk, Phys. Rept. **405**, 279 (2005) [arXiv:hep-ph/0404175].

[243] J. L. Feng, Ann. Rev. Astron. Astrophys. **48**, 495 (2010) [arXiv:1003.0904 [astro-ph.CO]].

[244] M. C. Gonzalez-Garcia, V. Niro and J. Salvado, [arXiv:1212.1472 [hep-ph]].

[245] K. R. Dienes and B. Thomas, Phys. Rev. D **85**, 083523 (2012) [arXiv:1106.4546 [hep-ph]].

[246] S. Schael *et al.* [ALEPH Collaboration, DELPHI Collaboration, L3 Collaboration, OPAL Collaboration, SLD Collaboration, LEP Electroweak Working Group, and SLD Electroweak and Heavy Flavour Groups], Phys. Rept. **427**, 257 (2006) [arXiv:hep-ex/0509008].

[247] M. Laine and Y. Schroder, Phys. Rev. D **73**, 085009 (2006) [hep-ph/0603048].

[248] A. Bazavov *et al.*, Phys. Rev. D **80**, 014504 (2009) [arXiv:0903.4379 [hep-lat]].

[249] J. M. Thijssen. *Computational Physics*. (Cambridge University Press, Cambridge UK 1999).

[250] U. M. Heller, F. Karsch and B. Sturm, Phys. Rev. D **60**, 114502 (1999) [arXiv:hep-lat/9901010].

[251] G. Steigman, B. Dasgupta and J. F. Beacom, Phys. Rev. D **86**, 023506 (2012) [arXiv:1204.3622 [hep-ph]].

[252] K. Cheung, W.-Y. Keung, and T.-C. Yuan, [arXiv:1308.4235].

[253] G. Abbiendi *et al.* [OPAL Collaboration], Phys. Lett. B **682**, 381 (2010) [arXiv:0707.0373 [hep-ex]].

[254] J. R. Ellis, K. Enqvist, D. V. Nanopoulos and S. Sarkar, Phys. Lett. B **167**, 457 (1986).

[255] M. C. Gonzalez-Garcia and J. W. F. Valle, Phys. Lett. B **240**, 163 (1990).

[256] J. L. Lopez and D. V. Nanopoulos, Phys. Lett. B **241**, 392 (1990).

[257] V. Barger, P. Langacker and H. S. Lee, Phys. Rev. D **67**, 075009 (2003) [arXiv:hep-ph/0302066].

[258] G. Aad *et al.* [ATLAS Collaboration], JHEP **1211**, 138 (2012) [arXiv:1209.2535 [hep-ex]].

[259] S. Chatrchyan *et al.* [CMS Collaboration], Phys. Lett. B **720**, 63 (2013) [arXiv:1212.6175 [hep-ex]].

[260] D. Cremades, L. E. Ibanez and F. Marchesano, JHEP **0307**, 038 (2003) [arXiv:hep-th/0302105].

[261] G. Aad *et al.* [ATLAS Collaboration], JHEP **1301**, 029 (2013) [arXiv:1210.1718 [hep-ex]].

[262] S. Chatrchyan *et al.* [CMS Collaboration], JHEP **1301**, 013 (2013) [arXiv:1210.2387 [hep-ex]].

[263] S. Chatrchyan *et al.* [CMS Collaboration], [arXiv:1302.4794 [hep-ex]].

[264] R.H. Cyburt, J.R. Ellis, B.D. Fields and K.A. Olive, Phys. Rev. D **67**, 103521 (2003).

[265] J.L. Feng, A. Rajaraman and F. Takayama, Phys. Rev. D **68**, 063504 (2003).

[266] A. L. Fitzpatrick, D. Hooper and K. M. Zurek, Phys. Rev. D **81**, 115005 (2010) [arXiv:1003.0014 [hep-ph]].

[267] S. Chang, J. Liu, A. Pierce, N. Weiner and I. Yavin, JCAP **1008**, 018 (2010) [arXiv:1004.0697 [hep-ph]].

[268] D. Hooper, J. I. Collar, J. Hall, D. McKinsey and C. Kelso, Phys. Rev. D **82**, 123509 (2010) [arXiv:1007.1005 [hep-ph]].

[269] M. R. Buckley, D. Hooper and T. M. P. Tait, Phys. Lett. B **702**, 216 (2011) [arXiv:1011.1499 [hep-ph]].

[270] L. Goodenough and D. Hooper, [arXiv:0910.2998 [hep-ph]].

[271] D. Hooper and L. Goodenough, Phys. Lett. B **697**, 412 (2011) [arXiv:1010.2752 [hep-ph]].

[272] D. Hooper and T. Linden, Phys. Rev. D **84**, 123005 (2011) [arXiv:1110.0006 [astro-ph.HE]].

[273] K. N. Abazajian and M. Kaplinghat, Phys. Rev. D **86**, 083511 (2012) [arXiv:1207.6047 [astro-ph.HE]].

[274] D. Hooper and T. R. Slatyer, Phys. Dark Univ. (to be published) [arXiv:1302.6589 [astro-ph.HE]].

[275] M. Su, T. R. Slatyer and D. P. Finkbeiner, Astrophys. J. **724**, 1044 (2010) [arXiv:1005.5480 [astro-ph.HE]].

[276] G. Dobler, D. P. Finkbeiner, I. Cholis, T. R. Slatyer and N. Weiner, Astrophys. J. **717**, 825 (2010) [arXiv:0910.4583 [astro-ph.HE]].

[277] D. P. Finkbeiner, Astrophys. J. **614**, 186 (2004) [arXiv:astro-ph/0311547].

[278] P. A. R. Ade *et al.* [Planck Collaboration], [arXiv:1208.5483 [astro-ph.GA]].

[279] S. L. Snowden, R. Egger, M. J. Freyberg, D. McCammon, P. P. Plucinsky, W. T. Sanders, J. H. M. Schmitt and J. Truemper *et al.*, Astrophys. J. **485**, 125 (1997).

[280] P. Mertsch and S. Sarkar, Phys. Rev. Lett. **107**, 091101 (2011) [arXiv:1104.3585 [astro-ph.HE]].

[281] D. Hooper, I. Cholis, T. Linden, J. Siegal-Gaskins and T. Slatyer, [arXiv:1305.0830 [astro-ph.HE]].

[282] F. Iocco, M. Pato, G. Bertone and P. Jetzer, JCAP **1111**, 029 (2011) [arXiv:1107.5810 [astro-ph.GA]].

[283] D. Hooper, Phys. Dark Univ. **1**, 1 (2012) [arXiv:1201.1303 [astro-ph.CO]].

[284] D. Hooper, F. Petriello, K. M. Zurek and M. Kamionkowski, Phys. Rev. D **79**, 015010 (2009) [arXiv:0808.2464 [hep-ph]].

[285] R. Kappl and M. W. Winkler, Nucl. Phys. B **850**, 505 (2011) [arXiv:1104.0679 [hep-ph]].

[286] E. Aprile *et al.* [XENON100 Collaboration], Phys. Rev. Lett. **107**, 131302 (2011) [arXiv:1104.2549 [astro-ph.CO]].

[287] M. Ackermann *et al.* [Fermi-LAT Collaboration], Phys. Rev. Lett. **107**, 241302 (2011) [arXiv:1108.3546 [astro-ph.HE]].

[288] A. Geringer-Sameth and S. M. Koushiappas, Phys. Rev. Lett. **107**, 241303 (2011) [arXiv:1108.2914 [astro-ph.CO]].

[289] M. Ackermann *et al.*, JCAP **1005**, 025 (2010) [arXiv:1002.2239 [astro-ph.CO]].

[290] K. N. Abazajian, P. Agrawal, Z. Chacko and C. Kilic, JCAP **1011**, 041 (2010) [arXiv:1002.3820 [astro-ph.HE]].

[291] A. A. Abdo *et al.* [Fermi-LAT Collaboration], JCAP **1004**, 014 (2010) [arXiv:1002.4415 [astro-ph.CO]].

[292] P. Sikivie, Phys. Rev. Lett. **48**, 1156 (1982).

[293] A. Vilenkin and A. E. Everett, Phys. Rev. Lett. **48**, 1867 (1982).

[294] C. T. Hill, D. N. Schramm and L. M. Widrow, FERMILAB-PUB-89-166-T.

[295] A. D. Linde and D. H. Lyth, Phys. Lett. B **246**, 353 (1990).

[296] M. S. Turner and F. Wilczek, Phys. Rev. Lett. **66**, 5 (1991).

[297] G. R. Dvali, Phys. Lett. B **265**, 64 (1991).

[298] T. Hiramatsu, M. Kawasaki, K. 'i. Saikawa and T. Sekiguchi, JCAP **1301**, 001 (2013) [arXiv:1207.3166 [hep-ph]].

[299] S. Chatrchyan *et al.* [CMS Collaboration], Phys. Lett. B **716**, 30 (2012) [arXiv:1207.7235 [hep-ex]].

[300] J. R. Espinosa, M. Muhlleitner, C. Grojean and M. Trott, JHEP **1209**, 126 (2012) [arXiv:1205.6790 [hep-ph]].

[301] P. P. Giardino, K. Kannike, I. Masina, M. Raidal and A. Strumia, [arXiv:1303.3570 [hep-ph]].

[302] J. Ellis and T. You, [arXiv:1303.3879 [hep-ph]].

[303] R. Bernabei, P. Belli, F. Montecchia, W. Di Nicolantonio, A. Incicchitti, D. Prosperi, C. Bacci and C. J. Dai *et al.*, Phys. Lett. B **424** 195 (1998).

[304] A. K. Drukier, K. Freese and D. N. Spergel, Phys. Rev. D **33** 3495 (1986).

[305] K. Freese, J. A. Frieman and A. Gould, Phys. Rev. D **37** 3388 (1988).

[306] R. Bernabei *et al.* [DAMA Collaboration], Eur. Phys. J. C **56** 333 (2008) [arXiv:0804.2741 [astro-ph]].

[307] F. Petriello and K. M. Zurek, JHEP **0809**, 047 (2008) [arXiv:0806.3989 [hep-ph]].

[308] J. Angle *et al.* [XENON10 Collaboration], Phys. Rev. Lett. **107**, 051301 (2011) [arXiv:1104.3088 [astro-ph.CO]].

[309] J. I. Collar, [arXiv:1010.5187 [astro-ph.IM]].

[310] J. I. Collar, [arXiv:1106.0653 [astro-ph.CO]].

[311] J. R. Ellis, A. Ferstl and K. A. Olive, Phys. Lett. B **481**, 304 (2000) [arXiv:hep-ph/0001005].

[312] M. Beltran, D. Hooper, E. W. Kolb and Z. C. Krusberg, Phys. Rev. D **80**, 043509 (2009) [arXiv:0808.3384 [hep-ph]].

[313] P. Gondolo and G. Gelmini, Nucl. Phys. B **360**, 145 (1991).

[314] T. J. Weiler, AIP Conf. Proc. **1534**, 165 (2012) [arXiv:1301.0021 [hep-ph]].

[315] W. -C. Huang, A. Urbano, W. Xue, [arXiv:1307.6862v1[hep-ph]].

[316] A. Sommerfeld, Annalen der Physik **403**, 257 (1931).

[317] N. Arkani-Hamed, D. P. Finkbeiner, T. R. Slatyer and N. Weiner, Phys. Rev. D **79**, 015014 (2009) [arXiv:0810.0713 [hep-ph]].

[318] S. Cassel, J. Phys. G **37**, 105009 (2010) [arXiv:0903.5307 [hep-ph]].

[319] J. L. Feng, M. Kaplinghat and H. -B. Yu, Phys. Rev. D **82**, 083525 (2010) [arXiv:1005.4678 [hep-ph]].

[320] R. J. Scherrer and M. S. Turner, Phys. Rev. D **33**, 1585 (1986) [Erratum-ibid. D **34**, 3263 (1986)].

[321] J. B. Dent, S. Dutta and R. J. Scherrer, Phys. Lett. B **687**, 275 (2010) [arXiv:0909.4128 [astro-ph.CO]].

[322] J. Chen and Y. -F. Zhou, JCAP **1304**, 017 (2013) [arXiv:1301.5778 [hep-ph]].

[323] E. Aprile [XENON1T Collaboration], [arXiv:1206.6288 [astro-ph.IM]].

[324] J. Lavalle, Phys. Rev. D **82**, 081302 (2010) [arXiv:1007.5253 [astro-ph.HE]].

[325] C. Evoli, I. Cholis, D. Grasso, L. Maccione and P. Ullio, Phys. Rev. D **85**, 123511 (2012) [arXiv:1108.0664 [astro-ph.HE]].

[326] R. Kappl and M. W. Winkler, Phys. Rev. D **85**, 123522 (2012) [arXiv:1110.4376 [hep-ph]].

[327] D. S. Akerib *et al.* [LUX Collaboration], Nucl. Instrum. Meth. A **704**, 111 (2013) [arXiv:1211.3788 [physics.ins-det]].

[328] D. J. Koskinen, Mod. Phys. Lett. A **26**, 2899 (2011).

[329] CMS Collaboration, *Projected Performance of an Upgraded CMS Detector at the LHC and HL-LHC: Contribution to the Snowmass Process* CMS-NOTE-13-002 [arXiv:1307.7135 [hep-ex]].

[330] L. A. Anchordoqui and B. Vlcek, Phys. Rev. D **88**, 043513 (2013) [arXiv:1305.4625 [hep-ph]].

[331] S. J. Waldman, (LIGO Scientific Collaboration) LIGO P0900115-v2 [arXiv:1103.2728 [gr-qc]].

[332] J. Crowder and N. J. Cornish, Phys. Rev. D **72**, 083005 (2005) [arXiv:gr-qc/0506015].

Brian J. Vlcek   *Curriculum Vitae*

Work Address

University of Wisconsin-Milwaukee

Department of Physics   e-mail: bvlcek@uwm.edu

1900 E. Kenwood Blvd.

Milwaukee, WI 53211 USA

Research Interests

- Theoretical high energy particle physics, with interests of beyond the standard model physics.

- High energy particle physics phenomenology.

- Astroparticle physics, and cosmology.

Education

PhD: University of Wisconsin-Milwaukee   (Milwaukee, WI)   Sept 2007 - Current

Graduation Date: August 2013 (GPA = 3.693/4.0)

Co-Advisors: Associate Professor Xavier Siemens and

Associate Professor Luis Anchordoqui.

Dissertation Title: "Beyond the Standard Model: LHC Phenomenology, Cosmology from Post-Inflationary Sources, and Dark Matter."

BSc: Illinois State University   (Bloomington-Normal, IL)   Aug. 2004 - May 2007

Graduated May 2007 with focus on Computational Physics. (Final GPA = 3.52/4.0)

Relavant Work Experience

Research Assistant (UW-Milwaukee)   Jan 2013- Aug 2013

Completed research with Luis Anchordoqui on projects concerning extensions of the Standard Model of particle physics.

Graduate Teaching Assistant (UW-Milwaukee)   Sept 2007 - Dec 2012

Taught various undergraduate level courses for the department of Physics.

11 courses taught, with an average evaluation score of $3.2/4.0$.

LIGO Collaboration Scientific Monitor (Hanford, WA USA)   Aug - Sept 2010

On-site observation of LIGO telescope for data quality monitoring.

Preparation Class Leader for Phd Written Qualifying Exam (UW-Milwaukee)

Jan '09, '10, '11
Invited/chosen by members of physics faculty to lead an open study session to assist 1st and
2nd year students in the department in preparation for taking the Spring semester qualifying
exam.

Graduate Astro-club TA/"Arciebo@UWM" Trainer (UW-Milwaukee)
Sept '09 - Sept '11
Trained undergraduates on how to analyze pulsar data for proper identification of possible pul-
sars, as well as monitoring students during remote usage of the Arciebo radio telescope for
pulsar search surveys. Additionally handled duties associated with hosting the UWM Astron-
omy Club.

Undergraduate Research Assistant (Illinois State Univ. Bloomington-Normal, IL) May '05 -
Sept '07
Conducted research in computational simulation of chaotic systems under the supervision of
Associate Professor Epaminondas Rosa Jr.

University Employed Tutor (Illinois State Univ. Bloomington-Normal, IL) May '05 - Sept '07
University employed tutor in math and physics (by appointment) available for all under-graduate
students, including specific tutoring for student athletes.

Skills

- 12+ years programing in C/C++

- 6+ years programming in Mathematica.

- Moderate level experience with UNIX systems.

Honors and Awards

**Univ. of Wisconsin- Milwaukee "Chancellor's Graduate Student Award" and "Research
Excellence Award"**
Competitive award given in order to supplement TA/RA salaries. Received this award/support
in numerous semesters during my PhD studies at UW-Milwaukee.

Skadron Computational Physics Award for Research   **2007 Recipient**
Award for outstanding research involving simulation by undergraduate physics student at Illi-
nois State University.

Skadron Prize Competition   **1st prize recipient - 2007**
1st prize recipient, in collaboration with Michael P. Morrissey, on programing/simulation com-
petition, hosted by the Physics Department at Illinois State University.

Talks, Conferences and Workshops

33rd International Cosmic Ray Conference (poster presentation) July 2013
Presented poster on non-thermal dark matter as explanation of excess relativistic degrees of
freedom from Planck and HST data, hosted by Centro Brasileiro de Pesquisas Fsicas (CBPF)
(Rio de Janeiro, RJ, Brazil)

Phenomenology 2010 Symposium (presenter) May 2010
Presented on gravitational wave cosmology and its relation to high energy physics; hosted by
University of Wisconsin-Madison (Madison, WI)

UW-Milwaukee, Center for Gravitation and Cosmology (presenter) May 20, 2011.
Friday seminar series attended by members of UWM's "Center for Gravitation and Cosmology"
(which includes graduate students, post docs and faculty). Talk title was: "Gravitational Waves
from Pre-Heating and Phase Transitions," which focused on my research of gravitational wave
cosmology, specifically on computational methods that improve the standard ways of calculat-
ing a stochastic background of gravitational waves from a phase transition in the early universe.

Gravitational-wave Physics and Astronomy Workshop (Attendee) January 2011
Hosted by University Wisconsin-Milwaukee (Milwaukee, WI)

20th Annual Midwest Relativity Meeting (Attendee) November 2010
Hosted by University of Guelph (Guelph, Ontario - Canada)

Scholarly publications in refereed journals

- "W-WIMP Annihilation as a Source of the Fermi Bubbles,"
  Luis A. Anchordoqui and **Brian J. Vlcek**,
  Phys. Rev. D **88**, 043513 (2013) [arXiv:1305.4625 [hep-ph]].

- "LHC phenomenology and cosmology of string-inspired intersecting D-brane models,"
  Luis A. Anchordoqui, Ignatios Antoniadis, Haim Goldberg, Xing Huang, Dieter Lüst,
  Tomasz R. Taylor, and **Brian Vlcek**,
  Phys. Rev. D **86**, 6 066004 (2012) [arXiv:1206.2537 [hep-ph]].

- "Vacuum Stability of SM++,"
  Luis A. Anchordoqui, Ignatios Antoniadis, Haim Goldberg, Xing Huang, Dieter Lüst,
  Tomasz R. Taylor, and **Brian Vlcek**,
  JHEP **1302**, 074 (2013) [arXiv:1208.2821[hep-ph]].

- "Gravitational Waves from Global Second Order Phase Transitions."
  John. T. Giblin, Jr., Larry R. Price, Xavier Siemens, and **Brian Vlcek**,
  JCAP **11**, 006 (2012) [arXiv:1111.4014 [astro-ph]].

Publications in conference proceedings

- "Tracing the Interplay between Non-Thermal Dark Matter and Right-Handed Dirac Neutrinos with LHC Data."
  Luis A. Anchordoqui, Haim Goldberg and **Brian Vlcek**;
  in Proceedings of the 33rd International Cosmic Ray Conference (ICRC 2013), Rio de Janeiro, Brazil, 2 - 9 July 2013 [arXiv:1305.0146 [astro-ph.CO.]].